Micropatterned Superconducting Film Circuitry for Operation in Hybrid Quantum Devices

Dissertation
der Mathematisch-Naturwissenschaftlichen Fakultät
der Eberhard Karls Universität Tübingen
zur Erlangung des Grades eines
Doktors der Naturwissenschaften
(Dr.rer.nat.)

vorgelegt von
Dipl.-Phys. Daniel Bothner
aus Filderstadt

Tübingen
2013

Tag der mündlichen Qualifikation:	10. 12. 2013
Dekan:	Prof. Dr. Wolfgang Rosenstiel
1. Berichterstatter	Prof. Dr. Reinhold Kleiner
2. Berichterstatter	Prof. Dr. Dieter Kölle
3. Berichterstatter	Prof. Dr. Britton Plourde

Abstract

This thesis discusses three aspects of the arduous way towards hybrid quantum systems consisting of superconducting circuits and ensembles of ultracold paramagnetic atoms. Such hybrid systems have been proposed in quantum information technology where the superconducting circuits constitute the processing unit and the atoms constitute a long lived quantum memory. Other exciting possibilities of such hybrid systems are the generation of a quantum transducer between photons in the microwave and photons in the optical regime or the realization of an on-chip microMASER. Very recently another interesting idea based on combining the two systems was raised. The vortex lattice in a superconducting film with possible lengthscales below those of optical lattices could be used as a nanoengineered magnetic potential landscape for atoms which would allow to enter a new regime of atomic interaction stength and possible potential symmetries. In all of these hybrid systems, the superconducting circuits are operated in magnetic fields which is required for the trapping and the manipulation of external and internal degrees of freedom of the atoms. Therefore the superconducting devices have to be investigated, optimized and tailored for the implementation in a magnetic environment.

In the first part of the thesis, superconducting coplanar microwave resonators as used for quantum information processing with superconducting qubits are investigated in magnetic fields. Such resonators are proposed as a quantum bus between superconducting qubits and atomic ensembles. Crucial for an efficient quantum state transfer between the subsystems hereby is that the coherence time of a single excitation in the resonator is much longer than the transfer time which it takes to swap the state from the resonator to the ensemble. By the penetration of energy dissipating and noisy Abrikosov vortices in a magnetic field, the performance of superconducting resonators, however, is considerably reduced to a level below that requirement. Different strategies to minimize this reduction of the performance due to vortices are explored in the first part of the thesis. We pattern the resonators with micrometric and submicrometric holes (antidots) which are supposed to trap and pin the vortices in order to suppress their harmful dissipative motion. Moreover, we investigate the influence of magnetic history on the resonator properties by spectroscopic characterization and by magneto-optical imaging. Finally, we develop a model for the vortex associated dissipation in order to explain the found hysteretic behaviour. Our efforts and investigations give new insights into the properties of superconducting resonators in magnetic fields and lead to an achieved vortex associated loss reduction by up to a factor of 40, approaching the required loss level for quantum information processing.

In the second part of the thesis integrated atom chips are designed and fabricated, which offer the possibility to trap an ensemble of ultracold atoms close to a superconducting coplanar resonator on that chip. By means of experimental observations and numerical simulations the atom trap position and properties on the atom chip are investigated, hereby focusing on the particularities related to field distortions due to the Meissner effect and related to magnetic flux conservation in superconducting closed loops. The flux conservation also allows to explore the possibility of creating a persistent current on-chip trap with the resonator leads. For the use of an atomic ensemble as quantum memory, a long coherence time of superposition states constitutes an indispensable prerequisite. Therefore, it is investigated within a collaboration with the Tübingen cold atom group whether the reported extraordinary coherence times of atomic ensembles on the order of tens of seconds can be maintained in the complex magnetic environment of a superconduting atom chip with resonator structures. In a second work, a novel integrated resonator trap design is proposed which is suitable to reduce the high structural complexity of the previously used atom chip without losing its functionality. By means of numerical simulations we investigate whether and how the atoms can be transferred to desirable positions on the chip while keeping the trap properties in a parameter regime favorable for quantum information purposes. In summary, the studies show that ultracold atoms on an atomchip with integrated resonator structures can be brought into the mode volume of the resonator and that atomic lifetimes and atomic coherence times suitable for quantum information processing can be achieved there.

In the third and last part of the thesis, unconventional disordered and quasiperiodic arrangements of microfabricated holes (antidots) in superconducting films are patterned and investigated with respect to the impact of the arrangement on the superconductor transport properties in magnetic fields. The focus hereby lies on identifying novel commensurable states between a vortex lattice and the antidot array by measuring the critical current for different temperatures and magnetic fields. Particularly stable states of the vortices in a given pinning array are then identified as maxima of the critical current for certain vortex densities. In the first experiment, disorder is gradually introduced into a periodic array of antidots by randomly removing a fraction of them. Both the static and the dynamic properties of Abrikosov vortices in these samples are investigated dependent on the amount of disorder. Secondly, we investigate a system of antidots patterned by a technique based on the self-assembly of sub-micrometric spheres. Although the resulting array is locally highly ordered, this system incorporates natural disorder on larger lengthscales due to the imperfect self-assembling process. Finally, superconducting film structures with several different quasiperiodic antidot arrangements are investigated by means of numerical simulations and transport measurements. The data reveal that, with respect to periodic arrays, pinning arrays with reduced symmetry can show favorable properties regarding the optimization of superconducting devices operated in the vortex state such as a reduced vortex velocity. Moreover, several unconventional vortex arrangements are identified in these arrays, which could be used as magnetic potential landscapes for atoms and which are impossible to be created by means of optical potentials.

The results presented and discussed in this thesis strongly encourage the continuation of the research towards hybrid systems consisting of superconducting circuits and ultracold atomic ensembles.

Kurzfassung

Die vorliegende Arbeit diskutiert drei Aspekte des beschwerlichen Weges in Richtung hybrider Quantensysteme bestehend aus supraleitenden Schaltkreisen und Ensembles ultrakalter paramagnetischer Atome. Derartige Hybridsysteme wurden im Bereich der Quanteninformationstechnologie vorgeschlagen, wobei die supraleitenden Schaltkreise als Quantenprozessor eingesetzt werden und die Atome als Quantenspeicher dienen. Weitere spannende Einsatzmöglichkeiten solcher Hybridsysteme sind die Herstellung eines Quantenwandlers zwischen Photonen des Mikrowellenspektrums und Photonen des optischen Spektrums oder die Realisierung eines Mikro-MASERs auf einem Chip. Kürzlich wurde eine weitere interessante Idee basierend auf der Kombinierung der beiden Systeme vorgeschlagen. Das Vortexgitter in einem supraleitenden Film mit möglichen Längenskalen unter denen optischer Gitter könnte demnach als nano-fabrizierte magnetische Potentiallandschaft für Atome verwendet werden, wodurch ein neuer Bereich der atomaren Wechselwirkungsstärke und möglicher Potentialsymmetrien in derartigen Modellsystemen zugänglich würde. In all diesen hybriden Systemen werden die supraleitenden Elemente in einem Magnetfeld betrieben, das benötigt wird um die Atome einzufangen und deren innere und äußere Freiheitsgrade zu beeinflussen. Für einen entsprechenden Einsatz müssen die supraleitenden Bauelemente daher bezüglich ihrer Eigenschaften in einer magnetischen Umgebung charakterisiert, optimiert und maßgeschneidert werden.

Im ersten Teil der vorliegenden Arbeit werden supraleitende koplanare Mikrowellenresonatoren, welche in der Quanteninformationsverarbeitung mit supraleitenden Qubits Verwendung finden, in Magnetfeldern untersucht. Solche Resonatoren wurden als Quantenbus zwischen supraleitenden Quantenbits und atomaren Ensembles vorgeschlagen. Einen kritischen Aspekt für den effizienten Transfer eines Quantenzustandes zwischen den Untersystemen stellt dabei die Kohärenzzeit einer einzelnen Anregung im Resonator dar, die deutlich länger sein sollte als die Zeitspanne, die für den Transfer vom Resonator in das Ensemble benötigt wird. Durch das Eindringen von Abrikosov Flussquanten in einem Magnetfeld, die Energie dissipieren und eine Rauschquelle darstellen, werden jedoch die Eigenschaften supraleitender Resonatoren dahingehend modifiziert, dass sie dieser Anforderung nicht mehr genügen. Im ersten Teil der Arbeit werden unterschiedliche Ansätze untersucht die unerwünschte Veränderung der Resonatoreigenschaften durch Abrikosov Flusswirbel (Vortizes) zu minimieren. Zum einen werden Resonatoren mit integrierten Löchern (Antidots) auf der Größenskala von Mikrometern und darunter strukturiert, deren Zweck darin besteht die Vortizes einzufangen und festzuhalten, und sie damit an einer dissipativen Bewegung zu hindern. Darüberhinaus wird mittels spektroskopischer Charakterisierungsmessungen und magneto-optischer Abbildungen der Einfluss der magnetischen Vorgeschichte auf die Resonatoreigenschaften untersucht. Um das hierbei gefundene hys-

teretische Verhalten zu erklären, wird schließlich ein Modell für die Verluste im Resonator entwickelt, die mit der Anwesenheit von Abrikosov Vortizes einhergehen. Die vorgestellten Ansätze und Untersuchungen gewähren neue Einsichten in die Eigenschaften supraleitender Resonatoren in Magnetfeldern. Sie erlauben im bisher besten Fall eine Reduktion der mit den Vortizes verknüpften Verlusten um einen Faktor 40, wodurch die Verlustraten in einen Bereich kommen, der für die Quanteninformationsarbeitung geeignet ist.

Im zweiten Teil der Arbeit werden integrierte Atomchips entworfen und hergestellt, die die Möglichkeit eröffnen ein Ensemble ultrakalter Atome in die Nähe eines supraleitenden koplanaren Resonators auf demselben Chip zu bringen. Mittels experimenteller Beobachtungen und numerischer Simulationen werden die Position und die Eigenschaften der Atomfalle untersucht, wobei der Fokus auf den Besonderheiten liegt, die mit den Magnetfeldverzerrungen aufgrund des Meissner-Effektes und der Erhaltung des magnetischen Flusses in geschlossenen supraleitenden Schleifen verknüpft sind. Die Flusserhaltung erlaubt es darüberhinaus, die Möglichkeit zu untersuchen, eine Atomfalle auf dem Chip zu erzeugen, die durch zirkulierende Dauerströme in den Leiterbahnen der Resonatorstruktur erzeugt wird. Für die Verwendung eines atomaren Ensembles als Quantenspeicher stellt eine lange Kohärenzzeit von Superpositionszuständen eine unerlässliche Voraussetzung dar. Daher wird im Rahmen einer Zusammenarbeit mit der Tübinger Arbeitsgruppe für die Physik kalter Atome untersucht, ob die früher berichteten, außergewöhnlich langen Kohärenzzeiten atomarer Ensembles in der Größenordnung einiger zehn Sekunden auch in der komplexen magnetischen Umgebung eines supraleitenden Chips mit Resonatorstrukturen erhalten werden können. In einer zweiten Arbeit wird eine neuartige, integrierte Resonatorfalle vorgeschlagen, die geeignet ist, die hohe strukturelle Komplexität des bisher verwendeten Atomchips zu reduzieren ohne dessen Funktionalität einzuschränken. Mittels numerischer Simulationen wird untersucht, ob und wie die Atome zu den gewünschten Positionen auf dem Chip geführt werden können und ob währenddessen die Eigenschaften der Falle in einem Parameterbereich gehalten werden, der für die Quanteninformationsverarbeitung geeignet ist. Zusammenfassend zeigen unsere Untersuchungen, dass ultrakalte Atome auf einem Atomchip mit integrierten Resonatorstrukturen in das Modenvolumen eines supraleitenden Resonators gebracht werden können und dass dort für die Quanteninformationsverarbeitung geeignete atomare Lebensdauern und Kohärenzzeiten erzielt werden können.

Im dritten und letzten Teil der Arbeit werden supraleitende Filme mit unkonventionellen ungeordneten und quasiperiodischen Anordnungen mikrostrukturierter Löcher (Antidots) hergestellt und im Hinblick auf den Einfluss der jeweiligen Anordnung auf die Transporteigenschaften der Filme in Magnetfeldern untersucht. Der Schwerpunkt liegt dabei darauf, durch die Messung des kritischen Stromes für verschiedene Temperaturen und Magnetfeldwerte neuartige kommensurable Zustände zwischen einem Vortexgitter und der Antidotanordnung zu identifizieren. Besonders stabile Zustände der Vortizes in einer gegebenen Antidotanordnung äußern sich hierbei als Maxima des kritischen Stromes für bestimmte Vortexdichten. Im ersten Experiment wird schrittweise Unordnung in eine periodische Antidotanordnung eingebracht, indem ein bestimmter Anteil davon nach dem Zufallsprinzip entfernt wird. In Abhängigkeit des Grades an Unordnung werden sowohl die statischen als auch die dynamischen Eigenschaften der Abrikosov Vortizes in diesen Proben untersucht. Als zweites wird ein System von Antidots untersucht, die durch eine

Technik basierend auf der Selbstorganisation von Kugeln mit einem Durchmesser unter einem Mikrometer strukturiert wurden. Obwohl die daraus resultierende Anordnung lokal eine hohe Ordnung aufweist, beinhaltet das System durch den unvollkommenen Prozess der Selbstorganisation eine natürliche Unordnung auf größeren Längenskalen. Schließlich werden mittels numerischer Simulationen und Transportmessungen mehrere supraleitende Filmstrukturen mit unterschiedlichen quasiperiodischen Antidotanordnungen untersucht. Die Daten zeigen auf, dass Pinninggitter mit reduzierter Symmetrie bezüglich der Optimierung supraleitender Bauelemente, die im Vortex-Zustand betrieben werden, vorteilhafte Eigenschaften wie eine reduzierte Vortexgeschwindigkeit gegenüber periodischen Antidotanordnungen aufweisen können. Darüberhinaus können mehrere unkonventionelle Vortexverteilungen in diesen Anordnungen identifiziert werden, die als magnetische Potentiallandschaften für Atome dienen könnten und die nicht mittels optischen Potentialen erzeugt werden können.

Die in dieser Arbeit vorgestellten und diskutierten Ergebnisse sind höchst ermutigend, die Forschung an hybriden Quantensystemen bestehend aus supraleitenden Schaltkreisen und ultrakalten atomaren Ensembles fortzusetzen.

Contents

List of publications

Appended publications

Publication I **D. Bothner**, T. Gaber, M. Kemmler, D. Koelle, and R. Kleiner
Improving the performance of superconducting microwave resonators in magnetic fields
Appl. Phys. Lett. **98**, 102504 (2011)

Publication II **D. Bothner**, T. Gaber, M. Kemmler, D. Koelle, R. Kleiner, S. Wünsch, and M. Siegel
Magnetic hysteresis effects in superconducting coplanar microwave resonators
Phys. Rev. B **86**, 014517 (2012)

Publication III **D. Bothner**, C. Clauss, E. Koroknay, M. Kemmler, T. Gaber, M. Jetter, M. Scheffler, P. Michler, M. Dressel, D. Koelle, and R. Kleiner
Reducing vortex losses in superconducting microwave resonators with microsphere patterned antidot arrays
Appl. Phys. Lett. **100**, 012601 (2012)

Publication IV S. Bernon, H. Hattermann, **D. Bothner**, M. Knufinke, P. Weiss, F. Jessen, D. Cano, M. Kemmler, R. Kleiner, D. Koelle, and J. Fortágh
Manipulation and coherence of ultra-cold atoms on a superconducting atom chip
Nat. Commun. **4**, 2380 (2013)

Publication V **D. Bothner**, M. Knufinke, R. Wölbing, B. Ferdinand, H. Hattermann, S. Bernon, P. Weiss, J. Fortágh, R. Kleiner, and D. Koelle
Inductively coupled superconducting half wavelength resonators as persistent current traps for ultracold atoms
New J. Phys. **15**, 093024 (2013)

Publication VI M. Kemmler, **D. Bothner**, K. Ilin, M. Siegel, R. Kleiner, and D. Koelle
Suppression of dissipation in Nb thin films with triangular antidot arrays by random removal of pinning sites
Phys. Rev. B **79**, 184509 (2009)

Publication VII **D. Bothner**, C. Clauss, E. Koroknay, M. Kemmler, T. Gaber, M. Jetter, M. Scheffler, P. Michler, M. Dressel, D. Koelle, and R. Kleiner
The phase boundary of superconducting niobium thin films with antidot arrays fabricated with microsphere photolithography
Supercond. Sci. Technol. **25**, 065020 (2012)

Publication VIII V. R. Misko, **D. Bothner**, M. Kemmler, R. Kleiner, D. Koelle, F. M. Peeters, and F. Nori
Enhancing the critical current in quasiperiodic pinning arrays below and above the matching flux
Phys. Rev. B **79**, 184509 (2010)

Publication IX **D. Bothner**, R. Seidl, V. R. Misko, R. Kleiner, D. Koelle, and M. Kemmler
Unusual commensurability effects in quasiperiodic pinning arrays induced by local inhomogeneities of the pinning site density
submitted to Supercond. Sci. Technol. (2013)

Publications not included in this thesis

Publication X P. Bushev, **D. Bothner**, J. Nagel, M. Kemmler, K. B. Konovalenko, A. Loerincz, K. Ilin, M. Siegel, D. Koelle, R. Kleiner, and F. Schmidt-Kaler
Trapped electron coupled to superconducting devices
Eur. Phys. J. D **63**, 17 (2011)

Publication XI R. Werner, A. Yu. Aladyshkin, I. M. Nefedov, A. V. Putilov, M. Kemmler, **D. Bothner**, A. Loerincz, K. Ilin, M. Siegel, R. Kleiner, and D. Koelle
Edge superconductivity in Nb thin film microbridges revealed by electric transport measurements and visualized by scanning laser microscopy
Supercond. Sci. Technol. **26**, 095011 (2013)

Publication XII C. Clauss, **D. Bothner**, D. Koelle, R. Kleiner, L. Bogani, M. Scheffler, and M. Dressel
Broadband electron spin resonance from 500 MHz to 40 GHz using superconducting coplanar waveguides
Appl. Phys. Lett. **102**, 162601 (2013)

Acronyms and physical constants

List of acronyms in alphabetic order

AFM	Atomic force microscopy
dc	Direct current
FWHM	Full width at half maximum
GL	Ginzburg-Landau
GR	Gittleman-Rosenblum
KIT	Karlsruhe Institute of Technology
MASER	Microwave amplification by stimulated emission of radiation
MOI	Magneto-optical image/imaging
MOT	Magneto-optical trap
NBI	Norris-Brandt-Indenbom
NV	Nitrogen vacancy
QED	Quantum electrodynamics
qubit	Quantum binary digit
rf	Radio frequency
SEM	Scanning electron microscopy
TEM	Transversal electromagnetic mode
UV	Ultraviolet
YBCO	Yttrium barium copper oxide ($YBa_2Cu_3O_{7-x}$)

List of constants in alphabetical order

$c_0 = 2.998 \cdot 10^8\,\mathrm{m/s}$	Vacuum speed of light
$e = 1.602 \cdot 10^{-19}\,\mathrm{C}$	Elementary charge
$\Phi_0 = 2.07 \cdot 10^{-15}\,\mathrm{Tm^2}$	Magnetic flux quantum
$h = 6.626 \cdot 10^{-34}\,\mathrm{Js}$	Planck constant
$\hbar = h/2\pi = 1.055 \cdot 10^{-34}\,\mathrm{Js}$	Reduced Planck constant
$k_\mathrm{B} = 1.381 \cdot 10^{-23}\,\mathrm{J/K}$	Boltzmann constant
$\mu_0 = 4\pi \cdot 10^{-7}\,\mathrm{Vs/Am}$	Magnetic vacuum permeability
$\mu_\mathrm{B} = 9.274 \cdot 10^{-24}\,\mathrm{J/T}$	Bohr magneton
$\tau = (1+\sqrt{5})/2$	Golden mean

Chapter 1

Introduction

This introductory section gives a general overview regarding the contents, the motivation and the objectives of this thesis. As the thesis covers three different but strongly connected branches, these three individual topics and their interconnections are briefly described. Then, the general basics of all three sub-topics will be introduced, namely the phenomenology of type-II superconductors in magnetic fields, in particular the most important static and dynamic properties of Abrikosov vortices.

1.1 Motivation

The three different research topics which constitute this thesis have some very individual aspects and particularities but at the same time are strongly related. Thus, the present thesis can be viewed as one whole divided into three parts. Figure 1.1 shows a scheme of the three parts and their interconnections. The main common basis of the three parts are micropatterned superconducting thin film structures which are investigated and optimized for operation in magnetic fields with the ultimate goal to build hybrid quantum systems consisting of superconducting circuits and atomic systems.

The first part of the thesis is concerned with superconducting resonant circuits based on a coplanar guide for electromagnetic waves. Superconducting resonators working in the microwave domain are used in a big variety of experimental environments and for different applications. Threedimensional versions of superconducting microwave resonators have been used to investigate the interaction between single microwave photons and individual atoms. This has led to groundbreaking experiments and results which were awarded with the nobel prize in physics 2012. In these experiments, it has for instance been possible to non-destructively resolve the number of photons down to the single quantum level [1] or to carry out a real-time observation of the repeated appearance and disappearance of a single photon in the cavity [2].

Since 2004, it has been demonstrated that very similar experiments can be performed on a chip using superconducting circuits only [3, 4]. One essential building block for these experiments have been nonlinear superconducting circuits based on Josephson junctions which show macroscopic quantum behaviour at sufficiently low temperatures [5, 6]. Such

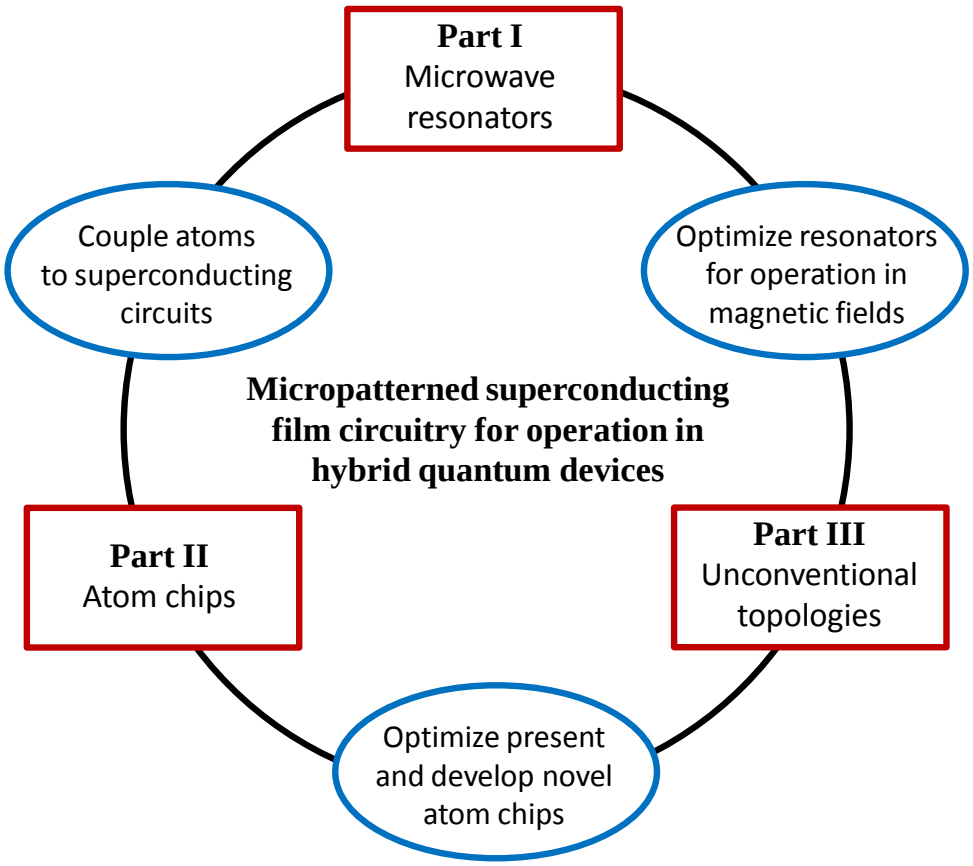

Figure 1.1: Schematic of the three research parts of this thesis and their main interconnections.

a nonlinear macroscopic quantum system can be viewed as an effective two-level system, i.e., as an artificial atom or a quantum binary digit (qubit). It can be placed inside a superconducting coplanar on-chip microwave cavity with resonance frequency $f_0 = \omega_0/2\pi$ as described in detail below which itself behaves as a harmonic quantum oscillator at a sufficiently low temperature T. The criterion for reaching the quantum ground state is given by $T \ll \hbar\omega_0/k_\mathrm{B}$, leading to required temperatures of approximately $T < 100\,\mathrm{mK}$ for frequencies in the GHz regime, which is easily achievable in typical dilution refrigerator systems. Due to the particular chip architecture with physically large qubits ($\sim 100\,\mu\mathrm{m}$) und quasi one-dimensional cavities, the dipole coupling between individual photons and single artificial atoms can be made several orders of magnitude stronger than with natural atoms in three-dimensional cavities. Moreover and in contrast to natural atoms, artificial atoms can be designed with desired properties and their position in the cavity is perfectly stationary.

During the last decade, there has been much pioneering work with such systems, regarding the creation of photon number states [7] or even arbitrary quantum states in such resonator-qubit devices [8], demonstrating the full quantum control over the electromagnetic fields. This has even led to the quantum control over the phonon state of a macroscopic mechanical resonator [9]. Other fundamental work with superconducting circuits targeted the spectroscopic investigation of the quantum nonlinearity in a

resonantly coupled atom-photon system [10], the ultrastrong coupling regime between a superconducting qubit and an electromagnetic mode [11, 12] or the creation of photons from vacuum by the circuit equivalence of a vibrating cavity mirror (dynamical Casimir effect) [13].

Another closely related area, in which superconducting resonators are considered as highly promising technological elements, is quantum information processing. Considerable progress has been made in this direction with superconducting qubits in coplanar resonators, starting from entangling two spatially separated qubits via one resonator [14, 15] to building elementary quantum information processors and solving simple quantum algorithms with systems of multiple qubits and resonators [16–22]. In these efforts, the resonators act as a bus for the quantum information and/or for buffering it on the order of nano- to microseconds. However, the long-time storage of quantum information constitutes a severe and yet unsolved challenge in quantum information processing with superconducting circuits which nevertheless is essential for practical applications. The problem with superconducting circuits and qubits is their rather fast decoherence on the order of 100 μs in the best case [23, 24], arising mainly from their strong coupling to any environmental noise sources or intrinsic material defects.

As a possible solution it has been proposed to use ensembles of natural atoms as quantum memory [25–31], as they can show extraordinarily long coherence times on the order of seconds. These ensembles could be atoms in a highly excited Rydberg state, which are electrically coupled to the superconducting circuits, or spin systems as para-magnetic atoms which are magnetically coupled to the solid state devices. First experiments regarding such hybrid systems have been carried out with superconducting qubits and resonators coupled to spin ensembles such as NV centers or erbium ions embedded in a solid state matrix [32–40]. Another approach investigates the coupling between microwave circuits and ensembles of Rydberg atoms flying across the chip [41].

In Tübingen, we would like to investigate the path with an ultracold ensemble of paramagnetic rubidium ^{87}Rb atoms, which can be either in a thermal state or in a Bose-Einstein condensed degenerate quantum state. One possible way to trap such an ensemble of paramagnetic atoms is to create spatially varying magnetic fields $\vec{B}(\vec{r})$ with a local minimum of $|\vec{B}(\vec{r})|$ at the desired trapping position $\vec{r}$. This can be done with superconducting chips, where on-chip current leads are combined with external homogeneous magnetic fields to create the desired magnetic configuration directly above the chip surface [42]. Hence, it seems very natural to combine superconducting quantum circuitry such as qubits or resonators with on-chip magnetic atom traps in a hybrid quantum system. However, two considerable challenges are hidden in this seemingly simple task.

First, the properties of superconducting quantum circuits are very sensitive to magnetic fields. One very problematic issue is due to Abrikosov vortices entering the film structures. These magnetic flux quanta constitute a source of dissipation in the resonators as they have a normal conducting core region, for more details see below. The inevitable basis for any quantum experiment with circuits is the requirement that the dissipation rate has to be much lower than the coupling rate between the different components (resonator-qubit and resonator-atoms). Therefore any resistive, dielectric and radiative dissipation needs

to be identified and minimized and many experimental efforts are made to achieve this [43–54].

In the first part of this thesis the properties of superconducting microwave resonators in magnetic fields are investigated. We did not only observe the field dependent resonator properties, however, we furthermore tried to optimize the resonator performance, i.e., to minimize the magnetic field induced dissipation. The corresponding experimental efforts have led to appended publications I-III and their main results will be discussed in the result section of part I of this thesis. The presented work is the result of collaborations between our group at the University of Tübingen, the group of M. Siegel from the Karlsruhe Institute of Technology and the groups of M. Dressel and P. Michler from the University of Stuttgart. In short, we have patterned the resonators with artificial pinning sites in order to trap the Abrikosov vortices and to suppress their dissipative motion. Moreover, we have investigated magnetic hysteresis effects in the resonators which occur due to intrinsic vortex pinning. Somewhat different approaches to optimize superconducting microwave devices in magnetic fields are discussed in Refs. [48, 55, 56]. As superconducting microwave resonators are also used in many other research areas, amongst others as microwave filters, single particle detectors or elements in particle accelerators, their low loss operation in magnetic fields might become important as well for these fields in the future.

The second big challenge of combining superconducting resonators with trapped atomic ensembles is that the atoms have to be positioned with micrometer accuracy to the maximum of the magnetic coplanar resonator fields, as only there the necessary magnetic coupling strength to the cavity mode can be achieved [30, 31]. Moreover, in this highly complex environment with superconducitng leads deforming all magnetic trap fields, the ensembles must still have the properties they were chosen for, i.e., life times and coherence times on the order of seconds. In a first study, which is a collaboration between our group and the cold atom group of J. Fortágh, both located in Tübingen, we have designed and fabricated an integrated atom chip with superconducting trap wires and coplanar microwave cavities and have characterized the atom cloud properties at different positions on this chip. The corresponding results are summarized in appended publication IV. Inspired by the observation that the closed loop resonator itself can be used to create persistent on-chip currents, the idea of a new kind of a combined resonator-trap has been developed. We have theoretically analyzed this resonator type with transmission line theory and performed three-dimensional simulations of the London equations for this geometry to demonstrate its feasibility as atom trap. In this work, which continues the collaboration between the solid state and cold atom research groups in Tübingen, we have also theoretically developed a method to bring the atoms into the most desired position of the resonator fields. The manuscript containing these considerations is appended as publication V. Together, these studies constitute part II of the present thesis.

Once an ultracold atomic ensemble can be trapped and manipulated at the surface of a superconducting chip, this opens up the possibility for a wide range of exciting experiments. For example, the atom cloud can be coupled to superconducting microelectronic quantum devices as Josephson junctions or superconducting quantum interferometers. When the ensemble is prepared in a Bose-Einstein condensed state, two different macroscopic quantum systems can be coupled and investigated. As both systems can be used as

highly sensitive detectors for different quantities as magnetic flux and gravity, the chance is high that a hybrid sensor device leads to novel high precision measurement technologies. However, what has been done in this thesis was to take the first steps towards the coupling of an ultracold atomic ensemble to a superconducting microwave cavity with the long-term goal to build a long lived quantum memory for quantum states processed by superconducting qubits, a microwave-to-optical quantum transducer [57] and/or an on-chip micromaser [30, 31].

The third and final part of this thesis is concerned with the topology of the superconducting films on the micro- and submicrometer scale. The optimization of the resonators in part I is done by introducing small circular holes into the superconducting films which corresponds to a modification of the microtopology. These holes - as any other defects - act as an energy minimum for Abrikosov vortices and by pinning them are able to suppress their dissipative motion induced by transport or high frequency currents. Moreover they cut out the normal conducting vortex cores and by this do not add normal conducting and dissipating fluid into the films. If there is an ensemble of Abrikosov vortices, which repulsively interact with each other, and an ensemble of defects present in a superconducting film at the same time, the static and dynamic properties of the vortex ensemble strongly depend on the defect arrangement. The interaction between the fixed defect lattice and the vortex ensemble can be experimentally investigated in a qualitative way by measuring the transport properties of the perforated superconducting film dependent on magnetic field and temperature. Testing different defect arrangements and understanding their properties thus can be very useful to properly design superconducting circuits for magnetic field applications. In our studies we have focused on defect arrangements with reduced order and symmetry, as former experiments have suggested that these might show strong pinning and an effective reduction of dissipation over a broad magnetic field range. The presented results have been obtained in collaboration with the theory group of F. M. Peeters at the University of Antwerpen (Belgium), F. Nori from RIKEN in Wako-shi (Japan), the group of M. Siegel from the Karlsruhe Institute of Technology and the groups of P. Michler and M. Dressel from the University of Stuttgart.

In our first study, we have investigated how gradually introducing disorder into the defect lattice influences the properties of the vortices inside the film. These experiments were triggered by a theoretical proposal [58] and the corresponding results are presented in publication VI. Furthermore, we have investigated a pinning array with short-range order but long-range disorder. This pattern is created by a self-assembly procedure and the corresponding results are summarized in publication VII. Finally we have investigated another class of pinning site arrangements with reduced symmetry. In 2006 and 2007, it has been demonstrated by several theoretical and experimental works [59–63] that arranging pinning defects in a quasiperiodic pattern instead of a periodic one can lead to enhanced properties regarding the usability over a broad magnetic field range and to stable magnetic vortex quasicrystals. In the following we have investigated the properties of several quasiperiodic antidot arrangements by means of numerical simulations and electrical transport measurements, which have been unexplored in the context of superconductors and pinning arrays before. The corresponding results are summarized in the appended publications VIII and IX.

Besides the optimization of microwave circuits and superconducting atom chips as discussed in part I and part II of the thesis, respectively, there is another interesting hybrid connection between unconventional antidot lattices and atoms. The idea is to trap paramagnetic atoms in the magnetic field potential landscape of vortices trapped in antidots [64]. This is similar to experiments performed with standing laser waves as an optical potential lattice [65]. When the potential landscape, however, is created with standing laser waves, it is limited to dimensions on the order of half a wavelength and only to these patterns which can be generated by superimposing laser modes. With modern patterning techniqes, the antidot lattice in a superconductor can be fabricated with lengthscales on the order of 100 nm or even below and the spatial arrangement is completely free. The knowledge of the vortex properties and their arrangement in a given antidot lattice hence will be of high interest for the design of such systems. In particular, it might be interesting to generate unordered or quasiperiodic vortex atom traps as this would lead to potential landscapes which would be impossible to generate with lasers. Finally, the magnetic landscapes could not only be used as trapping potentials but in a different kind of experiments as magnetic diffraction gratings for matter waves in the form of propagating atomic ensembles in a macroscopic quantum state [66, 67].

So with the perspective of building hybrid quantum systems consisting of superconducting circuits and magnetically trapped cold atoms, three related aspects with different challenges regarding such hybrid systems have been addressed in this thesis. Before the three parts will be discussed separately, we should introduce some important properties of type-II superconductors and Abrikosov vortices.

1.2 Type-II superconductors in magnetic fields

1.2.1 Type-I and type-II superconductors

Superconductivity was discovered in the year 1911 by H. K. Onnes at the Leiden Laboratory, while he was studying the temperature dependence of the electrical resistance of mercury [68]. He found that below the now called critical temperature T_c, which strongly depends on the material and is around $T_c = 4\,\mathrm{K}$ for mercury, the electrical resistivity completely vanishes. More than twenty years later, in 1933, another characteristic effect of superconductors was discovered by W. Meissner and R. Ochsenfeld [69]. They found that a superconductor behaves as an ideal diamagnet which means that its magnetization always cancels any external magnetic field in the interior of the material. In particular they found that the field expulsion also occurs if the magnetic field is already applied when the material undergoes the transition to the zero resistivity state, which would not be the case for a simple perfect conductor. By this, the Meissner-Ochsenfeld effect reveals that superconductivity is not just characterized by ideal conductivity, but had to be considered as novel thermodynamic phase. Two years later, the brothers H. and F. London presented the first consistent theoretical description of the linear electrodynamics of superconductors [70] including zero resistivity and the Meissner-Ochsenfeld effect. The London equations are discussed in Sec. 3.1.2 of this thesis.

The ideal Meissner effect, however, was only half of the magnetic story of classical superconductors. In 1937, L. Shubnikov [71] and later Zavaritskii [72] found that some superconductors get penetrated by magnetic flux above a certain threshold field while maintaining ideal conductivity. These superconductors were regarded as exotic and in order to discriminate them from pure Meissner superconductors, they were called superconductors of the second kind or type-II superconductors. Today, however, most known superconductors including the high temperature superconductors discovered much later are of the second kind, and type-I superconductors must be regarded as the exotic ones.

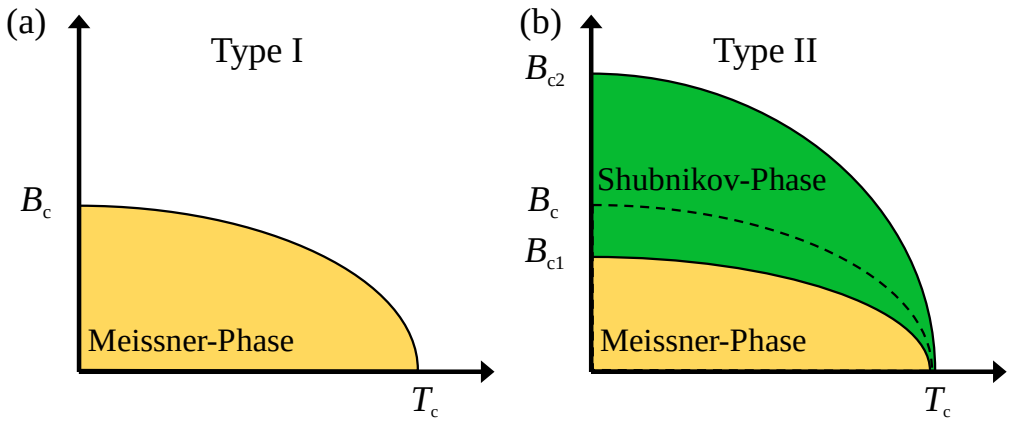

Figure 1.2: Schematic phase diagram of (a) type-I and (b) type-II superconductors dependent on temperature and magnetic field. T_c denotes the critical temperature, B_c is the thermodynamic critical field; B_{c1} and B_{c2} are the lower and upper critical field. Meissner- and Shubnikov phases belong to the superconducting state.

The phase diagram of type-I and type-II superconductors is schematically shown in Fig. 1.2. A type-I superconductor remains in the Meissner phase until the critical field is reached, at which the free energy of the superconductor including its magnetization energy related to the Meissner effect is equal to the energy of the normal conducting state. A type-II superconductor, however, has two critical fields. For fields smaller than the lower critical field, it shows the Meissner phase as a type-I superconductor. Above the lower critical field, however, more and more flux penetrates the superconductor with increasing field until superconductivity breaks down at the upper critical field.

In all studies discussed in this thesis, the superconducting structures are made of magnetron sputtered niobium films, a type-II superconductor.

1.2.2 Abrikosov vortices

An explanation of the physics of type-II superconductors was given by A. A. Abrikosov in [73] within the framework of the Ginzburg-Landau (GL) theory. The GL theory is a phenomenological description of superconductivity first presented in 1950 [74] based on Landau's theory for second order phase transitions. From a variational approach regarding the free energy of the superconductor two coupled differential equations for two quantities can be derived. The relevant variables are the supercurrent density $\vec{j}(\vec{r})$ and

the order parameter $\Psi(\vec{r})$, the latter being identified with a complex quantum mechanical wavefunction describing the ensemble of superconducting charge carriers. The order parameter is related to the density n_s of the charge carriers via $|\Psi|^2 = n_s$.

The GL equations also include two characteristic length scales, one related to the current density and one to the order parameter. The length scale related to the current density is the penetration depth λ_{GL}, describing the typical length scale on which a magnetic field penetrates the superconductor. The other characteristic length is the coherence length ξ_{GL} describing the typical distance on which perturbations of the order parameter are compensated. Both parameters are temperature dependent with $\lambda_{\mathrm{GL}}, \xi_{\mathrm{GL}} \propto (1 - T/T_c)^{-1/2}$, i.e., they diverge for $T \to T_c$. An important parameter, which can be used to discriminate between type-I and type-II superconductors, is the ratio between the two, also known as Ginzburg-Landau parameter $\kappa = \lambda_{\mathrm{GL}}/\xi_{\mathrm{GL}}$.

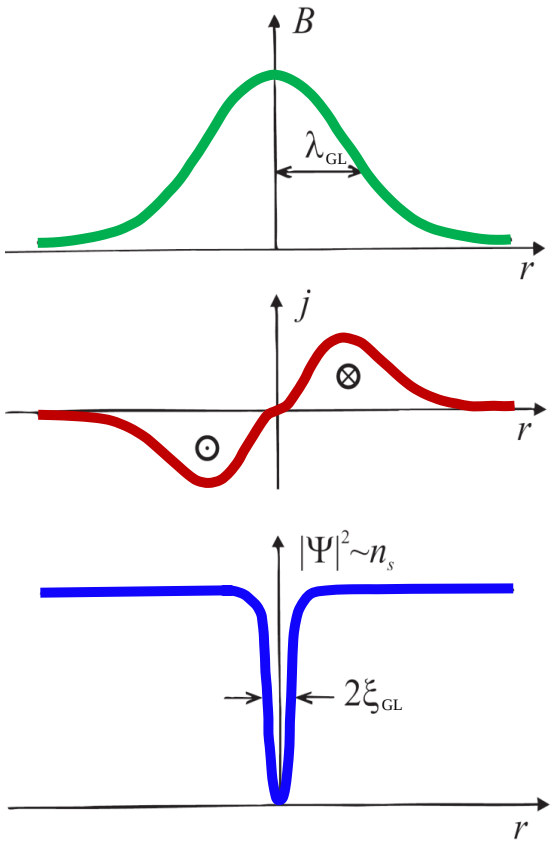

Figure 1.3: Schematic of the magnetic flux density B, the supercurrent density j and the Cooper pair density n_s vs distance r from the center of an Abrikosov vortex with $\kappa \gg 1$. λ_{GL} and ξ_{GL} denote the magnetic penetration depth and the coherence length, respectively. Figure modified from Ref. [75].

A. A. Abrikosov realized that for $\kappa > 1/\sqrt{2}$ the free energy of an interface between a superconductor and a normal conductor in a magnetic field is negative with respect to the superconducting and the normal conducting state [76]. As a consequence it is energetically favorable for the superconductor above a certain magnetic field B_{c1} to fragment into a mixture of normal conducting and superconducting regions. Through each

normal conducting region, a certain amount of flux is guided by circular supercurrents surrounding the normal region. These flux lines are now called Abrikosov vortices. As a consequence of the macroscopic phase coherence of the superconducting wavefunction and the requirement for its unambiguity, the smallest amount of flux which can be carried by one vortex is one flux quantum $\Phi_0 = h/2e$ (the factor of $2e$ originates in the Cooper pairing of electrons [77]). An Abrikosov vortex is characterized by its magnetic field profile, the corresponding circular current density and a normal conducting core region of diameter $\sim 2\xi_{\mathrm{GL}}$, in which the superconducting order parameter is suppressed. Figure 1.3 shows a sketch of the radial dependence of the three relevant vortex quantities, corresponding mathematical expressions can e.g. be found in Ref. [78]. A figurative explanation for the second critical field is that at B_{c2} the vortex density has become so high that the normal conducting core regions overlap and the whole sample gets normal conducting.

1.2.3 Interaction of vortices, flux flow and pinning

In general, it can be derived as a periodic solution from the Ginzburg-Landau theory that Abrikosov vortices tend to form a regular lattice with hexagonal symmetry [73].

However for $\kappa \gg 1$, it is also possible to calculate the free energy of two parallel, overlapping vortices dependent on the relative distance between their centers [79, 80]. The mutual force between the two vortices can then be derived as the energy gradient and is found to be repulsive for $\kappa \gg 1$, so an ensemble of vortices tries to maximize the distances between them. This as well leads to the conclusion that vortices favor to order in a hexagonal lattice.

The Lorentz force (per vortex unit length) $\vec{f}_{\mathrm{L}}$ between two vortices can be expressed in terms of the current density $\vec{j}$ generated by the first vortex at the center position of the second vortex according to

$$\vec{f}_{\mathrm{L}} = \vec{j} \times \vec{\Phi}_0, \tag{1.1}$$

where $\vec{\Phi}_0$ points into the direction of the vortex field and $|\vec{\Phi}_0| = h/2e$. Equation (1.1) does not only describe the force between two vortices but also the force which is exerted onto a vortex by a transport current density $\vec{j}$.

Due to this Lorentz force, vortices start to move when a transport current is applied to a superconductor in the Shubnikov phase. The vortex motion is in the direction perpendicular to the applied current and to the vortex axis. When the vortices move with velocity $\vec{v}$, an electric field parallel to the current density

$$\vec{E} = \vec{v} \times \vec{B} \tag{1.2}$$

is induced in the superconductor [79, 80]. $\vec{B}$ here denotes the average field of the vortices. This electric field accelerates the electrons in the normal conducting vortex cores which leads to dissipation by nonelastic scattering processes as in any normal conductor. Furthermore, it gives rise to a voltage drop along the superconductor.

In the linear regime, the dissipation induced by the vortex motion can be treated as a damping force $\eta\vec{v}$ with the vortex viscosity η. With the Ohmic expression for the resistivity $\rho = E/j$, where E and j denote the magnitudes of electric field and current density, the so-called flux flow resistivity

$$\rho_{\mathrm{ff}} = \frac{\Phi_0 B}{\eta} \tag{1.3}$$

can be derived.

For most applications, however, it is rather undesirable that a superconducting device shows a resistivity and dissipation. Fortunately, the vortex motion is not inevitable. There are several possibilities to create a local energy minimum for a vortex. In such a minimum the vortex will be pinned to its position, at least until the Lorentz force exceeds the corresponding pinning force. The most common mechanism to pin a vortex is related to the suppression of superconductivity in the vortex core, which raises the free energy of the superconductor. If there is a natural or artificial material defect around, at which the superconducting phase is weakened, the free energy of the superconductor is minimized if the vortex occupies that defect position. As the core has a diameter of $\sim 2\xi_{\mathrm{GL}}$, the energy gain is optimized when the defect is of the same size. This mechanism is for obvious reasons referred to as “core pinning”.

Other pinning mechanism are related to current density deformation when the vortex is placed close to a defect and to magnetic interactions between vortices and magnetic impurities. For this thesis however, the core pinning mechanism is the most important one.

Chapter 2

Part I - Superconducting microwave resonators in magnetic fields

Part I of this thesis discusses the investigation and optimization of superconducting resonators in magnetic fields. First, a short introduction to the physics of coplanar microwave resonators will be given. Then, we will briefly discuss the vortex penetration into thin films in perpendicular magnetic fields and common microwave vortex response models. Afterwards, the approaches used in this thesis regarding the investigation and optimization of the resonators in magnetic fields will be presented. The main results of these studies including the implementation of micrometric and submicrometric defects into the resonator films and an investigation of the magnetic hysteresis in the resonator properties will be discussed according to the corresponding appended publications I-III with a few additional data. Finally, the connection to hybrid quantum systems as discussed in part II will be given.

2.1 Basics Part I

2.1.1 Coplanar waveguide resonators Part I

The customary way to guide electromagnetic waves in the microwave domain with low loss is to use a transmission line typically consisting of two conducting wires which spatially confine the electromagnetic fields transversal to the propagation direction. Probably the most common transmission line is the coaxial cable. The coaxial cable consists of a signal line in the center and a shielding or ground conductor which concentrically surrounds the center line. In 1969, C. P. Wen proposed a similar but only two-dimensional version of a coaxial cable - the coplanar waveguide [81], which consists of a center conductor line flanked by two grounded planes, while all three conductors are arranged in a single plane, cf. Fig. 2.1.

If a periodic voltage is applied between the center conductor and the ground planes, an electromagnetic wave propagates along the waveguide. As long as the lateral dimensions of the waveguide are small compared to the wavelength of the electromagnetic wave, the

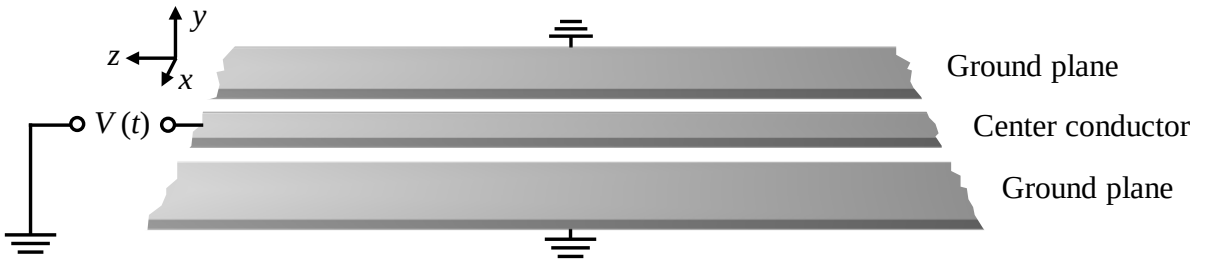

Figure 2.1: Sketch of a coplanar waveguide consisting of a center conductor flanked by two ground conductors. When a time varying voltage is applied between center conductor and ground, a correponding voltage and current wave propagates along the waveguide (here: from left to right).

coplanar waveguide can be treated with the distributed element model of transmission line theory. For low loss materials the electric field in propagation direction is small and the distributions of electric and magnetic fields in the waveguide can be derived in good approximation with a quasistatic approach. The result is a transversal electromagnetic (TEM) wave. As for this thesis the distribution of the microwave magnetic fields and the related current density are of importance, these two quantities are plotted in Fig. 2.2 for a cross section of the coplanar line according to the expressions given in Ref. [82]. The most important features are the magnetic field focusing into the gaps between center conductor and ground planes and the enhanced current density at the conductor edges.

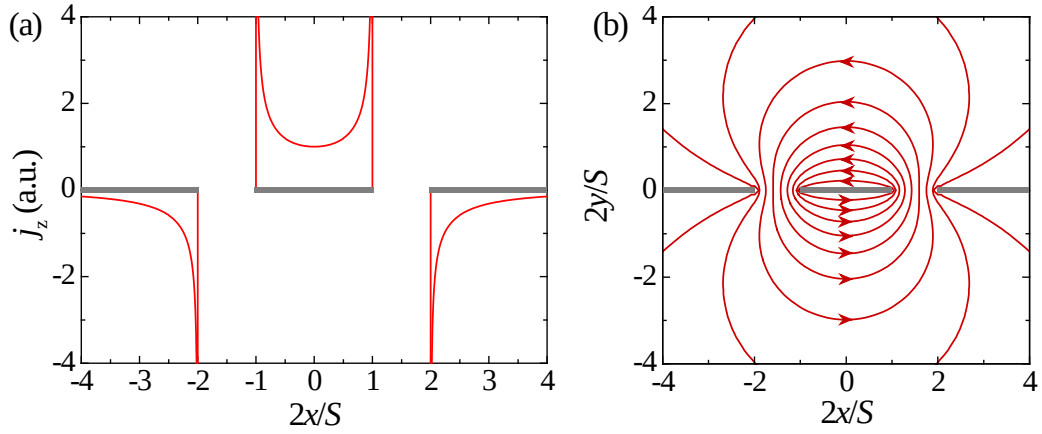

Figure 2.2: (a) Sketch of the microwave current density amplitude j_z in a superconducting coplanar waveguide with semi-infinite ground planes. The plotted sheet current density is integrated over the conductor thickness. The center conductor width is S and the gap width is $W = S/2$. In (b) the corresponding magnetic field lines are sketched. For the calculation, it has been assumed that the magnetic field penetration depth is much smaller than center conductor and gap width $\lambda_\mathrm{L} \ll S, W$ and that the film thickness is much smaller than S. Gray bars indicate the position of the coplanar waveguide electrodes. For more details on j_z and B see Ref. [82].

In terms of the transmission line theory, the coplanar waveguide is characterized by two parameters. The first is the characteristic impedance Z_0, which is defined as the ratio between voltage and current amplitudes of a single propagating harmonic wave. The second is the propagation constant $\gamma = \alpha_\mathrm{d} + i\beta$, composed by the damping constant of

the line α_d and the phase constant $\beta = 2\pi f/c'$. In the last expression, f is the frequency of the wave and c' is its phase velocity on the transmission line. For low loss lines the characteristic impedance is given by $Z_0 = \sqrt{L'/C'}$ with the inductance per unit length L' and the capacitance per unit length C', both defined by the geometrical parameters of the line. Expressions for L' and C' of a coplanar waveguide are typically derived with conformal mapping techniques and can be found for different types of coplanar waveguides in [83]. For a calculation of the damping constant, also the knowledge of resistive and dielectric dissipation per unit length R' and G' is necessary.

If at one point along the transmission line, the local impedance is different from the characteristic impedance, a part of the propagating wave is reflected at that discontinuity. One way to introduce such a local impedance mismatch is to pattern a gap into the center conductor. If two gaps with distance l are introduced into the center conductor, an electromagnetic resonator is formed because the two gaps act as two reflectors for the microwave and constructive interference of the waves between the two gaps only occurs for certain wavelengths. The supported modes are given by $l = n\lambda/2$ with $n = 1, 2, 3...$ and the electromagnetic wavelength λ. As the lowest mode corresponds to half a wavelength, such resonators are called half wavelength resonators or $\lambda/2$ resonators. Around the resonance modes, transmission line resonators can be described as damped harmonic lumped element oscillators, consisting of a resistor R, a capacitor C and an inductor L, which is a helpful model to gain a better understanding of the resonator properties. Figure 2.3 shows a capacitively coupled coplanar waveguide resonator, its transmission line representation and the lumped element equivalent as well as a sketch of the magnetic field amplitude along the resonator for its three lowest modes. A recommendable mathematical treatment of the resonators and the RLC equivalent is given in [84] and [85], see also appended publication V.

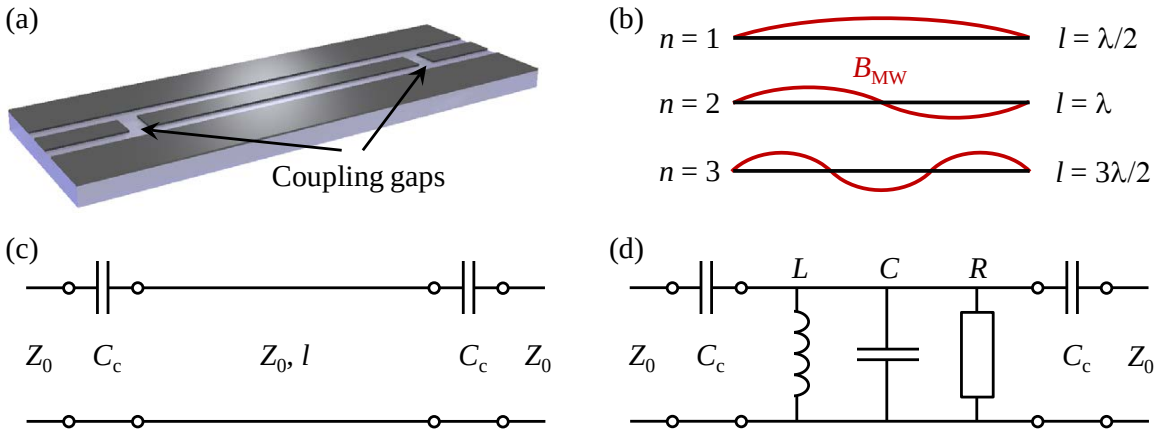

Figure 2.3: (a) Sketch of a capacitively coupled coplanar half wavelength resonator defined by two gaps with distance l in the center conductor. (b) shows the microwave magnetic field B_{MW} along the resonator for the three lowest resonant modes $n = 1, 2, 3$. In (c), the transmission line representation of (a) is depicted, where the line has a characteristic impedance Z_0, the gaps are represented by coupling capacitors C_c and the resonator by a segment with length l. (d) shows the parallel RLC lumped element approximation of (c), which is valid for frequencies close to f_0. The equivalent lumped elements are given by $R = Z_0/\alpha_d l$, $C = 1/4Z_0 f_0$ and $L = Z_0/f_0\pi^2$, cf. [84, 85]. (a), (c), (d) modified from appended publication V,

The most relevant properties of a coplanar resonator are the resonance frequency f_0 or f_{res} and the quality factor Q which is defined as 2π times the ratio between the energy stored in the resonator and the energy lost during one oscillation. For a linear resonator, whose resonance curve can be approximated by a Lorentzian line with full width at half maximum Δf, the quality factor can be determined by $Q = f_0/\Delta f$. The reciprocal of the quality factor is called the loss factor $1/Q$ and if there are several different linear loss mechanisms present, the loss factors add according to $1/Q = 1/Q_r + 1/Q_d + 1/Q_{\mathrm{rad}} + ...$ Here, $1/Q_r$ represents resistive losses, $1/Q_d$ represents losses in the dielectric substrate and $1/Q_{\mathrm{rad}}$ accounts for losses due to radiation. When superconducting coplanar resonators are exposed to a magnetic field high enough that Abrikosov vortices enter the structure, the vortices constitute an additional and field dependent damping mechanism $1/Q_v(B)$ due to their normal conducting cores. Then, also the total loss factor $1/Q(B)$ gets magnetic field dependent. As discussed in the next section, Abrikosov vortices also constitute an additional reactive element and due to the related change of the total inductance of the resonator, the resonance frequency $f_{\mathrm{res}}(B)$ is field dependent as well.

2.1.2 Flux penetration into film structures

An important question for understanding the results presented below is how Abrikosov vortices are distributed in a superconducting film. In principle, there are two possible ways to bring vortices with an external field into the film. First, a magnetic field can be applied during cooling the sample through the transition temperature T_c, which is referred to as field cooling procedure. Then, vortices will be trapped for fields above a certain threshold field, which depends on the superconductor geometry but typically is very low, on the order of 10^{-5} T [86, 87].

When the field is considerably higher than the threshold field, the vortices are practically homogeneously distributed in the film. This case is relevant mainly for results in appended publication III, IV and V, where we have field-cooled the samples or propose to do so.

A more complicated vortex distribution, however, results from cooling the sample in zero magnetic field through T_c and applying B perpendicular to the film afterwards. When the magnetic field at the film edges, where it is enhanced due to demagnetization effects, exceeds the lower critical field, vortices begin to enter from the edges. These first entering vortices get pinned at the first intrinsic or artificial defects they come across, which in most cases will be very close to the sample edge. When B then is increased further, more vortices enter the film and push the pinned vortices towards the sample interior. As soon as the pushing force from the additional vortices is strong enough, the first vortices get depinned and move sample-inwards to the next pinning sites, while the second vortices occupy their old positions. Now, more vortices are needed to depin the second generation, as these experience also a force by the first generation in front of them. This is the figurative and somewhat simplified explanation for the vortex density gradient which is established by this type of field application to samples with pinning. The vortex gradient situation here is also called the critical state as the vortices arrange in a way that each of them experiences nearly the critical depinning current density by the ensemble of all other vortices.

A first model for the critical state in bulk superconductors or superconducting slabs and cylinders in longitudinal fields was proposed by C. P. Bean in 1962 [88, 89]. The Bean model was later extended for thin films in perpendicular fields by Norris [90] and by Brandt and Indenbom [91], so we call this modification the NBI model. It was also discussed by Zeldov and co-authors [92]. However, all of these models do not account for individual vortices and pinning. They treat continuous current and flux densities under the assumption that there is a maximum possible current density in the superconductor and that any change in currents and magnetization is introduced from the sample edges. In the language of vortices, the maximum possible j_c hereby is the depinning current density, for which the Lorentz force onto the vortices exceeds the pinning force. Figure 2.4 (a) shows sketches of several subsequent flux density and current density profiles during an external field upsweep as described by the advanced thin film model. When the external field is increased, the flux front and the edge stripes with the critical current density extend more and more into the interior of the sample. The mathematical expressions for flux and current density can be found in Ref. [91] or appended publication II. The flux and current densities shown can be viewed as macroscopic superposition of all individual vortex fields and currents and hence it is also clear that this model only applies, if the strip width is much larger than an individual vortex. Such a field and current distribution has been confirmed in many experiments by magneto-optical imaging [93, 94].

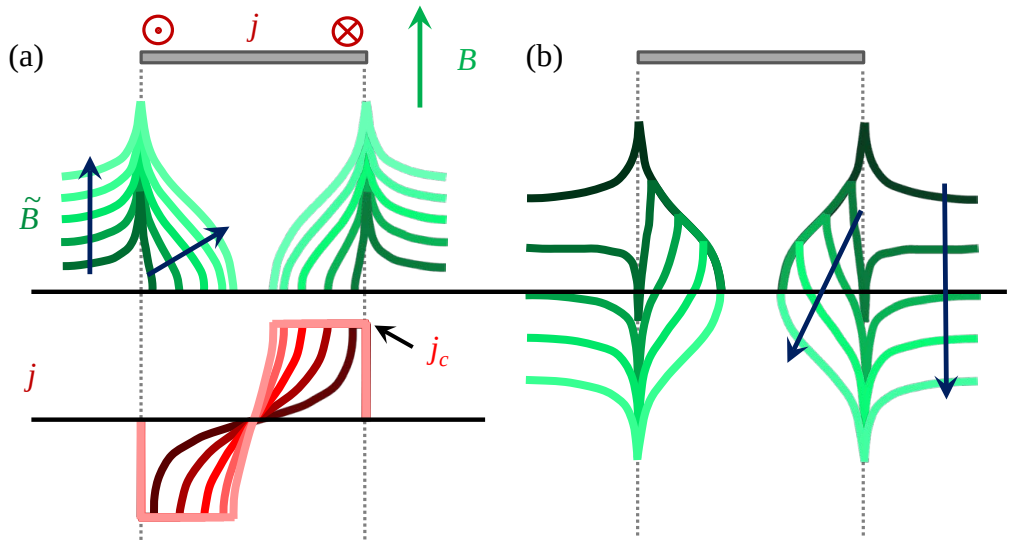

Figure 2.4: (a) Flux density (top) and current density (bottom) distributions across a thin superconducting during the increase of an external perpendicularly applied magnetic field B for five different field amplitudes according to the model by Norris, Brandt and Indenbom [90, 91]. (b) Flux density across the strip during the field downsweep to a negative external value. For more details and the corresponding mathematical expressions as well as for the current density during downsweep, see [91].

Very important for the results presented below is what happens, when the external field is swept back zo zero or even into the opposite direction. The according subsequent field profiles across the superconducting strip are sketched in Fig. 2.4 (b). According to this, the flux density reaches negative values directly at the strip edges although there is still a positive field applied. This effect can be imagined as induced by the field lines of

the pinned vortices which close around the film, when the external field is reduced. This negative flux partly also enters the superconductor at the edges as anti-vortices.

2.1.3 High frequency Abrikosov vortex response

The first experiments regarding the high-frequency impedance of type-II superconductors in the mixed state have been carried out during the 1960s on various superconducting materials [95–98], showing that the data can well be explained by assuming normal conducting regions embedded into the superconductor. The first theoretical descriptions of the mixed state microwave surface impedance have been based on a simple two-fluid approach [95, 96]. However, a more accurate modelling of the vortex response required to inlude pinning forces, elastic vortex interactions and for the case of high temperature superconductors thermally assisted vortex hopping ("flux creep").

At first, Gittleman and Rosenblum (GR) developed a high-frequency response model for vortices based on a damped equation of motion for particles in a sinusoidal or parabolic potential [97, 98]. In their approach, the vortex lattice was assumed to be completely rigid and the particles were assumed to be massless, as justified by the vortex inertial mass estimations done by Suhl [99].

Later, Brandt [100] and independently Coffey and Clem [101, 102] have extended the GR model by considering also elastic deformations of the vortex lattice and thermally activated flux motion. More recently, it has been stated and discussed by Pompeo and Silva [103] that all these models basically lead to the same mathematical expression for the complex and frequency-dependent vortex related resistivity

$$\rho_v = \frac{\Phi_0 B}{\eta} \frac{\epsilon + i\omega/\tilde{\omega}_c}{1 + i\omega/\tilde{\omega}_c} \tag{2.1}$$

with the vortex viscosity η and the angular microwave frequency $\omega = 2\pi f$. ϵ is the so-called flux creep factor, a number between 0 and 1 describing the contribution of thermally activated vortex motion to the overall resistivity and $1/\tilde{\omega}_c$ is a characteristic time constant related to the relaxation time of a vortex in a pinning potential. Note that the prefactor is just the flux flow resistivity $\rho_{\mathrm{ff}} = \Phi_0 B/\eta$, cf. Eq. (1.3). The detailed expressions for ϵ and $\tilde{\omega}_c$ depend on the details of the corresponding model. Equation (2.1) can be derived from the basic equation of vortex motion

$$\eta\vec{v} + k_p\vec{x} = \vec{j} \times \vec{\Phi}_0 + \vec{f}_{\mathrm{thermal}}. \tag{2.2}$$

with a damping force $\eta\vec{v}$, a harmonic pinning force $k_p\vec{x}$ with pinning constant k_p, the Lorentz force on a vortex $\vec{j} \times \vec{\Phi}_0$ due to the transport current density $\vec{j}$ and a thermal force $\vec{f}_{\mathrm{thermal}}$. Note that Eq. (2.2) describes forces per unit length of the vortex. For details, see [97, 98, 100–102].

For negligible flux creep $\epsilon = 0$, which is typical for low temperature superconductors as used in this thesis, the GR expression for ρ_v

$$\rho_v^{\mathrm{GR}} = \frac{\Phi_0 B}{\eta} \frac{1}{1 - i\omega_c/\omega} \tag{2.3}$$

is obtained. Here, $\omega_c = 2\pi k_p/\eta$ is the frequency, above which the vortex response goes from the elastic ($\mathrm{Im}(\rho_v) > \mathrm{Re}(\rho_v)$) to the dissipative ($\mathrm{Im}(\rho_v) < \mathrm{Re}(\rho_v)$) regime. For a vortex in a pinning site without driving force, $t_c = 1/2\pi\omega_c$ is moreover the characteristic $1/e$ relaxation time after a single displacement from the equilibrium position.

However, the important information hidden in Eq. (2.3) is the dependence of its real, dissipative part on the pinning force constant k_p and on the viscosity η. As it is a monotonously decreasing function of k_p, it seems very reasonable to introduce strong pinning in order to reduce the microwave dissipation due to vortices. However, one must be very careful if using antidots as pinning sites, which by cutting out the normal vortex cores also change the viscosity η at the same time. And ρ_v^{GR} is a non-trivial function of η, as $\rho_v^{\mathrm{GR}} \to 0$ for $\eta \to 0$ and for $\eta \to \infty$, going through a maximum in between for $\eta = 2\pi k_p/\omega$. So at least in principle it is possible according to the discussed models to increase the resistivity by the introduction of pinning sites, if these pinning sites at the same time change the vortex viscosity.

Finally, we see that the Abrikosov vortices also constitute an additional reactive element as the resistivity also has an imaginary part. For a superconducting resonator in the mixed state, we therefore do not only expect an increased damping but also a shift of the resonance frequency.

2.2 Results Part I

2.2.1 Resonators with micrometric defects - Publication I

As the basis for our first experiments with superconducting resonators, we used a 3.3 GHz resonator design which has been developed at the Karlsruhe of Technology [104] and which is shown in Fig. 2.5 (a). The idea of the first work was to fabricate resonators with and without artificial defects as pinning centres and to compare their properties in magnetic fields. In order to permit patterning and fabrication of the resonators with optical lithography, relatively large artificial defects on the micrometer scale were designed. As micrometric defects we chose circular antidots which we strategically positioned at the presumably most sensitive locations and not over the whole chip to introduce as little damage as possible. These sensitive positions are the edges of the waveguide center conductor and the ground planes because the microwave current density along the waveguide is peaked there, see e.g. Refs. [82, 87, 105–107] and Fig. 2.2 (a). Moreover, in this first experiment we only applied the magnetic field B (perpendicular to the film plane) after cooling the sample to the superconducting state and thus according to the flux penetration described in the last section, we expected the vortex density at the edges to be enhanced. By means of optical lithography, dc magnetron sputtering and lift-off technique we fabricated 300 nm thick niobium resonators on sapphire substrates without, with one row and with three rows of antidots next to the conductor edges, cf. Fig. 2.5 (b)-(d). The

resonators with antidots have been fabricated in two different designs, one with additional antidots on the feedlines (marked with a "+" in Fig. 2.5 (a)) and one without.

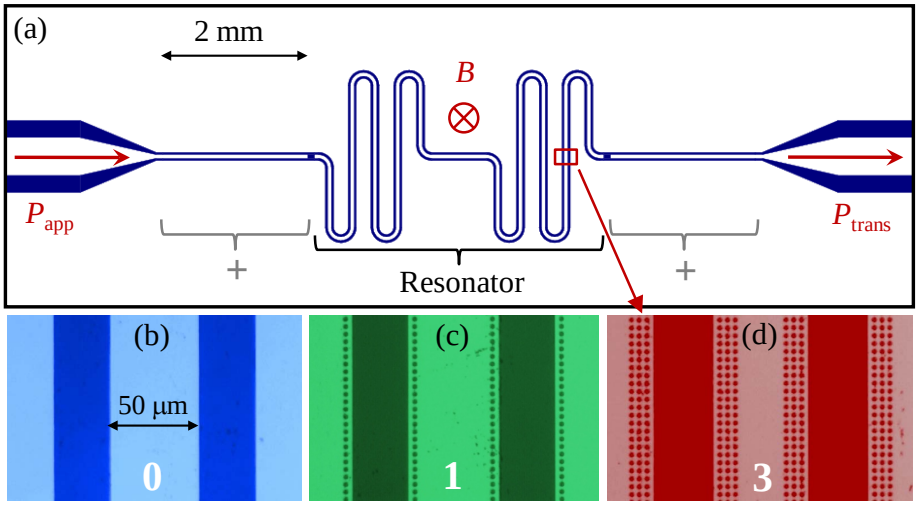

Figure 2.5: (a) Layout of a $12 \times 4\,\mathrm{mm}^2$ chip with a capacitively coupled 3.3 GHz transmission line resonator and optical images of resonators with (b) **0**, (c) **1** and (d) **3** rows of antidots. The parts of the feedlines which are perforated with antidots are marked with a +. Figure modified from appended publication I. © 2011 by the American Institute of Physics.

For the sample characterization, we have applied a microwave signal with constant power P_{app} and variable frequency f on one side of the resonator and measured the transmitted power P_{trans} with a spectrum analyzer. The result is a resonance peak with maximum transmission at the resonance frequency f_{res} which can very accurately be approximated by a Lorentzian lineshape. Figure 2.6 shows a series of resonance curves for different magnetic fields for (a) a resonator without antidots and (b) a resonator with three rows of antidots including the feed lines at $T = 4.2\,\mathrm{K}$. For each resonance curve, we have calculated the quality factor $Q(B) = f_{\mathrm{res}}(B)/\Delta f(B)$ as a measure for the energy dissipation, where $f_{\mathrm{res}}(B)$ is the resonance frequency and $\Delta f(B)$ is the full width at half maximum (FWHM). The result is plotted in Fig. 2.6 (c) and clearly shows that in magnetic fields the quality factor of the resonator with antidots is significantly enhanced with respect to the resonator without defects.

To quantify this reduction in dissipation independently of the zero field quality factor $Q(0)$, which statistically varies between different resonators, we substract all field-independent loss contributions $1/Q(0)$ from the total loss $1/Q(B)$ and get the field induced losses $1/Q_v(B) = 1/Q(B) - 1/Q(0)$ only. For the resonator ground mode $n = 1$ the losses, which we attribute to the presence and the microwave current induced motion of Abrikosov vortices, are plotted for our five resonators and for both magnetic field directions in Fig. 2.7 (a). The data reveal that micrometric antidots close to the conductor edges can reduce dissipation in the resonators by up to a factor of ~ 5, and that the reduction increases with increasing number of defects. Figure 2.7 (b) shows the losses at the highest applied magnetic field $B = 4\,\mathrm{mT}$ not only for the fundamental mode but also for the three higher order harmonics $n = 2, 3, 4$ and according to these data, the effect of loss reduction remains stable in the range of frequencies investigated.

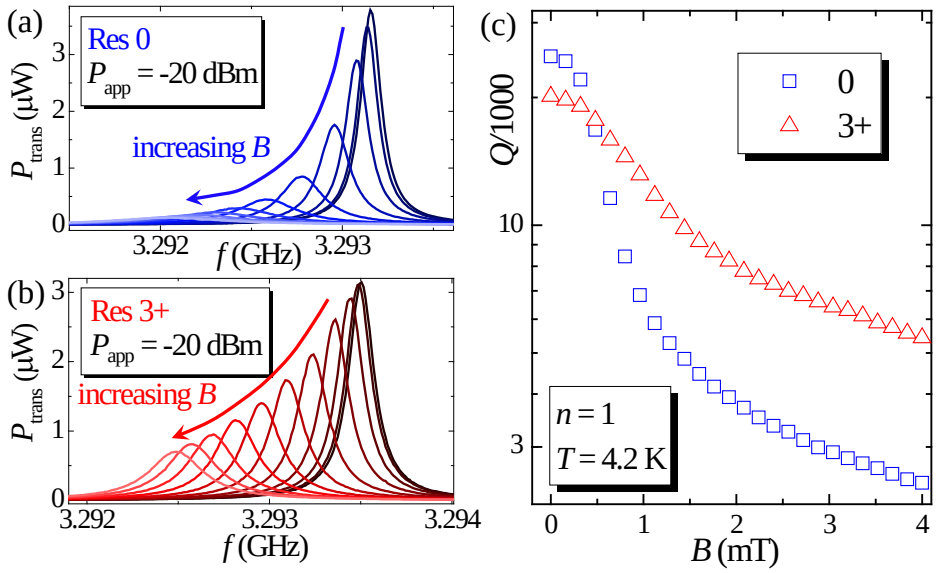

Figure 2.6: Transmitted power P_{trans} vs frequency f of (a) a resonator without and (b) a resonator with three rows of microscopic defect rows for magnetic field $0 \leq B \leq 1.6\,\mathrm{mT}$ in 0.16 mT steps. (c) shows the corresponding magnetic field dependent quality factors $Q(B)$ for fields up to $B = 4\,\mathrm{mT}$. Figure from appended publication I. © 2011 by the American Institute of Physics.

We repeated the same measurements over four orders of magnitude of applied microwave power P_{app} and found the presented results to be nearly independent of the input power in the characterized range between 0 dBm and −40 dBm. More details regarding the power dependence can be found in appended publication I.

Our findings clearly show a reduction of the vortex associated losses by the introduction of micrometric antidot arrays. However, some questions regarding the exact mechanisms behind this reduction are not solved yet and might be addressed by future studies. The first issue is the question whether the reduction of dissipation is due to a reduction of normal fluid in the resonator by cutting out the vortex cores or due to a reduction of the vortex oscillation velocity by real pinning. This might get relevant, when other vortex pinning cites as e.g. magnetic dots, which already induce normal conducting regions just by their presence, enter the stage of superconducting resonators. To shed light onto this question, we currently work on a deeper analysis of the magnetic field dependence of losses $1/Q_v(B)$ and resonance frequency $f_{\mathrm{res}}(B)$ which in combination can give insight into the nature of the microwave vortex response and behaviour, cf. Sec. 2.1.3 or [87] and references therein.

Another phenomenon, which has been observed in experimental and theoretical studies on flux distributions in high temperature superconductors, might as well play a role in our resonators. According to these studies, a micrometric hole placed in the vicinity of a superconductor edge can lead to a reduction of the flux density directly at this edge compared to an edge region without hole nearby [108, 109]. Interestingly, the simulations reproducing these results assume a continuous flux distribution instead of a fragmentation into vortices and do not consider the energetic favorability of a pinning site location for

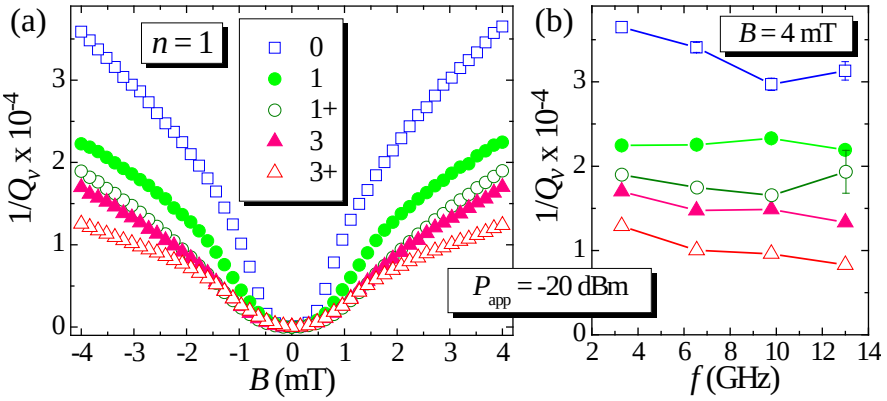

Figure 2.7: Vortex associated energy losses $1/Q_v$ of five resonators with different antidot distributions (a) vs applied magnetic field B for the fundamental mode $n = 1$ and (b) vs frequency f for $n = 1, 2, 3, 4$ at $B = 4\,\mathrm{mT}$. Figure from appended publication I. © 2011 by the American Institute of Physics.

an Abrikosov vortex. This mechanism of flux guidance by micrometric defects might nevertheless play a role for our results, because in our resonators a flux density reduction directly at the edge, where the microwave currents peak, would also lead to a significant reduction of vortex associated dissipation as also suggested by the results presented in the next section. However, if and how far these results on the flux distribution in high T_c superconductors can be transferred to our samples is not completely clear, because the characteristic length scales defining the size and interaction of vortices, are very different between our niobium resonators and the YBCO superconductor investigated in Ref. [108]. We hope that this question will be answered by high-resolution magneto-optical imaging of the samples, for which a new microscope has been built in our group during the last years.

Own contributions to publication I

For this work, I have designed the antidot patterns and fabricated the resonators. I have developed a LabView based measurement software and carried out the experiments. Finally, I have analyzed and interpreted the data with a self-written data processing software, and I have written the first draft of the manuscript.

2.2.2 Hysteresis effects in the resonators - Publication II and more

In a second study we investigated magnetic hysteresis effects in the resonators shown in Fig. 2.5 (a). As a magnetic hysteresis only occurs if the magnetic fields are applied and swept in the superconducting state, we again cooled down the resonators first to $T = 4.2\,\mathrm{K}$. Then we applied and swept a magnetic field in the mT range and monitored the magnetic field associated losses $1/Q_v(B)$ and the resonance frequency $f_{\mathrm{res}}(B)$. The result for a resonator without antidots is shown in Fig. 2.8. Both loss factor and resonance

frequency show a significant hysteretic behaviour and both do not reach their virgin values again. In the following discussion and analysis, we focus on the field history dependence of the losses, because the frequency shift can also be partly caused by Meissner currents [110] and thus is more complicated.

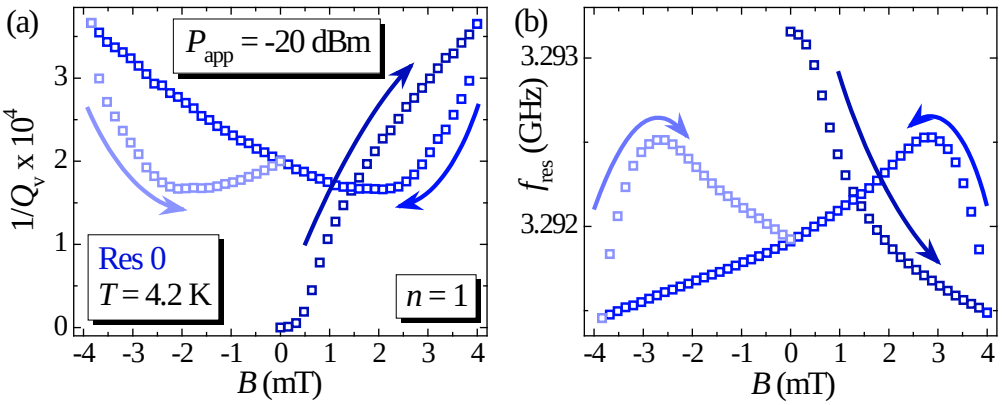

Figure 2.8: (a) Vortex associated energy losses $1/Q_v(B)$ and (b) resonance frequency $f_{\mathrm{res}}(B)$ of a resonator without antidots for a full cycle of applied magnetic field starting from $B = 0$. Figure modified from appended publication II, © 2012 by the American Physical Society.

In order to understand the hysteresis found, which according to our measurements also appears in the resonators with antidots, we formulated a very simple model for the vortex associated losses inside the resonator. In our simple mechanical model for the vortex motion and dissipation we treat the vortices as independent, massless particles which are driven by a Lorentz force due to the rf current and which experience a mechanical friction due to their normal conducting cores, more details can be found in appended publication II. It is very similar to the models mentioned in Sec. 2.1.3. However, we do not include a pinning force but allow for a spatial variation of the vortex density. When we then assume the vortex density to be represented in good approximation by a continuous flux density inside the superconductor, we find the total dissipation to depend quadratically on the local microwave current density and linearly on the local magnetic flux density. Thus, we have calculated the expression

$$\delta e(B) = \int_S |\tilde{B}(x)|[j_0^{\mathrm{rf}}(x)]^2 dx \tag{2.4}$$

for a single superconducting strip of width S in the x-direction and infinitely long in the z-direction. Here, $\tilde{B}(x)$ is the flux density inside the strip and $j_0^{\mathrm{rf}}(x)$ is the microwave current density amplitude in z-direction. Assuming a flux density distribution according to a penetration model for thin superconducting strips [90–92] as presented in Sec. 2.1.2 and with a current density peaked at the conductor edges as shown in Fig. 2.2 (a), we find good qualitatively agreement with the hysteresis loop experimentally found. For comparison, we have furthermore calculated the expected behaviour for other field and current distributions and found that the shape of the hysteresis is very sensitive to these parameters. Figure 2.9 shows such numerically obtained hysteresis curves for the NBI model and (a) for a homogeneous j_0^{rf} and (b) for a highly inhomogeneous $j_0^{\mathrm{rf}}(x)$ as expected

for the center conductor of a coplanar waveguide with a center conductor width $S \gg \lambda_L$, cf. Fig. 2.2 (a). Obviously, the hysteresis curve in (b) resembles very well the characteristic features of the experimental data in Fig. 2.8 (a).

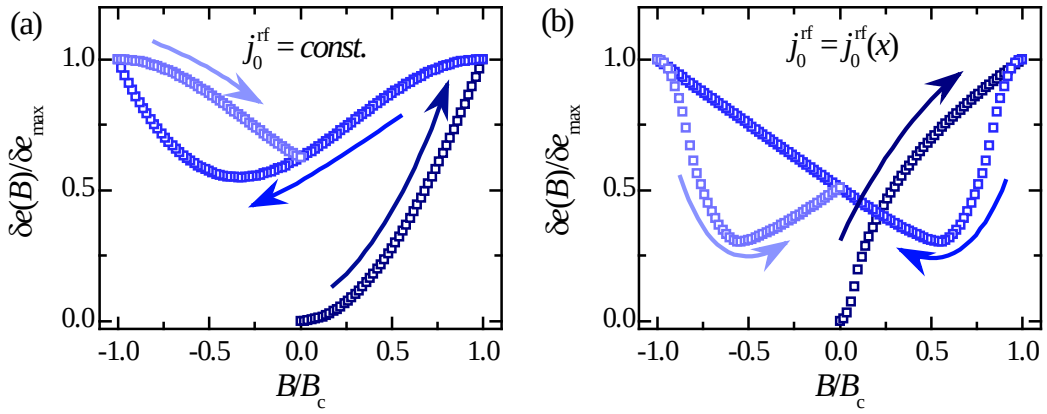

Figure 2.9: Numerically calculated microwave energy dissipation $\delta e(B)$ in a superconducting strip exposed to a perpendicularly applied magnetic field according to expression (2.4) during a full cycle of B. The flux distribution in the strip $\tilde{B}(x)$ was assumed to be desribed by the penetration model of Ref. [91], the current density j_{rf} was assumed (a) homogeneous or (b) highly inhomogeneous [106]. More details regarding the field cycle parameters and the assumed superconductor properties can be found in appended publication II. Figure modified from appended publication II. © 2012 by the American Physical Society.

The interpretation of the hysteresis is related to the very inhomogeneous current distribution weighting the vortex location quadratically, so the most relevant vortices for the dissipation are those close to the superconductor edges. When the external magnetic field is swept down after a virgin upsweep, according to [91] the absolute value of the flux density at the edges goes through a minimum considerably before the external field has reached zero again, cf. Fig. 2.4 (c). At zero external field, negative flux has entered the superconductor from the edges which dissipates energy just like positive flux and thus the dissipation is increased again.

We have also measured the hysteresis curve for higher resonator modes and for angles α between chip plane and magnetic field different from $\alpha = 90°$. The corresponding results can be found in appended publication II. A brief discussion of what should be additionally considered in a more accurate model describing the hysteresis in such highly complex resonator systems can be also found there.

In order to learn more about the flux penetration into the relatively complicated resonator structures and to check the used model and our interpretation of the hysteresis curves, we performed magneto-optical imaging in the group of T. Johansen at the university of Oslo.[1] With this experimental technique, it is possible to directly image the flux density distribution at the surface of a superconducting chip [94] and hence to evaluate whether our approach in explaining the hysteresis data from transmission spectroscopy experiments is justified. Fig. 2.10 shows magneto-optical images of a resonator chip as

[1]The measurements were done by M. Grünzweig from our group together with P. Mikheenko from the Oslo group and are not part of publication II.

shown in Fig. 2.5 (a) during and after a single field upsweep as well as during and after the downsweep to zero external field. The resonator chip used has reduced ground planes on the upper and lower side by 0.5 mm compared to the one in Fig. 2.5 (a). The modulus of the magnetic field in the magneto-optical images is encoded in light intensity, so bright regions correspond to a high and dark regions to a low flux density. In (e) and (f) we show linescans of the intensity during upsweep and downsweep along the red dashed line indicated in (a)-(d).

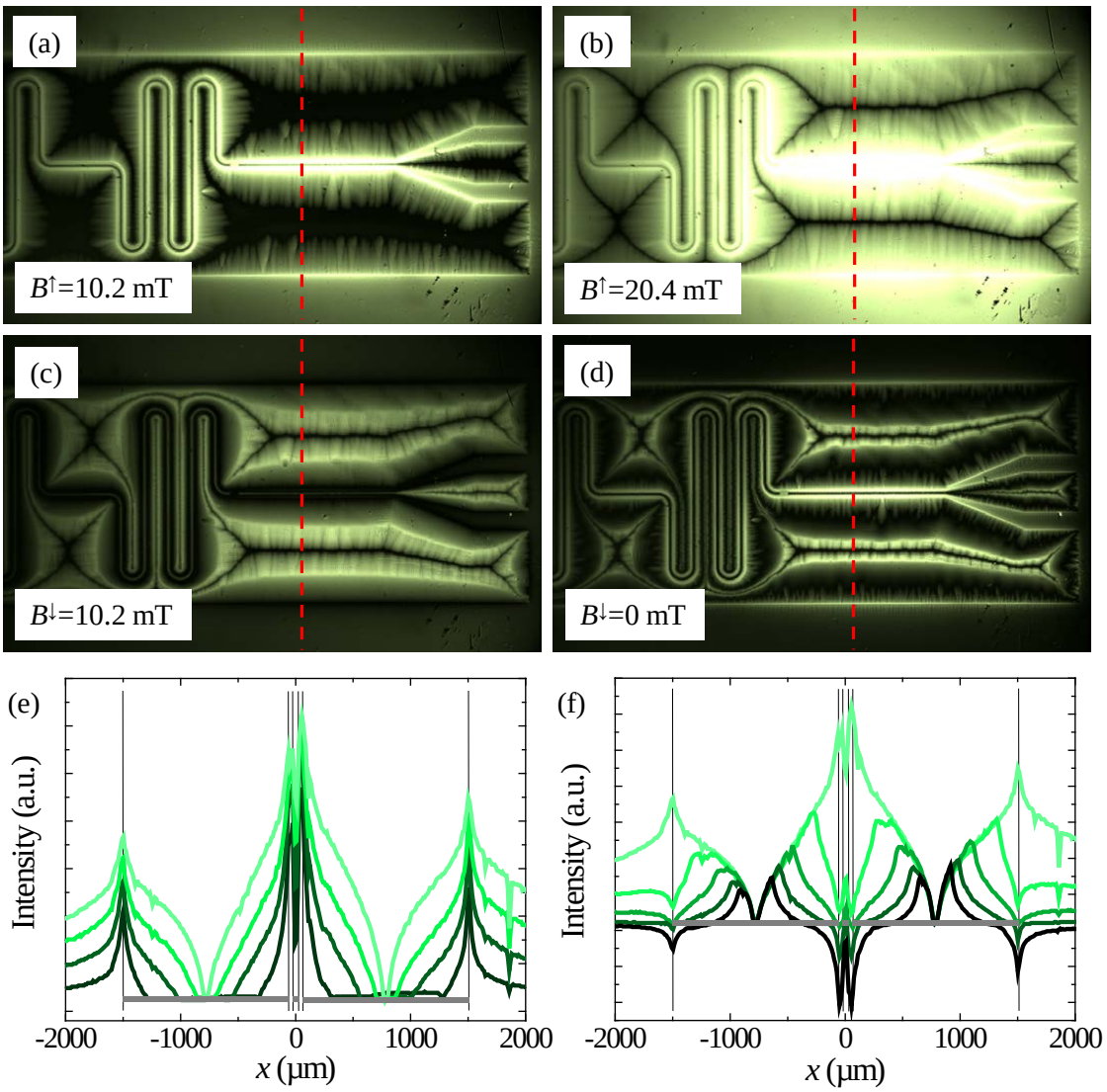

Figure 2.10: (a)-(d) Magneto-optical images of a resonator chip in a perpendicular magnetic field during field upsweep (a, b) and downsweep (c, d) at the given B values. The red dashed line indicates the position of the linescans shown in (e) and (f) for applied fields $B^{\uparrow} = 5.1, 10.2, 15.3$ and 20.4 mT (e) and $B^{\downarrow} = 20.4, 15.3, 10.2, 5.1$ and 0 mT (f). The position of the superconducting planes is indicated by horizontal bars in (e) and (f) (thickness not to scale) and the conductor edges are indicated by vertical lines. Note that in (f), the negative intensity values are positive in the raw data and inverted by hand, as the MOI does not discriminate between positive and negative flux.

Although we plot only the intensity and although we do not know the precise relation between brightness and magnetic field, it is obvious that the field distribution is very similar to the expectations from the model shown in Fig. 2.4 for a single superconducting strip. In particular, it can be seen that during downsweep the flux density at the edges is minimized at approximately half the maximum field $B = 20.4\,\mathrm{mT}$, which is also the field range at which the loss hysteresis shows its minimum, cf. Fig. 2.8 (a). And at the end of the downsweep, there is much remanent flux frozen into the structures, positive flux in the center of the planes and negative at its edges. Of course, due to the complex geometry, there are also some specialties present, for example the enhanced flux density at the resonator center conductor and in the gaps between center conductor and ground plane. Nevertheless, the images support our conclusions on the origin of the frequency and loss hysteresis measurements.

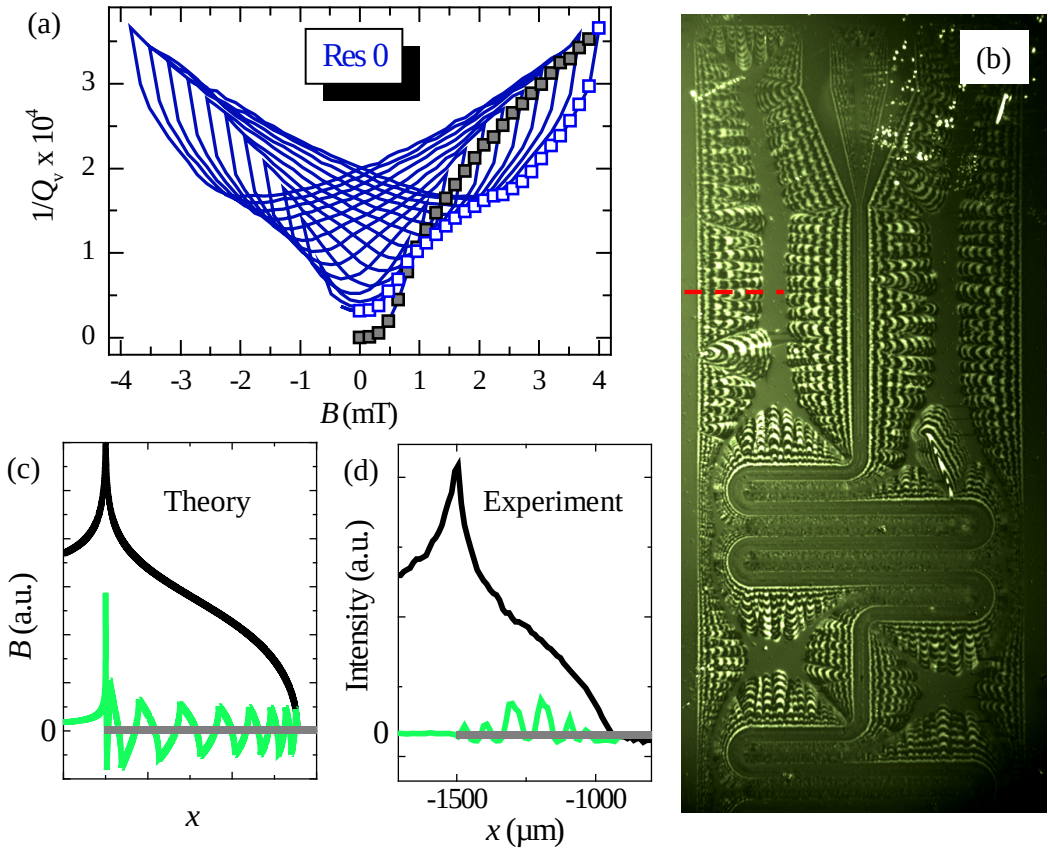

Figure 2.11: (a) Vortex associated loss factor in a superconducting resonator as shown in Fig. 2.5 (a) during a demagnetization field sweep sequence (blue line, for details see appended publication III). (b) Magneto-optical image of the flux pattern in a superconducting resonator chip after a demagnetization sequence with first peak field of $B = 13.6\,\mathrm{mT}$ and a peak field reduction of $\Delta B = 1.6\,\mathrm{mT}$ per cycle resulting in eight cycles to $B = 0$. (c) Flux density distribution after virgin upsweep and after an eight-cycle demagnetization according to the NBI model. (d) Linescan of the intensity in the MOI along the red dashed line in (b) after the virgin upsweep and after the eight-cycle demagnetization. Gray horizontal bars represent the superconducting film. (a) from appended publication II.

As during the field cycling described above the superconductor does not get vortex free again, the virgin state of losses and frequency is never reached either. However, we tried to demagnetize the sample by repeatedly ramping the magnetic field between positive and negative values with decreasing peak values. The idea behind this procedure is that vortices and antivortices almost completely annihilate each other during the repeated cycles and at the end only a stripe-like flux-antiflux pattern with small vortex density remains inside the resonator. Figure 2.11 shows the experimentally determined demagnetization curve of the vortex associated losses $1/Q_v$. At the very end, we arrive at a dissipation state which is very close to the virgin one. For the interpretation of the demagnetization, we have also imaged the flux distribution after a corresponding field demagnetization cycle in the magneto-optical setup. The result is shown in Fig. 2.11 (b). It shows a stripe-like flux pattern as expected by the NBI model. When comparing qualitatively the theoretical expectation (for a single strip) and the result of the imaging in Fig. 2.11 (c) and (d), which both show the flux/intensity profile after a virgin upsweep (black) and after a demagnetization (green), we find a very good agreement between the two which strongly supports the idea behind the demagnetization cycle used for the measurements shown in (a). The results presented can be used to reduce the losses in superconducting resonators for fixed magnetic field values only by choosing the proper magnetic history, cf. Fig. 2.11 (a). The open blue squares showing the minimum values during the demagnetization lie considerably below the virgin values shown as gray squares for fields larger than 1 mT. The hysteresis can also be used to somewhat tune the resonance frequency at a desired external magnetic field as can be seen from Fig. 2.8 (b), see also appended publication II.

Currently a publication of the MOI data including a detailed analysis is in preparation. Moreover there is room for refining the gained experimental data. As the MOI system in Oslo was restricted to low spatial resolutions during the measurements, we had to apply higher magnetic fields than in the spectroscopy experiments. Also, we were only able to clearly resolve the flux distribution in the ground planes and not in the much narrower center conductor which in the images is only approximately five pixels large. However, the images in Fig. 2.10 suggest, in accordance with the NBI model, that the relative flux penetration depth and the flux front shape do not depend on the conductor width. As already discussed for the work on micrometric antidots, we are implementing a high-resolution magneto-optical imaging system in Tübingen, which hopefully facilitates the confirmation of this behaviour.

Own contributions to publication II and more

For publication II, I have fabricated the resonators. I have written a LabView based measurement software and carried out the experiments. Furthermore, I have developed the resonator loss model and the software, with which the numerical results were obtained. With a self-written data processing software, I have analyzed and interpreted the data and I have written the first draft of the manuscript. Regarding the magneto-optical imaging, I have proposed the experiment and analyzed the data.

2.2.3 Microsphere patterned resonators - Publication III

In order to extend the successful experiments on micrometric antidots to higher fields and to field cooled resonators, we have performed a further study with new resonators completely patterned with sub-micrometer sized antidots. This was in the first place suggested by our previous results, which showed that the vortex loss reduction is increased with increasing number of antidots. Moreover, the vortices are expected to be almost homogeneously distributed in the superconducting film, when the chip is cooled through the transition temperature in a perpendicular and homogeneous magnetic field. Finally, the observation that the pinning efficiency is optimized, when vortex and defect lattice have similar characteristic length scales (cf. Sec. 1.2 and Sec. 4.1), leads to the conclusion that smaller antidots with a higher density than before might lead to better results in higher fields. At a magnetic field of 1 mT, the intervortex distance of a homogeneous, hexagonal vortex lattice is about 1.5 μm, so a defect lattice with a comparable lattice constant or even below seems desirable. So for interdefect distances of around 1 μm, the defect size should be on the order of a few 100 nm.

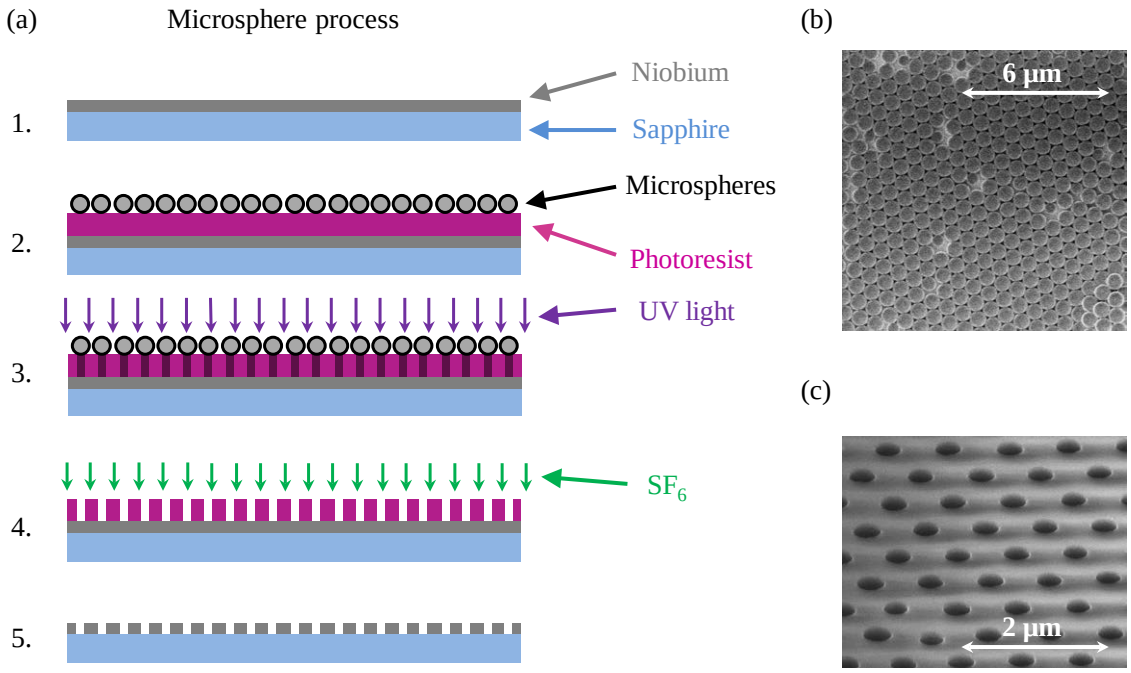

Figure 2.12: (a) Schematic of microsphere lithography. First (1.), we deposited 150 nm niobium by dc magnetron sputtering on a sapphire substrate. Then (2.), we spincoated a photosensitive layer of resist onto the yet unpatterned sample and added a monolayer of self-assembled polystyrene microspheres. (b) shows a scanning electron microscopy (SEM) image of the spheres at this step of the process. After irradiation with UV light (3.), we developed the resist and transferred the resulting quasi hexagonal hole array from the resist into the niobium via reactive ion etching (4.) with SF_6. (c) shows an SEM image of the photoresist after development (angular view). Finally we removed any remaining resist (5.) and proceeded device fabrication with the pre-patterned samples.

However, large area patterning of densely packed submicron structures is challenging, time consuming and expensive with standard lithography techniques. Instead, we have adopted self-assembling microsphere lithography [111, 112] to superconducting films. This technique is based on optical lithography but uses a monolayer of self-assembled microspheres as lithography mask where each sphere acts as a microlense for the incident light. The method allows to achieve hexagonal hole lattices with characteristic dimensions below the light wavelength on almost arbitrarily large areas in a single lithographic step. It is sketched in Fig. 2.12. We used polystyrene spheres with a diameter of $D_s = 770\,(\pm 25)\,\mathrm{nm}$, resulting in antidots with average diameter $D_a = 370\,\mathrm{nm}$ and density $n_a = 1.55\,\mu\mathrm{m}^{-2}$. A more detailed description and analysis of the resulting antidot lattice is given in appended publication V.

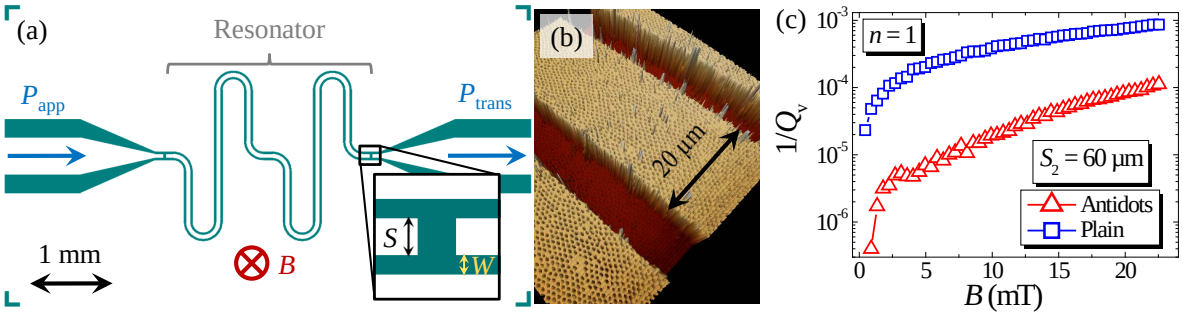

Figure 2.13: (a) Layout of a $7 \times 4\,\mathrm{mm}^2$ large chip with a capacitively coupled 6.25 GHz coplanar waveguide resonator with $S = 60\,\mu\mathrm{m}$ and $W = 25\,\mu\mathrm{m}$. (b) Atomic force microscopy image of a resonator (around the center conductor) patterned with antidots by means of microsphere lithography. The shown resonator has a center conductor width $S = 20\,\mu\mathrm{m}$ and a gap width $W = 8\,\mu\mathrm{m}$. (c) Vortex associated loss factor $1/Q_v(B)$ of a resonator with microsphere patterned antidots (red triangles) in comparison with the corresponding losses of a plain resonator (blue squares). Figure modified from appended publication III. © 2012 by the American Institute of Physics.

From the superconducting niobium chips, which were pre-patterned with microsphere lithography, we fabricated coplanar 6.25 GHz resonators very similar to the ones discussed above, cf. Fig. 2.13 (a) and (b). For a comparison we also fabricated identical but plain resonators, i.e., from niobium films which have not been prepatterned with microspheres. The niobium film had a thickness of approximately 150 nm and was deposited by dc magnetron sputtering on an r-cut sapphire substrate. Afterwards, two series of spectroscopic resonator characterization were performed. In the first experiments we proceeded as in the two studies above, i.e., the samples were cooled to $T = 4.2\,\mathrm{K}$ and then a magnetic field perpendicular to the resonator plane was applied. Again, we found a significant reduction of the magnetic field induced losses in the samples with antidots, for more details see appended publications III.

In a second experiment, the samples were heated above the critical temperature each time before the magnetic field value was changed and as a consequence, the applied field was nearly homogeneously frozen into the superconducting film. The comparison between the resonators with antidots and those without revealed an extremely high loss reduction by antidots of more than one order of magnitude. Figure 2.13 (c) shows in comparison the

magnetic field induced losses $1/Q_v(B)$ in a resonator with antidots and in one without for the field cooled experiments. It can be seen that for magnetic fields $B \sim 1\,\mathrm{mT}$ the vortex quality factor Q_v can in principle reach $10^5 - 10^6$ for the resonator with antidots which is considered as necessary for reaching the strong coupling regime between ultracold atom clouds and the cavity mode [30, 31]. We have done these experiments with two sets of samples, differing in the width of waveguide center conductor $S_1 = 20\,\mu\mathrm{m}$, $S_2 = 60\,\mu\mathrm{m}$ and gap width $W_1 = 8\,\mu\mathrm{m}$, $W_2 = 25\,\mu\mathrm{m}$ and found the results to be valid for both geometries.

With our studies presented we have achieved a good qualitative understanding of superconducting coplanar resonators operated in magnetic fields and how the vortex induced losses can be significantly reduced. However, the operation conditions in temperature and driving power have been far away from the values typically used in quantum experiments with superconducitng circuits. So in the future we will have to investigate our resonators also in the temperature range of $\sim 10\,\mathrm{mK}$. At these temperatures and with suitable supporting electronics such as cryogenic amplifiers, we will also investigate if and how far the results presented above can be transferred to very low oscillating energies in the range of single photons. With regard to quantum coherence in the resonator state, it might also be inevitable to investigate the noise introduced by the presence of vortices.

Own contributions to publication III

For this work, I have contributed to the resonator fabrication (sputtering, standard lithography, etching). I have written a LabView based measurement software and carried out the experiments. With a self-written data processing software, I have analyzed and interpreted the data and I have written the first draft of the manuscript.

2.3 Relation to Part II

Coplanar waveguide resonators as described above are considered as potential buses for the transfer of quantum states from superconducting qubits to atomic or molecular ensembles. To achieve the required coupling strength of the atoms to the cavity fields, the atoms must be trapped and manipulated directly at the superconducting circuits. Here, the idea of atom chips and magnetic fields at the chip surface come into play. By a proper pattern of current leads on a chip in combination with external magnetic fields, an energy minimum for paramagnetic atoms can be created close to the chip surface. Using superconducting leads for the atom chips reduces noise and increases the atomic lifetime in the trap. At the same time, using superconducting wires leads to a deformation of the applied magnetic fields and of the fields related to the on-chip currents which must be carfully considered when superconducting chip traps are designed. The question which arises from the idea of a superconductor/cold atom hybrid is how an atom ensemble can be brought into the mode volume of a superconducting resonator and what are the quantum properties there. Possible answers are discussed in the next section. Once the trapping and manipulation of atoms in the mode volume of a superconducting on-chip resonator has been achieved, the resonator properties must be optimized in the present magnetic fields, for which the results of part I constitute a valuable basis.

Chapter 3

Part II - Towards hybrid devices with atom chips

In this section the results regarding our efforts towards integrated superconducting atom chips containing microwave resonators are presented. First, the concept of trapping paramagnetic atoms with magnetic fields on superconducting chips is introduced. Then we briefly discuss the London equations and a somewhat different type of coplanar resonator than the one used in the first part of the thesis. In the following, the main results of the appended publications IV and V will be presented. For the first, an integrated superconducting atom chip containing trapping wires and coplanar resonator structures has been designed and fabricated and the properties of an ensemble of ultracold atoms trapped on that chip have been determined. The second publication is the proposal to use a short-ended half wavelength resonator which can act as quantum bus and atom trap at the same time and thus might be able to significantly reduce the complexity of a future atom chip. An analysis of the modified resonator and a numerical simulation of the trap as well as a discussion of its properties is included. At the end of this part we state the relation between part II and part III.

3.1 Basics Part II

3.1.1 Superconducting atom chips

A highly promising candidate as quantum memory in a hybrid quantum system are paramagnetic atoms, whose magnetic states are coupled to the magnetic fields of a superconducting microwave cavity [29, 30]. The coupling strength of a single electronic spin to the fields in a typical coplanar superconducting microwave cavity, however, is by far too small to achieve a strong, quantum coherent coupling, which is inevitable for a reliable quantum state transfer between the two systems. The solution is to use not a single atom, but an ensemble of atomic or molecular systems, which collectively couple to the resonator. This enhances the coupling strength by $\sqrt{N_{\mathrm{at}}}$, where N_{at} is the number of atoms. For spins with an individual coupling rate of $\sim 10\,\mathrm{Hz}$ (given by the single spin dipole moment and the magnetic field strength per photon) in a cavity with a frequency of a few GHz and

a quality factor $Q \sim 10^6$, the minimum number of spins to achieve the strong coupling regime between the ensemble and the cavity is $N_{\mathrm{at}} \approx 10^5 - 10^6$. An important challenge is to bring the ensemble to the maximum microwave magnetic field of the resonator and to control the internal and external degrees of freedom of the atoms with high precision there.

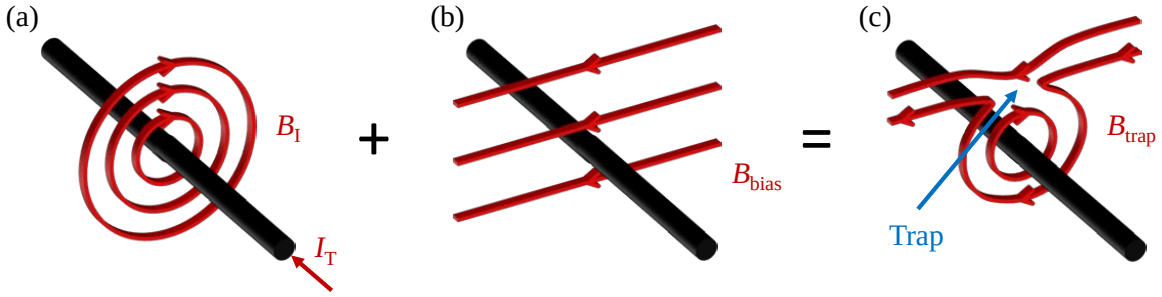

Figure 3.1: Sketch of the working principle of a magnetic trap for neutral, paramagnetic atoms. The radially decreasing magnetic field of a wire carrying a current I_{T} (a) is superimposed with a homogeneous magnetic field B_{bias} (b). The two fields compensate each other at a certain distance from the wire, which can be adjusted by varying the strength of I_{T} or B_{bias}. Around the compensation point the potential energy of low field seeking atomic states is minimized and therefore a trap is formed there (c).

One way to trap paramagnetic atoms such as the rubidium isotope ^{87}Rb is to generate a local minimum of the magnetic field magnitude $|\vec{B}(\vec{r})|$ by a combination of homogeneous magnetic fields and the inhomogeneous field of a current wire as shown in Fig. 3.1. At one point above the wire, the wire field B_{I} and the homogeneous bias field B_{bias} cancel, yielding a minimum of the absolute value of the magnetic field. For so-called low field seeking atomic states, the potential energy in the field is given by [42]

$$U(\vec{r}) = |\vec{\mu}| \cdot \left|\vec{B}(\vec{r})\right|. \tag{3.1}$$

and an atom trap is formed by the minimum of $|\vec{B}(\vec{r})|$. Here, $|\vec{\mu}| = m_F g_F \mu_{\mathrm{B}}$ is the projection of the magnetic moment of the atoms onto the B-field axis with the magnetic quantum number m_F, the Landé factor g_F and the Bohr magneton μ_{B}. Note, that low field seeking states are defined by $m_F g_F > 0$.

In general, an additional homogeneous offset field B_{off} along the trapping wire is applied, which generates a harmonic trap minimum and lifts the degeneracy of Zeeman sublevels, thereby reducing atom losses due to Majorana spin-flip transitions (transitions of atoms from trapped to untrapped states) [113]. Finally, a potential minimum has to be created also in the direction along the trapping wire, because otherwise the atoms can freely propagate in this direction. Such a longitudinal confinement can be achieved by two additional wires perpendicular to the original one, which carry a current such that the related magnetic field points into the direction of the offset field. It turns out that, although the three wire configuration gives higher flexibility regarding the trapping parameters, it is sufficient to use a single wire shaped like a Z for ensuring the longitudinal confinement.

The current carrying wires described above do not need to be circular wires, but can as well be microstructures with a rectangular cross-section patterned from metal films on a substrate. This is the basic idea of the atom chip [42]. By varying the magnitude of the trapping current I_{T} through the wire or by varying the magnitude or direction of the homogeneous field B_{bias} perpendicular to the on-chip wire, a trap can be generated at any point above the chip surface and the atoms can be brought into controlled interaction with the chip surface itself or with micro- and nanostructured circuits on that surface.

Although the experimental difficulties of using a setup, which combines a magneto-optical system at room temperature with a cryostat are rather high, it has considerable advantages to use a superconducting chip instead of a normal conducting one. First, a superconducting wire can carry very high dc current densities without any resistive dissipation. Second, a superconducting trap wire has a highly reduced Johnson-Nyquist noise compared to a normal conducting one. This leads to a lower spin flip and atom loss rate close to superconducting surfaces with respect to normal conducting ones [114–119]. Third, it is possible to use superconducting loops in which a persistent current has been induced [120].

A very important issue with superconducting atom chips is the magnetic trap field distortion by any superconducting structure, whether in the Meissner state [121–123] or in the vortex state [124–126]. This is in particular relevant, when the trap is moved very close to any superconducting structure, as necessary for any electromagnetic coupling between the systems, because there all magnetic fields are highly modified due to screening currents. For a proper design and understanding of what happens on the chip, careful numerical simulations of the magnetic fields are necessary. As we were working with low magnetic fields, it was sufficient to consider the London equations for the corresponding simulations which are introduced below.

3.1.2 The London equations

The first macroscopic theoretical description of the electrodynamics of superconducting materials was given by the London brothers in 1935 [70]. Following the classical approach, the London equations can be derived assuming an undamped equation of motion for the superconducting charge carrier velocity

$$m\frac{\mathrm{d}\vec{v}_s}{\mathrm{d}t} = q\vec{E}, \tag{3.2}$$

where m is the charge carrier mass, q is the charge and $\vec{E}$ is an electric field. With the general expression for the current density $\vec{j}_s = n_s q \vec{v}_s$, we get

$$\vec{E} = \frac{\mathrm{d}}{\mathrm{d}t}\left(\Lambda\vec{j}_s\right), \tag{3.3}$$

where we have introduced $\Lambda = m/n_s q^2$ with the superconducting charge carrier density n_s. This is the first London equation. It states that for stationary currents $\mathrm{d}\vec{j}_s/\mathrm{d}t = 0$, there is no electric field present in the superconductor.

Taking the curl of the first London equation and using Faraday's law of induction

$$\vec{\nabla} \times \vec{E} = -\frac{\partial \vec{B}}{\partial t} \tag{3.4}$$

we obtain

$$\vec{\nabla} \times \Lambda \dot{\vec{j}} = -\dot{\vec{B}}. \tag{3.5}$$

With the time derivative of Ampère's law (neglecting Maxwell's displacement current)

$$\vec{\nabla} \times \dot{\vec{B}} = \mu_0 \dot{\vec{j}} \tag{3.6}$$

and the solenoidality of the magnetic induction $\vec{\nabla} \cdot \vec{B} = 0$ we obtain

$$\Delta \dot{\vec{B}} = \frac{\mu_0 n_s q^2}{m} \dot{\vec{B}} = \frac{1}{\lambda_\mathrm{L}^2} \dot{\vec{B}} \tag{3.7}$$

where we have introduced the London penetration depth $\lambda_\mathrm{L} = \sqrt{m/\mu_0 n_s q^2}$. Eq. (3.7) states that a change of the magnetic field in time is screened from the interior of the superconductor except for a thin surface layer on the order of λ_L.

It has been observed by Meissner and Ochsenfeld [69] that not only any change of magnetic field is screened from the interior of a superconductor but also any magnetic field itself. Hence, the London brothers assumed Eq. (3.5) which led to Eq. (3.7) to be also valid in the stationary case

$$\vec{\nabla} \times \vec{j} = -\frac{n_s q^2}{m} \vec{B}, \tag{3.8}$$

which is now known as the second London equation. This equation implies the screening of $\vec{B}$ from the interior of the superconductor which with the help of Maxwell's equations can be expressed by

$$\Delta \vec{B} = \frac{1}{\lambda_\mathrm{L}^2} \vec{B}. \tag{3.9}$$

The software package 3D-MLSI, which we have used for the numerical simulations in publication V, mainly solves Eqs. (3.8) and (3.6) simultaneously as described in Refs. [127–129]. The simulations of the London equations presented in publication IV have been performed with a different software [122], but the results have been reproduced with good comparability by means of 3D-MLSI.

Note that the superconductor does not remain completely flux free but gets penetrated on a length scale of λ_L by $\vec{B}$, which is due to the kinetic energy of the charge carriers contributing to the screening current density. As the superconductor is found in the state with the lowest free energy, not only the magnetization energy has to be considered.

Actually it is possible to derive the second London equation by a variational problem considering the total free energy of a superconducting volume, cf. e.g. [79]. If the charges would not have any inertial mass, $\lambda_L = 0$.

The London equations can also be derived from the Ginzburg-Landau equations assuming a constant order parameter or from the fluxoid quantization condition. However, the derivation above corresponds to the historically first one presented by the London brothers when superconductivity has not been recognized as a macroscopic quantum phenomenon.

3.1.3 Coplanar waveguide resonators Part II

When designing an integrated chip containing atom trap wires and superconducting resonators at the same time with the possibility to bring the atoms into the mode volume of the resonator, the very particular requirements for manipulating and detecting the atoms have to be carefully considered. In our case, it was necessary that the chip is completely flat on one half as from that side the prepared atom cloud is delivered with a dipole trap (optical tweezers) which is moved parallel to the chip surface at a distance of some hundred micrometers and which must remain optically unperturbed during that transfer. For this reason, all contact pads on which microwave and trap current wires are mounted had to be on one side of the chip. Secondly, optical access must be granted to the position of the cloud also in the direction perpendicular to that of the optical tweezer. This enables the electronic state manipulation and absorption imaging of the atoms which is inevitable for a trap and cloud characterization and to reliably detect the position of the atoms. Finally, we wanted to have several resonators at the same time on one chip, as on one hand it is hardly possible to exactly determine the temperature and field dependent resonance frequency in the final setup and on the other hand it would be nice to have the possibility to investigate the influence of resonator-atom detuning by means of several resonators with different frequencies.

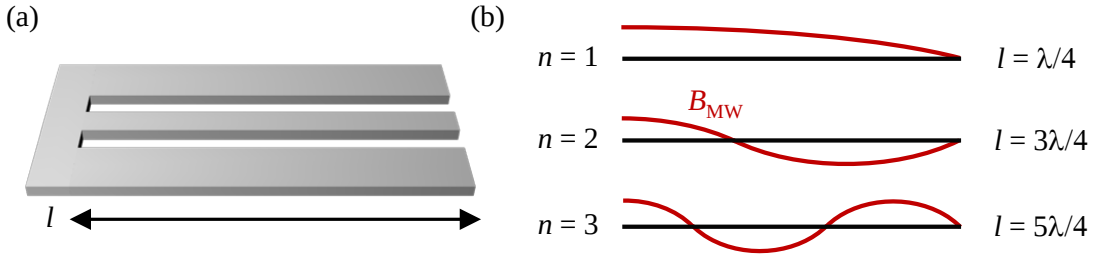

Figure 3.2: (a) Sketch of a coplanar quarter wave resonator with a shorted end (left side) and an open end (right side). (b) shows schematically the magnetic field amplitude along the resonator for the three lowest modes $n = 1, 2, 3$ of the resonator shown in (a). For all modes, there is a magnetic field node at the open end and a magnetic field antinode at the shorted end.

All these requirements can be fulfilled by using a somewhat different kind of resonator as the half wavelength resonators desribed in part I. One of them is schematically depicted in Fig. 3.2 (a). Instead of two open ends, it has only one open end and one end directly shorted to ground leading to a voltage node at the open and to a current node at the shorted side. The different modes of such a resonator correspond to the condition $l =$

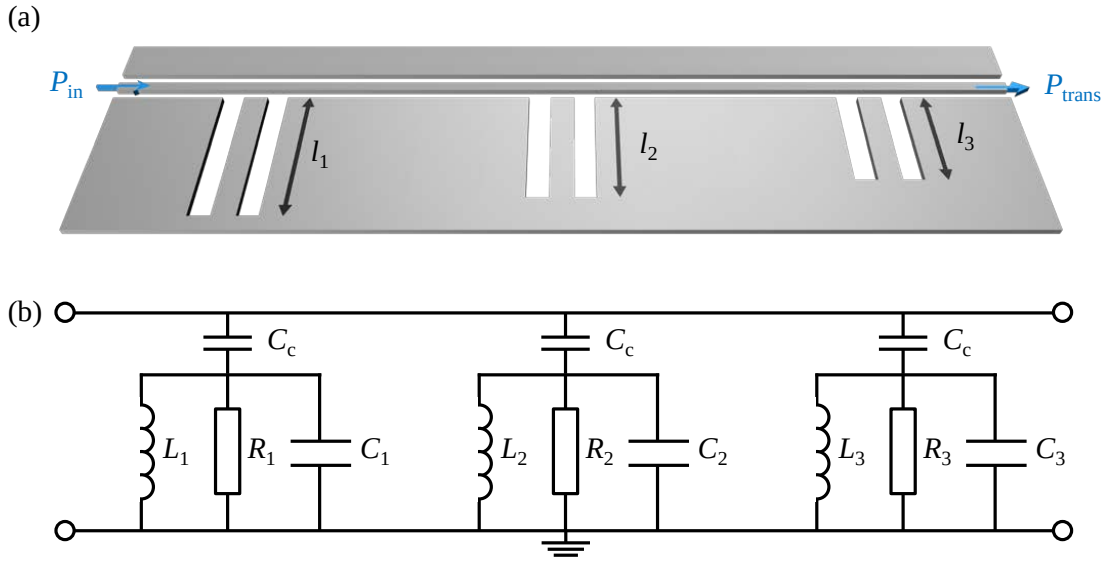

Figure 3.3: (a) Sketch of a chip layout with three quarter wave resonators with different lengths l_i coupled to a common coplanar feedline. A characterization of all resonators is possible by measuring the frequency dependent transmitted power across the common feedline. (b) shows the generalized transmission line and lumped element circuit representation of (a), where each quarter wave resonator is represented by a parallel RLC circuit coupled by a capacitance C_c to the signal line of a transmission line.

$(2n-1)\lambda/4$ with $n = 1, 2, 3...$ and so the resonator is called a quarter wave resonator. Its three lowest modes are schematically shown in Fig. 3.2 (b).

Such a resonator can be capacitively coupled to a continuous coplanar waveguide by placing its open end into the transmission line, cf. Fig. 3.3 (a) where three resonators with different lengths are simultaneously coupled to one common feedline. Then, the power transmitted across the transmission line shows a minimum at the resonance frequencies of each resonator, which extracts energy from the feedline around its resonance, cf. e.g. [130]. Similar to the half wavelength resonators, it is possible to approximate the quarter wave resonators as RLC circuits around the resonance frequency [84]. Figure 3.3 (b) shows the equivalent circuit representation of such a multiple resonator configuration. Note that the latter is only valid piecewise, as each quarter wave resonator can only be approximated as a parallel RLC circuit around its own resonance frequency.

3.2 Results Part II

3.2.1 Manipulation and coherence of atoms on a chip - Publication IV

During this thesis, a superconducting chip based on 500 nm thick dc magnetron sputtered niobium on a sapphire substrate has been designed and fabricated. An optical image of the corresponding chip is shown in Fig. 3.4 (a). It contains four parallel trapping wires

with different widths from 100 μm down to 10 μm which can be seen in more detail in Fig. 3.4 (b) at the bottom of the image. The trap wires are running over the chip in a meandering way, hereby forming six Z-shaped atom traps at different positions.

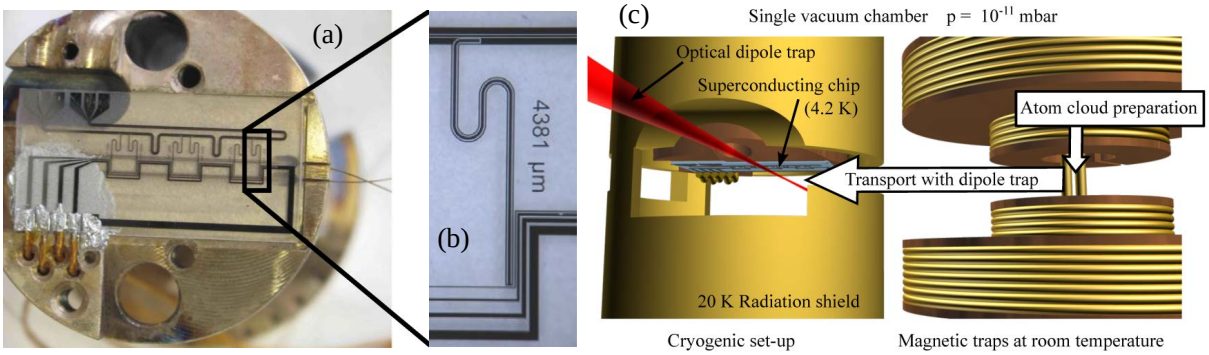

Figure 3.4: (a) Photograph of the integrated atom chip mounted on a copper sample holder. The chip has a size of $20 \times 10\,\mathrm{mm}^2$. It contains four Z-shaped trapping wires (lower part of the chip), and six coplanar quarter wave resonator structures coupled to a common feedline (upper part). The shorted resonator end is positioned directly besides the Z-trap structures as can be seen in the zoomed image (b). (c) shows a sketch of the ultra high vacuum setup combining room temperature magnetic traps for the atom cloud preparation and a helium flow cryostat, on which the chip is mounted. The atom transfer between the room temperature part and the cryogenic part of the setup is done with an optical dipole trap. Figure modified from appended publication IV,

The chip also contains a coplanar transmission line with six quarter wave resonators coupled to the continuous line with elbow capacitors. The six resonators slightly differ in length and resonance frequency, respectively. Each of the resonator structures ends with the shorted end, where the microwave magnetic field is supposed to have a maximum, directly besides the narrowest Z-trap wire, cf. Fig. 3.4 (b). To keep the magnetic field and trap distortions due to the Meissner effect of the microwave lines as small as possible, we have designed the ground conductors of the coplanar line with only finite extensions. With this decision, we did not follow the common design rules for coplanar waveguides for an effective suppression of spurious resonances in the substrate and induced by stray capacitances to other metallization structures, which should be attended in particular for microwave lines on large chips, cf. [131]. Besides a large amount of parasitic resonances, we found a considerable crosstalk of the individual resonators in microwave spectroscopy measurements, possibly induced or enhanced by the trap current wires. However, on that chip we wanted to minimize the magnetic field distortions which would come with large area superconductors and focused on demonstrating the possibility of atom state manipulation and their quantum coherence in this highly complex environment. To keep the atoms unperturbed, we have chosen a resonator designed to be some 100 MHz off-resonant from the atomic transition and did not contact the microwave lines on the chip. The experiments with atoms on the chip described from here have been carried out by the Tübingen cold atom group on a superconducting atom chip fabricated within this thesis. The corresponding numerical simulations have partly been performed in the cold atom group as well.

An ensemble of rubidium atoms (^{87}Rb) is first prepared in a room temperature setup, i.e., it is trapped in a magneto-optical trap (MOT), where it is cooled by six orthogonal laser beams. Then it is transferred to a magnetic trap where the ensemble is cooled further down by radiofrequency evaporative cooling, before it is loaded into an optical dipole trap [132] and shuttled to the chip, which sits upside down on the cold finger surface of a helium flow cryostat at $T = 4.2\,\mathrm{K}$. A sketch of the setup (without MOT) is shown in Fig. 3.4 (c). For more details on the setup, the preparation and cooling of the ensemble and the transfer to the chip, see [133].

First, the possibility to position the cloud in a controlled way on the chip within the complex magnetic environment was investigated. In particular, the atoms had to be brought into the mode volume of the quarter wave resonator which means either close to the gap between center conductor and ground conductor or to a position closely above the center conductor [30]. For this purpose, the cloud was loaded onto the chip from the tweezers by sending a current of $I_\mathrm{T} \sim 1\,\mathrm{A}$ through the widest Z-wire. From there the atoms were transferred one by one to the narrower wires by turning the current in these on and switching the current in the neighboring wider wire off. Due to a unknown noise source when biasing the smallest wire, the atoms had to be kept in the second narrowest one and the trap position dependent on the current amplitude and on the angle α between the bias field and the chip surface was investigated there. For small α the trap position - determined by in-situ absorption imaging of the trapped atom cloud - moves on a nearly straight line towards the trapping wire when the current though the wire is reduced, which is shown in Fig. 3.5 (b). In the following, the magnetic field component of B_bias parallel to the chip surface was kept constant and the field component perpendicular to the surface was varied, which effectively corresponds to a change of α. For different angles α the current dependence determination of the trap position was repeated and this revealed a surprising but very welcome effect. When for large α the atoms approach a position above the resonator gap, a further reduction of the trap wire current I_T does not move the trap position linearly closer to the trapping wire, but the cloud is attracted into the gap, cf. Fig. 3.5. Exactly where the cloud has to be for maximized coupling.

In order to better understand this focusing effect, numerical simulations of the system have been performed by solving the London equations for our geometry with two different software packages described in Refs. [122, 127–129], which yielded almost identical results. The corresponding trap positions extracted from one of these simulation packages [122] are shown in Fig. 3.5 (b) in comparison with the experimentally determined positions and the agreement is rather high. With the simulations, we have been able to identify the physical reasons for the trap focusing into the resonator gap. The quarter wave resonator geometry contains a large and closed superconducting loop, cf. Fig. 3.5 (a), in which the magnetic flux is conserved due to Faraday's law of induction and the perfect conductivity of the superconductor. As all magnetic fields in this first experiment have been applied after the sample has been cooled to $T = 4.2\,\mathrm{K}$, i.e., to the superconducting state, the field component perpendicular to the superconducting chip induced a net screening current I_Scr circulating in the resonator ground planes and keeping the magnetic flux in the loop zero. This flux conservation in addition with the field expulsion due to the Meissner effect from the superconducting films and a related field enhancement close to the edges, the gap develops to an energetically favorable spot for the atoms under the given conditions.

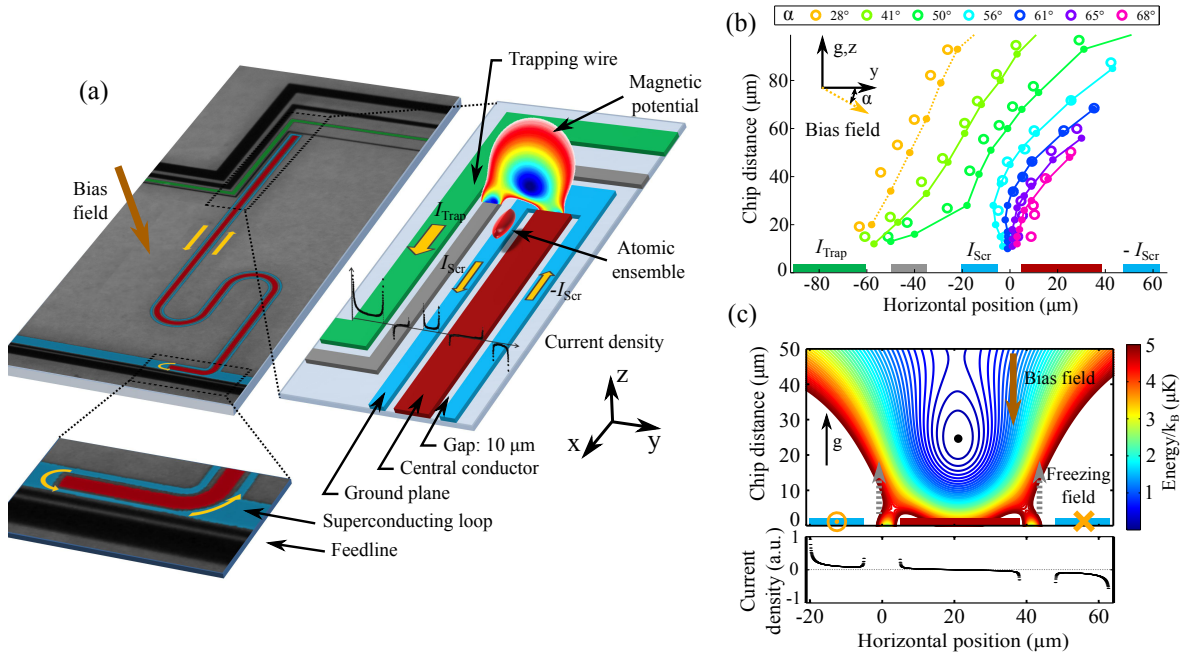

Figure 3.5: (a) Scheme of trapping atoms in the gap of a superconducting coplanar quarter wave resonator structure. The trap above the gap is a result of a homogeneous magnetic bias field and magnetic fields generated by the trapping wire current I_{Trap} and the screening current I_{Scr} circulating in the ground conductor loop to guarantee flux conservation. The color map shows the potential landscape numerically obtained and the black lines/dots show the corresponding current density in the wires. (b) Position of the trap for different currents in the trapping wire and different angles α between the bias field and the surface of the chip. Circles are experimental data and small dots connected by lines are the result of numerical simulations. For more details see appended publication IV. (c) Top: numerically obtained potential energy above the resonator shown in (a) with flux frozen into the closed loop by applying $B^{\mathrm{freezing}} = 80\,\mu\mathrm{T}$ during cooldown through T_c and applying an opposite bias field $B^{\mathrm{bias}} = 120\,\mu\mathrm{T}$ afterwards. Isolines are separated by 100 nK. Bottom: Current density distribution induced by the combination of bias field and freezing field. Figure modified from appended publication IV, © 2013 Nature Publishing Group.

Cloud focusing, however, is not the only possibility how the flux conservation in the superconducting loop can be exploited. By applying a homogeneous magnetic field perpendicular to the chip surface during the transition to the superconducting state, it is possible to freeze in a desired amount of flux into the closed loop, which afterwards is conserved, even if the field is swept into the opposite direction. By exactly this method, it has been able to create another magnetic trap structure, a persistent current trap which for symmetry reasons is formed directly above the center conductor. In Fig. 3.5 (c) the numerically obtained potential energy (in temperature units) for ^{87}Rb atoms in such a persistent current trap is plotted (including gravity).

Finally, the properties of the atomic ensemble on the superconducting chip have been investigated by creating and characterizing a quantum superposition of two internal atomic states. The most interesting transition of ^{87}Rb with respect to quantum information hybrid systems with superconductors is the transition between the two trapped hyperfine ground states $|0\rangle := \left|5S_{1/2}, F = 1, m_F = -1\right\rangle$ and $|1\rangle := \left|5S_{1/2}, F = 2, m_F = 1\right\rangle$ with a

transition frequency $\omega_r/2\pi \approx 6.834\,\mathrm{GHz}$. For the relevant energy level diagram of ^{87}Rb, see the appended publication IV. As it is not possible to drive this transition with a single photon, two electromagnetic waves have been combined which together are able to induce two-photon transitions between $|0\rangle$ and $|1\rangle$. One of the two waves is a microwave with a frequency $f \approx 6.833\mathrm{GHz}$, which is already close to the transition, and the second is a radio wave with a frequency of around 1.3 MHz. By inducing and measuring Rabi oscillations between $|0\rangle$ and $|1\rangle$ and the corresponding state occupation probability, the optimal microwave pulse time for $\pi/2$ pulses has been determined first. Then, a Ramsey interferometry experiment [134] with a reference oscillator detuned by some Hz with respect to the atomic transition has been carried out to characterize the time development of the superposition state and the decay of the quantum coherence. This determination of the coherence time has been done at three different positions on the chip. In a standard trap $60\,\mu$m directly above the second narrowest trapping wire with $\alpha = 0$, in a trap focused into the resonator gap at $14\,\mu$m above the surface and finally in the persistent current trap $25\,\mu$m above the resonator center conductor. In all three traps, atomic coherence times of at least several seconds were found, which demonstrates that ultracold atoms trapped in a complex environment still show the favorable properties for which they have been proposed as quantum memory in hybrid systems. For more details regarding the coherence measurements, the atom cloud preparation and the imaging on the chip, see the appended publication IV.

Own contributions to publication IV

For this work, I have designed the microwave structures and resonators on the atom chip and fabricated the device. I have contributed to the numerical simulations and to the data interpretation.

3.2.2 Short-ended half wavelength resonators as atom traps - Publication V

The work in the appended publication V is the consistent continuation after the experiences with the atom chip described in the previous work. Due to a large amount of microwave crosstalk and many spurious resonances, which appeared on the large atom chip with six resonators and many trap wires, we have not been able to perform experiments regarding the coupling between the cavity and the atom cloud under well-defined conditions. So for the next experimental step, which will be targeting the question of that coupling, a system with reduced structural complexity is highly desirable. First, we want to use only a single resonator on a considerably smaller chip, as large chips make spurious resonances more probable to appear at low frequencies. A single resonator approach requires an in-situ tunability of the resonance frequency and several possibilities to achieve this are currently developed. Secondly, it would be desirable to be able to work without additional trap wires on the chip which probably lead to crosstalk and stray capacitances and by this induce additional parasitic resonances. Finally, we would like to keep the possibility to use the resonator itself as persistent current trap as it was demonstrated in the previous work.

As for a persistent current trap closed superconducting loops are inevitable, we cannot just use a simple capacitively coupled half wavelength resonator as customary in circuit quantum electrodynamics and as discussed in part I of this thesis. Instead we investigated the possibility to use a different type of half wavelength resonator with two shorted ends as shown in Fig. 3.6 (a). The shorts between the center conductor of the waveguide and the ground conductors constitute to first order a shunt inductance coupling the feedlines to the resonator analogously to the gap capacitors usually discussed. The main difference between this configuration and the capacitively coupled one is that nodes and antinodes of the microwave magnetic (and also electric) fields in the resonator change position. The lumped element representation of the short-ended transmission line resonator around the resonance frequency is shown in Fig. 3.6 (b).

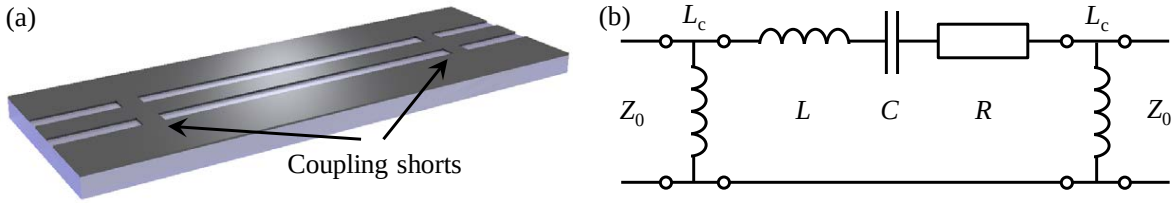

Figure 3.6: (a) Sketch of a short-ended half wavelength resonator based on a coplanar waveguide. The shorts correspond to coupling inductances as indicated in (b), which shows the series lumped element equivalent of (a) valid close to the resonances. The lumped element equivalents for a resonator with length l and characteristic impedance Z_0 are given by $R = Z_0\alpha_d l$, $C = 1/Z_0 f_0 \pi^2$ and $L = Z_0/4f_0$. Figure modified from appended publication V, © 2013 IOP Publishing Ltd.

In our work, we have first investigated the accessible range of coupling strength between the feedlines and the resonator which is directly related to the external quality factor Q_{ext}. The external quality factor Q_{ext} is a figure of merit for the amount of energy lost per oscillation due to the coupling to the external circuitry and for circuit QED typically takes values between 10^3 and 10^6. With an analytical analysis of the resonator around the resonance frequency, we show in the appended publication V that $Q_{\text{ext}} \propto 1/L_c^2$ where L_c is the inductance of the shorts. With the simulation software package 3D-MLSI [129], we have numerically calculated the inductance of such coupling shorts in typical waveguide geometries and found that the desired external quality factors are absolutely comparable to those achievable by gaps. So inductively coupled resonators including two closed superconducting loops are equivalent to the capacitively coupled ones from the circuit point of view but superior from the viewpoint of persistent current traps for paramagnetic atoms.

By means of numerical simulations, we have developed a method for using the inductively coupled resonator as a persistent current trap, a way to load the persistent current trap with an additional transport current across the resonator (making extra trap wires on the chip unnecessary) and a field sweep sequence which allows to transfer the atoms into the resonator gap for optimized magnetic coupling to the cavity photons. We have performed these simulations for three different ground plane widths $G = 20, 50, 100\,\mu$m and found that for all widths a parameter set can be found which allows to create a trap close to the surface with favorable properties for quantum information processing.

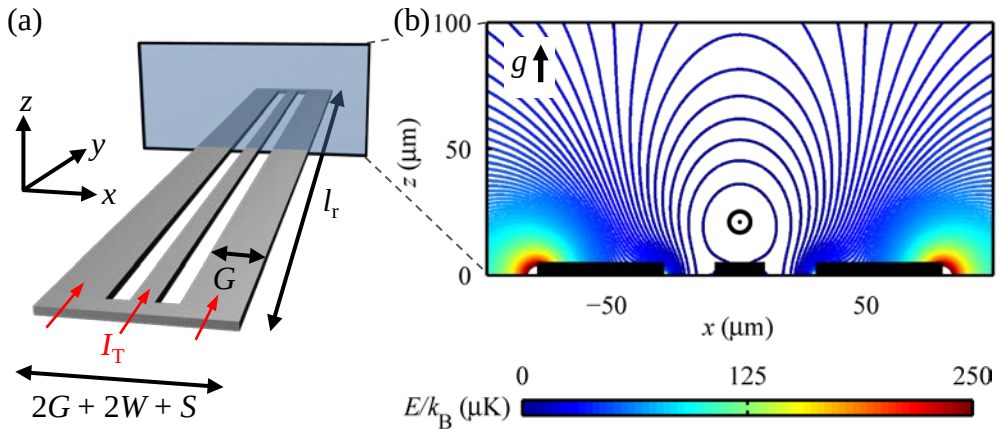

Figure 3.7: (a) Superconducting geometry used for the simulation of magnetic trapping fields. The x–z-plane, where we extract the magnetic fields for the trap calculations, is marked by a transparent rectangle.The width of the center conductor is $S = 20\,\mu$m, the width of the gap is $W = 20\,\mu$m and the groud plane width is $G = 50\,\mu$m. (b) Example for the trapping potential landscape which can be created above the resonator by a combination of flux frozen into the loops, homogeneous magnetic fields applied in $z-$ and y-direction and gravity. Isolines are separated by $\Delta E/k_B = 2\,\mu$K. For details regarding the different fields see appended publication V. Figure modified from appended publication V, © 2013 IOP Publishing Ltd.

Figure 3.7 (a) shows the simulated superconductor geometry, which is a somewhat simplified short-ended half wavelength resonator with a ground plane width of $G = 50\,\mu$m. In Fig. 3.7 (b) the potential energy landscape for ^{87}Rb atoms in the $|0\rangle$ state above that resonator is depicted. The trap is created analogously to the one presented in publication IV, i.e., by freezing a certain amount of magnetic flux into the loops and afterwards superimposing an external bias field into the opposite direction. The field parameters for the calculations shown in (b) are given in the appended publication V.

For using the atom cloud as a quantum memory it is important that the coherence time of quantum superposition states is not too short. And there are many important mechanisms in the ensemble dynamics which have an impact on the coherence time. Amongst others there are magnetic field inhomogeneities in the trap and different atom-atom interactions such as spin exchanging collisions. However, it has turned out that in magnetic traps characterized by trap frequencies on the order of $\sim 100\,$Hz the conditions for coherence times of $\sim 10\,$s can be achieved experimentally [135, 136] by allowing favorable regimes of ensemble temperature and atom densities. The trap frequencies correspond to the mechanical oscillation frequencies of the atoms in the trap and can be extracted from the simulations by a harmonic approximation around the trap minimum. So we additionally checked whether in our persistent current resonator trap the frequencies can be brought to a regime favorable for long coherence times. We found that by properly choosing freezing and bias field, a trap can be created at any distance above the center conductor between $5\,\mu$m and $50\,\mu$m with trap frequencies in the range of some hundreds of Hz, cf. appended publication V.

Finally, we present the result of the developed field and current sweep sequence which allows to load the atoms into the trap from optical tweezers some hundreds of μm above

the chip surface and to continuously shuttle the ensemble into the resonator gap, where the coupling to the magnetic fields of the cavity photons is maximized. During the whole atom transfer from far above the chip into the gap, the trap frequencies can be kept in the desirable regime of hundreds of Hz. Figure 3.8 (a) and (b) show the numerically calculated position and trap frequencies during the shuttle process, for more details regarding the field and current sweep sequence see the appended publication V.

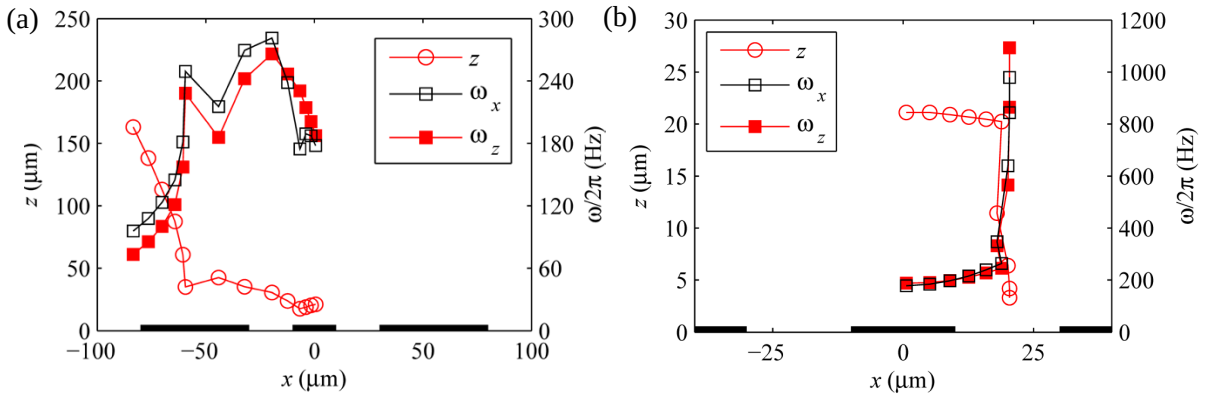

Figure 3.8: (a) Trap position and corresponding trap frequencies as obtained from numerical simulations during current and field sweeps developed to load the persistent current trap with atoms delivered at $\sim 100\,\mu$m above the chip surface. (b) Trap position and corresponding trap frequencies during the field sweep sequence which shifs the trap and the atoms in it from the configuration shown in Fig. 3.7 (a) into the resonator gap. Black bars at the bottom indicate the position of the superconducting resonator wires. For details regarding the current and field parameters during the sweeps, cf. appended publication V. Figure from appended publication V, © 2013 IOP Publishing Ltd.

In the paper, we finally give a discussion on possible trapping of Abrikosov vortices during the different current and field sweeps and show that in principle it should be possible to drive the chip with full functionality but without trapping vortices. If it turns out that such a short-ended resonator can indeed be used as a quantum bus and atom trap at the same time and if the long coherence times of publication IV can be maintained in such a trap, this method seems suitable as an important element in future hybrid quantum circuits.

Own contributions to publication V

I have proposed the idea of this work and developed the theoretical description of the resonator. Furthermore, I have contributed to the numerical simulations of the coupling inductances and of the atom trap. Finally, I have written the first draft of the manuscript.

3.3 Relation to Part III

Using the superconducting resonator structures as persistent current traps requires a magnetic field which is frozen into the loops. When doing so, however, magnetic flux

will also be trapped in the superconducting trapping wires and resonator leads. This can have several different undesired consequences. The first was extensively discussed in part I and is related to the energy dissipation induced by the vortices. Another aspect is magnetic noise introduced by thermally activated vortex hopping, which leads to heating of the ultracold atom cloud and thus to reduced atomic lifetimes in the trap [137]. Finally, vortices trapped at arbitrary positions in the wires lead to a reduced reproducibility of the trap properties and to an uncontrolled magnetic trap inhomogeneity at small distances to the surface.

One way to control the trapping to a certain amount is the introduction of energetically favorable locations for the vortices, i.e., of artificial pinning sites as antidots. Of course, it is not sufficient to use a single pinning site but it needs a lot of them and one critical and interesting parameter of the ensemble is its arrangement and symmetry. The pinning efficiency and in particular its field dependence is strongly dependent on the antidot arrangement, and the investigation of pinning lattices with periodic and quasiperiodic geometry and with gradually introduced disorder is presented in the next and last part of the thesis.

Very recently, there has been a proposal for a novel magnetic atom trapping method which is related to the next section [64]. The idea is to use a superconducting film patterned with antidots which are filled with Abrikosov vortices. By each vortex in an antidot, one or more atoms can be trapped and a model system for particles in a potential landscape with the same symmetry as the antidot lattice is created. This would lead to potential landscapes similar to those created in optical lattice experiments. However, the use of a superconducting vortex lattice instead of optical lattices might have two interesting advantages. First, the lattice constant of antidot lattices can be made considerably smaller than optical wavelengths and thus a new regime of particle interaction range can be investigated. Second and more relevant for this thesis, potential landscapes for the atoms with disorder and quasiperiodicity (in general of arbitrary geometry) become easily accessible, which is not the case in standing laser wave patterns. However, for the creation of such potentials with reduced order it is important to know, which antidots are occupied with how many vortices. This is a question, which amongst others we have investigated in the following thesis part III.

Chapter 4

Part III - Antidot arrays with unconventional topology

In part III of the thesis, the magnetic field dependent transport properties of superconducting films patterned with antidot arrays of reduced symmetry compared to periodic ones are discussed. First, we introduce how an ensemble of Abrikosov vortices interacts with an ensemble of antidots and how this interaction and the antidot arrangement influences the measurable properties of the sample, in particular the critical current in a magnetic field. As not only the critical current can be modified through holes in the superconducting film, but also the magnetic field dependence of the critical temperature, the corresponding Little-Parks effect will be briefly introduced as well. Then, we present our results on three different disordered systems. First, we followed a theoretical proposal and fabricated different samples with gradually increasing disorder in the antidot array. We characterized these samples by means of electric transport measurements and summarized the results in the appended publication VI. In the appended publication VII, we have investigated the naturally disordered system of antidots arrays fabricated with self-assembling microsphere lithography as used for the resonators in publication III. Finally, we have investigated different types of quasiperiodic antidot arrays by means of numerical simulations and transport measurements. The corresponding results can be found in the appended publications VIII and IX. At the very end, we discuss the connection to part I of the thesis.

4.1 Basics Part III

4.1.1 Matching between a vortex lattice and an antidot array

Abrikosov vortices tend to arrange in a periodic, hexagonal pattern as they try to maximize their mutual distance in order to minimize their interaction energy [79, 80], cf. also Sec. 1.2. If at the same time there is an ensemble of antidots present in the superconductor, the vortices try to occupy as many of the antidots in order to minimize the condensation energy required for breaking the Cooper pairs in each normal conducting vortex core. The detailed arrangement of the vortex ensemble in a particular antidot

array thus is determined by an interplay between these two effects. From the viewpoint of a collectively pinned vortex ensemble, the pinning strength onto the vortex lattice as a whole increases with decreasing lattice deformation energy [60, 78, 138]. For the particular case that the energetically most favorable vortex distribution is equal to the antidot arrangement, the deformation energy vanishes and the pinning is maximized.

A common probe for the determination of the pinning efficiency is to measure the current-voltage characteristics of the superconducting specimen dependent on the vortex density. In such measurements, a voltage drop occurs along the sample above a certain threshold current (depinning or critical current) due to the dissipative vortex motion. The higher the pinning force on the vortex ensemble hereby is, the higher is the critical current. With this electric transport characterization, it is possible to resolve commensurable states between the vortex lattice and the antidot array. At any magnetic field value, at which the ensemble is pinned extraordinarily strong, the critical current $I_c(B)$ shows a local maximum which is called a commensurability or matching effect. Although we mainly focus on measuring the critical current to determine matching effects, the critical current is not the only property modulated by vortex-defect commensurabilities. Other quantities which show matching effects are the magnetization, the magnetic ac susceptibility, the magnetoresistance or the voltage noise. Matching effects have first been observed in superconducting samples with periodic material modulations [139], thickness modulations [140] and in superconducting films with periodically arranged holes [141]. They have been investigated in different superconductors with different kinds of pinning sites as antidots, magnetic dots or carbon nanotubes [142–148]. The variety of experimental and theoretical work done in the field of vortex pinning with artificial defects and matching targets the influence of shape and size of the defects [149–154] as well as their arrangement and geometry [58, 59, 61, 63, 155–160]. By different imaging techniques as Lorentz microscopy, scanning Hall bar microscopy or bitter decoration with single vortex resolution it is also possible to directly visualize the vortex configurations in the matching fields [161–164] and check theoretical predictions and intuitive expectations.

Figure 4.1 (a) shows several experimentally determined $I_c(B)$ curves at different temperatures of a superconducting niobium film patterned with a triangular array of antidots. The antidot density of this sample was $n_a \approx 2\,\mu\mathrm{m}^{-2}$, the antidot diameter was $D \approx 300\,\mathrm{nm}$ and the film thickness was $d = 60\,\mathrm{nm}$. For integer multiples of the first matching field $B/B_1 = n$ there are clear maxima of the critical current visible, which correspond to a commensurability between the antidots and the vortices. It is not clear in any case, however, which vortex configuration is present for matching fields such as $B/B_1 = 2$ or $B/B_1 = 3$. In principle there are (at least) two possibilities. The first is that each antidot is occupied by two or three vortices in the corresponding fields. Despite the repulsive interaction between two vortices it can be energetically favorable to occupy an antidot with multiple vortices. How many vortices occupy an antidot hereby is a complex function of antidot size and next-neighbour distance both relative to λ_{GL} and ξ_{GL} as well as on the vortex density itself [165–168]. A second possibility for the vortex configuration at $B/B_1 = 2$ is that each antidot is only occupied by one vortex and the additional vortices occupy interstitial positions in between the antidots. Similar different possibilities exist for higher order matching fields. The corresponding matching peaks are then explained by energy minima created in between occupied antidots by the magnetic vortex-vortex inter-

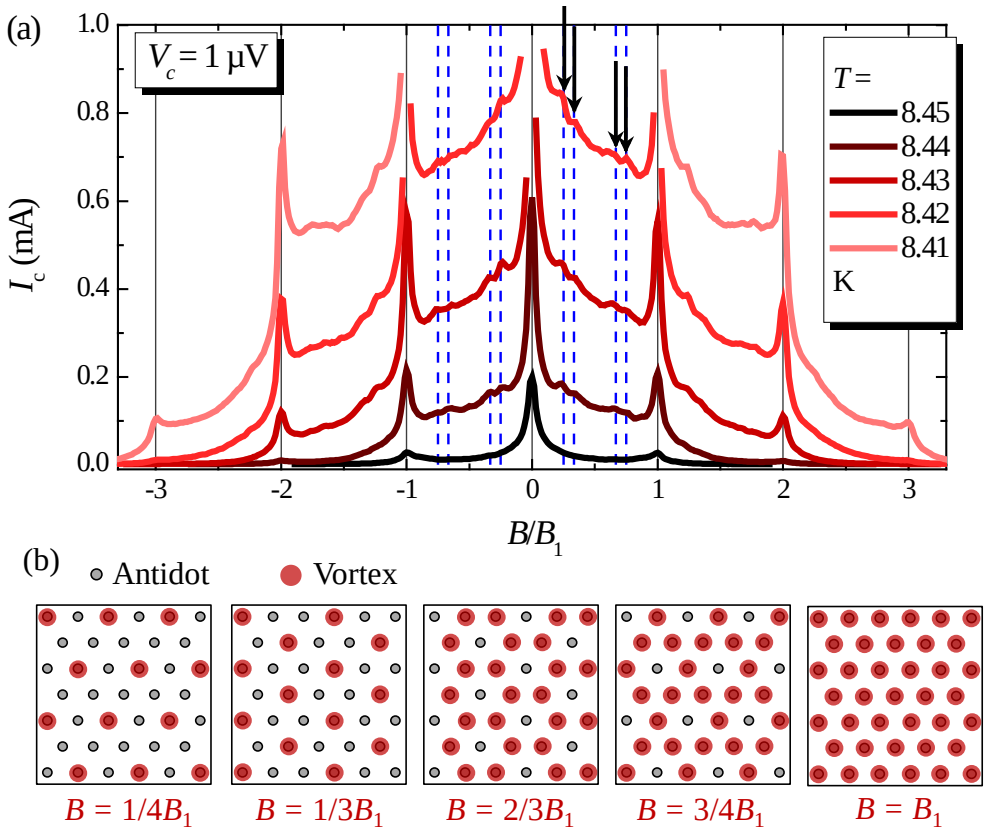

Figure 4.1: (a) Critical current I_c vs magnetic flux density B of a niobium thin film with a triangular lattice of antidots at five temperatures T. B is normalized to the first first matching field B_1; dashed vertical lines (blue) indicate the fractional matching fields for $B/B_1 = 1/4, 1/3, 2/3$ and $3/4$ and black arrows point to the corresponding local maxima. The voltage criterion $V_c = 1\,\mu$V defines the onset of voltage and hence the critical current. For more details regarding the niobium and antidot properties, cf. appended publication IX. (b) Sketches of (possible) vortex configurations corresponding to local maxima of the critical current at $B/B_1 = 1/4, 1/3, 2/3, 3/4$ and 1.

action. In these minima, the interstitial vortices are trapped and pinned [142, 167, 168]. Such a mechanism, which is also called caging effect, can lead to the situation that a higher order matching field $B/B_1 = n$ is related to an equal or even enhanced critical current compared to I_c in the previous matching field $B/B_1 = n - 1$ [167, 169, 170].

Commensurability effects, however, can not only occur at integer multiples of the first matching field but also at fractional multiples. For periodic pinning arrays, the fractionals can be found at rational numbers [148, 171]. In the critical current curves of Fig. 4.1 (a) there are four small peaks visible between two subsequent matching fields. For $B < B_1$ there are four dashed lines drawn at $B/B_1 = 1/4, 1/3, 2/3, 3/4$ and the possible corresponding vortex configuration with the favorable sixfold symmetry (rotational symmetry for $n\pi/3$) are shown in (b) together with full occupation at $B = B_1$. With this at hand, it seems possible to identify the extraordinarily stable vortex configurations from a study of the commensurability maxima.

In most experiments, however, it is only possible to find clear matching effects very close to the critical temperature. There are mainly two mechanisms playing a role for this effect. First, the London penetration depth defining the length scale for vortex-vortex interaction decreases with decreasing temperature and if it gets smaller than the antidot-antidot distance the deformation energy of the vortex lattice does not play a significant role anymore. Second, with decreasing temperature the randomly distributed intrinsic defects play a stronger role as pinning sites due to the decreasing size of the vortex cores. This modifies the pinning landscape from periodic to periodic plus random, hereby desturbing the symmetry of the pinning array and the related matching effects. For very clean superconducting films or for very dense pinning arrays, matching effects can be observed also at temperatures far below the critical temperatures [172–174]. The samples used in this work, however, showed strong matching in particular close to T_c and thus we had to be aware of another effect when characterizing the commensurabilities.

4.1.2 Little-Parks effect

The relevant effect was discovered by Little and Parks in 1962 [175] when investigating the magnetoresistance close to the critical temperature of a superconducting cylinder in a magnetic field parallel to the cylinder symmetry axis. The corresponding experimental situation is sketched in Fig. 4.2 (a). Little and Parks observed that the electrical resistance of the cylinder with radius r close to the transition temperature periodically oscillates with the applied magnetic field.

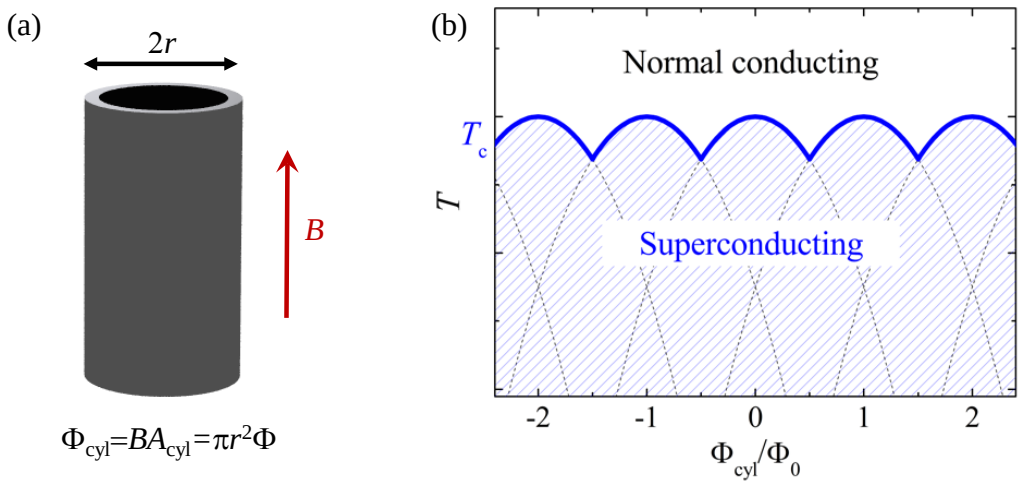

Figure 4.2: (a) Sketch of the configuration of the Little-Parks experiment [175]. A superconducting cylinder with radius r is exposed to a magnetic field B along its symmetry axis. For negligible wall thickness the total magnetic flux through the cylinder is given by the product of B and the cross sectional area of the cylinder $A_{\mathrm{cyl}} = \pi r^2$. (b) Sketch of the results of the Little-Parks experiment. The critical temperature of the cylinder T_c is reduced quadratically with the flux difference from the closest integer multiple of Φ_0.

The periodicity hereby corresponded to one flux quantum $\Phi_0 = h/2e$ per cross sectional area $A_{\mathrm{cyl}} = \pi r^2$ of the cylinder. They attributed this observation to a periodic oscillation

of the critical temperature. As in a superconductor, the fluxoid quantization must be fulfilled along any closed path, this is also true for a path around a cylinder. If the externally applied field does not correspond to an integer multiple of Φ_0 going through the cylinder, the superconductor must carry a circulating current to fulfill the quantization condition. This current is largest for half a flux quantum deviation from an integer multiple of Φ_0 because if the deviation is larger, the current turns direction and compensates for the next number of flux quanta. As the flux through the cylinder is linear in the circulating current and the kinetic energy of the charge carriers is quadratic in the current, the free energy of the superconducting state oscillates quadratically with the applied flux through the cylinder. The critical temperature is given by the energetic equality of normal state and superconducting state, so this point is shifted to lower temperatures, when the superconducting state is inevitably accompanied by a circulating current to fulfill fluxoid quantization, cf. Fig. 4.2 (b). As close to the critical temperature the critical current of a superconductor depends on how far one is away from T_c, the Little-Parks effect also leads to a modulation of the (depairing) critical current.

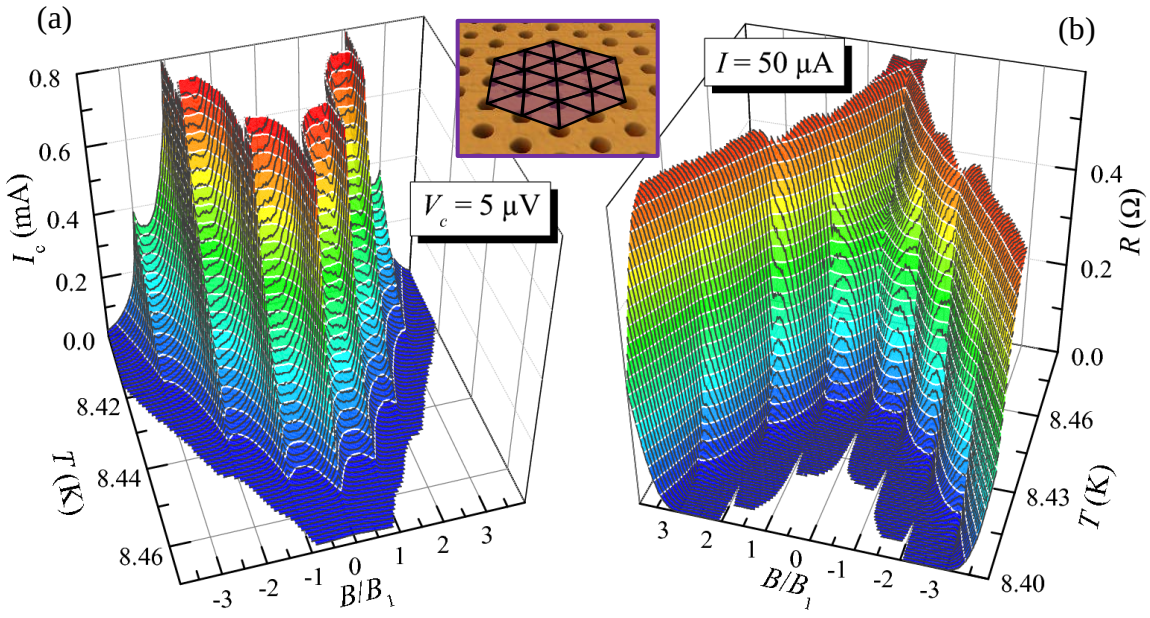

Figure 4.3: (a) Critical current I_c vs temperature T and magnetic flux density B of a superconducting thin film with a triangular lattice of antidots for a voltage criterion $V_c = 5\,\mu$V; (b) Resistance R of the film vs temperature T and magnetic flux density B measured with a constant current $I = 50\,\mu$A. Flux density axes are normalized to the first matching flux density $B_1 \approx 4\,$mT. For more details regarding the niobium and antidot properties, cf. appended publication IX.

Later, different authors have investigated the Little-Parks effect in periodic, quasiperiodic or fractal superconducting wire networks [176–180]. A wire network is a two-dimensional array of quasi one-dimensional superconducting wires, whose individual wire width w is smaller than the Ginzburg-Landau coherence length ξ_{GL}. They can be viewed as thin films with (non-circular) antidots so large that the remaining superconducting wires in between become smaller than the coherence length. In this limit $w < \xi_{\mathrm{GL}}$, Abrikosov vortices cannot exist in the superconducting wires. When a wire network is

cooled below the critical temperature in a magnetic field, the fluxoid quantization must be fulfilled for each closed wire loop of the network and so currents in the wires appear to ensure this. The amplitude and distribution of these currents depend on the network geometry and typically induce a complex oscillational behaviour of the critical temperature with a rich finestructure [176–178], similar to integer and fractional matching effects due to collective vortex pinning, cf. Fig. 4.1. As there is also kinetic energy related to the currents of Abrikosov vortices trapped in antidots, the Little-Parks effect is not limited to wire networks but also has an influence on the T_c of films with antidots [181]. Hence the two effects are closely related and lead to a magnetic field dependent modulation of the sample parameters close to the critical temperature. We thus decided for the experiments presented in appended publications VII and IX to monitor and plot the phase boundary as a whole as depicted in Fig. 4.3 for the triangular antidot array of Fig. 4.1, which again shows that $T_c(B)$, $I_c(B)$ and $R(B)$ cannot be treated as independent quantities, especially close to T_c. By taking horizontal or vertical slices for constant voltage, current or temperature, $I_c(B)$, $T_c(B)$, and $R(B)$ curves can be extracted on demand.

We note that the term phase boundary might be somewhat misleading here, as there is not a real phase transition related to the depinning critical current or the magnetoresistance. However, the two quantities are obviously directly related to the "real" phase boundary $T_c(B)$ and so we use the term for the measured parameter ensemble as a whole.

4.2 Results Part III

4.2.1 Suppression of vortex channeling with controlled disorder - Publication VI

Periodic arrays of antidots can be related to strong matching effects at integer multiples of the first matching field as shown in the previous section. However, with regard to applications of superconducting microelectronic devices, it might be desirable that the critical current is not only strongly enhanced at a few almost discrete values of B but over a broader magnetic field range. The first important idea regarding this requirement led to the proposal of quasiperiodic pinning arrays [59, 60]. As also verified by experimental studies soon after [61–63], such quasiperiodic pinning arrays can show several strong and broad matching peaks in the critial current for fields smaller than B_1, which is attributed to the many periods inherent to quasiperiodic patterns. More details on quasiperiodic pinning arrays and their properties can be found below in the discussion of appended publications VIII and IX.

The properties of quasiperiodic pinning arrays are related to their reduced symmetry compared to periodic arrangements or in other words to an increased amount of disorder, which leads to the appearance of multiple weak periodicities instead of a single strong one. In 2007, Reichhardt and Olson-Reichhardt made the proposal to create additional matching effects by a novel kind of pinning array [58]. The idea was to start with a periodic triangular pinning array and randomly remove a certain fraction of the pinning sites. According to the corresponding molecular dynamics simulations [58], this should

lead to two different possible matching effects, one occurring when the density of pinning sites n_p matches the density of vortices and one when the ideal triangular vortex lattice has the same lattice constant a as the undiluted triangular array. The former matching effect is also called "density matching" and the latter "lattice matching", both configurations are sketched in Fig. 4.4.

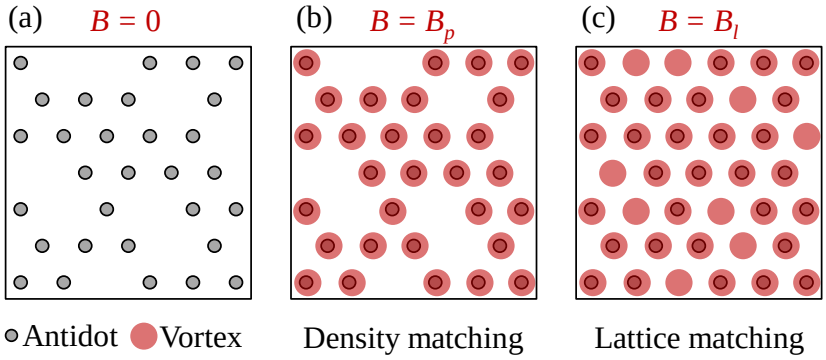

Figure 4.4: Schematic of the two different matching effects predicted in a randomly diluted, originally hexagonal antidot lattice as shown in (a). (b) At the density matching field B_p antidot and vortex density are equal and all antidots are occupied with one vortex. (c) At the lattice matching matching field B_l the lattice constant of the vortices is equal to the lattice constant of the (undiluted) antidot array.

In addition to study an additional matching effect, the method also allows for the controlled investigation of two interesting transitions. First, removing more and more pinning sites from a triangular array and hereby keeping the lattice parameter a constant corresponds to creating a gradual transition to a plain sample without artificial pinning. The second possibility is to keep the mean antidot density constant while removing more and more pinning sites. To do so, the remaining diluted lattice must be appropriately scaled down and the lattice parameter decreases with increasing dilution. This corresponds to a gradual transition from a periodic to a random pinning array.

For our studies, we fabricated 60 nm thick niobium film bridges with circular antidots and implemented both array dilution methods. For both methods, we fabricated samples with dilution factors $P_d = 0.0, 0.2, 0.4, 0.6, 0.8$, corresponding to 0%, 20%, 40%, 60% and 80% removed pinnings sites. Fig. 4.5 (a)-(d) show scanning electron microscopy images of four samples with constant antidot density $n_p = 0.1\,\mu\text{m}^{-2}$ but different dilution factors. The solid lines indicate the respective undiluted triangular array, the lattice parameter scales as $a(P_d) = 3.4\,\mu\text{m}/\sqrt{1-P_d}$. The second sample series with the unscaled diluted lattices was fabricated with a constant lattice parameter $a = 1.5\,\mu\text{m}$ and hence these samples have a pinning site density $n_p(P_d) = (1-P_d)\cdot 0.5\,\mu\text{m}^{-2}$.

Figure 4.6 (a) and (b) show the measured $I_c(B)$ curves for the unscaled samples and for two different reduced temperatures $t = T/T_c$. For both temperatures, the gradual transition from the undiluted sample to the plain sample is clear and continuous. The first matching peak gets smaller and moves towards lower magnetic fields with increasing dilution, showing the importance of density matching in this regime. Different from the expectations according to the simulation results of Ref. [58], at the first lattice matching field B_l only the undiluted sample has a peak. However, there seems to be a lattice

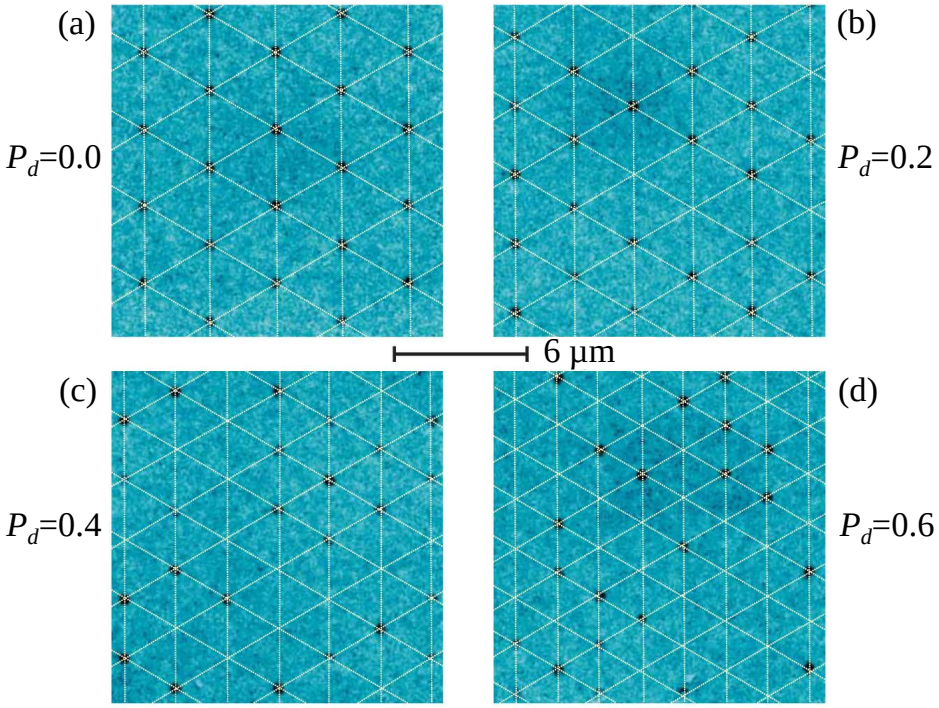

Figure 4.5: Scanning electron microscopy images of niobium thin films with randomly diluted antidot arrays; lines illustrate the triangular lattice. Lattice parameters $a(P_d) = 3.4 - 2.1\,\mu$m for dilutions $P_d = 0 - 0.6$ are scaled to maintain constant antidot density $n_p = 0.1\,\mu\text{m}^{-2}$. Figure modified from appended publication VI, © 2009 by the American Physical Society.

matching for the second lattice matching field $B = 2B_l$ (at least for $P_d = 0.2$ and $P_d = 0.4$) but no second order density matching effect. So in principle both matching effects have been observed in the samples although somewhat different than expected.

In Fig. 4.6 (c) and (d) the corresponding data are shown for the scaled antidot lattices with dilution independent mean density. Due to the smaller antidot density, the matching effects are less pronounced than in the unscaled samples, cf. (a) and (b). However, it seems as if the dominant matching here is the lattice matching as with decreasing lattice parameter $a(P_d) = 3.4\,\mu\text{m}\sqrt{1 - P_d}$, the matching peak/shoulder is shifted to higher magnetic fields despite a constant antidot density. With increasing magnetic field the corresponding samples with increasing dilution exceed the others with respect to the highest critical current, which is in agreement with the theoretical results [58].

The global shape of the $I_c(B)$ curves does not seem to approach the one of a plain sample here. This is exactly what we expected because the gradual transition with a fixed antidot density corresponds to the transition to a random pinning site array. Indeed, it has been observed before that a pinning landscape with random distribution of antidots leads to a triangular shape of $I_c(B)$ [61], practically linearly decreasing with B.

Besides these matching effects in the critical current, we have observed a significant difference in the flux flow properties of the individual samples of the scaled sampleset. In Fig. 4.7 the current-voltage characteristics of the five differently diluted samples and a plain sample in the second density matching field $B = 2B_p$ are depicted. Two kinks are

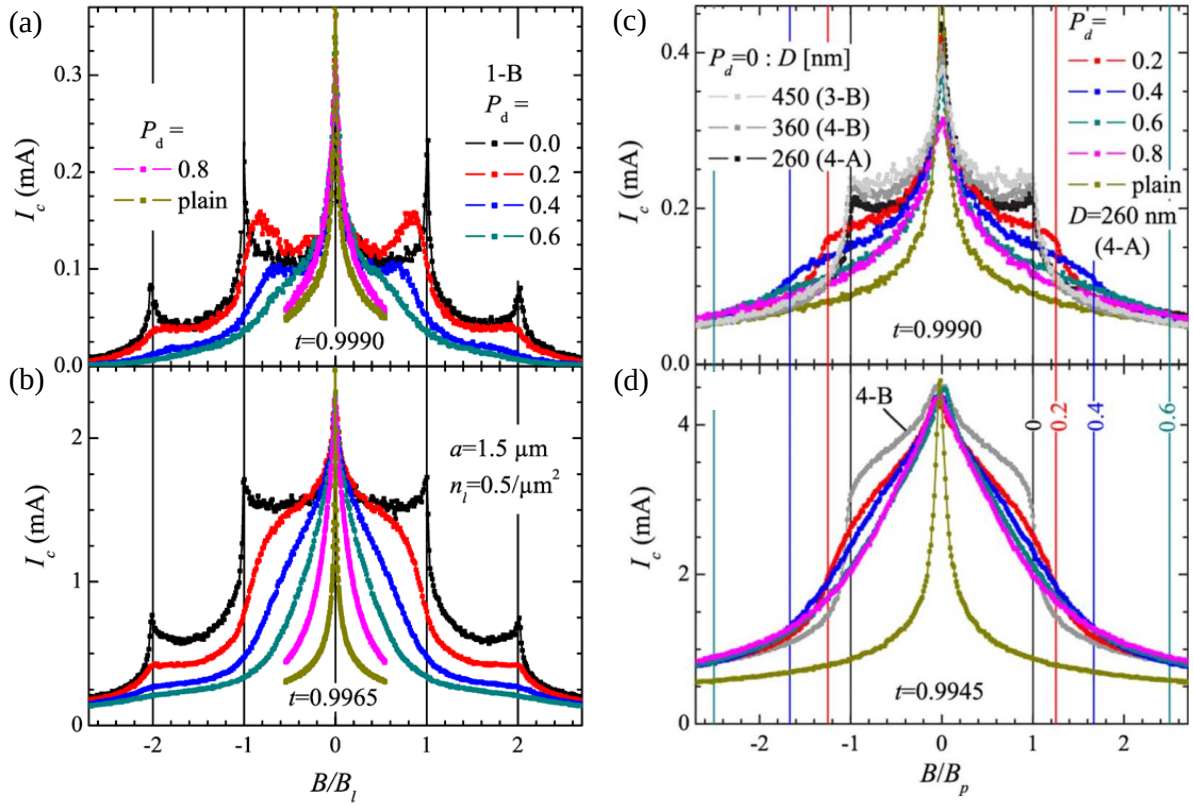

Figure 4.6: (a, b) Critical current I_c vs B/B_l of niobium films containing diluted antidot arrays with fixed lattice parameter a and variable dilution P_d for two different reduced temperatures $t = T/T_c$. (c, d) Critical current I_c vs B/B_p of niobium films containing diluted antidot arrays with scaled lattice parameter $a(P_d)$ and fixed antidot density $n_p = 0.1\,\mu\text{m}^{-2}$ for two different reduced temperatures $t = T/T_c$. Vertical solid lines indicate the lattice matching fields B_l/B_p for each sample and are labeled with the corresponding value for P_d. The voltage criterion for all critical currents was $V_c = 1\,\mu\text{V}$. More details regarding the niobium and antidot properties can be found in appended publication VI. Figure modified from appended publication VI, © 2009 by the American Physical Society.

visible in the curve of the undiluted triangular lattice (gray). The vortex configuration in this second matching field probably corresponds to each antidot occupied with one vortex and a complete, weakly pinned vortex lattice occupying interstitial positions. According to this, the interstitial vortices are depinned at the first kink (onset of voltage) and then start to move between the antidots through the sample, a phenomenon also called channeling. With increasing driving current, the velocity of these interstitials increases linearly, explaining the approximately linear increase of voltage. At the second kink then, the strongly pinned vortices in the antidots are depinned. Strikingly, this second kink occurs at exactly the critical current in the first matching field $I_c(B_p) = 3\,\text{mA}$, cf. Fig. 4.6 (d).

When we compare the five samples in between the two kinks of the undiluted sample curve, we find that the voltage onset occurs at practically the same current for all samples except for the plain one. In the current range between the first and the second kink, however, the voltage decreases with increasing dilution of the corresponding pinning array

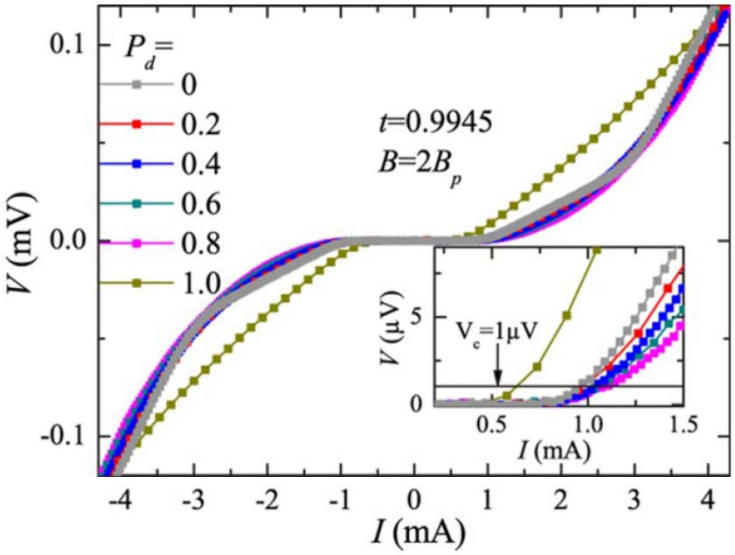

Figure 4.7: Current voltage characteristics $I(V)$ of the samples with diluted antidot arrays with scaled lattice parameter and fixed antidot density in comparison. Inset shows magnification of V vs I at small voltages, where the critical currents shoen in Fig. 4.6 (c, d) have been determined. Figure from appended publication VI, © 2009 by the American Physical Society.

up to a factor of two between $P_d = 0$ and $P_d = 0.8$. We attribute this effect to a reduction of the mobility in the disordered systems. Figuratively speaking one can imagine that due to the disorder and the locally closely packed obstacles (pinned vortices), the interstitials cannot reach the same velocity under the same driving force (current), which are possible in a periodic array where the moving interstitial vortices just follow straight lines.

With this experimental work we have not only been able to confirm the predicted two different matching features related to the static properties of the vortex lattice but also found a new effect related to the vortex dynamics.

Own contributions to publication VI

I have carried out most of the experiments of this work and contributed to the data interpretation.

4.2.2 Pinning sites via naturally disordered self-assembly - Publication VII

In this work, we have fabricated 150 nm thick niobium film microbridges patterned with antidots created with the fabrication technique used for the resonators in publication III. This fabrication process with a self-assembling monolayer of microspheres as microlense lithography mask naturally leads to a certain amount of disorder in the resulting antidot lattice. Figure 4.8 (a) shows the cross-shaped microbridge geometry in an optical image and an atomic force microscopy (AFM) image of the antidot lattice. The AFM image

reveals a quasihexagonal antidot lattice, but also the existence of several domains with imperfections and dislocations. Similar disordered pinning arrays based on different fabrication techniques have been discussed in Refs. [172, 173, 182]. As the microsphere diameter was $D_s \approx 770\,\mathrm{nm}$, we would expect a perfect lattice to have a hole density $n_h \approx 1.95\,\mu\mathrm{m}^{-2}$. The AFM images, however, revealed a mean antidot density of $n_a \approx 1.55\,\mu\mathrm{m}^{-2}$ which is considerably smaller than that of the perfect packing and corresponds to a dilution of approximately $P_d = 0.2$.

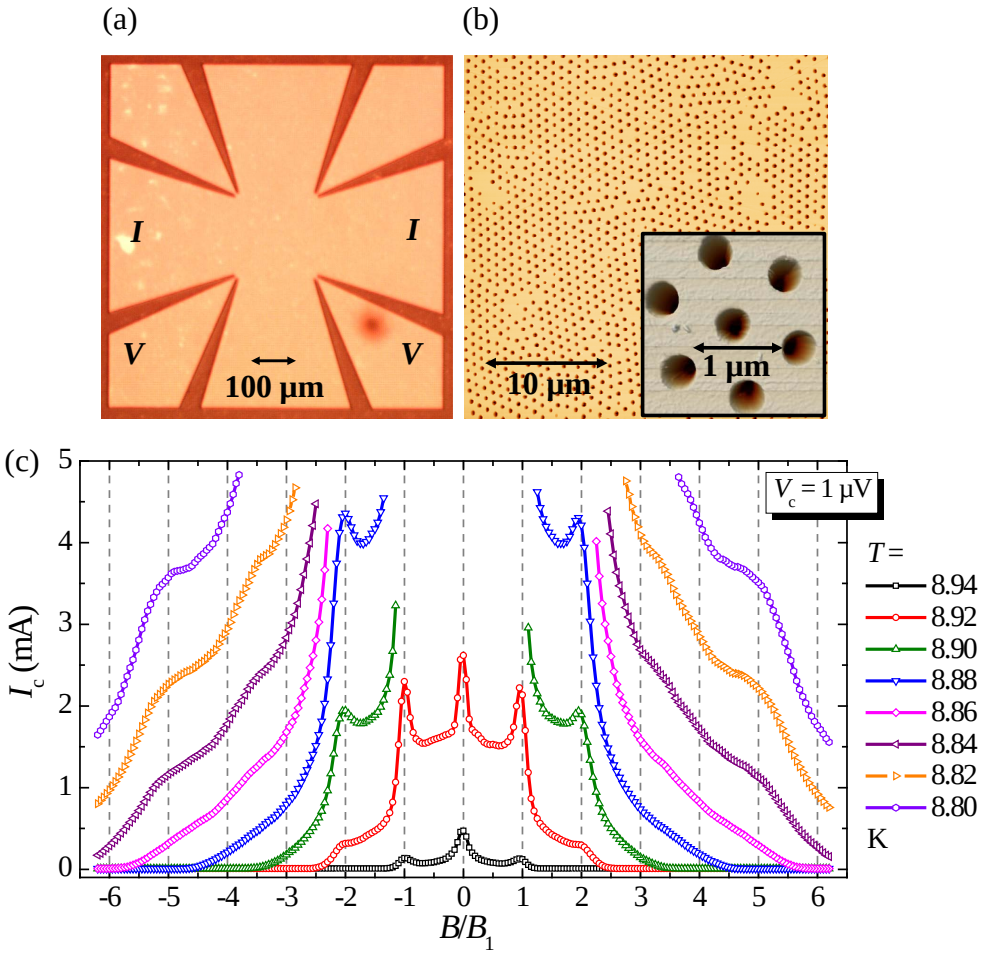

Figure 4.8: (a) Optical image of the $800 \times 800\,\mu\mathrm{m}^2$ large cross-shaped bridges structure with a square center area of $200 \times 200\,\mu\mathrm{m}^2$ for the four-probe current voltage characterization of of superconducting thin films with pinning landscapes. (b) Atomic force microscope image of a $30 \times 30\,\mu\mathrm{m}^2$ large section of the niobium film patterned with antidots via microsphere lithography; inset shows a zoom-in. (c) Critical current $I_c(B)$ of (a), (b); different curves correspond to different temperatures T. Flux density axis is normalized to the first (density) matching field $B_1 \approx 3.4\,\mathrm{mT}$. Figure modified from appended publication VII, © 2012 IOP Publishing Ltd.

We have measured the current-voltage characteristics of the bridges close to the critical temperature for different values of magnetic field and temperature and reconstructed the 3D phase boundary as described in Sec. 4.1. By taking vertical slices we have extracted $I_c(B)$ curves for different temperatures in order to analyze the matching effects. The result is plotted in Fig. 4.8 (b) vs B normalized to the density matching field $B_1 \approx 3.4\,\mathrm{mT}$. There

are pronounced peaks visible at $B = B_1$ and $B = 2B_1$, but none at $B = 3B_1$ and $B = 4B_1$. Instead two shoulders in the critical current appear around $B = 3.5B_1 \approx 11.9\,\mathrm{mT}$ and $B = 5B_1 \approx 17\,\mathrm{mT}$. These values appear to be close to multiples of the lattice matching field $B_1^* = 4\,\mathrm{mT}$, in particular close to $B = 3B_1^* = 12\,\mathrm{mT}$ and $B = 4B_1^* = 16\,\mathrm{mT}$.

This observation is in accordance with the result of the previous section and appended publication VII. For the unscaled samples with $P_d = 0.2$ we found the low order matching effect to be related to the antidot density and the higher order matching effect to be related to the lattice parameter, cf. Fig. 4.6. The data of the previous section also suggest that the density matching at low order matching peaks gets more important with increasing antidot density (although we had only two different densities). Following that argument, it is conclusive that we find more lattice matching peaks here compared to the randomly diluted samples as we have a considerably higher antidot density here. However, it must be stated that the disorder in the microsphere samples has a chaotic moment and hence the results might not be fully comparable to those of the randomly diluted samples, where all remaining antidots belonged to the same original triangular lattice.

We have also performed an analysis of the critical temperature $T_c(B)$ in this sample and identified a regime very close to T_c, where the antidot sample behaves like a superconducting wire network. From this viewpoint, the oscillations of the critical temperature with magnetic field can be attributed to the collective Little-Parks effect. For more details, see the appended publication VIII.

Own contributions to publication VII

For this work, I have contributed to the sample fabrication by sputtering the niobium films and by designing and patterning the bridge structures. I have developed LabView based measurement and data analysis softwares, with which I have carried out the experiments and interpreted the data. Finally, I have written the first draft of the manuscript.

4.2.3 Vortex quasicrystals - Publications VIII and IX

Finally, we have investigated the properties of several different quasiperiodic pinning arrays by means of numerical simulations and electric transport characterization of the critical parameters close to the transition temperature. As mentioned earlier, it has been proposed in 2005 to use a quasiperiodic instead of a periodic antidot array in order to achieve strong pinning over an extended magnetic field range, as quasiperiodic patterns have many built-in periodicities to which the vortex lattice can be commensurable [59, 60]. Figure 4.9 (a) shows a sketch of the Penrose tiling [183] which was used as a basis for the quasiperiodic antidot array in the aforementioned proposal. It does not have any translational symmetry but an unconventional fivefold rotational symmetry.[1] The idea was that by this there would not be strong pinning for only few matching fields as in a

[1] Such a symmetry was thought to be impossible for natural systems for a long time before Dan Shechtman found the first real quasicrystal in 1984 [184], a discovery which was awarded with the Nobel prize in chemistry 2011.

periodic array but over a broad range of applied fields, seeming favorable for any application in which the magnetic fields are not constant. Some very characteristic matching effects for antidots arranged according to a Penrose tiling have been predicted by means of numerical simulations in 2005 [59, 60] and confirmed by experimental studies soon after [61, 63]. Moreover, a comparitive study between the critical currents of superconducting films with triangular and quasiperiodic pinning arrays has indeed demonstrated that the Penrose array leads to an enhanced critical current below the first matching field. Although not of practical use, it is very interesting that the additional matching effects in quasiperiodic arrays for $B < B_1$ can be found at irrational fractionals of B_1 which in the case of the Penrose array are related to the golden mean $\tau = (1 + \sqrt{5})/2$ [59, 61].

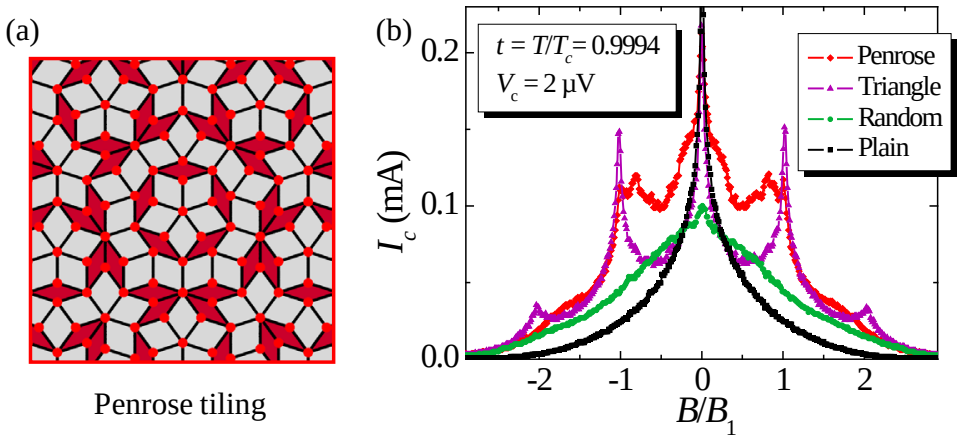

Figure 4.9: (a) Sketch of the quasiperiodic Penrose tiling. Red dots at the vertices indicate positions of antidots in the corresponding superconducting film sample. (b) Critical current I_c vs magnetic field B of niobium films with antidot arrays arranged in a triangular pattern, in a pattern according to the Penrose tiling and randomly distributed. The critical current of a plain film is shown for comparison. Modified from [61].

In Fig. 4.9 (b) the critical current of a superconducting film with antidots arranged according to the vertices of the Penrose tiling is shown [61]. For comparison, $I_c(B)$ is shown for a sample with a triangular antidot array, a sample with randomly distributed antidots and one without any pinning sites (plain). For magnetic fields $B < B_1$ the Penrose sample shows a significantly enhanced critical current compared to all other samples. There are furthermore several broad peaks visible which are in agreement with theory and can be attributed to favorable vortex configurations in the antidot array. For fields $B > B_1$, also the critical current of the Penrose sample shows a rapid decay and no strong matching peaks anymore. However, the Penrose pattern is not the only quasiperiodic tiling. Many others with different rotational symmetries are known and several of them have been implemented as pinning arrays within this thesis. At first, numerical simulations on the critical current of seven different quasiperiodic tilings have been performed. All seven tilings and the results of the simulations are shown in the appended publication VIII. The simulations were performed by V. R. Misko from the university of Antwerpen by means of treating the vortices as repulsively interacting massless point-like particles, where the ith vortex is described by the equation of motion

$$\eta\vec{v}_i = \vec{f}_i^{vv} + \vec{f}_i^{vp} + \vec{f}_i^{T} + \vec{f}_i^{d}. \tag{4.1}$$

Here, $\eta\vec{v}_i$ is the damping force (cf. Sec. 2.1.3), $\vec{f}_i^{vv}$ is the vortex-vortex interaction, $\vec{f}_i^{vp}$ is the vortex-pinning interaction, $\vec{f}_i^{T}$ is a thermal force and $\vec{f}_i^{d}$ is the driving force. For details regarding the simulations, cf. Refs. [59, 60] and the appended publication VIII. For two of the seven tilings, the simulations revealed unusual matching peaks in the critical currents for $B > B_1$. These two particular tilings are shown in Fig. 4.10 (a) and Fig. 4.12 (a) and the corresponding results of the simulations are depicted in (b).

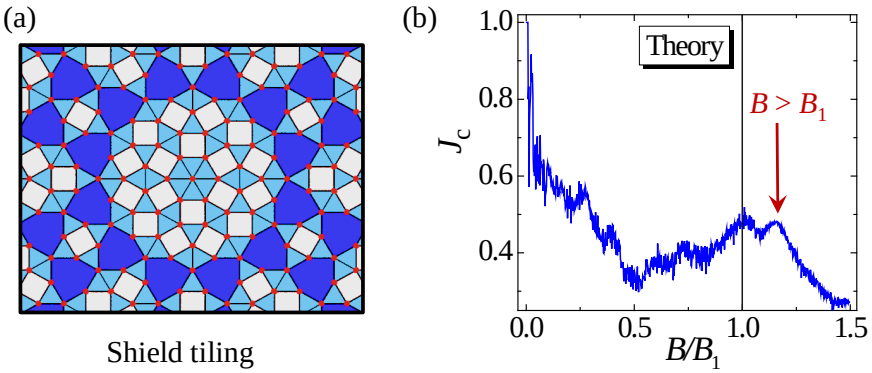

Figure 4.10: (a) Sketch of the quasiperiodic Shield tiling consisting of squares (gray), triangles (light blue) and irregular hexagons (dark blue). Red dots at the vertices indicate the positions of the antidots in the corresponding pinning array. (b) Numerically calculated critical current J_c (for definition see appended publication VIII) vs magnetic field B/B_1 of a sample with potential minima arranged at the vertices of the Shield tiling. For details regarding the simulaions see Refs. [59, 60] and appended publication VIII.

One of them, the Shield tiling [185] shown in Fig. 4.10 (a), consists of three basic shapes: triangles, squares and big hexagons, the latter shown in dark blue. The simulated critical current of vortices in an antidot array arranged according at the vertices of the Shield tiling shows a local maximum at the first matching field B_1 and another clear maximum for $B \approx 1.18B_1$. The interpretation of the double-peak structure is related to the big blue hexagons in the Shield tiling. The most simple picture suggests that for $B = B_1$ simply all antidots are occupied with one vortex while for $B = 1.18B_1$ all antidots are occupied and there is one additional, interstitial vortex within each hexagon. In some sense, this picture would correspond to the quasiperiodic version of density and lattice matching discussed above. According to the simulations shown in the appended publication VIII, it might also be that the vortices around the hexagonal structures do not occupy all antidots at $B = B_1$ due to the high deformation energy which is related to that arrangement. Instead, the interstitials in the hexagons at $B = 1.18B_1$ compensate for that deformation energy and all antidots become occupied. We assume that depending on the parameter range (pinning strength, vortex-vortex interaction strength) both situations can occur.

In first experiments on superconducting films with antidots arranged in a Shield pattern, we have not found this characteristic double peak structure but only an enhanced current density compared with the Penrose tiling for $B > B_1$. The corresponding experimental data can be found in the appended publication VIII. As the visibility of matching effects

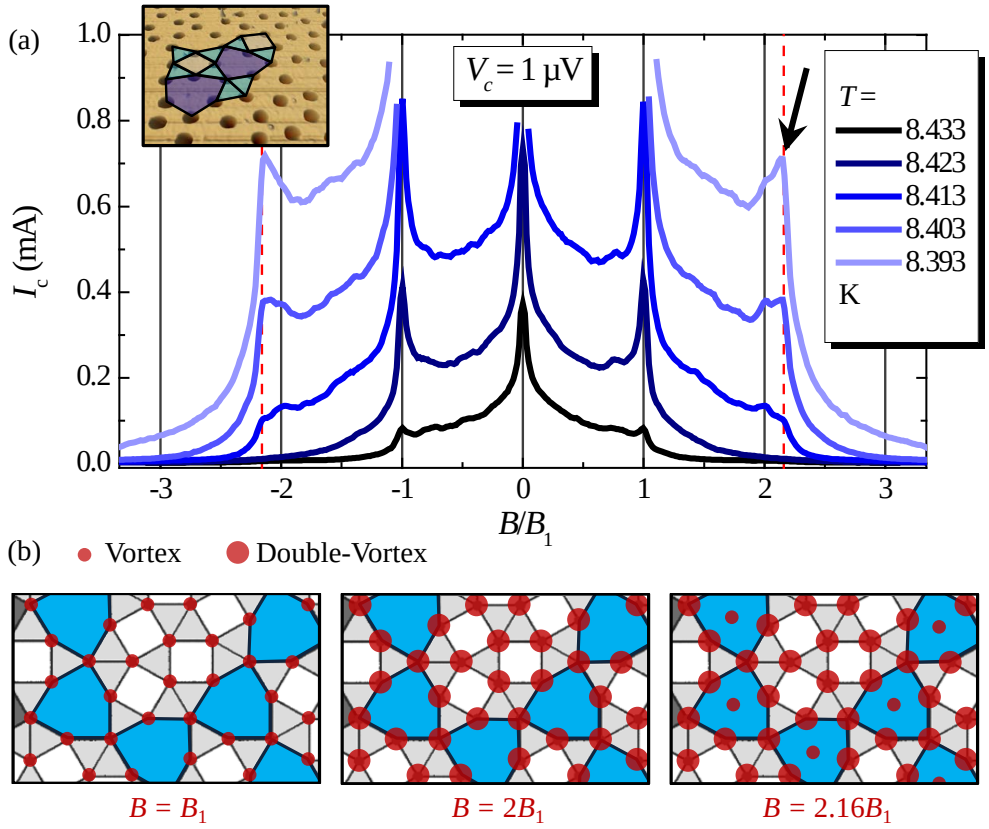

Figure 4.11: (a) Critical current I_c vs normalied magnetic flux density B/B_1 of a Nb film with antidots arranged at the vertices of the Shield tiling at five temperatures T; dashed vertical lines indicate the fractional flux density $B/B_1 = \pm 2.16$ and arrows point to the corresponding local maxima. Inset shows AFM image of the sample with lines indicating the tiling. (b) Sketches of (possible) vortex configurations at $B/B_1 = 1, 2$ and 2.16.

is usually related to the antidot density we have fabricated a second set of samples with an antidot density increased by a factor of ~ 4 compared to the first samples discussed in publication VIII. The cross-shaped sample geometry in these studies was similar to the one shown in Fig. 4.8 (a), more details regarding the antidots and the niobium films can be found in the appended publication IX. The critical current of these new samples patterned with antidots according to the Shield tiling is shown in Fig. 4.11 (a) for five different temperatures. Around the first matching field $B_1 \approx 4\,\mathrm{mT}$, there is still no additional maximum visible. However, around the second matching field develops a temperature dependent double feature. There is one small peak at $B = 2B_1$, mainly visible and dominating for high temperatures. And then, there is another peak emerging slightly above $2B_1$ with a strong temperature dependence. This second peak gets even higher than the one at $B = 2B_1$ for lower temperatures. In Fig. 4.11 (b) the possible configurations of the vortices at $B/B_1 = 1, 2$ and 2.16 are shown. $B/B_1 = 2.16$ corresponds to the field value with two vortices per antidot and one interstitial in the hexagons. A vertical dashed line in Fig. 4.11 (a) indicates the value, perfectly matching the position of the peak and supporting our conclusion. The small difference of 0.16 compared to the theoretical value of 0.18 for the deviation from the next integer matching field is explained by the

use of differently sized parts of the tiling for the simulation and the experiments. As can be suggested from Fig. 4.10 (a), the exact ratio of number of antidots to the number of hexagons depends on which part of the tiling is chosen.

In summary, we found the predicted additional matching effect in antidot arrays with the Shield tiling geometry, for the first time demonstrating the caging effect in a quasiperiodic pinning array. In contrast to the numerical simulations, we have found the matching peak slightly above the second matching field instead of the first matching field, which we interprete as a consequence of differing parameters between experiment and theory such as vortex-antidot and vortex-vortex interaction ranges. In particular, we have found that the critical current at $B = 2.16B_1$ can exceed the one at $B = 2B_1$, i.e., that interstitial vortices lead to an enhancement of the critical current, an effect previously only observed in periodic pinning arrays [167, 170].

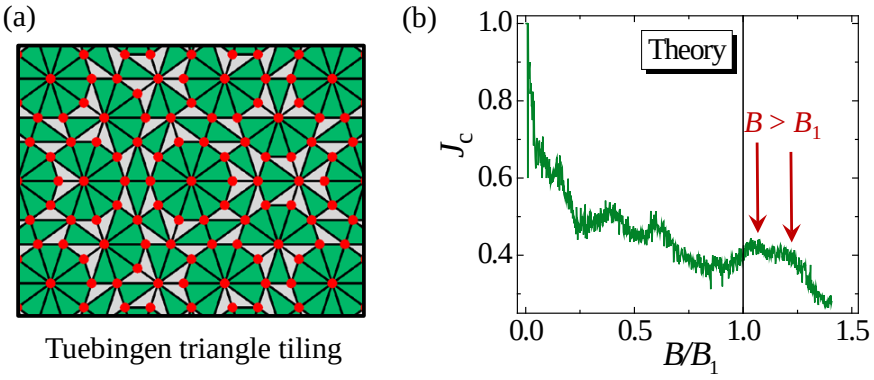

Figure 4.12: (a) Sketch of the quasiperiodic Tuebingen triangle tiling consisting of squares (gray), triangles (light blue) and irregular hexagons (dark blue). Red dots at the vertices indicate the positions of the antidots in the corresponding pinning array. (b) Numerically calculated critical current J_c (for definition see appended publication VIII) vs magnetic field B/B_1 of a sample with potential minima positioned at the vertices of the Tuebingen triangle tiling. For details regarding the simulaions see Refs. [59, 60] and appended publication VIII.

The second tiling we investigated in more detail is the Tuebingen triangle tiling (TTT) [186] shown in Fig. 4.12 (a). It consists of two different triangles. The numerically obtained critical current of this tiling, shown in Fig. 4.12 (b), does not show a maximum of the critical current exactly at $B = B_1$. Instead, there are two hardly separated maxima visible for $B > B_1$, cf. arrows in Fig. 4.12 (b).

We have also fabricated corresponding niobium samples with antidots positioned at the TTT vertices. The critical current $I_c(B)$ of one of these samples is shown for different temperatures in Fig. 4.13 (a). In (b) and (c) zooms around $B = B_1$ and $B = 2B_1$ are shown. First, we find two pronounced maxima in the critical current for $B < B_1$ marked with two orange arrows in Fig. 4.13 (a) and at similar field positions between the first and the second matching field. These two peaks are also visible in the simulation but we have not been able to identify these peaks with certain vortex distributions in the antidot array.

A detailed look at the critical current around the matching fields reveals an unconventional matching peak around $B = B_1$. First, we find a clear maximum at $B = B_1$

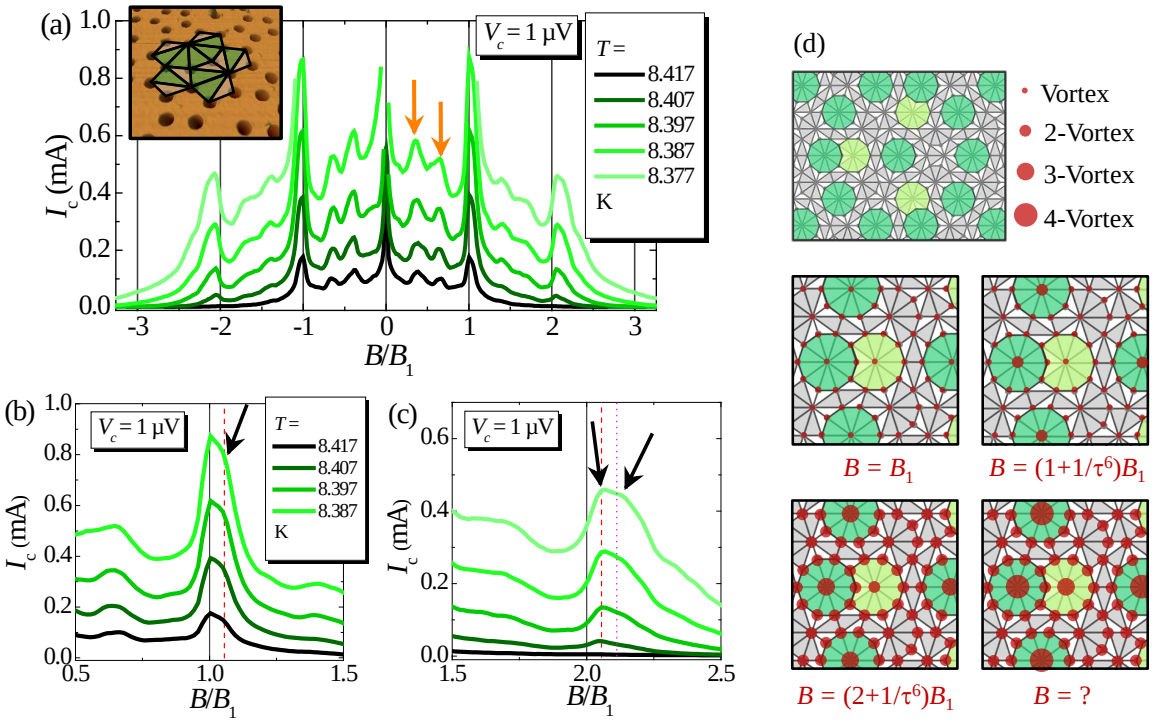

Figure 4.13: (a) Critical current I_c vs normalied magnetic flux density B/B_1 of a Nb film with antidots arranged at the vertices of the Tuebingen triangle tiling at five temperatures T. Inset shows AFM image of the sample with lines indicating the tiling. (b) and (c) show $I_c(B)$ in more detail around B_1 and $2B_1$, respectively. Arrows point to matching effects slightly above the integer multiples of B_1. Dashed vertical lines indicate the fractional flux densities $B/B_1 = (1+1/\tau^6)$ (a) and $B/B_1 = (2+1/\tau^6)$. Dotted vertical lines indicates $B/B_1 = (2+2/\tau^6)$. (d) Sketches of (possible) vortex configurations at the specified magnetic field values in the TTT. Circles and almost-circles are colored in dark and light green, respectively.

in contrast to the theoretical results. However, the peak is somewhat broadened and a kink can be seen somewhat above B_1. The position of this kink can be attributed to a characteristic structure in the TTT pattern. The tiling has structures where ten antidots are arranged in a circle and one single antidot is in the center. These circular structures are colored in dark green in Fig. 4.13 (d). Assuming that in the center antidot of such a circle a double vortex is formed to stabilize the configuration, cf. Fig. 4.13 (d), leads to a field value for that configuration of $B = (1 + 1/\tau^6)B_1$ with τ the golden mean. $1/\tau^6$ is the ratio between the number of all antidots and the number of antidots in the center of a ten-circle. A dashed vertical line indicates the corresponding field value in Fig. 4.13 (b) showing good agreement with the field value of the kink. Strikingly, such a symmetry induced giant vortex formation has been found in a very similar antidot structure recently by Hall bar imaging [163].

The experimentally found double peak around $B = B_1$, however, seems not to be the one predicted by the simulations as the peaks are at different field values. The investigation of the Shield tiling, however, revealed that something different could happen around the second matching field. Figure 4.13 (c) shows in detail the critical current around $B = 2B_1$ and reveals a broad double peak structure (or even multi-peak) – similar to the what we

found around B_1. In contrast to the peaks around B_1, none of the two around B_2 is exactly at $B = B_2$ similar to what we expected according to the result of the simulation. The interpretation of the peak positions, however, is difficult. First, we considered the situation that all antidots are occupied by two vortices and the antidots in the center of the circle structures are occupied by three. This corresponds to the configuration shown in the lower left image of Fig. 4.13 (d) and to the field value indicated by the dashed vertical line in (c). The agreement with the peak value seems rather convincing. For the second kink, we considered the situation that all antidots are occupied by two vortices and the circle centers by four. This would lead to a corresponding field value as indicated by the dotted vertical line in Fig. 4.13 (c), which seems somewhat too low. In the TTT, however, there are two more structures, which can be described as almost-circular. These are colored in light green in Fig. 4.13 (d). If our interpretation of the giant vortices in the circle centers is correct, it would be reasonable that also the almost-circles must be considered as potential giant vortex positions, which would shift the second peak to higher values in accordance with the observations. The lower right image of Fig. 4.13 (d) shows one possible configuration for the field value of second kink in the critical current maximum shown in Fig. 4.13 (c). However, we do not know the exact fraction of almost-circles, so we cannot give an exact value for B there.

In summary, we have found unconventional matching features in the TTT, of which some have been predicted by numerical simulations and some have not. Questions for upcoming experiments are the vortex configurations in the corresponding fields, as our proposals are matching to the field values but are more or less speculative.

Own contributions to publication VIII

For this work, I have proposed to investigate the presented quasiperiodic antidot arrangements. I have contributed to the numerical simulations by calculating the quasiperiodic antidot distributions with a self-written PovRay based software. Moreover, I have contributed to the sample fabrication and measurements as well as to the editing of the manuscript.

Own contributions to publication IX

For this work, I have contributed to the sample fabrication by calculating the quasiperiodic antidot distributions with a self-written PovRay based software. Moreover, I have developed LabView based measurement and data analysis softwares, with which I have carried out the experiments and analyzed the data. Finally, I have written the first draft of the manuscript.

4.3 Relation to Part I

When buidling a hybrid system consisting of superconducting circuits and magnetically trapped atomic ensembles on a chip, the superconducting leads are inevitably exposed to

magnetic fields. By the introduction of Abrikosov vortices, these magnetic fields influence both the microwave circuits as discussed in part I and the trap wires as discussed in part II of the thesis. Microwave quantum circuits suffer considerably from the vortex presence regarding quantum state life times and coherence times. A promising route to use microwave resonators as a quantum bus in the presence of vortices is to pattern them with antidots and to pin the vortices there.

The arrangement of the antidots in the resonators is a free parameter, which can have a significant influence on the collective pinning strength. As long as the antidot lattices have characteristic lengthscales of $\sim 1\,\mu$m, this arrangement is not expected to have a strong impact on the pinning efficiency at temperatures far below the transition temperature. However, we have demonstrated that the losses are further reduced with increasing pinning site density, and in denser pinning arrays matching effects remain important down to arbitrarily low temperatures. For an optimization of the pinning structures, it therefore will be important which arrangement and symmetry the underlying array has. The results presented in part III can help to make the appropriate choice.

Chapter 5

Summary and Outlook

In this thesis, a variety of niobium film circuitry was designed, fabricated and investigated with the ultimate goal of building hybrid quantum systems consisting of superconducting circuits and cold paramagnetic atoms on a chip. The focus was to understand and optimize the properties of the superconducting devices and chips in external magnetic fields which are required for trapping and manipulation of the atomic systems. The generation of such hybrid systems is a complex challenge with many yet unsolved questions and tasks. Three of these topics were adressed in this thesis with results encouraging further research on hybrid quantum systems.

The first part of the thesis discussed superconducting coplanar microwave resonators which are considered as a potential quantum bus for the quantum state transfer between superonducting qubits and atomic ensembles. We patterned resonators with micrometric holes as vortex traps and showed that these antidots significantly reduce the microwave energy dissipation due to Abrikosov vortices. In further experiments we demonstrated that the magnetic field induced losses in the resonators show a strong hysteresis, which can be used to further reduce the vortex induced losses and to tune the resonance frequency. A simple model for the experimentally found hysteresis was developed, which is able to qualitatively explain the observations. By magneto-optical imaging of the resonators during the corresponding magnetic field cycles the assumptions of this model were comfirmed. Based on the loss reduction in resonators patterned with micrometric defects, we implemented microsphere lithography to superconducting resonator chips, a suitable method for the generation of sub-micrometric defects over a large area. This led to the demonstration of a reduction of vortex associated losses by more than one order of magnitude, approaching the loss levels required for quantum information processing in hybrid systems.

However, there are still open questions, and many interesting aspects regarding resonators in magnetic fields have not yet been explored to full extent. The mechanisms leading to the loss reduction by micrometric defects are not completely clear and require further investigations as antidots also modify the vortex viscosity and can modify the global flux profile. An important contribution to answer these questions in the future might be given by high resolution magneto-optical imaging of resonators with antidots. Such a high resolution imaging would also be desirable for a more detailed investigation

of the flux distribution related to the hysteresis effects. Up to now, we were restricted to low resolution images, which are only suitable for a very rough confirmation of the model developed to describe the hysteresis effects. Finally, the experiments described in this thesis were performed at liquid helium temperatures and at high powers where the resonators behave classically. A very important question for further studies is therefore, if and how the found results can be applied to resonators in the milliKelvin temperature regime and at single photon powers, conditions under which the resonators have to be operated for quantum experiments.

In the second part of the thesis, superconducting atom chips with integrated coplanar microwave resonators were investigated. For this purpose, an atom chip containing coplanar quarter wave resonators as well as current carrying wires to magnetically trap atoms were designed and fabricated. It was demonstrated that ultracold atom clouds can be trapped in the resonator mode volume and that the quantum coherence time of the atoms can reach several seconds there. The use of quarter wave resonators including closed superconducting loops was demonstrated to intrinsically facilitate the cloud positioning at the most favorable position in the resonator, where the coupling between the atoms and cavity photons is expected to be maximized. Moreover, trapping flux in the closed loop enables the use of the resonator as a persistent current trap. Based on these results, we developed and analyzed a highly simplified integrated resonator trap, which would allow for a significant reduction of the atom chip complexity.

Whether the integrated resonator trap can indeed be used as proposed has to be investigated within upcoming experiments, yet there are other challenges which must be addressed. One of them is the development of frequency tunable resonators, where the tunability is insensitive to magnetic fields. Another important question is whether the atomic coherence time can be maintained in the tens of seconds range on the modified chip. Finally and most important, the coupling between the atomic ensemble and the resonator must be demonstrated. Regarding this, many further questions such as the position dependence, the optimal resonator geometry and the differences between using a thermal and a Bose condensed atom cloud have to be addressed.

In the third and final part of the thesis, the influence of the antidot arrangement on the pinning efficiency and on possible commensurate states between vortex and antidot ensembles was investigated. In a first experiment, we gradually introduced disorder into an originally periodic antidot lattice and observed that the disorder can lead to new non-periodic commensurate vortex arrangements and to a reduction of vortex associated dissipation. The results helped to understand the properties of an antidot lattice with natural disorder, which was generated by self-assembling microsphere lithography as also used for resonator fabrication. Both experiments revealed that the vortex lattice is sensitive to both the antidot density and the characteristic length scales of the antidot ensemble. Finally, superconducting films with quasiperiodic antidot arrays were designed, fabricated and investigated by means of numerical simulations and electric transport measurements. Several interesting commensurability effects were observed, in particular related to the caging of interstitial vortices in a quasiperiodic pattern and to the symmetry-induced formation of giant vortices.

The investigations of different unconventional antidot arrangements without translational symmetry was carried out by observing matching effects in the critical current and transition temperatures of the different samples. Whether the attributed vortex configurations indeed correspond to the prescribed ones, however, should be confirmed by further studies which are able to test the presented interpretations locally, e.g., by high resolution imaging techniques. Another important question is whether the observed matching effects and the magnetic field dependence of the pinning efficiency of the investigated antidot arrays, are still relevant at lower frequencies and for high frequency applications as coplanar microwave resonators. For the use of vortex arrays as generators of unconventional potential landscapes for ultracold paramagnetic atoms, although an interesting motivation, it remains to be demonstrated by an experiment that this system is indeed feasible for that particular application. Up to now, this is just a proposal originated in idealized theoretical considerations.

In conclusion, several important questions regarding hybrid systems of superconductors and atomic ensembles were discussed in this thesis and the road to hybrid systems with superconducting circuits was paved a piece further; time will reveal whether in the right direction.

Bibliography

[1] C. Guerlin, J. Bernu, S. Deléglise, C. Sayrin, S. Gleyzes, S. Kuhr, M. Brune, J.-M. Raimond, and S. Haroche, Nature **448**, 889 (2007)

[2] S. Gleyzes, S. Kuhr, C. Guerlin, J. Bernu, S. Deléglise, U. Busk Hoff, M. Brune, J.-M. Raimond, and S. Haroche, Nature **446**, 297 (2007)

[3] A. Wallraff, D. I. Schuster, A. Blais, L. Frunzio, R.-S. Huang, J. Majer, S. Kumar, S. Girvin, and R. J. Schoelkopf, Nature **431**, 162 (2004)

[4] D. I. Schuster, A. A. Houck, J. A. Schreier, A. Wallraff, J. M. Gambetta, A. Blais, L. Frunzio, J. Majer, B. Johnson, M. H. Devoret, S. Girvin, and R. J. Schoelkopf, Nature **445**, 515 (2007)

[5] J. Clarke, A. N. Cleland, M. H. Devoret, D. Esteve, and J. M. Martinis, Science **239**, 992 (1988)

[6] J. Clarke and F. K. Wilhelm, Nature **453**, 1031 (2008)

[7] M. Hofheinz, E. M. Weig, M. Ansmann, R. C. Bialczak, E. Lucero, M. Neeley, A. D. O'Connell, H. Wang, J. M. Martinis, and A. N. Cleland, Nature **454**, 310 (2008)

[8] M. Hofheinz, H. Wang, M. Ansmann, R. C. Bialczak, E. Lucero, M. Neeley, A. D. O'Connell, D. Sank, J. Wenner, J. M. Martinis, and A. N. Cleland, Nature **459**, 546 (2009)

[9] A. D. O'Connell, M. Hofheinz, M. Ansmann, R. C. Bialczak, M. Lenander, E. Lucero, M. Neeley, D. Sank, H. Wang, M. Weides J. Wenner, J. M. Martinis, and A. N. Cleland, Nature **464**, 697 (2010)

[10] J. M. Fink, M. Göppl, M. Baur, R. Bianchetti, P. J. Leek, A. Blais, and A. Wallraff, Nature **454**, 315 (2008)

[11] T. Niemczyk, F. Deppe, H. Huebl, E. P. Menzel, F. Hocke, M. J. Schwarz, J. J. Garcia-Ripoll, D. Zueco, T. Hümmer, E. Solano A. Marx, and R. Gross, Nature Physics **6**, 772 (2010)

[12] P. Forn-Díaz, J. Lisenfeld, D. Marcos, J. J. García-Ripoll, E. Solano, C. J. P. M. Harmans, and J. E. Mooij, Phys. Rev. Lett. **105**, 237001 (2010)

[13] C. M. Wilson, G. Johansson, A. Pourkabirian, M. Simoen, J. R. Johansson, T. Duty, F. Nori, and P. Delsing, Nature **479**, 376 (2011)

[14] J. Majer, J. M. Chow, J. M. Gambetta, J. Koch, B. R. Johnson, J. A. Schreier, L. Frunzio, D. I. Schuster, A. A. Houck, A. Wallraff A. Blais, M. H. Devoret, S. M. Girvin, and R. J. Schoelkopf, Nature **449**, 443 (2007)

[15] M. A. Sillanpää, J. I. Park, and R. W. Simmonds, Nature **449**, 438 (2007)

[16] L. DiCarlo, J. M. Chow, J. M. Gambetta, L. S. Bishop, B. Johnson, D. I. Schuster, J. Majer, A. Blais, L. Frunzio, S. M. Girvin, and R. J. Schoelkopf, Nature **460**, 240 (2009)

[17] L. DiCarlo, M. D. Reed, L. Sun, B. R. Johnson, J. M. Chow, J. M. Gambetta, L. Frunzio, S. M. Girvin, M. H. Devoret, and R. J. Schoelkopf, Nature **467**, 574 (2010)

[18] M. Neeley, R. C. Bialczak, M. Lenander, E. Lucero, M. Mariantoni, A. D. O'Connell, D. Sank, H. Wang, M. Weides, J. Wenner, Y. Yin, T. Yamamoto, A. N. Cleland, and J. M. Martinis, Nature **467**, 570 (2010)

[19] M. Mariantoni, H. Wang, T. Yamamoto, M. Neeley, R. Bialczak, Y. Chen, M. Lenander, E. Lucero, A. D. O'Connell, D. Sank, M. Weides, J. Wenner, Y. Yin, J. Zhao, A. N. Korotkov, A. N. Cleland, and J. M. Martinis, Science **334**, 61 (2011)

[20] M. D. Reed, L. DiCarlo, S. E. Nigg, L. Sun, L. Frunzio, S. M. Girvin, and R. J. Schoelkopf, Nature **482**, 382 (2012)

[21] E. Lucero, R. Barends, Y. Chen, J. Kelly, M. Mariantoni, A. Megrant, P. O'Malley, D. Sank, A. Vainsencher, J. Wenner, T. White, Y. Yin, A. N. Cleland, and J. M. Martinis, Nature Physics **8**, 719 (2012)

[22] A. Fedorov, L. Steffen, S. Filipp, M. P. da Silva, and A. Wallraff, Nature **481**, 170 (2012)

[23] H. Paik, D. I. Schuster, L. V. Bishop, G. Kirchmair, G. Catelani, A. P. Sears, B. R. Johnson, M. J. Reagor, L. Frunzio, L. I. Glazman, S. M. Girvin, M. H. Devoret, and R. J. Schoelkopf, Phys. Rev. Lett. **107**, 240501 (2011)

[24] C. Rigetti, J. M. Gambetta, S. Poletto, B. L. T. Plourde, J. M. Chow, A. D. Córcoles, J. A. Smolin, S. T. Merkel, J. R. Rozen, G. A. Keefe, M. B. Rothwell, M. B. Ketchen, and M. Steffen, Phys. Rev. B **86**, 100506(R) (2012)

[25] A. André, D. DeMille, J. M. Doyle, M. D. Lukin, S. E. Maxwell, P. Rabl, R. J. Schoelkopf, and P. Zoller, Nature Physics **2**, 636 (2006)

[26] P. Rabl, D. DeMille, J. M. Doyle, M. D. Lukin, R. J. Schoelkopf, and P. Zoller, Phys. Rev. Lett. **97**, 033003 (2006)

[27] D. Petrosyan and M. Fleischhauer, Phys. Rev. Lett. **100**, 170501 (2008)

[28] K. Tordrup and K. Mølmer, Phys. Rev. A **77**, 020301(R) (2008)

[29] A. Imamoğlu, Phys. Rev. Lett. **102**, 083602 (2009)

[30] J. Verdú, H. Zoubi, C. Koller, J. Majer, H. Ritsch, and J. Schmiedmayer, Phys. Rev. Lett. **103**, 043603 (2009)

[31] K. Henschel, J. Majer, J. Schmiedmayer, and H. Ritsch, Phys. Rev. A **82**, 033810 (2010)

[32] D. I. Schuster, A. P. Sears, E. Ginossar, L. DiCarlo, L. Frunzio, J. J. L. Morton, H. Wu, G. A. D. Briggs, B. B. Buckley, D. D. Awschalom, and R. J. Schoelkopf, Phys. Rev. Lett. **105**, 140501 (2010)

[33] Y. Kubo, F. R. Ong, P. Bertet, D. Vion, V. Jacques, D. Zheng, A. Dréau, J.-F. Roch, A. Auffeves, F. Jelezko, J. Wrachtrup, M. F. Barthe, P. Bergonzo, and D. Esteve, Phys. Rev. Lett. **105**, 140502 (2010)

[34] H. Wu, R. E. George, J. H. Wesenberg, K. Mølmer, D. I. Schuster, R. J. Schoelkopf, K. M. Itoh, A. Ardavan, J. J. L. Morton, and G. A. D. Briggs, Phys. Rev. Lett. **105**, 140503 (2010)

[35] R. Amsüss, C. Koller, T. Nöbauer, S. Putz, S. Rotter, K. Sandner, S. Schneider, M. Schramböck, G. Steinhauser, H. Ritsch, J. Schmiedmayer, and J. Majer, Phys. Rev. Lett. **107**, 060502 (2011)

[36] Y. Kubo, C. Grezes, A. Dewes, T. Umeda, J. Isoya, H. Sumiya, N. Morishita, H. Abe, S. Onoda, T. Ohshima, V. Jacques, A. Dréau, J.-F. Roch, I. Diniz, A. Auffeves, D. Vion, D. Esteve, and P. Bertet, Phys. Rev. Lett. **107**, 220501 (2011)

[37] X. Zhu, S. Saito A. Kemp K. Kakuyanagi S. Karimoto H. Nakano, W. J. Munro, Y. Tokura, M. S. Everitt K. Nemoto, M. Kasu, N. Mizuochi, and K. Semba, Nature **478**, 221 (2011)

[38] P. Bushev, A. K. Feofanov, H. Rotzinger, I. Protopopov, J. H. Cole, C. M. Wilson, G. Fischer, A. Lukashenko, and A. V. Ustinov, Phys. Rev. B **84**, 060501(R) (2011)

[39] M. U. Staudt, I.-C. Hoi, P. Krantz, M. Sandberg, M. Simoen, P. Bushev, N. Sangouard, M. Afzelius, V. S. Shumeiko, G. Johansson, P. Delsing, and C. M. Wilson, J. Phys. B **45**, 124019 (2012)

[40] S. Probst, H. Rotzinger, S. Wünsch, P. Jung, M. Jerger, M. Siegel, A. V. Ustinov, and P. Bushev, Phys. Rev. Lett. **110**, 157001 (2013)

[41] S. D. Hogan, J. A. Agner, F. Merkt, T. Thiele, S. Filipp, and A. Wallraff, Phys. Rev. Lett. **108**, 063004 (2012)

[42] J. Fortágh and C. Zimmermann, Rev. Mod. Phys. **79**, 235 (2007)

[43] J. Gao, M. Daal, A. Vayonakis, S. Kumar, J. Zmuidzinas, B. Sadoulet, B. A. Mazin, P. K. Day, and H. G. Leduc, Appl. Phys. Lett. **92**, 152505 (2008)

[44] W. Chen, D. A. Bennett, V. Patel, and J. E. Lukens, Supercond. Sci. Technol. **21**, 075013 (2008)

[45] A. D. O'Connell, M. Ansmann, R. C. Bialczak, M. Hofheinz, N. Katz, E. Lucero, C. McKenney, M. Neeley, H. Wang, E. M. Weig, A. N. Cleland, and J. M. Martinis, Appl. Phys. Lett. **92**, 112903 (2008)

[46] R. Barends, H. L. Hortensius, T. Zijlstra, J. J. A. Baselmans, S. J. C. Yates, J. R. Gao, and T. M. Klapwijk, Appl. Phys. Lett. **92**, 223502 (2008)

[47] H. Wang, M. Hofheinz, J. Wenner, M. Ansmann, R. C. Bialczak, M. Lenander, E. Lucero, M. Neeley, A. D. O'Connell, D. Sank, M. Weides, A. N. Cleland, and J. M. Martinis, Appl. Phys. Lett. **95**, 233508 (2009)

[48] C. Song, M. P. DeFeo, K. Yu, and B. L. T. Plourde, Appl. Phys. Lett. **95**, 232501 (2009)

[49] P. Macha, S. H. W. van der Ploeg, G. Oelsner, E. Il'ichev, H.-G. Meyer, S. Wünsch, and M. Siegel, Appl. Phys. Lett. **96**, 062503 (2010)

[50] R. Barends, N. Vercruyssen, A. Endo, P. J. de Visser, T. Zijlstra, T. M. Klapwijk, P. Diener, S. J. C. Yates, and J. J. A. Baselmans, Appl. Phys. Lett. **97**, 023508 (2010)

[51] M. R. Vissers, J. S. Kline, J. Gao, D. S. Wisbey, and D. P. Pappas, Appl. Phys. Lett. **100**, 082602 (2012)

[52] M. R. Vissers, M. P. Weides, J. S. Kline, M. Sandberg, and D. P. Pappas, Appl. Phys. Lett. **101**, 022601 (2012)

[53] K. Geerlings, S. Shankar, E. Edwards, L. Frunzio, R. J. Schoelkopf, and M. H. Devoret, Appl. Phys. Lett. **100**, 192601 (2012)

[54] M. Sandberg, M. R. Vissers, J. S. Kline, M. Weides, J. Gao, D. S. Wisbey, and D. P. Pappas, Appl. Phys. Lett. **100**, 262605 (2012)

[55] N. Pompeo, R. Rogai, E. Silva, A. Augieri, V. Galluzzi, and G. Celentano, Appl. Phys. Lett. **91**, 182507 (2007)

[56] S. E. de Graaf, A. V. Danilov, A. Adamyan, T. Bauch, and S. E. Kubatkin, J. Appl. Phys. **112**, 123905 (2012)

[57] M. Hafezi, Z. Kim, S. L. Rolston, L. A. Orozco, B. L. Lev, and J. M. Taylor, Phys. Rev. A **85**, 020302(R) (2012)

[58] C. Reichhardt and C. J. Olson Reichhardt, Phys. Rev. B **76**, 094512 (2007)

[59] V. Misko, S. Savel'ev, and F. Nori, Phys. Rev. Lett. **95**, 177007 (2005)

[60] V. R. Misko, S. Savel'ev, and F. Nori, Phys. Rev. B **74**, 024522 (2006)

[61] M. Kemmler, C. Gürlich, A. Sterck, H. Pöhler, M. Neuhaus, M. Siegel, R. Kleiner, and D. Koelle, Phys. Rev. Lett. **97**, 147003 (2006)

[62] J. E. Villegas, M. I. Montero, C.-P. Li, and I. K. Schuller, Phys. Rev. Lett. **97**, 027002 (2006)

[63] A. V. Silhanek, W. Gillijns, V.-V. Moshchalkov, B. Y. Zhu, J. Moonens, and L. H. A. Leunissen, Appl. Phys. Lett. **89**, 152507 (2006)

[64] O. Romero-Isart, C. Navau, A. Sanchez, P. Zoller, and J. I. Cirac, Phys. Rev. Lett. **111**, 145304 (2013)

[65] I. Bloch, Nature Physics **1**, 23 (2005)

[66] A. Günther, S. Kraft, M. Kemmler, D. Koelle, R. Kleiner, C. Zimmermann, and J. Fortágh, Phys. Rev. Lett. **95**, 170405 (2005)

[67] A. Günther, S. Kraft, C. Zimmermann, and J. Fortágh, Phys. Rev. Lett. **98**, 140403 (2007)

[68] H. K. Onnes, Commun. Phys. Lab. Univ. Leiden **12**, 120 (1911)

[69] W. Meissner and R. Ochsenfeld, Naturwissenschaften **21**, 44 (1933)

[70] F. London and H. London, Proc. Roy. Soc. (London) **A149**, 866 (1935)

[71] L. V. Shubnikov, V. I. Khotkevich, Yu. D. Shepelev, and Yu. N. Ryabinin, Zh. Eksp. Teor. Fiz. **7**, 221 (1937)

[72] N. V. Zavaritskii, Doklady Akad. Nauk. SSSR **86**, 501 (1952)

[73] A. A. Abrikosov, Zh. Eksp. Teor. Fiz. **32**, 1442 (1957)

[74] V. L. Ginzburg and L. D. Landau, Zh. Eksp. Teor. Fiz. **20**, 1064 (1950)

[75] M. Kemmler, Dissertation, Eberhard Karls Universität Tübingen (2008)

[76] A. A. Abrikosov, Doklady Akad. Nauk. SSSR **86**, 489 (1952)

[77] J. Bardeen, L. N. Cooper, and J. R. Schrieffer, Phys. Rev. **108**, 1175 (1957)

[78] E. H. Brandt, Rep. Prog. Phys. **58**, 1465 (1995)

[79] V. V. Schmidt, *The Physics of Superconductors* (Springer Verlag, Berlin, 1997)

[80] M. Tinkham, *Introduction to Superconductivity* (McGraw-Hill, NewYork, 1996)

[81] C. P. Wen, IEEE Trans. Microwave Theory Tech. **17**, 1087 (1969)

[82] J. R. Clem, J. Appl. Phys. **113**, 013910 (2013)

[83] R. N. Simons, *Coplanar Waveguide Circuits, Components, and Systems* (John Wiley & Sons Inc., 2001)

[84] D. M. Pozar, *Microwave Engineering* (Second Edition, John Wiley & Sons Inc., 1998)

[85] M. Göppl, A. Fragner, M. Baur, R. Bianchetti, S. Filipp, J. M. Fink, P. J. Leek, G. Puebla, L. Steffen, and A. Wallraff, J. Appl. Phys. **104**, 113904 (2008)

[86] G. Stan, S. B. Field, and J. M. Martinis, Phys. Rev. Lett. **92**, 097003 (2004)

[87] C. Song, T. W. Heitmann, M. P. DeFeo, K. Yu, R. McDermott, M. Neeley, J. M. Martinis, and B. L. T. Plourde, Phys. Rev. B **79**, 174512 (2009)

[88] C. P. Bean, Phys. Rev. Lett. **8**, 250 (1962)

[89] C. P. Bean, Rev. Mod. Phys. **36**, 31 (1964)

[90] W. T. Norris, J. Phys. D: Appl. Phys. **3**, 489 (1970)

[91] E. H. Brandt and M. Indenbom, Phys. Rev. B **48**, 12893 (1993)

[92] E. Zeldov, J. R. Clem, M. McElfresh, and M. Darwin, Phys. Rev. B **49**, 9802 (1994)

[93] T. H. Johansen, M. Baziljevich, H. Bratsberg, Y. Galperin, P. E. Lindelof, Y. Shen, and P. Vase, Phys. Rev. B **54**, 16264 (1996)

[94] C. Jooss, J. Albrecht, H. Kuhn, S. Leonhardt, and H. Kronmüller, Rep. Prog. Phys. **65**, 651 (2002)

[95] M. Cardona, G. Fischer, and B. Rosenblum, Phys. Rev. Lett. **12**, 101 (1964)

[96] B. Rosenblum and M. Cardona, Phys. Rev. Lett. **12**, 657 (1964)

[97] J. I. Gittleman and B. Rosenblum, Phys. Rev. Lett. **16**, 734 (1966)

[98] J. I. Gittleman and B. Rosenblum, J. Appl. Phys. **39**, 2617 (1968)

[99] H. Suhl, Phys. Rev. Lett. **14**, 226 (1965)

[100] E. H. Brandt, Phys. Rev. Lett. **67**, 2219 (1991)

[101] M. W. Coffey and J. R. Clem, Phys. Rev. Lett. **67**, 386 (1991)

[102] M. W. Coffey and J. R. Clem, Phys. Rev. B **46**, 11757 (1992)

[103] N. Pompeo and E. Silva, Phys. Rev. B **78**, 094503 (2008)

[104] G. Hammer, S. Wuensch, M. Roesch, K. Ilin, E. Crocoll, and M. Siegel, Supercond. Sci. Technol. **20**, 408 (2007)

[105] J. C. Culbertson, H. S. Newman, and C. Wilker, J. Appl. Phys. **84**, 2768 (1998)

[106] P. Lahl and R. Wördenweber, Appl. Phys. Lett. **81**, 505 (2002)

[107] A. P. Zhuravel, A. G. Sivakov, O. G. Turutanov, A. N. Omelyanchouk, and S. M. Anlage, Low Temp. Phys. **32**, 592 (2006)

[108] J. I. Vestgården, D. V. Shantsev, Y. M. Galperin, and T. H. Johansen, Phys. Rev. B **77**, 014521 (2008)

[109] J. I. Vestgården, V. V. Yurchenko, R. Wördenweber, and T. H. Johansen, Phys. Rev. B **85**, 014516 (2012)

[110] J. E. Healey, T. Lindström, M. S. Colclough, C. M. Muirhead, and A. Ya. Tzalenchuk, Appl. Phys. Lett. **93**, 043513 (2008)

[111] W. Wu, A. Katsnelson, O. G. Memis, and H. Mohseni, Nanotechnology **18**, 485302 (2007)

[112] W. Wu, D. Dey, O. G. Memis, A. Katsnelson, and H. Mohseni, Nanoscale Res. Lett. **3**, 351 (2008)

[113] C. V. Sukumar and D. M. Brink, Phys. Rev. A **56**, 2451 (1997)

[114] M. P. A. Jones, C. J. Vale, D. Sahagun, B. V. Hall, and E. A. Hinds, Phys. Rev. Lett. **91**, 080401 (2003)

[115] Y. Lin, I. Teper, C. Chin, and V. Vuletić, Phys. Rev. Lett. **92**, 050404 (2004)

[116] S. Scheel, P. K. Rekdal, P. L. Knight, and E. A. Hinds, Phys. Rev. A **72**, 042901 (2005)

[117] B.-S. K. Skagerstam, U. Hohenester, A. Eiguren, and P. K. Rekdal, Phys. Rev. Lett. **97**, 070401 (2006)

[118] U. Hohenester, A. Eiguren, S. Scheel, and E. A. Hinds, Phys. Rev. A **76**, 033618 (2007)

[119] B. Kasch, H. Hattermann, D. Cano, T. E. Judd, S. Scheel, C. Zimmermann, R. Kleiner, D. Koelle, and J. Fortágh, New J. Phys. **12**, 065024 (2010)

[120] T. Mukai, C. Hufnagel, A. Kasper, T. Meno, A. Tsukada, K. Semba, and F. Shimizu, Phys. Rev. Lett. **98**, 260407 (2007)

[121] D. Cano, B. Kasch, H. Hattermann, R. Kleiner, C. Zimmermann, D. Koelle, and J. Fortágh, Phys. Rev. Lett. **101**, 183006 (2008)

[122] D. Cano, B. Kasch, H. Hattermann, D. Koelle, R. Kleiner, C. Zimmermann, and J. Fortágh, Phys. Rev. A **77**, 063408 (2008)

[123] V. Dikovsky, V. Sokolovsky, B. Zhang, C. Henkel, and R. Folman, Eur. Phys. J. D **51**, 247 (2009)

[124] F. Shimizu, C. Hufnagel, and T. Mukai, Phys. Rev. Lett. **103**, 253002 (2009)

[125] A. Emmert, A. Lupaşcu, M. Brune, J.-M. Raimond, S. Haroche, and G. Nogues, Phys. Rev. A **80**, 061604(R) (2009)

[126] T. Müller, B. Zhang, R. Fermani, K. S. Chan, M. J. Lim, and R. Dumke, Phys. Rev. A **81**, 053624 (2010)

[127] M. M. Khapaev, IEEE Trans. Microwave Theory Tech. **49**, 217 (2001)

[128] M. M. Khapaev, A. Yu. Kidiyarova-Shevchenko, P. Magnelind, and M. Yu. Kupriyanov, IEEE Trans. Appl. Supercond. **11**, 1090 (2001)

[129] M. M. Khapaev, M. Yu. Kupriyanov, E. Goldobin, and M. Siegel, Supercond. Sci. Technol. **16**, 24 (2003)

[130] B. A. Mazin, AIP Conf. Proc. **1185**, 135 (2009)

[131] J. Wenner, M. Neeley, R. C. Bialczak, M. Lenander, E. Lucero, A. D. O'Connell, D. Sank, H. Wang, M. Weides, A. N. Cleland, and J. M. Martinis, Supercond. Sci. Technol. **24**, 065001 (2011)

[132] R. Grimm, M. Weidemüller, and Y. B. Ovchinnikov, Adv. At. Mol. Opt. Phys. **42**, 95 (2000)

[133] D. Cano, H. Hattermann, B. Kasch, C. Zimmermann, R. Kleiner, D. Koelle, and J. Fortágh, Eur. Phys. J. D **63**, 17 (2011)

[134] N. F. Ramsey, Phys. Rev. **78**, 695 (1950)

[135] P. Rosenbusch, Appl. Phys. B **95**, 227 (2009)

[136] C. Deutsch, F. Ramirez-Martinez, C. Lacroúte, F. Reinhard, T. Schneider, J. N. Fuchs, F. Piéchon, F. Laloë, J. Reichel, and P. Rosenbusch, Phys. Rev. Lett. **105**, 020401 (2010)

[137] G. Nogues, C. Roux, T. Nirrengarten, A. Lupaşcu, A. Emmert, M. Brune, J.-M. Raimond, S. Haroche, B. Plaçais, and J.-J. Greffet, Eur. Phys. Lett. **87**, 13002 (2009)

[138] A. I. Larkin and Yu. N. Ovchinnikov, J. Low Temp. Phys. **24**, 409 (1979)

[139] H. Raffy, J. C. Renard, and E. Guyon, Solid State Commun. **11**, 1679 (1972)

[140] O. Daldini, P. Martinoli, J. L. Olsen, and G. Berner, Phys. Rev. Lett. **32**, 218 (1974)

[141] A. T. Fiory, A. F. Hebard, and S. Somekh, Appl. Phys. Lett. **32**, 73 (1978)

[142] M. Baert, V. V. Metlushko, R. Jonckheere, V. V. Moshchalkov, and Y. Bruynseraede, Phys. Rev. Lett. **74**, 3269 (1995)

[143] J. I. Martín, M. Veléz, J. Nogués, and I. K. Schuller, Phys. Rev. Lett. **79**, 1929 (1997)

[144] A. Castellanos, R. Wördenweber, G. Ockenfuss, A. v. d. Hart, and K. Keck, Appl. Phys. Lett. **71**, 962 (1997)

[145] D. J. Morgan and J. B. Ketterson, Phys. Rev. Lett. **80**, 3614 (1998)

[146] M. J. Van Bael, K. Temst, V. V. Moshchalkov, and Y. Bruynseraede, Phys. Rev. B **59**, 14674 (1999)

[147] M. Häffner, M. Kemmler, R. Löffler, B. Vega Gómez, M. Fleischer, R. Kleiner, D. Koelle, and D. P. Kern, Microelectronic Engineering **86**, 147003 (2009)

[148] S. Ooi, T. Mochiku, and K. Hirata, Physica C **469**, 1113 (2009)

[149] V. V. Moshchalkov, M. Baert, V. V. Metlushko, E. Rosseel, M. J. Van Bael, K. Temst, Y. Bruynseraede, and R. Jonckheere, Phys. Rev. B **57**, 3615 (1998)

[150] A. Hoffmann, P. Prieto, and I. K. Schuller, Phys. Rev. B **61**, 6958 (2000)

[151] L. Van Look, B. Y. Zhu, R. Jonckheere, B. R. Zhao, Z. X. Zhao, and V. V. Moshchalkov, Phys. Rev. B **66**, 214511 (2002)

[152] J. E. Villegas, S. Savel'ev, F. Nori, E. M. Gonzalez, J. V. Anguita, R. García, and J. L. Vicent, Science **302**, 1188 (2003)

[153] A. V. Silhanek, W. Gillijns, V. V. Moshchalkov, V. Metlushko, and B. Ilic, Appl. Phys. Lett. **89**, 182505 (2006)

[154] A. V. Silhanek, W. Gillijns, M. V. Milo$\check{\text{s}}$evi$\acute{\text{c}}$, A. Volodin, V. V. Moshchalkov, and F. M. Peeters, Phys. Rev. B **76**, 100502(R) (2007)

[155] Y. J. Rosen, A. Sharoni, and I. K. Schuller, Phys. Rev. B **82**, 014509 (2010)

[156] D. Ray, C. J. Olson Reichhardt, B. Jankó, and C. Reichhardt, Phys. Rev. Lett. **110**, 267001 (2013)

[157] V. R. Misko and F. Nori, Phys. Rev. B **85**, 184506 (2012)

[158] Y. L. Wang, M. L. Latimer, Z. L. Xiao, R. Divan, L. E. Ocola, G. W. Crabtree, and W. K. Kwok, Phys. Rev. B **87**, 220501(R) (2013)

[159] M. Motta, F. Colauto, W. A. Ortiz, J. Fritzsche, J. Cuppens, W. Gillijns, V. V. Moshchalkov, T. H. Johansen, A. Sanchez, and A. V. Silhanek, Appl. Phys. Lett. **102**, 212601 (2013)

[160] S. Guénon, Y. J. Rosen, A. C. Basaran, and I. K. Schuller, Appl. Phys. Lett. **102**, 252602 (2013)

[161] T. Matsuda, K. Harada, H. Kasai, O. Kamimura, and A. Tonomura, Science **271**, 1393 (1996)

[162] K. Harada, O. Kamimura, H. Kasai, T. Matsuda, A. Tonomura, and V. V. Moshchalkov, Science **274**, 1167 (1996)

[163] R. B. G. Kramer, A. V. Silhanek, J. Van de Vondel, B. Raes, and V. V. Moshchalkov, Phys. Rev. Lett. **103**, 067007 (2009)

[164] S. Rablen, M. Kemmler, T. Quaglio, R. Kleiner, D. Koelle, and I. V. Grigorieva, Phys. Rev. B **84**, 184520 (2011)

[165] M. M. Doria, S. C. B. de Andrade, and E. Sardella, Physica C **341-348**, 1199 (2000)

[166] M. M. Doria and G. F. Zebende, Phys. Rev. B **66**, 064519 (2002)

[167] G. R. Berdiyorov, M. V. Milošević, and F. M. Peeters, Phys. Rev. B **74**, 174512 (2006)

[168] G. R. Berdiyorov, M. V. Milošević, and F. M. Peeters, Phys. Rev. Lett. **96**, 207001 (2006)

[169] R. Cao, L. Horng, T. C. Wu, J. C. Lin, J. C. Wu, T. J. Yang, and J. Koláček, J. Appl. Phys. **109**, 083902 (2011)

[170] M. L. Latimer, G. R. Berdiyorov, Z. L. Xiao, W. K. Kwok, and F. M. Peeters, Phys. Rev. B **85**, 012505 (2012)

[171] C. Reichhardt, and N. Grønbech-Jensen, Phys. Rev. B **63**, 054510 (2001)

[172] U. Welp, Z. L. Xiao, J. S. Jiang, V. K. Vlasko-Vlasov, S. D. Bader, G. W. Crabtree, J. Liang, H. Chik, and J. M. Xu, Phys. Rev. B **66**, 212507 (2002)

[173] J. Eisenmenger, M. Oettinger, C. Pfahler, A. Plettl, P. Walther, and P. Ziemann, Phys. Rev. B **75**, 144514 (2007)

[174] P. Sabatino, C. Cirillo, G. Carapella, M. Trezza, and C. Attanasio, J. Appl. Phys. **108**, 053906 (2010)

[175] W. A. Little and R. D. Parks, Phys. Rev. Lett. **9**, 9 (1962)

[176] B. Pannetier, J. Chaussy, R. Rammal, and J. C. Villegier, Phys. Rev. Lett. **53**, 1845 (1984)

[177] A. Behrooz, M. J. Burns, H. Deckman, D. Levine, B. Whitehead, and P. M. Chaikin, Phys. Rev. Lett. **57**, 368 (1986)

[178] J. M. Gordon, A. M. Goldman, J. Maps, D. Costello, R. Tiberio, and B. Whitehead, Phys. Rev. Lett. **56**, 2280 (1986)

[179] F. Nori, Q. Niu, E. Fradkin, and S.-J. Chang, Phys. Rev. B **36**, 8338 (1987)

[180] C. W. Wilks, R. Bojko, and P. M. Chaikin, Phys. Rev. B **43**, 2721 (1991)

[181] U. Patel, Z. L. Xiao, J. Hua, T. Xu, D. Rosenmann, V. Novosad, J. Pearson, U. Welp, W. K. Kwok, and G. W. Crabtree, Phys. Rev. B **76**, 020508(R) (2007)

[182] W. Vinckx, J. Vanacken, and V. V. Moshchalkov, J. Appl. Phys. **100**, 044307 (2006)

[183] R. Penrose, Math. Intell. **2**, 32 (1979)

[184] D. Shechtman, I. Blech, D. Gratias, and J.-W. Cahn, Phys. Rev. Lett. **53**, 1951 (1984)

[185] F. Gähler, *Quasicrystalline Materials*, edited by Ch. Janot and M. J. Dubois (World Scientific, Singapore, 1988)

[186] M. Baake, P. Kramer, M. Schlottmann, and D. Zeidler, Int. J. Mod. Phys. B **4**, 2217 (1990)

Appended publications

Publication I

Improving the performance of superconducting microwave resonators in magnetic fields

D. Bothner,[a] T. Gaber, M. Kemmler, D. Koelle, and R. Kleiner
Physikalisches Institut, Experimentalphysik II and Center for Collective Quantum Phenomena, Universität Tübingen, Auf der Morgenstelle 14, D-72076 Tübingen, Germany

(Received 11 January 2011; accepted 9 February 2011; published online 8 March 2011)

The operation of superconducting coplanar waveguide cavities, as used for circuit quantum electrodynamics and kinetic inductance detectors, in perpendicular magnetic fields normally leads to a reduction in the device performance due to energy dissipating Abrikosov vortices. We experimentally investigate the vortex induced energy losses in such Nb resonators with different spatial distributions of micropatterned pinning sites (antidots) by transmission spectroscopy measurements at 4.2 K. In comparison to resonators without antidots we find a significant reduction in vortex induced losses, and thus increased quality factors over a broad range of frequencies and applied powers in moderate fields. © *2011 American Institute of Physics*. [doi:10.1063/1.3560480]

During the past decade coplanar microwave cavities made of superconducting thin films have attained an increasing importance for various experiments and applications. In circuit quantum electrodynamics, they form besides superconducting artificial atoms/qubits[1] the elementary building blocks for the fundamental investigation of light-matter interaction on a chip.[2–4] These integrated systems have also shown to be suitable candidates for quantum information processing.[5] As low energy losses, that is high quality factors, are an essential requirement to these resonators, there are currently many efforts to identify and minimize the different dissipation mechanisms.[6–9] Recently, even more advanced hybrid systems have been proposed,[10–14] coupling real atoms, molecules, or electrons to superconducting microwave cavities or combining artificial and real atoms. Here, microscopic particles need to be trapped and manipulated in the vicinity of the resonator, thereby often requiring external magnetic fields.

Operating superconducting resonators in magnetic fields can lead to considerable energy dissipation due to Abrikosov vortex motion,[15] and therefore lower quality factors. Recently, there have been some first approaches to overcome this problem under special experimental conditions. If experimentally feasible, the magnetic field can be applied parallel to the thin film. This enabled the coupling of spin ensembles in diamond and ruby to superconducting cavities in applied magnetic fields of ~100 mT.[16] For the case of residual ambient fields it has been shown, that energy losses due to a small number of vortices, caught while cooling through the superconducting transition temperature, can be reduced by trapping the vortices within a slot patterned into the resonator.[17] However, for magnetic fields with a considerable component (milli-Tesla up to Tesla) perpendicular to the superconducting chip, these approaches will not be sufficient.

In this letter, we report on the experimental investigation of a method, which leads to a significant reduction of microwave losses in superconducting Nb resonators in perpendicular magnetic fields, as required e.g., for the trapping of ultracold atom clouds on a chip[18] or electrons in planar Penning traps.[19] We use strategically placed micropatterned holes (antidots) in the superconducting film to provide well-known and highly controllable pinning sites for Abrikosov vortices.[20–22] The presented results are also transferable to other superconducting microwave thin film devices, e.g., kinetic inductance detectors, mixers and filters, when operated in external magnetic fields.

We fabricated half wavelength transmission line resonators with a resonance frequency $f_{res} \approx 3.3$ GHz. They are capacitively and symmetrically coupled to feed lines via 90 μm wide gaps at both ends, bringing the device into the undercoupled regime with external quality factors above 10^5 in zero magnetic field. Figure 1(a) shows a sketch of the resonator layout. As the oscillating supercurrents are expected to mainly flow at the edges of the resonator, Abrikosov vortices located there will experience a larger driving force than vortices far away from the edges, and therefore give a larger contribution to the losses. Furthermore, if the magnetic field B is applied with the resonators in the superconducting state, as always in this work, the vortex density will be higher at the edges, where the flux enters.[23,24] Hence, we placed the antidots at the edges of the center conductor and the ground planes in zero (reference sample), one and three rows, denoted as (resonator type) **0**, **1**, and **3**, cf. Figs. 1(b)–1(d). The antidots have a diameter $d=2$ μm and an antidot-antidot distance $a=4$ μm as design parameters. As

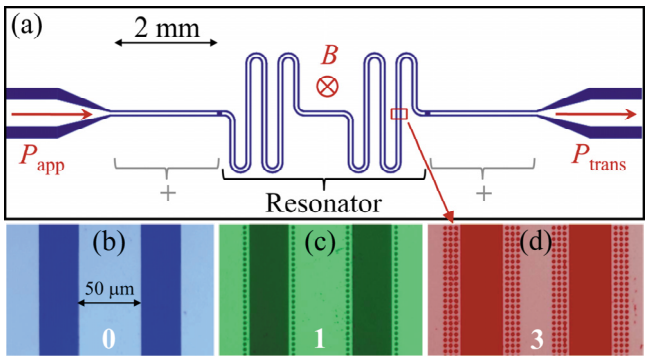

FIG. 1. (Color online) Layout of a 12×4 mm^2 chip with a capacitively coupled 3.3 GHz transmission line resonator (a), and optical images of resonators with **0** (b), **1** (c), and **3** (d) rows of antidots.

[a]Electronic mail: daniel.bothner@uni-tuebingen.de.

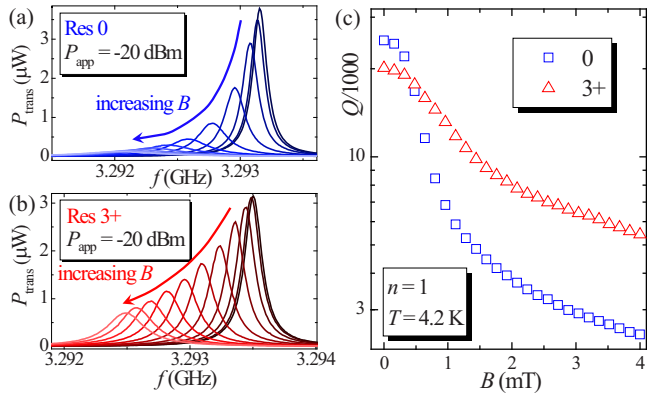

FIG. 2. (Color online) Transmitted power P_{trans} vs frequency f of (a) resonator **0** and (b) resonator **3+** for magnetic fields $0 \leq B \leq 1.6$ mT (in 0.16 mT steps); (c) shows corresponding quality factors $Q(B)$ up to $B=4$ mT.

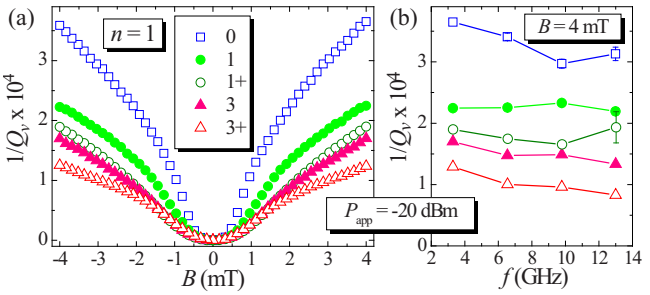

FIG. 3. (Color online) Vortex associated energy loss $1/Q_v$ of five resonators with different antidot distributions (a) vs applied field B for fundamental mode ($n=1$, $f_{res} \approx 3.3$ GHz) and (b) vs frequency f ($n=1,2,3,4$) at $B=4$ mT.

vortices in the feed lines will also contribute to the overall losses and lower the (loaded) quality factor $Q(B)$, we implemented two different designs for resonators **1** and **3**; one with antidots only on the resonator (**1**, **3**) and one with additional antidots on the feed lines (**1+**, **3+**), cf. Fig. 1(a). The antidots on the feed lines have the same configuration as on the respective resonator.

All structures including the antidots were fabricated on a single 330 μm thick 2 in. r-cut sapphire wafer by optical lithography (limiting the antidot smallness to the chosen micron-range), dc magnetron sputtering of a 300 nm thick Nb film and lift-off patterning. On sapphire, the widths of the center conductor $S=50$ μm and the ground plane gaps $W=30$ μm (originally designed for another substrate) result in a characteristic impedance of $Z_0 \approx 54$ Ω for resonator **0**. The Nb has a critical temperature of $T_c \approx 9$ K and a residual resistance ratio of $R_{300\ K}/R_{10\ K} \approx 3.6$. The whole wafer was cut into single chips of 12×4 mm^2. Each chip containing one resonator was mounted in a brass box and contacted with Indium to sub-miniature-A stripline connectors. After zero-field cooling to $T=4.2$ K, we measured the frequency dependent transmitted power P_{trans} with a spectrum analyzer for different values of applied magnetic field $|B| \leq 4$ mT, which is perpendicular to the resonator chip. Due to flux focusing we estimate the flux density seen by the resonator to be one order of magnitude larger than the applied field. Consequently, the results presented below might be applicable to much higher applied fields, if the ground plane area is properly reduced. Figure 2 shows resonance curves $P_{trans}(f)$ for the fundamental mode $n=1$ of resonator **0** (a) and of resonator **3+** (b) for different values of B and fixed applied power at the HF generator output P_{app}. No attenuators or amplifiers were used in the measurements but we estimate the power at the resonator input to be 5–10 dB less than P_{app} due to cable and connector losses. For both resonators f_{res} shifts to lower frequencies with increasing magnetic field and the resonance peak becomes smaller and broader. The decrease in transmitted power and broadening of the resonance peak though is much smaller for resonator **3+**, indicating reduced field dependent energy losses compared to resonator **0**. For a quantitative analysis we determined resonance frequency $f_{res}(B)$ and full width at half maximum $\Delta f(B)$ by fitting the curves with a Lorentzian. We subsequently calculated the quality factor $Q(B)=f_{res}(B)/\Delta f(B)$, shown in Fig. 2(c) for the resonators **0** (blue squares) and **3+** (red triangles). At $B=0$ the resonator without antidots has the higher $Q(0)$. However, for $B \geq 0.5$ mT the quality factor of resonator **3+** significantly exceeds $Q(B)$ of resonator **0** up to a factor of ~ 2.5 at $B=4$ mT. We attribute this enhancement to an effective trapping and pinning of vortices by the antidots.

In general many different field-dependent and field-independent mechanisms contribute to the total energy loss $1/Q(B)$. To be able to quantitatively compare the different antidot structures with respect to their ability to suppress vortex induced energy dissipation, we eliminated field independent factors via $1/Q_v(B)=1/Q(B)-1/Q(0)$, cf. Refs. 15 and 17. Figure 3(a) shows the vortex associated energy losses $1/Q_v(B)$ for $n=1$ of five different resonators. The losses of all resonators with antidots are significantly smaller than the losses of resonator **0**, although the magnitude of the reduction varies for the different antidot arrangements. The reduction in losses increases with increasing number of antidots; three rows of antidots yield about twice the effect of one row of antidots. The scaling of the loss reduction with the number of antidot rows probably mirrors the nonuniform current and vortex distribution across the resonator: vortices near the edges contribute more to the losses than those further away. The resonators **1+** and **3+** (open circles and triangles) show even lower losses compared to their counterparts **1** and **3** without pinning sites on the feed lines (full circles and triangles). This suggests that the ac vortex resistivity in the feed lines has a considerable impact on the overall losses and can be reduced by suitable pinning sites.

We note here, that the quality factor of the five resonators in zero magnetic field varied between $Q(0) \approx 15000$(**1**) and $Q(0) \approx 43000$(**1+**) but we neither found a correlation between zero field quality factor and antidot configurations nor between $Q(0)$ and $1/Q_v(B)$. This leads to the conclusion, that the observed reduction in $1/Q_v(B)$ can purely be attributed to effective vortex pinning by the antidots.

We also determined the losses $1/Q_v(B)$ for the first three higher order harmonics $n=2,3,4$. Figure 3(b) shows $1/Q_v(f)$ for $n=1,2,3,4$ of the five resonators at $B=4$ mT. We found that $1/Q_v(f)$ is nearly constant for all five resonators, with a small tendency to decrease with frequency. This frequency dependence can basically be explained by applying standard models for the microwave response of vortices[25–27] to resonant structures, as it was done by Song *et al.*[15] A detailed analysis and discussion of the data in terms of these models will be given elsewhere. Here we note, that the reduction in vortex associated losses by the introduction of antidots is

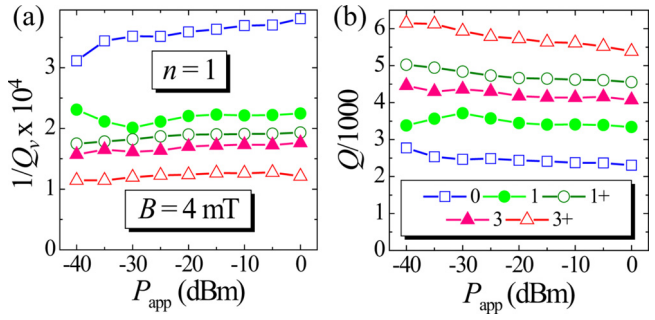

FIG. 4. (Color online) Experimentally determined energy loss $1/Q_v$ (a) and quality factor Q (b) vs applied microwave power P_{app} at $B=4$ mT and $T=4.2$ K of five resonators with different antidot distributions.

quantitatively and qualitatively stable over a broad frequency range at least from 3.3 to 13 GHz.

We finally determined the power dependence of the quality factors $Q(B)$ and energy losses $1/Q_v(B)$ for applied powers from –40 to 0 dBm. For $P_{app}>0$ dBm the resonance peak is cut off, indicating the ac supercurrents to be overcritical near the maximum of the resonance. For smaller values of P_{app} the resonance curves showed no indication of nonlinearities. Figure 4 depicts (a) $1/Q_v(P_{app})$ and (b) $Q(P_{app})$ for the five different resonators at $B=4$ mT. Both quantities are almost independent of P_{app} with a slight tendency of $1/Q_v$ to increase and Q to decrease with increasing applied power. Note that the absolute quality factor $Q(4$ mT) is dominated by the vortex induced losses, as it mirrors the behavior of $1/Q_v(4$ mT) almost independently of $Q(0)$. $Q(0)$ is nevertheless somewhat perceivable at $B=4$ mT. Resonator **1+** for example shows a higher Q than resonator **3** despite the higher vortex associated losses of resonator **1+**. Essentially, the ratios of the vortex losses and the quality factors of the five resonators, and therefore the effectiveness of the antidots are almost constant for the investigated power range.

In conclusion, we demonstrated experimentally, that energy losses in superconducting microwave resonators due to the presence of Abrikosov vortices can be significantly reduced by the introduction of antidots. Accordingly, the quality factor $Q(B)$ at finite applied fields in the milli-Tesla range can be considerably increased with this method. We have demonstrated this result to hold for a broad frequency range $3.3\ \text{GHz} \leq f \leq 13\ \text{GHz}$ and four orders of magnitude of the applied power $-40\ \text{dBm} \leq P_{app} \leq 0\ \text{dBm}$ at a temperature of $T=4.2$ K. Strategies for transferring these results to higher magnetic fields might include the proper reduction of flux focusing ground plane areas as well as the implementation of pinning arrays with typical length scales well in the submicron range. As for many experiments in circuit quantum electrodynamics the resonators are operated in the milli-Kelvin and single photon regime, the effects presented here have to be investigated under these experimental conditions in further studies.

This work has been supported by the Deutsche Forschungsgemeinschaft via Grant No. SFB/TRR 21 and by the European Research Council via SOCATHES. D.B. acknowledges support by the Evangelisches Studienwerk Villigst e.V., M.K. acknowledges support by the Carl-Zeiss Stiftung. We thank Stefan Wünsch from the Karlsruhe Institute of Technology for sharing his expertise in fabrication and characterization of superconducting resonators, and we thank Roger Wördenweber for inspiring discussions.

[1] J. Clarke and F. K. Wilhelm, Nature (London) **453**, 1031 (2008).
[2] A. Wallraff, D. I. Schuster, A. Blais, L. Frunzio, R.-S. Huang, J. Majer, S. Kumar, S. Girvin, and R. J. Schoelkopf, Nature (London) **431**, 162 (2004).
[3] M. Hofheinz, H. Wang, M. Ansmann, R. C. Bialczak, E. Lucero, M. Neeley, A. D. O'Connell, D. Sank, J. Wenner, J. M. Martinis, and A. N. Cleland, Nature (London) **459**, 546 (2009).
[4] T. Niemczyk, F. Deppe, H. Huebl, E. P. Menzel, F. Hocke, M. J. Schwarz, J. J. Garcia-Ripoll, D. Zueco, T. Hümmer, E. Solano, A. Marx, and R. Gross, Nat. Phys. **6**, 772 (2010).
[5] L. DiCarlo, J. M. Chow, J. M. Gambetta, L. S. Bishop, B. Johnson, D. I. Schuster, J. Majer, A. Blais, L. Frunzio, S. M. Girvin, and R. J. Schoelkopf, Nature (London) **460**, 240 (2009).
[6] H. Wang, M. Hofheinz, J. Wenner, M. Ansmann, R. C. Bialczak, M. Lenander, E. Lucero, M. Neeley, A. D. O'Connell, D. Sank, M. Weides, A. N. Cleland, and J. M. Martinis, Appl. Phys. Lett. **95**, 233508 (2009).
[7] P. Macha, S. H. W. van der Ploeg, G. Oelsner, E. Il'ichev, H.-G. Meyer, S. Wünsch, and M. Siegel, Appl. Phys. Lett. **96**, 062503 (2010).
[8] R. Barends, N. Vercruyssen, A. Endo, P. J. de Visser, T. Zijistra, T. M. Klapwijk, P. Diener, S. J. C. Yates, and J. J. A. Baselmans, Appl. Phys. Lett. **97**, 023508 (2010).
[9] T. Lindström, J. E. Healey, M. S. Colclough, C. M. Muirhead, and A. Y. Tzalenchuk, Phys. Rev. B **80**, 132501 (2009).
[10] P. Rabl, D. DeMille, J. M. Doyle, M. D. Lukin, R. J. Schoelkopf, and P. Zoller, Phys. Rev. Lett. **97**, 033003 (2006).
[11] A. Imamoğlu, Phys. Rev. Lett. **102**, 083602 (2009).
[12] J. Verdú, H. Zoubi, C. Koller, J. Majer, H. Ritsch, and J. Schmiedmayer, Phys. Rev. Lett. **103**, 043603 (2009).
[13] K. Henschel, J. Majer, J. Schmiedmayer, and H. Ritsch, Phys. Rev. A **82**, 033810 (2010).
[14] P. Bushev, D. Bothner, J. Nagel, M. Kemmler, K. B. Konovalenko, A. Loerincz, K. Ilin, M. Siegel, D. Koelle, R. Kleiner, and F. Schmidt-Kaler, Eur. Phys. J. D (to be published).
[15] C. Song, T. W. Heitmann, M. P. DeFeo, K. Yu, R. McDermott, M. Neeley, J. M. Martinis, and B. L. T. Plourde, Phys. Rev. B **79**, 174512 (2009).
[16] D. I. Schuster, A. P. Sears, G. Ginossar, L. DiCarlo, L. Frunzio, J. J. L. Morton, H. Wu, G. A. D. Briggs, B. B. Buckley, D. D. Awschalom, and R. J. Schoelkopf, Phys. Rev. Lett. **105**, 140501 (2010).
[17] C. Song, M. P. DeFeo, K. Yu, and B. L. T. Plourde, Appl. Phys. Lett. **95**, 232501 (2009).
[18] J. Fortágh and C. Zimmermann, Science **307**, 860 (2005).
[19] P. Bushev, S. Stahl, R. Natali, G. Marx, E. Stachowska, G. Werth, M. Hellwig, and F. Schmidt-Kaler, Eur. Phys. J. D **50**, 97 (2008).
[20] A. T. Fiory, A. F. Hebard, and R. P. Minnich, J. Phys. Colloq. **39**, C6-633 (1978).
[21] V. V. Moshchalkov, M. Baert, V. V. Metlushko, E. Rosseel, M. J. V. Bael, K. Temst, Y. Bruynseraede, and R. Jonckheere, Phys. Rev. B **57**, 3615 (1998).
[22] R. Wördenweber, P. Dymashevski, and V. R. Misko, Phys. Rev. B **69**, 184504 (2004).
[23] P. Lahl and R. Wördenweber, IEEE Trans. Appl. Supercond. **13**, 2917 (2003).
[24] E. H. Brandt and M. Indenbom, Phys. Rev. B **48**, 12893 (1993).
[25] J. I. Gittleman and B. Rosenblum, J. Appl. Phys. **39**, 2617 (1968).
[26] E. H. Brandt, Phys. Rev. Lett. **67**, 2219 (1991).
[27] M. W. Coffey and J. R. Clem, Phys. Rev. Lett. **67**, 386 (1991).

Publication II

PHYSICAL REVIEW B **86**, 014517 (2012)

Magnetic hysteresis effects in superconducting coplanar microwave resonators

D. Bothner,* T. Gaber, M. Kemmler, D. Koelle, and R. Kleiner
Physikalisches Institut–Experimentalphysik II and Center for Collective Quantum Phenomena in LISA$^+$, Universität Tübingen, Auf der Morgenstelle 14, 72076 Tübingen, Germany

S. Wünsch and M. Siegel
Institut für Mikro- und Nanoelektronische Systeme, Karlsruher Institut für Technologie, Hertzstrasse 16, 76187 Karlsruhe, Germany
(Received 27 February 2012; revised manuscript received 31 May 2012; published 20 July 2012)

We performed transmission spectroscopy experiments on coplanar half-wavelength niobium resonators at temperature $T = 4.2$ K. We observe not only a strong dependence of the quality factor Q and the resonance frequency $f_{\rm res}$ on an externally applied magnetic field but also on the magnetic history of our resonators, i.e., on the spatial distribution of trapped Abrikosov vortices in the device. This is valid for a broad range of frequencies and angles between the resonator plane and the magnetic field direction and holds for resonators with and without antidots near the edges of the center conductor and the ground planes. In a detailed analysis, we show that characteristic features of the experimental data can only be reproduced by calculations if we assume a highly inhomogeneous rf current density and a flux density gradient with maxima at the edges of the superconductor. We furthermore demonstrate that the hysteretic behavior of the resonator properties can be used to considerably reduce the vortex-induced losses and to fine-tune the resonance frequency by the proper way of cycling to a desired magnetic field value.

DOI: 10.1103/PhysRevB.86.014517 PACS number(s): 74.25.Ha, 84.40.Dc, 03.67.Lx

I. INTRODUCTION

When Charles P. Bean introduced his model for the magnetization of hard superconductors in 1962,[1,2] he probably had not foreseen that related magnetic history effects may become of importance for circuit quantum electrodynamics,[3–5] quantum information processing,[6] or single-particle detection.[7] Of particular importance in these highly topical branches of research are superconducting coplanar microwave cavities. In many cases, the cavity quality factor Q, which defines the photon lifetime in the resonator and the sharpness of the resonance, is demanded to be rather high. Thus, there are many current efforts to identify and suppress the various energy-loss mechanisms.[8–11]

Recently, advanced hybrid systems have been proposed,[12–16] consisting of ultracold atoms, molecules, or electrons coupled to both superconducting microwave cavities and artificial atoms based on superconducting circuits. The magnetic fields required for trapping and manipulating the atomic systems[17,18] will lead to energy dissipating Abrikosov vortices,[19] adding a significant loss channel for the energy stored in the resonator. Lately, there have been different approaches to reduce the vortex-associated energy losses in particular experimental situations. In some experiments the magnetic field can be applied parallel to the plane of the superconducting film, which reduces the flux in typical coplanar resonators by orders of magnitude. This approach was used in experiments with spin ensembles, which were coupled to microwave photons in superconducting transmission line cavities.[20,21] For experiments requiring an out-of-plane magnetic field component, it has been demonstrated that losses due to vortices can effectively be reduced by trapping and pinning the flux lines either in a slot in the center of the resonator[22] or in antidots patterned at the resonator edges[23] and all over the chip.[24] Patterning with antidots is particularly suitable for zero-field cooling experimental conditions, when the vortices enter the superconductor from the edges and form a flux density gradient, called the Bean critical state. Under zero-field cooling conditions there is also a number of hysteresis effects, which on the mesoscopic scale are related to the spatial distribution of Abrikosov vortices.[25,26]

In this paper we present experimental results concerning a considerable hysteretic behavior of the characteristic quantities of coplanar superconducting resonators (with and without antidots), i.e., the quality factor Q, the loss factor $1/Q$, and the resonance frequency $f_{\rm res}$. We find that for fixed values of a perpendicularly applied magnetic flux density B, the resonator losses due to vortices $1/Q_v(B)$ can be reduced and $f_{\rm res}(B)$ can be tuned by the proper choice of magnetic history. A detailed analysis reveals strong indications that essential features of the measured hysteresis effects are best described by a combination of a highly inhomogeneous rf current distribution and field penetration models for thin films.[27,28]

The paper is organized as follows. After this introductory Sec. I we describe the sample fabrication and characterization techniques in Sec. II. In Sec. III we present and discuss our experimental data, which show a hysteretic behavior of the vortex-associated energy losses and the resonance frequency in perpendicular magnetic fields. In Sec. IV we develop a simple model to describe the dependence of the vortex-associated losses on the rf-current and vortex distribution and compare our measurements with numerical calculations. In Sec. V we discuss the possibility of exploiting the hysteresis to improve and tune the properties of the resonator in a specific magnetic field. Hysteresis effects at higher modes of the resonator and for nonperpendicular orientations between resonator plane and magnetic field are presented and discussed in Sec. VI. Finally, Sec. VII concludes the paper.

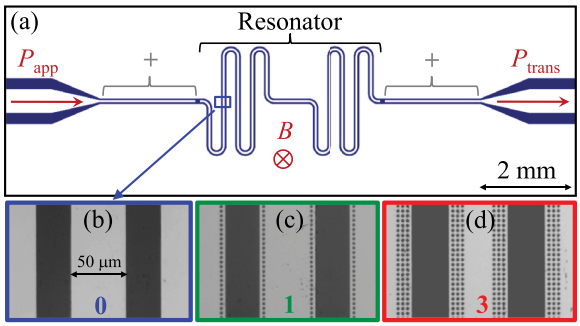

FIG. 1. (Color online) (a) Layout of 12×4 mm^2 chip with a capacitively coupled 3.3 GHz transmission line resonator. Optical images of resonators with (b) **0**, (c) **1**, and (d) **3** rows of antidots. The parts of the feedlines, which are perforated with antidots are marked with + (cf. Ref. 23).

II. RESONATOR FABRICATION AND CHARACTERIZATION

We fabricated half-wavelength coplanar transmission line resonators with a designed resonance frequency $f_{res} = 3.3$ GHz. They are capacitively and symmetrically coupled to feed lines via 90-μm-wide gaps at both ends. Due to the small coupling capacitances $C_c \approx 1$ fF[29] the resonators are undercoupled with an external quality factor $Q_c > 10^5$. Hence, the overall cavity losses in zero magnetic field and at liquid helium temperature $T = 4.2$ K are dominated by intrinsic, resistive losses. Figure 1(a) shows a sketch of the resonator layout together with optical images of the resonators without (b), with one row (c), and with three rows (d) of antidots at the edges of the center conductor and the ground planes. These resonators are denoted as Res **0**, Res **1**+, and Res **3**+, respectively, with a + indicating that also the feed lines are partially perforated, cf. Fig. 1(a). The antidots have a radius $R = 1\,\mu$m and an antidot-antidot distance $D = 4\,\mu$m. For further design considerations of the antidots regarding size and arrangement, see Ref. 23.

The structures were fabricated on a 330-μm-thick, 2-inch sapphire wafer (r-cut) by optical lithography and subsequent dc magnetron sputtering of a $d = 300$-nm-thick Nb film. After sputtering, the wafer was cut into 12×4 mm^2 chips with a single resonator. Finally, the surplus Nb was lifted-off with acetone. The transmission line has a characteristic impedance $Z_0 \approx 54\,\Omega$, where the width of the center conductor is $S = 50\,\mu$m and the gap to the ground plane is $W = 30\,\mu$m. The Nb film has a critical temperature $T_c \approx 9$ K and a residual resistance ratio $R(300\,\text{K})/R(10\,\text{K}) \approx 3.6$.

Each chip was mounted into a small brass box and the transmission line was electrically connected to subminiature-A (SMA) stripline connectors using indium as contact material. All measurements were performed at $T = 4.2$ K in liquid helium (helium-gas in the angle-dependent measurements). A magnetic field perpendicular to the resonator plane could be applied with a pair of Helmholtz coils. For angle-dependent measurements, the sample was rotated in the field of a superconducting high-field split coil. We estimate the flux density seen by the resonator to be one order of magnitude larger than the applied external field due to flux-focusing effects. As we are interested in the resonator properties at magnetic fields of some mT, no measures were taken to shield the samples from the Earth's magnetic field. Therefore, in all zero-field cooling experiments, some residual field was present, but much smaller than any field we applied (except for the angle-dependent measurements). To characterize the resonators we applied a microwave signal of power $P_{app} = -20$ dBm and frequency f to one of the feed lines and measured the frequency-dependent transmitted power $P_{trans}(f)$ with a spectrum analyzer. No attenuators or amplifiers were used. We estimate the effective power at the resonator input to be about 5–10 dB lower than P_{app}. Similarly, P_{trans} is about 5–10 dB smaller than the power directly at the resonator output.

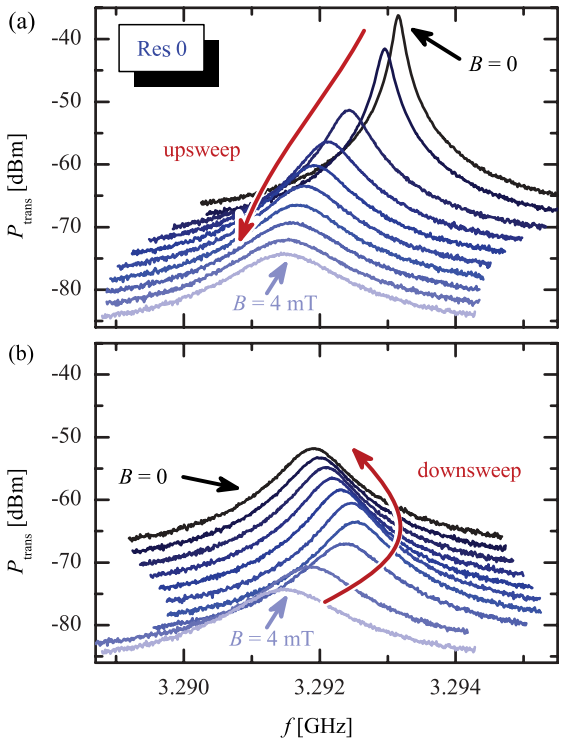

FIG. 2. (Color online) Measured transmitted power P_{trans} vs. frequency f of resonator **0** after zero-field cooling, when (a) the applied magnetic field was increased from 0 in 0.48 mT steps, with an additional curve at 4 mT and (b) B was decreased back to zero. Adjacent curves are shifted by +2 dBm for better visibility, with $P_{trans}(4\,\text{mT})$ being the unshifted reference. The applied microwave power was $P_{app} = -20$ dBm.

III. HYSTERESIS EFFECTS

Figure 2(a) shows $P_{trans}(f)$ around the fundamental mode $n = 1$ of a resonator without antidots (Res **0**) for different values of applied magnetic field between $B = 0$ and $B = 4$ mT. As reported before, we find that with increasing B the resonance frequency decreases and the resonance peak gets smaller and broader, indicating increasing losses.[19,22,23] When we reduce the magnetic field from $B = 4$ mT back to $B = 0$, we find a strong hysteresis in the resonance characteristics. Figure 2(b) depicts the corresponding spectra [for the same values of B as in (a)], showing that the original state of (a) is not restored at $B = 0$. Interestingly, $\partial f_{res}/\partial B$ changes sign at

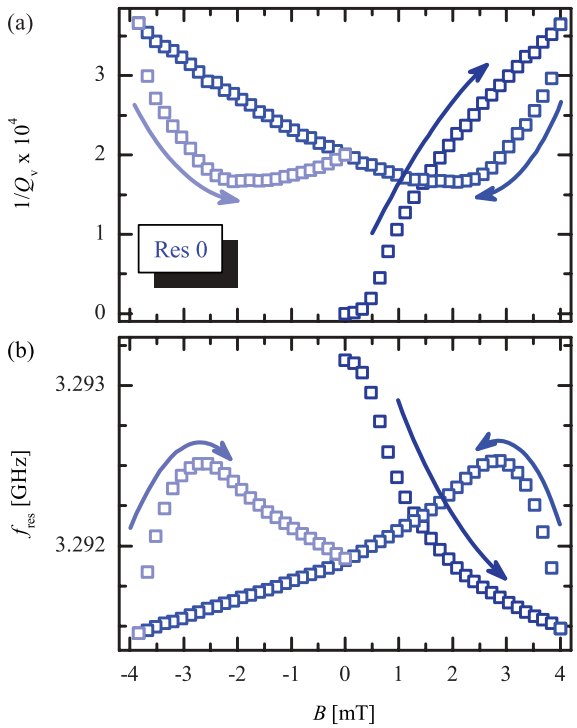

FIG. 3. (Color online) (a) Vortex associated energy losses $1/Q_v(B)$ and (b) resonance frequency $f_{\rm res}(B)$ of the fundamental mode $n = 1$ of resonator **0** for a full cycle of B. Arrows indicate the sweep direction of the field.

$B \approx 3\,\mathrm{mT}$: After a first increase of the resonance frequency with decreasing B, $f_{\rm res}$ decreases again for $B \to 0$.

We fitted the measured transmission spectra with a Lorentzian and extracted the resonance frequency $f_{\rm res}(B)$ and the full width at half maximum $\Delta f(B)$ to quantitatively analyze the hysteresis in the resonator properties. Using $f_{\rm res}(B)$ and $\Delta f(B)$ we calculate the magnetic field-dependent quality factor $Q(B) = f_{\rm res}(B)/\Delta f(B)$ and the magnetic field dependent losses $1/Q(B)$. In order to quantify the losses associated with the magnetic field, i.e., the presence of Abrikosov vortices, we define $1/Q_v(B) \equiv 1/Q(B) - 1/Q(0)$, cf. Refs. 19, 22, and 23. Figure 3 shows (a) the vortex associated losses $1/Q_v(B)$ and (b) the resonance frequency $f_{\rm res}(B)$ for a full magnetic field cycle. Both $1/Q_v(B)$ and $f_{\rm res}(B)$ show a pronounced hysteresis. Interestingly, immediately after the sweep direction is reversed at $B = 4\,\mathrm{mT}$, the losses decrease considerably and are significantly smaller than the losses for the same field values, when coming from the virgin state. In the following we indicate properties, that refer to the upsweep (downsweep) of B with $\uparrow$ ($\downarrow$). For the very first upsweep from the virgin state we use $\Uparrow$. Over a considerable range of applied magnetic field ($B \gtrsim 1.4\,\mathrm{mT}$), $1/Q_v^{\downarrow}(B) < 1/Q_v^{\Uparrow}(B)$ with a minimum of the losses $1/Q_v^{\downarrow}$ at $B \approx 2\,\mathrm{mT}$. For negative B we find a similar behavior and $1/Q_v^{\uparrow}(B) < 1/Q_v^{\downarrow}(B)$. When we repeatedly sweep the magnetic field between $\pm B_{\rm max} = \pm 4\,\mathrm{mT}$, $1/Q_v(B)$ follows a butterfly like curve and never returns to the virgin value. This indicates that during the field cycles the sample does never return to the vortex-free state.

The resonance frequency in Fig. 3(b) shows a hysteretic behavior very similar to the losses but inverted regarding absolute values. Immediately after the sweep direction is inverted, $f_{\rm res}$ increases, and after reaching a local maximum it decreases again with further decreasing magnetic field. Note that the magnetic field values at the downsweep, where $1/Q_v(B)$ reaches a minimum and $f_{\rm res}(B)$ reaches a maximum, are not equal. This discrepancy was observed for all resonators. We believe that $1/Q_v(B)$ and $f_{\rm res}(B)$ have their extrema at different field values because the frequency shift due to a change in the kinetic inductance has not only contributions from the normal conducting vortex cores but also from the global and local screening currents, which have a slightly different distribution than the vortex cores.

Remanent vortices in type-II superconductors, observed and investigated in various studies,[25] have been reported to lead to hysteresis effects in the microwave properties of superconducting structures.[30–32] In the next section we will show that by taking a closer look at the measured hysteresis curves one can gain new insights into the underlying physics, as the particular shape of these curves is intimately related to the microwave current and vortex distribution in the resonator.

Before we proceed with the discussion and the analysis of our results, we give a rough estimate for the circulating power and the corresponding rf current density in the resonator under our experimental conditions. The power circulating in the resonator is given by $P_{\rm circ} = 4P_{\rm in}r(1-r)Q/\pi$ with $r = \sqrt{P_{\rm out}/P_{\rm in}}$.[33] Here, $P_{\rm in}$ ($P_{\rm out}$) denotes the power at the resonator input (output) in Watt. We estimate $P_{\rm in} = 2 \cdot 10^{-6}\,\mathrm{W}$ and $P_{\rm out} = 1.5 \cdot 10^{-8}\,\mathrm{W}$ for $B = 0$. With $Q = 2 \cdot 10^4$ we find $P_{\rm circ} = 4 \cdot 10^{-3}\,\mathrm{W}$ for $B = 0$. Due to the high quality factor, $P_{\rm circ}$ is predominantly reactive, so the corresponding maximum current on resonance is $I \approx \sqrt{P_{\rm circ}/(2\pi f_{\rm res} L)}$. The total inductance $L = 2L'l/\pi^2 \approx 1.66\,\mathrm{nH}$ can be calculated with the line inductance $L' \approx 424\,\mathrm{nH/m}$ and the resonator length $l \approx 1.94\,\mathrm{cm}$.[34] With the center conductor cross section $A = 1.5 \cdot 10^{-7}\,\mathrm{cm}^2$ we find a current density $j = I/A = 7 \cdot 10^4\,\mathrm{Acm}^{-2}$, which is almost two orders of magnitude smaller than the critical current density of our Nb films at $B = 0$. Of course, due to uncertainties in $P_{\rm in}$ and $P_{\rm out}$, this estimate is not very precise. However, the order of magnitude seems to be correct, as the first signs for a distortion of the Lorentzian resonance curve (indicating significant nonlinearities) appear for power levels exceeding the ones discussed here by a factor of 10^3.

IV. THE RESONATOR LOSS MODEL

In this section we introduce a simplified model that allows us to derive an approximate expression for the dependence of the vortex-associated losses $1/Q_v$ on a spatially varying flux density $\tilde{B}(x,B)$ and on the microwave current density $j^{\rm rf}(x)$ in a superconducting coplanar resonator, cf. Fig. 4(a). B still denotes the externally applied field in y direction, and $j^{\rm rf}(x)$ points in z direction. For simplicity we only calculate the vortex associated losses in the center conductor and discuss a possible influence of the ground planes at the end of this section.

We treat an Abrikosov vortex in the superconducting strip as a massless point-like particle under the influence of a driving Lorentz force $f_L = j^{\rm rf}\Phi_0$ with the sheet current density $j^{\rm rf} = j_0^{\rm rf}\sin(\omega t)$ and a friction $f_F = \eta v$, which leads to the one-dimensional equation of motion $\eta v = j^{\rm rf}\Phi_0$. In

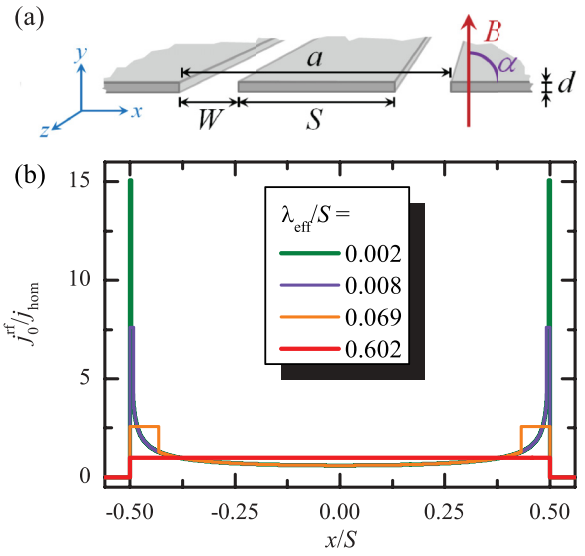

FIG. 4. (Color online) (a) Sketch of a coplanar waveguide with center conductor width S, ground-to-ground distance a, and thickness d; (b) Microwave current density distribution $j_0^{\mathrm{rf}}(x)$ normalized to the homogeneous distribution $j_{\mathrm{hom}} = I/S$ (I is the total current on the center conductor) of a coplanar waveguide for different values of λ_{eff}/S, according to Eqs. (2) and (3).

this picture the amplitude of the vortex velocity v is directly proportional to the amplitude of the alternating driving force, and we find the energy dissipated per cycle ΔE to obey the proportionality $\Delta E = \int_0^T f_L v dt \propto (j_0^{\mathrm{rf}})^2$ with $T = 2\pi/\omega$. If we have several vortices at different positions x_i with local current densities $j_0^{\mathrm{rf}}(x_i)$ we must sum up over all $\Delta E(x_i)$ from single vortices to get the overall dissipation $\Delta E_{\mathrm{total}} = \sum_i \Delta E(x_i) \propto \sum_i j_0^{\mathrm{rf}}(x_i)^2$.

The flux density $\tilde{B}(x,B)$ (divided by the flux quantum $\Phi_0 = 2.07 \times 10^{-15}\,\mathrm{Tm}^2$) can approximately be treated as a continuous representation of the vortex density in the superconductor. With this we rewrite the total dissipated energy per cycle and unit length in y direction as

$$\Delta E_{\mathrm{total}} \propto \int_{-S/2}^{S/2} |\tilde{B}(x,B)| \left[j_0^{\mathrm{rf}}(x)\right]^2 dx := \delta e(B), \qquad (1)$$

where $|\tilde{B}(x,B)|$ reflects the independence of the dissipation from the vortex polarity. $\delta e(B)$ contains all information on the spatial distributions of vortices and driving forces. It allows for a qualitative analysis of the experimentally found hysteresis curves. Within our approach, $1/Q_v(B) \propto \delta e(B)$ and the proportionality factor is eliminated below, as we only consider the normalized quantity $\delta e(B)/\delta e_{\mathrm{max}}$.

Another possibility to find the same proportionalities between δe, $j^{\mathrm{rf}}(x)$, and $\tilde{B}(x,B)$ from an electrotechnical point of view starts with the dissipated power density $p_d(x) = \mathrm{Re}[\rho_v(x)] j_0^{\mathrm{rf}}(x)^2$, which must be integrated over the width S to get the overall dissipation per unit length $D = \int_{-S/2}^{S/2} p_d(x) dx$. The hereby used real part of the vortex resistivity $\rho_v(x)$ can be obtained from the formulas given by different models.[35–37] All of these models have the linear proportionality $\rho_v(x) \propto \tilde{B}(x,B)$ in common, which again leads us to the above expression for $\delta e(B)$. This argument is closely related to the one given in Ref. 19 to obtain an expression for $1/Q_v(B)$. Interestingly, the expressions in these models are derived by treating the vortices as a vortex crystallite and not as individual particles and by adding a pinning potential. For a complete model, which provides absolute values of losses and which also considers the frequency response of the vortices, a pinning potential has to be included. However, as we are mainly interested in a qualitative understanding of the shape of the hysteresis curves, we can neglect the pinning force in the equation of motion without changing the proportionalities between $1/Q_v$, $j^{\mathrm{rf}}(x)$ and $\tilde{B}(x)$. Note that in all calculations below, we are treating $j^{\mathrm{rf}}(x)$ and $\tilde{B}(x)$ as independent quantities and discuss the justification of this assumption at the end of this section.

According to Ref. 26 and references therein, the microwave current density distribution $j_0^{\mathrm{rf}}(x)$ in the center conductor of a (flux-free) superconducting coplanar line can be approximated by

$$j_0^{\mathrm{rf}}(x) = \frac{I}{K\left(\frac{S}{a}\right) S \sqrt{\zeta(x)}}, \qquad (2)$$

where

$$\zeta(x) = \begin{cases} \frac{\lambda_{\mathrm{eff}}}{S}\left[1 - \left(\frac{S}{a}\right)^2\right], & 0 \leqslant \frac{S}{2} - |x| < \lambda_{\mathrm{eff}}, \\ \left[1 - \left(\frac{2x}{S}\right)^2\right]\left[1 - \left(\frac{2x}{a}\right)^2\right], & |x| \leqslant \frac{S}{2} - \lambda_{\mathrm{eff}}. \end{cases} \qquad (3)$$

Here, $a = S + 2W$ denotes the distance between the ground planes; in our case $a = 110\,\mu$m. K is the complete elliptic integral and I is the total current. $\lambda_{\mathrm{eff}} = \lambda_{\mathrm{L}} \coth(d/\lambda_{\mathrm{L}})$ is the effective penetration depth and λ_{L} is the London penetration depth.[38,39] For $\lambda_{\mathrm{eff}}/S \ll 1$, the current distribution Eq. (2) is very inhomogeneous and has pronounced maxima at the edges of the strip. However, with increasing λ_{eff}/S the maxima continuously decrease until $j_0^{\mathrm{rf}}(x)$ becomes completely homogeneous, i.e., $j_0^{\mathrm{rf}}(x) = I/S = \mathrm{const.}$ for $\lambda_{\mathrm{eff}} \geqslant S/2$. For our samples we find $\lambda_{\mathrm{eff}} \approx \lambda_{\mathrm{L}} = 100\,\mathrm{nm}$ and $\lambda_{\mathrm{eff}}/S \approx 0.002$. Figure 4(b) shows the current distribution according to Eq. (2) for four different ratios λ_{eff}/S. For $d/S = 0.006$, as in our sample, these values correspond to $\lambda_{\mathrm{L}}/S = 0.002, 0.006, 0.02$, and 0.06. The discrete edge maxima (visible for $\lambda_{\mathrm{eff}}/S = 0.069$) are due to the particular approximation Eq. (2) for the current density: The current in the edge region of width λ_{eff} is assumed to be distributed homogeneously, while the current in the inside is independent of λ_{eff}. We have also done the calculations shown below with a different, continuous current distribution for a single superconducting strip. The results looked very similar, seeming only to require maxima near the edges. We decided to use the current distribution Eq. (2) for two reasons. First, this approximates the current density for a coplanar waveguide geometry and not only for a single strip. Second, and more important, it has inherently incorporated the transition to a homogeneous current density with increasing λ_{eff}.

To describe the magnetic flux density $\tilde{B}(x)$ in the center conductor of the resonator we start with the classical Bean profile.[1] The basic Bean model was the first model, which explained the magnetization curves of type-II superconductors on a macroscopic scale. It is thus the first choice for trying to understand our data, although technically it applies to

infinite superconducting slabs in parallel fields. The idea behind the model is that the interior of a superconductor is shielded from external magnetic fields by a macroscopic current of critical density, which continuously builds up from the surface to the interior with increasing applied field until the critical current density flows everywhere inside. Connected to the shielding current is a flux density gradient inside the superconducting sample, which according to Ampère's law is directly proportional to the critical current density. On the mesoscopic scale, the flux gradient inside the superconductor is quantized into Abrikosov vortices and the critical current density is equivalent to the depinning current density of these vortices, but this is not part of the macroscopic model. As any change in the interior flux and current state due to a change of the external fields is induced from the sample edges, the overall state of the superconductor depends on its magnetic history. During an upsweep from the virgin state, the flux density decreases linearly from the edges of the strip and can be expressed as

$$\tilde{B}^{\Uparrow}(x,B) = \begin{cases} \frac{2B^*}{S}|x| - (B^* - B), & \frac{S}{2} \geqslant |x| > \frac{S}{2}b, \\ 0, & |x| \leqslant \frac{S}{2}b, \end{cases} \quad (4)$$

where $b = (1 - \frac{B}{B^*})$, and B^* represents the applied field, when the flux fronts from both edges of the strip meet at $x = 0$. After the virgin upsweep to $B_{\max}$, the flux profile for the downsweep is given by

$$\tilde{B}^{\downarrow}(x,B) = \tilde{B}^{\Uparrow}(x,B_{\max}) - 2\tilde{B}^{\Uparrow}\left(x, \frac{B_{\max} - B}{2}\right). \quad (5)$$

The flux density profiles $\tilde{B}^{\Uparrow}(x,B)$ and $\tilde{B}^{\downarrow}(x,B)$ are shown in Figs. 5(a) and 5(b) for several values of B during (a) a field upsweep to $B_{\max} = B^*$ and (b) during the downsweep from $B = B^*$ to $B = -B^*$. Note, for each applied magnetic field B, $|\tilde{B}^{\Uparrow}(x,B)| \leqslant |B|$ and $|\tilde{B}^{\downarrow}(x,B)| \geqslant |\tilde{B}^{\Uparrow}(x,B)|$. The aforementioned relation also affects the dissipation, i.e., for the same values of applied magnetic field the losses during the downsweep should be larger than in the upsweep.

The lower part of Fig. 5 shows the calculated quantity $\delta e/\delta e_{\max}$ for the Bean model flux profile with a homogeneous [$\lambda_{\text{eff}}/S > 1$, (c)] as well as a highly inhomogeneous [$\lambda_{\text{eff}}/S = 0.002$, (d)] microwave current distribution. All calculations of $\delta e(B)$ were carried out numerically with a spatial resolution of $\Delta x = 2\,\text{nm}$. We repeated our calculations with different spacings ($1\,\text{nm} \leqslant \Delta x \leqslant 20\,\text{nm}$) and found relative deviations <3%.

In case of a homogeneous microwave current density, the dissipation only depends on the number of vortices in the sample, not on their spatial distribution, cf. Eq. (1). Starting in the virgin state, the total amount of flux increases quadratically with applied field. Therefore, $\delta e^{\Uparrow}(B)$ also has a positive curvature. As expected for this field profile (see above), $\delta e^{\downarrow} > \delta e^{\Uparrow}$ and the minimum value of $\delta e^{\downarrow}$, which corresponds to the smallest amount of flux in the sample, is reached for a negative value of applied field.

In case of a highly inhomogeneous current distribution [Fig. 5(d)] only a small region near the edges of the center conductor is responsible for almost all of the dissipation, cf. Fig. 4(b). The flux density in this area is almost identical to B, hence the hysteresis is much smaller than in the homogeneous

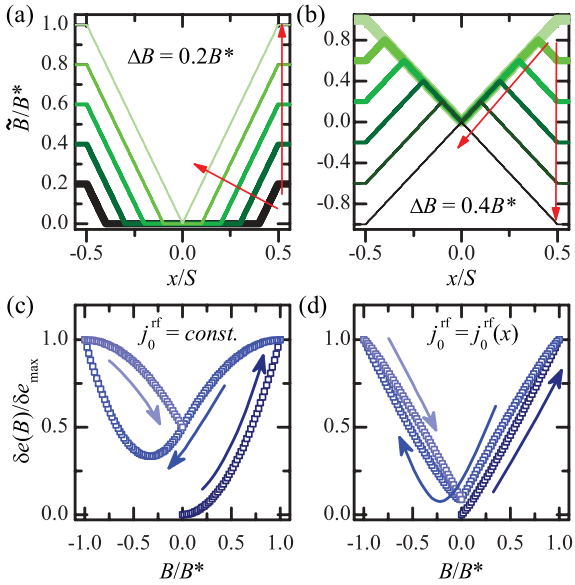

FIG. 5. (Color online) Classical Bean model flux density $\tilde{B}/B^*$ in a superconducting strip of width S during (a) the upsweep to $B = B^*$ ($B/B^* = 0.2, 0.4, 0.6, 0.8$, and 1) and (b) during downsweep from $B = B^*$ to $B = -B^*$ ($B/B^* = 1, 0.6, 0.2, -0.2, -0.6$, and -1); calculated $\delta e(B)/\delta e_{\max}$ during a magnetic field cycle $B/B^* = 0 \to 1 \to -1 \to 0$ assuming the classical Bean flux density and (c) a homogeneous as well as (d) a highly inhomogeneous microwave current density with $\lambda_{\text{eff}}/S = 0.002$. Arrows in (a) and (b) indicate the progression of the subsequent flux profiles; arrows in (c) and (d) indicate the sweep direction.

case. Although the hysteresis loop is significantly smaller, certain characteristic features of $\delta e(B)$ remain unchanged, such as the positive curvature of $\delta e^{\Uparrow}(B)$, the relation $\delta e^{\downarrow} > \delta e^{\Uparrow}$, and the fact that the position of the dissipation minimum during the downsweep is found at $B < 0$. Consequently, the classical Bean field profile does not properly describe the hysteresis as observed in our experiments.

An alternative model of the flux density distribution in thin film geometries was first considered by Norris[27] and later discussed by Brandt and Indenbom.[28] It is basically the aforementioned Bean model adapted to the geometry of thin superconducting strips in perpendicular magnetic fields. In this Norris-Brandt-Indenbom (NBI) model the flux density is given by

$$\tilde{B}^{\Uparrow}(x,B) = B_c \begin{cases} \tanh^{-1}\frac{\sqrt{(x-S')(x+S')}}{|x|\tanh(B/B_c)}, & \frac{S}{2} \geqslant |x| > S' \\ 0, & |x| \leqslant S', \end{cases} \quad (6)$$

where $S' = S/2\cosh(B/B_c)$, $B_c = \mu_0 d j_c/\pi$ is the characteristic field,[28] and j_c is the critical current density of the superconductor. Using the estimated $j_c \approx 5 \times 10^6\,\text{A/cm}^2$ of our Nb, we calculate $B_c \approx 6\,\text{mT}$. As can be seen from Eq. (6), the NBI model leads to an excess flux density at the edges of the strip compared to the classical Bean profile. The downsweep flux density $\tilde{B}^{\downarrow}(x,B)$ is again defined according to Eq. (5).

The NBI flux density profile is shown in Fig. 6(a) for several values of B during a field upsweep to $B = 3B_c$ and in Fig. 6(b) during the downsweep from $B = 3B_c$ to $B = -3B_c$. $\tilde{B}^{\downarrow}$ shows

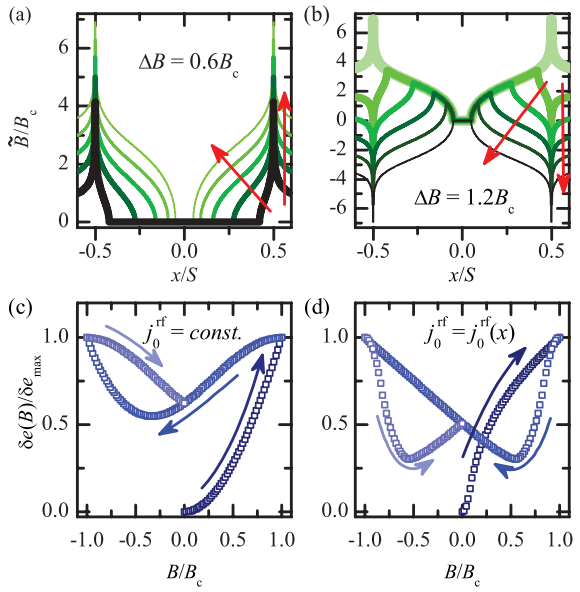

FIG. 6. (Color online) NBI model flux density $\tilde{B}/B_c$ in a superconducting strip of width S during (a) the upsweep to $B = 3B_c$ ($B/B_c = 0.6, 1.2, 1.8, 2.4$, and 3) and (b) during downsweep from $B = 3B_c$ to $-3B_c$ ($B/B_c = 3, 1.8, 0.6, -0.6, -1.8$, and -3). Calculated $\delta e(B)/\delta e_{max}$ during a magnetic field cycle $B/B_c = 0 \rightarrow 1 \rightarrow -1 \rightarrow 0$ assuming the NBI flux density and (c) a homogeneous as well as (d) a highly inhomogeneous microwave current density with $\lambda_L/S = 0.002$ and $d/S = 0.006$. Arrows in (a) and (b) indicate the progression of the flux profile, arrows in (c) and (d) indicate the sweep direction.

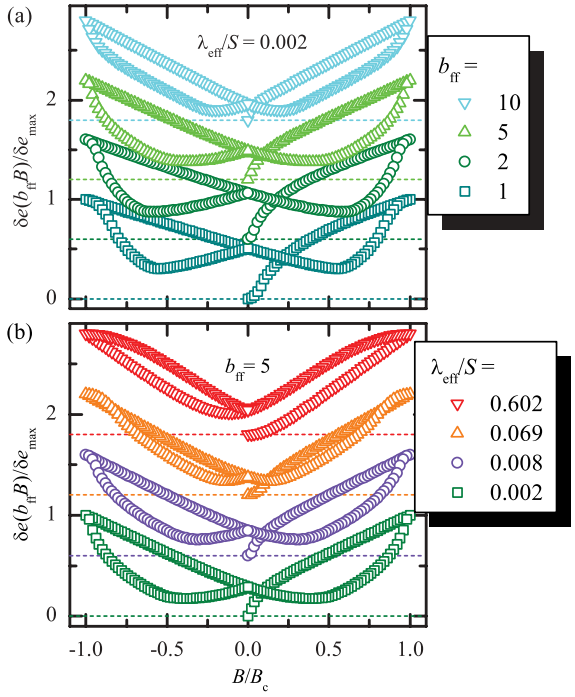

FIG. 7. (Color online) (a) $\delta e(b_{ff}B)/\delta e_{max}$ vs. external flux density B/B_c calculated for the NBI model with different flux-focusing factors b_{ff}. (b) $\delta e(b_{ff}B)/\delta e_{max}$ vs. cycled flux density B/B_c calculated for the NBI model for different ratios λ_{eff}/S. Adjacent curves are subsequently shifted by $+0.6$ for better visibility.

a remarkable behavior. For an externally applied field that is still positive, the flux density close to the edge of the thin film is already zero. When B is decreased further, $\tilde{B}^{\downarrow}$ at the film edge becomes negative and the point of zero flux density moves deeper into the sample, separating areas with antivortices from those with vortices.

To achieve comparability with experimental results, where $B_{max} = 4\,\text{mT}$, a field range of $|B| \lesssim B_c \approx 6\,\text{mT}$ was chosen for numerical calculations. Figures 6(c) and 6(d) show $\delta e(B)/\delta e_{max}$ for (c) a homogeneous and (d) a highly inhomogeneous current density. In the calculations we avoided the divergence of the NBI flux density at the strip edges by positioning them between two integration points, i.e., by effectively introducing a cutoff for $\tilde{B}$ at $\Delta x/2$ from the conductor edges. In case of $j_0^{rf}(x) = \text{const.}$, the NBI and the classical Bean model lead to similar $\delta e(B)/\delta e_{max}$ dependences, cf. Fig. 5(c), which—as already mentioned—disagree with our experimental data. For the inhomogeneous rf current distribution, however, $\delta e(B)/\delta e_{max}$ reproduces almost all characteristic features of the measured curve, cf. Figs. 3(a) and 6(d). In particular, the hysteresis loop has a butterfly like shape, where $\delta e^{\downarrow}(B) < \delta e^{\Uparrow}(B)$ for a considerable range of B. Also, $\delta e^{\Uparrow}(B)$ exhibits a predominantly negative curvature and the minimum of $\delta e^{\downarrow}(B)$ can be found at $B > 0$.

Yet, there is still a difference between experiment and theory. The slow increase of the losses at very small fields and the abrupt decrease immediately after the inversion of the sweep direction is clearly visible in experiment, but not in theory. Using the models described before, the curvatures $\partial^2\tilde{B}^{\Uparrow}(x)/\partial B^2$ at $B = 0$ and $\partial^2\tilde{B}^{\downarrow}(x)/\partial B^2$ at $B = B_{max}$ are directly linked, cf. Eq. (5). Therefore, there is always a symmetry between the first slow increase of the losses at the beginning of the upsweep and the slow decrease at the beginning of the downsweep. We believe that the asymmetry in experiment originates from the small but nonzero lower critical field B_{c1} of the superconductor, which is not included in the calculations. The existence of B_{c1} inherently leads to an asymmetry between the upsweep from the virgin state and any following sweep. The critical field value, however, at which the first vortex enters the superconductor, is not B_{c1}. It is moreover determined by the geometry of the sample and might be different for ground planes and center conductor. It also may depend on the position along the resonator.

In Fig. 7 the dependence of the hysteresis loop on the ratio λ_{eff}/S and the flux-focusing factor $b_{ff} = B_{eff}/B$ with the effective flux density B_{eff} is shown. Due to the ground planes, the flux density seen by the center conductor B_{eff} certainly is larger than the applied B. This is approximately taken into account by b_{ff}, where spatial variations of B_{eff} are neglected. Figure 7(a) shows $\delta e(b_{ff}B)/\delta e_{max}$ for $b_{ff} = 1, 2, 5$, and 10. All curves exhibit the same essential features of the hysteresis with some minor differences. With increasing b_{ff}, the field regions around $B = 0$ and $B = B_{max}$, where curvatures of $\delta e^{\Uparrow}$ and $\delta e^{\downarrow}$ change sign, become effectively compressed. Furthermore, the position of the downsweep minimum shifts with b_{ff}. By comparing calculations with experimental data, we find best qualitative agreement for a flux-focusing factor between $b_{ff} \approx 2$ and 5. Although the estimated value of $B_c \approx 6\,\text{mT}$ is comparable to $B_{max} = 4\,\text{mT}$ in experiment and a flux-focusing

factor of $b_{\rm ff} \approx 5$ seems reasonable, we would like to emphasize that the theoretical model presented in this paper is too simple to be used for a quantitative analysis of our experimental data.

Besides the flux-focusing factor, the homogeneity of the rf current distribution described by $\lambda_{\rm eff}/S$ determines the shape of the hysteresis loop. Figure 7(b) shows $\delta e(b_{\rm ff}B)/\delta e_{\rm max}$ for four different ratios $\lambda_{\rm eff}/S$, corresponding to current distributions shown in Fig. 4(b). Starting from $\lambda_{\rm eff}/S = 0.002$, which corresponds to our experimental conditions, the hysteresis loop becomes smaller with increasing homogeneity. For $\lambda_{\rm eff}/S \approx 0.069$ hardly any hysteresis can be seen. When $\lambda_{\rm eff}$ is increased further, up- and downsweep curves do not even cross anymore.

In our calculations we have assumed that the microwave current density and the flux profile (vortex density distribution) can be treated independently from each other. In general, however, the presence of a flux gradient leads to a redistribution of the transport current and vice versa.[28] Also, the oscillation amplitude of the vortices δx is assumed to be smaller than the length scale on which the current distribution varies, such that $j_0^{\rm rf}(x \pm \delta x) \approx j_0^{\rm rf}(x)$. We believe that both assumptions are reasonable, as in experiment the vortex associated losses $1/Q_v$ are almost independent of the applied microwave power, as long as $P_{\rm app} < 0\,{\rm dBm}$.[23] If the microwave self-field would significantly disturb and rearrange the static magnetic field configuration, e.g., by introducing additional vortices, we would expect nonlinearities,[41] which would lead to a power dependence of the losses.

Another simplification is the field-independent flux-focusing factor. In reality $b_{\rm ff}$ depends on B, which is only partially focused into the gaps of the coplanar waveguide; some of the flux also penetrates the superconductor in the form of Abrikosov vortices and this amount is field-dependent. Moreover, due to the geometry of our samples with a meandering resonator line, $b_{\rm ff}$ is expected to vary along the resonator. Consequently, also the losses δe depend on the position along the resonator.

Finally, we have not taken into account dissipation in the ground planes. If the vortices symmetrically penetrate the ground planes and the center conductor, the presence of ground planes would not affect the shape of the hysteresis at all but only increase the absolute values of the losses due to return currents at their edges. If there is an asymmetry in vortex penetration due to different demagnetizing factors of center conductor and ground planes, this can be viewed as equivalent to different flux-focusing factors for the ground planes and the center conductor. The resulting hysteresis of the whole system with ground planes would be a mixture of two slightly different hysteretic curves like those in Fig. 7(a). The influence of the ground plane losses, however, is in any case reduced by a factor $a/S \approx 2.2$ compared to the losses in the center conductor due to the smaller current density.[42]

In the experiments all the above mentioned effects are merged together, but we think that none of them fundamentally changes the observed and analyzed hysteretic behavior.

V. DEMAGNETIZATION AND TUNABILITY

In order to explore the possibility to return to the virgin state after magnetic cycling, we performed a demagnetization procedure, i.e., we repeatedly swept the magnetic field up and down with decreasing $B_{\rm max}$ and monitored the corresponding resonances. The procedure slightly differs from commonly used demagnetization cycles, as we kept the sweep rate $\partial B/\partial t$ constant, i.e., the period for one field cycle decreases with decreasing $B_{\rm max}$. The idea behind this procedure is based on the Bean and NBI model. Repeatedly sweeping the field up and down with decreasing $B_{\rm max}$ creates a sawtooth-like flux pattern in the superconductor, with a sawtooth amplitude, which depends on the difference $\Delta B_{\rm max} = |+B_{\rm max}| - |-B_{\rm max}|$ between consecutive extrema (here $\Delta B_{\rm max} = 0.16\,{\rm mT}$). During each second half cycle of this procedure Abrikosov antivortices are pushed into the sample almost as far as the vortices from the half cycle before reach. The field distribution at the end resembles narrow alternating regions of vortices and antivortices, whose density is determined by $\Delta B_{\rm max}$.

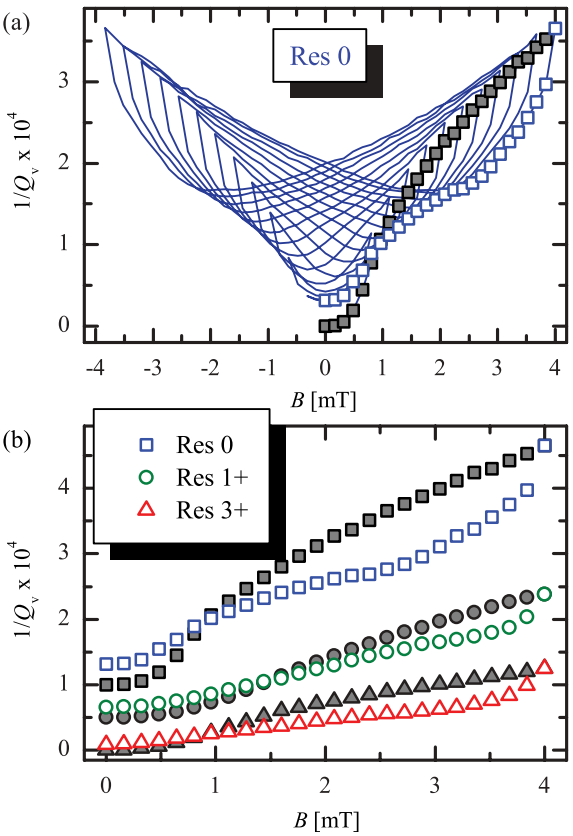

FIG. 8. (Color online) (a) $1/Q_v(B)$ of Res **0** ($n = 1$) during demagnetization (line); solid and open squares indicate the virgin field sweep and minimum values after virgin field sweep for $B \geqslant 0$, respectively; (b) $1/Q_v(B)$ of the resonators **3**+, **1**+ (hifted by $+5 \cdot 10^{-5}$), and **0** (shifted by $+1 \cdot 10^{-4}$) for the virgin field sweep (full symbols) and the minimum values after virgin field sweep (open symbols).

Figure 8(a) shows the measured energy losses $1/Q_v(B)$ during demagnetization (solid line). As can be seen with decreasing $B_{\rm max}$, the losses at $B = 0$ are decreasing and approach the virgin state value. The small but finite value for $1/Q_v$ after demagnetization is probably due to the presence of remanent (anti-)vortices, which were not annihilated during

the repeated cycles. To avoid nonequilibrium effects, we waited about one minute after each field step, i.e., a full demagnetization procedure took about one day.

The demagnetization curve in Fig. 8(a) shows that over almost the whole magnetic field range ($B \geqslant 1$ mT) the envelope of the full curve after the virgin field sweep, i.e., the minimum values of the vortex associated losses (open squares), lie considerably below the values of the virgin field sweep (full squares). This provides the opportunity to significantly reduce the losses of resonators or other microwave circuitry components operated in magnetic fields (e.g., when it comes to trapping of an ultracold atom cloud in the vicinity of a resonator) by proper choice of magnetic history. We are aware that the achievable reduction is small compared to other approaches such as using antidots or slots. However, for resonators patterned with antidots our procedure can be used to additionally improve the device performance as shown in Fig. 8(b), where we plot the virgin sweep data as well as the minimum values during demagnetization for the resonators **0**, **1**+, and **3**+. Although the losses are already significantly reduced in the resonators with antidots,[23] cycling in magnetic fields can further reduce $1/Q_v$ up to 30%. As can be seen in the next section, where we explicitly show data for resonator **3**+, also the shape of the hysteresis curves seems rather independent of the presence of antidots. By consulting our simple model, we can see how this somewhat surprising independence might be explained. The reasonable assumption that the antidots increase the mean pinning force acting on the vortices, i.e., increase the critical current density j_c, leads to a higher characteristic flux density B_c in the NBI model. For the calculated hysteresis curves, an increase of B_c is equivalent to a decrease of b_{ff}, which does not considerably change the nature of the hysteresis, as long as the change of b_{ff} is not too large, cf. Fig. 7(a). In reality, of course, the situation is probably more complicated, as the relatively large antidots will modify the flux density profiles more than just globally increasing j_c and a detailed analysis would be much more difficult.

The evolution of the resonance frequency f_{res} during demagnetization is depicted in Fig. 9(a). The variation in f_{res} covers a range of $\sim$1 MHz. For a quantification, we define the frequency tunability of the resonator as the difference between the maximum and the minimum resonance frequency $t_{\mathrm{res}} \equiv f_{\mathrm{res,max}} - f_{\mathrm{res,min}}$ for each value of B. The resulting $t_{\mathrm{res}}(B)$ of the three resonators with and without antidots is shown in Fig. 9(b) for $B \geqslant 0$. For all three resonators $t_{\mathrm{res}}(B) \approx 1$ MHz, almost independent of perforation and B, with a small tendency to increase with the number of antidots.

A tunability like this might be useful, e.g., for fine-tuning a superconducting cavity to the (fixed) transition frequencies of ultracold atom clouds. As for any value of B, each f_{res} value within the tunability range is accessible by at least two different histories, and as the maxima (minima) of the frequency (loss) hysteresis are not at the same field values, one has to check all possibilities to find the optimum combination of desired frequency and losses. As the exact parameters of the hysteresis slightly differ from device to device and probably from setup to setup, we cannot give a common recipe for finding the best working point here. Instead, each device has to be precharacterized in the corresponding experimental situation.

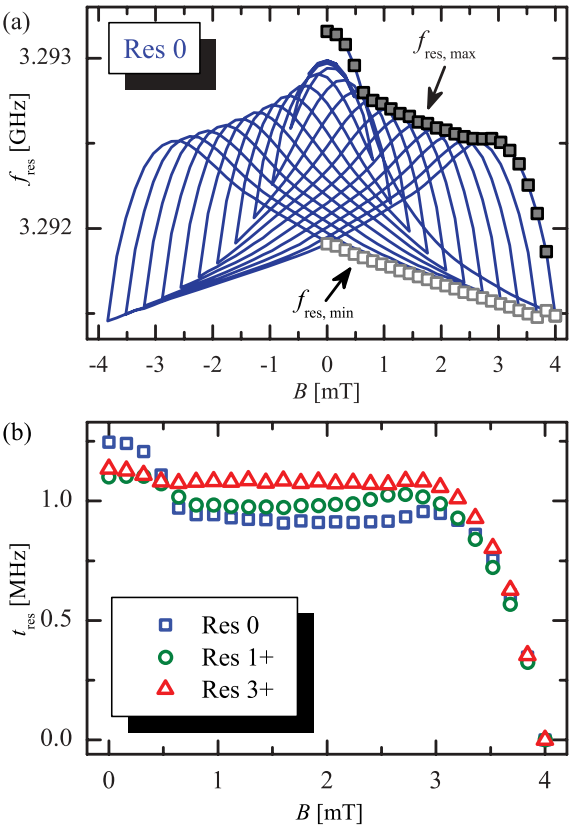

FIG. 9. (Color online) (a) Measured resonance frequency $f_{\mathrm{res}}(B)$ of Res **0** for a full demagnetization cycle (line) with maximum values (full squares) and minimum values (open squares) for positive magnetic fields; (b) Tunability $t_{\mathrm{res}}(B) = f_{\mathrm{res,max}}(B) - f_{\mathrm{res,min}}(B)$ of the resonators **3**+ (triangles), **1**+ (circles), and **0** (squares).

We emphasize that we do not propose to tune the properties of planar superconducting microwave components by just applying a magnetic field and introducing Abrikosov vortices here. If one just would like to fabricate a frequency tunable device for instance, other approaches with larger ranges and tunability velocities seem more promising.[43–45] However, if the microwave components have to be operated in specific magnetic fields anyway, magnetic history effects provide a nice additional possibility to reduce the losses and tune the resonance frequencies by spatially rearranging Abrikosov vortices.

VI. HIGHER MODES AND OTHER ANGLES

So far we have only considered the fundamental mode of our resonators and an operation in a perpendicular magnetic field. In the following we will present measurement results on higher modes and discuss the influence of the tilt angle α (cf. Fig. 4) between resonator plane and magnetic field on the hysteresis loop.

Figure 10 exemplarily shows the measured energy losses $1/Q_v(B)$ of resonator **3**+ for (a) the fundamental mode $n = 1$ and (b), (c), (d) the first three harmonics $n = 2,3,4$ in perpendicular magnetic fields. Clearly, the characteristic

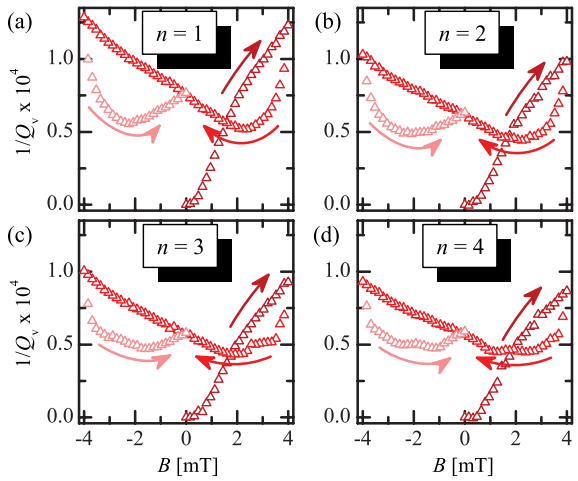

FIG. 10. (Color online) Measured vortex associated energy loss $1/Q_v(B)$ for the four lowest modes $n = 1$ to 4 of Res **3**+ for a full cycle of magnetic field.

features of the hysteresis loop can also be seen for higher modes.

Interestingly, with increasing frequency a fine structure within the hysteresis curves emerges; see, e.g., Fig. 10(d) at $B \approx \pm 1.5$ mT. This fine structure might be related to inhomogeneously distributed losses along the resonator. Depending on the resonator mode n, nodes and antinodes of the microwave current standing wave probe different parts of the resonator, i.e., they contribute differently to the overall losses. As already pointed out, there is a variation of the flux-focusing factor and, thus, the effective flux density along the resonator due to its geometry. The flux focusing is smaller in the meandering lines than in the straight part at the midpoint of the resonator, as the adjacent gaps of the meander allow for partial sharing of flux. Consequently, for different flux-focusing factors the downsweep minima might occur at different applied magnetic fields and the superposition of the $1/Q_v$ curves of several antinodes (which is what we measure) might lead to a fine structure on the hysteresis loop with multiple minima.

Figure 11 shows the measured $Q(B)$ of the fundamental mode of resonator **3**+ for three different angles. In perpendicular field, $\alpha = 90°$, we find the already described hysteresis with significantly increased Q (reduced $1/Q_v$) on the downsweep branch; see Fig. 11(a). For $\alpha < 90°$, the hysteresis loop hardly changes, as can exemplarily be seen in Fig. 11(b), where $\alpha \approx 15°$. Note that the field range is about four times larger than compared to the measurement with perpendicular orientation. The general shape of the hysteresis and the downsweep improvement in Q are very similar for both angles. As $\sin(15°) \approx 0.26$, this strongly suggests that the resonator losses are primarily determined by the component of B perpendicular to the sample.

The situation changes dramatically for $\alpha \approx 0°$, where the magnetic field was swept between ± 0.2 T, as can be seen in Fig. 11(c). For $B < 80$ mT the decrease in Q is relatively small and also reversible (not shown). When the magnetic field is increased further, the quality factor rapidly decreases. After sweep direction inversion, Q remains low until at $B \approx 50$ mT

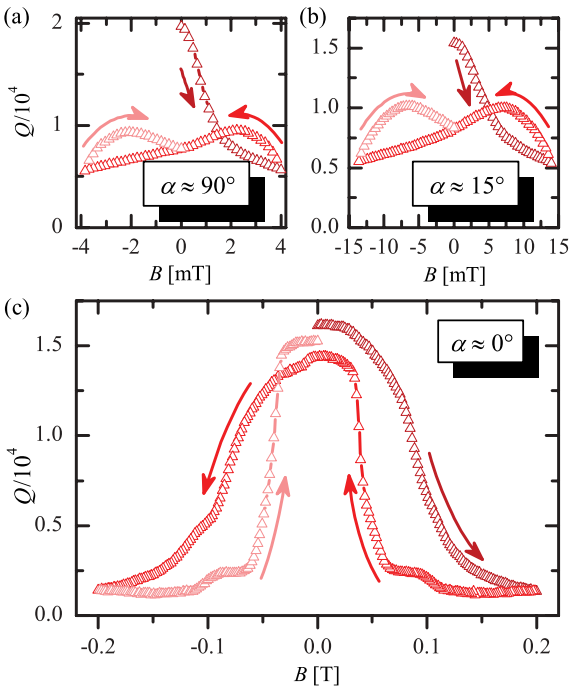

FIG. 11. (Color online) Typical measured hysteresis curves of the quality factor Q of the fundamental mode $n = 1$ (resonator 3+) during a full cycle of the magnetic field for three different angles (a) $\alpha = 90°$, (b) $\alpha \approx 15°$, and (c) $\alpha \approx 0°$ between resonator plane and applied field.

the quality factor increases and almost completely recovers to the original value of $Q(0)$. For negative fields we observe qualitatively the same behavior. It is also important to note that $Q^{\downarrow} \leqslant Q^{\Uparrow}$.

Interestingly, a comparison of measurement results with the theoretical curves presented in Sec. IV shows the best agreement with the prediction of the classical Bean model and not the NBI model; cf. Fig. 5. Although at first sight one would indeed expect the classical Bean model to be the adequate description for the flux density profile in this experimental situation (field parallel to a superconducting plane), one has to be careful with this interpretation for two reasons. First, one has to consider that the film thickness $d = 300$ nm is about three times the penetration depth ($\lambda_{\text{eff}} \approx 100$ nm) and, therefore, only 1.5 times the diameter of one Abrikosov vortex. Hence, the Bean model as a kind of a mean field theory might probably need a modification to properly describe the resonator losses in this case. The step-like structures in $Q(B)$ (e.g., at $B \approx \pm 0.1$ T) might reflect some kind of a discrete and nonsmooth flux entry into and exit out of the superconductor. Moreover, it is likely that the measured hysteresis is also partly the result of a small misalignment between the applied field and the resonator plane. At flux densities of $B \approx 100$ mT, an alignment error of only 0.5° already introduces a field of ≈1 mT perpendicular to the film, which is large enough to significantly reduce Q; cf. Fig. 11(a). Obviously, the hysteresis loop seems not to allow for reducing the microwave losses in the resonator if the magnetic field is applied close to parallel to the superconducting film.

VII. CONCLUSIONS

We experimentally investigated the properties of 3.3 GHz superconducting coplanar transmission line resonators in magnetic fields. In particular, we focused on resonators that were zero-field cooled to $T = 4.2$ K and then exposed to magnetic field cycles in the milli-Tesla range. We measured the resonance frequency f_{res} and quality factor Q of the resonators and found strong hysteresis effects, which on the mesoscopic scale are due to the presence of Abrikosov vortices in the superconducting film and their spatial redistribution during the field cycles. By using a simple model for the vortex-associated resonator losses, we shown that different combinations of microwave current and flux density distributions lead to characteristically different hysteresis loops. We find best agreement between experiment and theory for a current distribution that is strongly peaked at the resonator edges and with a modified Bean flux gradient for thin films, as described by Norris, Brandt, and Indenbom. We have also shown that the hysteresis may be used to improve the resonator performance for fixed values of applied magnetic field by proper choice of magnetic history. Accordingly, the resonance frequency can be tuned by about 1 MHz, i.e., for our resonators by a few zero-field linewidths at liquid Helium temperature. Both the reduction of the losses and the tunability of the frequency are found to be possible for resonators with and without antidots. Furthermore, we show that the hysteresis can also be found for higher modes $n = 2,3,4$ of the resonators and for angles between 90° and a few degrees between the field direction and the resonator plane. In the parallel field orientation, the hysteresis showed a very different behavior with presumably no possibility for a resonator improvement with magnetic history.

For many experiments in circuit quantum electrodynamics, superconducting resonators are operated in the Millikelvin and single photon regime. Hence, the effects presented here have to be investigated under these conditions in further studies. Still, there are no obvious reasons why the reported hysteresis effects should qualitatively change with decreasing temperature and power. Other parameters that are expected to change the nature of the hysteresis and that have to be considered for possible applications are the geometric dimensions of the transmission line and the thickness of the films, which together with the magnetic penetration depth have a strong influence on current distribution and flux density profile.

ACKNOWLEDGMENTS

This work has been supported by the Deutsche Forschungsgemeinschaft via the SFB/TRR 21 and by the European Research Council via SOCATHES. It was partly funded by the German Federal Ministry of Education and Research (Grant No. 01BQ1061). D.B. acknowledges support by the Evangelisches Studienwerk e.V. Villigst. M.K. acknowledges support by the Carl-Zeiss Stiftung. The authors thank Roger Wördenweber for fruitful discussions.

*daniel.bothner@uni-tuebingen.de

[1] C. P. Bean, Phys. Rev. Lett. **8**, 250 (1962).
[2] C. P. Bean, Rev. Mod. Phys. **36**, 31 (1964).
[3] A. Wallraff, D. I. Schuster, A. Blais, L. Frunzio, R.-S. Huang, J. Majer, S. Kumar, S. Girvin, and R. J. Schoelkopf, Nature (London) **431**, 162 (2004).
[4] M. Hofheinz *et al.*, Nature (London) **459**, 546 (2009).
[5] T. Niemczyk *et al.*, Nature Physics **6**, 772 (2010).
[6] L. DiCarlo *et al.*, Nature (London) **460**, 240 (2009).
[7] P. K. Day, H. G. LeDuc, B. A. Mazin, A. Vayonakis, and J. Zmuidzinas, Nature (London) **425**, 817 (2003).
[8] H. Wang *et al.*, Appl. Phys. Lett. **95**, 233508 (2009).
[9] P. Macha, S. H. W. van der Ploeg, G. Oelsner, E. Il'ichev, H.-G. Meyer, S. Wünsch, and M. Siegel, Appl. Phys. Lett. **96**, 062503 (2010).
[10] R. Barends, N. Vercruyssen, A. Endo, P. J. de Visser, T. Zijistra, T. M. Klapwijk, P. Diener, S. J. C. Yates, and J. J. A. Baselmans, Appl. Phys. Lett. **97**, 023508 (2010).
[11] T. Lindström, J. E. Healey, M. S. Colclough, C. M. Muirhead, and A. Y. Tzalenchuk, Phys. Rev. B **80**, 132501 (2009).
[12] P. Rabl, D. DeMille, J. M. Doyle, M. D. Lukin, R. J. Schoelkopf, and P. Zoller, Phys. Rev. Lett. **97**, 033003 (2006).
[13] A. Imamoglu, Phys. Rev. Lett. **102**, 083602 (2009).
[14] J. Verdú, H. Zoubi, C. Koller, J. Majer, H. Ritsch, and J. Schmiedmayer, Phys. Rev. Lett. **103**, 043603 (2009).
[15] K. Henschel, J. Majer, J. Schmiedmayer, and H. Ritsch, Phys. Rev. A **82**, 033810 (2010).
[16] P. Bushev *et al.*, Eur. Phys. J. D **63**, 9 (2011).
[17] J. Fortágh and C. Zimmermann, Science **307**, 860 (2005).
[18] P. Bushev, S. Stahl, R. Natali, G. Marx, E. Stachowska, G. Werth, M. Hellwig, and F. Schmidt-Kaler, Eur. Phys. J. D **50**, 97 (2008).
[19] C. Song, T. W. Heitmann, M. P. DeFeo, K. Yu, R. McDermott, M. Neeley, J. M. Martinis, and B. L. T. Plourde, Phys. Rev. B **79**, 174512 (2009).
[20] D. I. Schuster *et al.*, Phys. Rev. Lett. **105**, 140501 (2010).
[21] Y. Kubo, F. R. Ong, P. Bertet, D. Vion, V. Jacques, D. Zheng, A. Dréau, J.-F. Roch, A. Auffeves, F. Jelezko, J. Wrachtrup, M. F. Barthe, P. Bergonzo, and D. Esteve, Phys. Rev. Lett. **105**, 140502 (2010).
[22] C. Song, M. P. DeFeo, K. Yu, and B. L. T. Plourde, Appl. Phys. Lett. **95**, 232501 (2009).
[23] D. Bothner, T. Gaber, M. Kemmler, D. Koelle, and R. Kleiner, Appl. Phys. Lett. **98**, 102504 (2011).
[24] D. Bothner, C. Clauss, E. Koroknay, M. Kemmler, T. Gaber, M. Jetter, M. Scheffler, P. Michler, M. Dressel, D. Koelle, and R. Kleiner, Appl. Phys. Lett. **100**, 012601 (2012).
[25] C. Jooss, J. Albrecht, H. Kuhn, S. Leonhardt, and H. Kronmüller, Rep. Prog. Phys. **65**, 651 (2002).
[26] P. Lahl and R. Wördenweber, Appl. Phys. Lett. **81**, 505 (2002).
[27] W. T. Norris, J. Phys. D: Appl. Phys. **3**, 489 (1970).
[28] E. H. Brandt and M. Indenbom, Phys. Rev. B **48**, 12893 (1993).
[29] G. Hammer, S. Wuensch, M. Roesch, K. Ilin, E. Crocoll, and M. Siegel, Supercond. Sci. Technol. **20**, 408 (2007).
[30] P. Lahl and R. Wördenweber, IEEE Trans. Appl. Supercond. **13**, 2917 (2003).

[31]M. Bonura, E. Di Gennaro, A. Agliolo Gallitto, and M. Li Vigni, Eur. Phys. J. B **52**, 459 (2006).
[32]M. Bonura, A. Agliolo Gallitto, and M. Li Vigni, Eur. Phys. J. B **53**, 315 (2006).
[33]D. E. Oates, S.-H. Park, and G. Koren, Phys. Rev. Lett. **93**, 197001 (2004).
[34]M. Göppl, A. Fragner, M. Baur, R. Bianchetti, S. Filipp, J. M. Fink, P. J. Leek, G. Puebla, L. Steffen, and A. Wallraff, J. Appl. Phys. **104**, 113904 (2008).
[35]J. I. Gittleman and B. Rosenblum, J. Appl. Phys. **39**, 2617 (1968).
[36]E. H. Brandt, Phys. Rev. Lett. **67**, 2219 (1991).
[37]M. W. Coffey and J. R. Clem, Phys. Rev. Lett. **67**, 386 (1991).
[38]N. Klein, H. Chaloupka, G. Müller, S. Orbach, H. Piel, B. Rosa, L. Schultz, U. Klein, and M. Peiniger, J. Appl. Phys. **67**, 6940 (1990).
[39]A. I. Gubin, K. S. Ilin, S. A. Vitusevich, M. Siegel, and N. Klein, Phys. Rev. B **72**, 064503 (2005).
[40]A. G. Zaitsev, R. Schneider, R. Hott, Th. Schwarz, and J. Geerk, Phys. Rev. B **75**, 212505 (2007).
[41]M. A. Golosovsky, H. J. Snortland, and M. R. Beasley, Phys. Rev. B **51**, 6462 (1995).
[42]P. Lahl and R. Wördenweber, J. Appl. Phys. **97**, 113911 (2005).
[43]J. E. Healey, T. Lindström, M. S. Colclough, C. M. Muirhead, and A. Ya. Tzalenchuk, Appl. Phys. Lett. **93**, 043513 (2008).
[44]A. Palacios-Laloy, F. Nguyen, F. Mallet, P. Bertet, D. Vion, and D. Esteve, J. Low Temp. Phys. **151**, 1034 (2008).
[45]M. Sandberg, C. M. Wilson, F. Persson, T. Bauch, G. Johansson, V. Shumeiko, T. Duty, and P. Delsing, Appl. Phys. Lett. **92**, 203501 (2008).

Publication III

Reducing vortex losses in superconducting microwave resonators with microsphere patterned antidot arrays

D. Bothner,[1,a)] C. Clauss,[2] E. Koroknay,[3] M. Kemmler,[1] T. Gaber,[1] M. Jetter,[3] M. Scheffler,[2] P. Michler,[3] M. Dressel,[2] D. Koelle,[1] and R. Kleiner[1]
[1]*Physikalisches Institut and Center for Collective Quantum Phenomena in LISA$^+$, Universität Tübingen, Auf der Morgenstelle 14, D-72076 Tübingen, Germany*
[2]*1. Physikalisches Institut, Universität Stuttgart, Pfaffenwaldring 57, D-70550 Stuttgart, Germany*
[3]*Institut für Halbleiteroptik und Funktionelle Grenzflächen and Research Center SCoPE, Universität Stuttgart, Allmandring 3, D-70569 Stuttgart, Germany*

(Received 28 October 2011; accepted 10 December 2011; published online 4 January 2012)

We experimentally investigate the vortex induced energy losses in niobium coplanar waveguide resonators with and without quasihexagonal arrays of nanoholes (antidots), where large-area antidot patterns have been fabricated using self-assembling microsphere lithography. We perform transmission spectroscopy experiments around 6.25 GHz in magnetic field cooling and zero field cooling procedures with perpendicular magnetic fields up to $B = 27$ mT at a temperature $T = 4.2$ K. We find that the introduction of antidot arrays into resonators reduces vortex induced losses by more than one order of magnitude. © *2012 American Institute of Physics*. [doi:10.1063/1.3673869]

The importance of superconducting microwave circuitry devices has continuously grown during the last years. In particular, coplanar microwave resonators have become very popular and are used in various fields such as circuit quantum electrodynamics,[1–3] quantum information processing,[4] and kinetic inductance particle detection.[5] As low energy losses are an essential requirement to these resonators, there are currently many efforts to identify and minimize the individual dissipation mechanisms.[6–8] Most recently, it has been proposed to couple superconducting devices to trapped magnetic molecules, single electrons, or ultracold atom clouds,[9–13] which requires superconducting low-loss circuitry to be operated in magnetic environments.[14,15] However, operating type-II superconducting resonators in magnetic fields leads to considerable energy dissipation due to Abrikosov vortex motion.[16] Recently, some approaches have been made to reduce the vortex associated losses under special experimental conditions. Amongst others,[17,18] patterning the resonators with antidots, well-known and highly controllable pinning sites for Abrikosov vortices,[19,20] has shown promising results.[21] It was demonstrated that a few antidots with diameters on the micron scale, strategically positioned at the resonator edges, are able to significantly reduce vortex associated losses in zero field cooling (zfc) experiments with magnetic fields of ~10 G. In addition, we found that the losses decreased with increasing number of antidots. Thus, in order to expand the magnetic field range for the operation of the resonators, it is necessary to increase the antidot density and, at the same time, reduce the antidot diameter. In the past, there have been various approaches based on self-assembling techniques,[22–24] as they allow to cover the whole substrate area with a large amount of tiny antidots. Yet, for high-frequency applications, these techniques cannot be easily applied, as some of them depend on the substrate material[23,25] itself and most of them change the substrate properties during the fabrication process significantly.

In this letter, we adopt a different fabrication technique and demonstrate it to be feasible for patterning large area antidot lattices into superconducting microwave resonators. We use self-assembled polystyrene colloids as a quasi-hexagonal array of microlenses which can be used for the patterning of antidots by optical lithography.[26] Such patterned samples show vortex associated microwave losses in perpendicular magnetic fields $B \leq 27$ mT, which are more than one order of magnitude smaller than for reference samples without antidots. The presented results may also be relevant for other superconducting thin film microelectronic devices, e.g., kinetic inductance detectors, filters, or quantum interference devices, when operated in external magnetic fields.

The fabrication process starts with dc magnetron sputtering of a ~150 nm thick Nb layer onto a 2″ r-cut sapphire wafer. These Nb films have a critical temperature $T_c \approx 9$ K and a residual resistance ratio of $R_{300K}/R_{10K} \approx 6$. After cutting the wafer into single chips, lithography was performed. We covered the chips with photoresist and transferred a monolayer of water suspended polystyrene microspheres onto them in a Langmuir-Blodgett deposition process. The microspheres have an average diameter of 770 nm (± 25 nm) and act as microlenses for UV-light, leading to a focused energy density directly below each sphere and, thus, after development to a quasihexagonally arranged hole pattern. With reactive ion etching (SF_6), the hole array was transferred into the Nb film.

Electric transport measurements on test structures with antidots, which were performed close to T_c, showed pronounced matching effects. From these measurements, we estimate the antidot density to $n_p \approx 1.65\,\mu\text{m}^{-2}$. A detailed discussion of these results together with a deeper analysis of the properties of the self organized quasi-hexagonal antidot lattice will be given elsewhere.

Into the perforated as well as plain Nb films, we patterned half wavelength transmission line resonators with a

[a)]Author to whom correspondence should be addressed. Electronic mail: daniel.bothner@uni-tuebingen.de.

resonance frequency $f_{res} \approx 6.25$ GHz using standard optical lithography and reactive ion etching (SF_6). The resonators are capacitively and symmetrically coupled to feed lines via gaps at both ends. For this study, we fabricated two types of resonators with the same general layout and length, but with different widths of the center conductor ($S_1 = 20\,\mu$m, $S_2 = 60\,\mu$m), of the gap between center conductor and ground planes ($W_1 = 8\,\mu$m, $W_2 = 25\,\mu$m) and of the coupling gaps ($G_1 = 10\,\mu$m, $G_2 = 30\,\mu$m). Both designs result in a characteristic impedance of the transmission line $Z_0 \approx 50\,\Omega$. Figure 1 shows (a) the resonator layout (parameter set 2) and (b) a partial AFM image of a resonator with antidots (parameter set 1).

For the characterization of the resonators, we mounted each of them into brass boxes and contacted them with silver paste to sub-miniature A (SMA) stripline connectors (signal line/center conductor) and the box (ground planes). We determined the frequency dependent transmitted power P_{trans} with a spectrum analyzer for different values of perpendicularly applied magnetic field $|B| \leq 27$ mT at a temperature $T = 4.2$ K. No attenuators or amplifiers were used in the measurements, but due to cable and connector losses, we estimate the effective power at the resonator input to be at least 10 dB lower than at the generator output, to which all values of the variable applied power P_{app} refer. We fit each resonance curve $P_{trans}(f)$ with a Lorentzian, from which we extract the resonance frequency $f_{res}(B)$ and the width of the resonance at half maximum $\Delta f(B)$. This allows us to calculate the quality factor $Q(B) = f_{res}(B)/\Delta f(B)$ and, alternatively, the energy loss $1/Q(B)$. In general, the overall losses $1/Q(B)$ are the result of different (field independent and field dependent) loss mechanisms such as dielectric, resistive, or radiative losses. The quantity $1/Q_v(B) = 1/Q(B) - 1/Q(0)$ allows us to extract the field dependent contribution, which we associate with Abrikosov vortices, cf. also Refs. 16 and 21. Similarly, we calculate the relative frequency shift due to the magnetic field $\delta f(B)/f_0 = (f_0 - f_{res}(B))/f_0$ with $f_0 = f_{res}(B = 0)$.

In one measurement series, we performed field cooling (fc) experiments, i.e., we apply each magnetic field value at a temperature above T_c and, subsequently, cool down the resonator below T_c. With this procedure, the vortices are expected to be nearly homogeneously distributed within the film.

Figure 2 compares (a) $1/Q_v(B)$ and (b) $\delta f(B)/f_0$ for the fundamental mode $n = 1$ of two resonators with identical parameters (set 2): one with and one without antidots. The resonator with antidots shows more than one order of magnitude lower losses (maximum factor ~40) and an about one order of magnitude reduced frequency shift (maximum factor ~11) than its plain counterpart over the whole investigated field range. We attribute this strong reduction of the vortex response to an effective trapping and pinning of vortices by the antidots. Note, that the first data point in Fig. 2 corresponds to $B = 0.45$ mT, i.e., to about 10 times Earth magnetic field, which is already well above the field range investigated in Ref. 18. In what we refer to as zero field here, that is, in Earth magnetic field and possible remanent fields in our setup, the resonators showed a comparable absolute quality factor of several thousands.

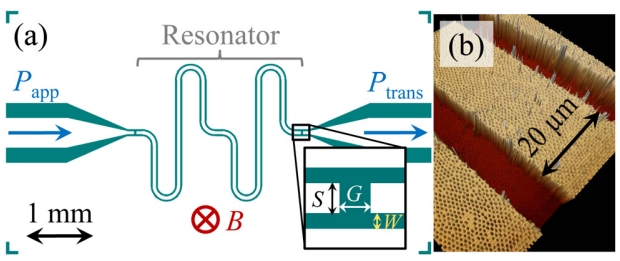

FIG. 1. (Color online) (a) Layout of a 7×4 mm^2 chip with a capacitively coupled 6.25 GHz transmission line resonator (parameter set 2). (b) AFM image of a part of a resonator perforated with antidots (parameter set 1).

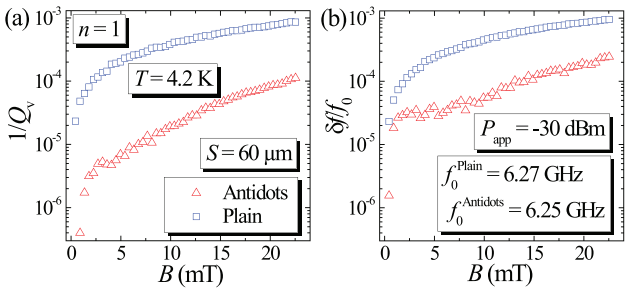

FIG. 2. (Color online) Comparison of (a) the vortex associated energy losses $1/Q_v(B)$ and (b) the relative frequency shift $\delta f(B)/f_0$ in fc measurements for the fundamental mode $n = 1$ of a perforated resonator (triangles) and a plain resonator (squares) with identical design parameters (set 2).

We also performed measurements for higher resonator modes, i.e., $n = 2,3$, and for resonators with parameter set 1 which all showed similar results. At higher frequencies, however, we were only able to reliably determine the losses for a somewhat smaller field range ($\lesssim 15$ mT) than for $n = 1$ due to a combination of suppressed cavity resonances and the appearance of parasitic ones.

In another set of experiments, resonators were cooled down to $T = 4.2$ K in $B = 0$ before applying a magnetic field. Here, the vortices are expected to penetrate the superconductor with a Bean-like flux profile,[27] which leads to an *enhanced* flux density close to the edges of the Nb structures. Figure 3 shows the vortex associated losses $1/Q_v(B)$ of (a) two resonators with parameter set 1 and (b) two resonators with parameter set 2. Within each parameter set, we compare a resonator with antidots to a plain one.

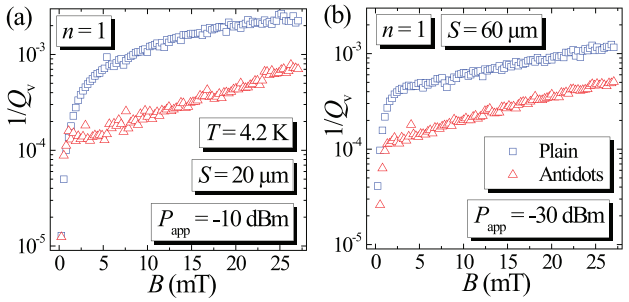

FIG. 3. (Color online) Vortex associated energy losses $1/Q_v(B)$ for zfc measurements of two resonators with (a) parameter set 1 and (b) parameter set 2. One resonator of each parameter set was patterned with antidots (red triangles), and one was not (blue squares).

We find higher losses $1/Q_v(B)$ than in the corresponding fc measurements. This result, which *prima facie* is somehow counterintuitive, since the number of vortices within the superconductor is smaller for the zfc than for the fc case, has already been reported before.[28,29] It can be explained by the inhomogeneous flux distribution for the zfc situation which has its maximum near the Nb film edges. Since the microwave current density is also higher at the edges, this leads to increased losses $1/Q_v(B)$ when compared to the field-cooled case.

In the zfc case, for both parameter sets, the resonator with antidots shows significantly reduced losses $1/Q_v(B)$ over the whole field range (up to a factor of about 6). Yet, the absolute values of $1/Q_v(B)$ are higher for resonators with parameter set 1 than those of parameter set 2. There are two possible mechanisms, which may explain this observed behavior. As parameter set 1 corresponds to smaller gaps between the center conductor and the ground planes, the flux focusing and, hence, the effective flux density seen by the resonator are higher. The other mechanism reveals itself by occasionally observable sudden jumps in the transmitted power corresponding to a small shift of the resonance curve which are an indication for the appearance of flux avalanches[29] (also represented in the noise of $1/Q_v(B)$). Those flux avalanches reduce the flux density at the conductor edges by transporting flux towards the center of the conductor, where the microwave current density is considerably smaller. Obviously, the flux can be transported farther away from the edges for the case of a wider center conductor. Therefore, flux avalanches in resonators with parameter set 2 may result in a stronger flux reduction at the edges of the center conductor than in resonators with parameter set 1.

In conclusion, we have used microsphere photolithography for the fabrication of large area periodic micron-sized antidot arrays in superconducting thin film microwave devices to significantly improve the device performance in magnetic fields. We have demonstrated, that energy losses in superconducting microwave resonators due to the presence of Abrikosov vortices can be reduced by more than one order of magnitude with quasihexagonal antidot arrays. We have shown this result to be valid for magnetic fields up to at least $B \approx 27\,\mathrm{mT}$ for fc procedures as well as for zfc measurements.

This work has been supported by the DFG via SFB/TRR 21 and by the ERC via SOCATHES. D.B. acknowledges support by the Evangelisches Studienwerk e.V. Villigst. M. K. acknowledges support by the Carl-Zeiss Stiftung.

[1]A. Wallraff, D. I. Schuster, A. Blais, L. Frunzio, R.-S. Huang, J. Majer, S. Kumar, S. Girvin, and R. J. Schoelkopf, Nature (London) **431**, 162 (2004).
[2]M. Hofheinz, H. Wang, M. Ansmann, R. C. Bialczak, E. Lucero, M. Neeley, A. D. O'Connell, D. Sank, J. Wenner, J. M. Martinis *et al.*, Nature (London) **459**, 546 (2009).
[3]T. Niemczyk, F. Deppe, H. Huebl, E. P. Menzel, F. Hocke, M. J. Schwarz, J. J. Garcia-Ripoll, D. Zueco, T. Hümmer, E. Solano *et al.*, Nat. Phys. **6**, 772 (2010).
[4]L. DiCarlo, J. M. Chow, J. M. Gambetta, L. S. Bishop, B. Johnson, D. I. Schuster, J. Majer, A. Blais, L. Frunzio, S. M. Girvin *et al.*, Nature (London) **460**, 240 (2009).
[5]P. K. Day, H. G. LeDuc, B. A. Mazin, A. Vayonakis, and J. Zmuidzinas, Nature (London) **425**, 817 (2003).
[6]H. Wang, M. Hofheinz, J. Wenner, M. Ansmann, R. C. Bialczak, M. Lenander, E. Lucero, M. Neeley, A. D. O'Connell, D. Sank *et al.*, Appl. Phys. Lett. **95**, 233508 (2009).
[7]P. Macha, S. H. W. van der Ploeg, G. Oelsner, E. Il'ichev, H.-G. Meyer, S. Wünsch, and M. Siegel, Appl. Phys. Lett. **96**, 062503 (2010).
[8]T. Lindström, J. E. Healey, M. S. Colclough, C. M. Muirhead, and A. Y. Tzalenchuk, Phys. Rev. B **80**, 132501 (2009).
[9]P. Rabl, D. DeMille, J. M. Doyle, M. D. Lukin, R. J. Schoelkopf, and P. Zoller, Phys. Rev. Lett. **97**, 033003 (2006).
[10]A. Imamoglu, Phys. Rev. Lett. **102**, 083602 (2009).
[11]J. Verdú, H. Zoubi, C. Koller, J. Majer, H. Ritsch, and J. Schmiedmayer, Phys. Rev. Lett. **103**, 043603 (2009).
[12]K. Henschel, J. Majer, J. Schmiedmayer, and H. Ritsch, Phys. Rev. A **82**, 033810 (2010).
[13]P. Bushev, D. Bothner, J. Nagel, M. Kemmler, K. B. Konovalenko, A. Loerincz, K. Ilin, M. Siegel, D. Koelle, R. Kleiner *et al.*, Eur. Phys. J. D **63**, 9 (2011).
[14]J. Fortágh and C. Zimmermann, Science **307**, 860 (2005).
[15]P. Bushev, S. Stahl, R. Natali, G. Marx, E. Stachowska, G. Werth, M. Hellwig, and F. Schmidt-Kaler, Eur. Phys. J. D **50**, 97 (2008).
[16]C. Song, T. W. Heitmann, M. P. DeFeo, K. Yu, R. McDermott, M. Neeley, J. M. Martinis, and B. L. T. Plourde, Phys. Rev. B **79**, 174512 (2009).
[17]D. I. Schuster, A. P. Sears, G. Ginossar, L. DiCarlo, L. Frunzio, J. J. L. Morton, H. Wu, G. A. D. Briggs, B. B. Buckley, D. D. Awschalom *et al.*, Phys. Rev. Lett. **105**, 140501 (2010).
[18]C. Song, M. P. DeFeo, K. Yu, and B. L. T. Plourde, Appl. Phys. Lett. **95**, 232501 (2009).
[19]A. T. Fiory, A. F. Hebard, and R. P. Minnich, J. Phys. Colloq. **39**, 633 (1978).
[20]R. Wördenweber, P. Dymashevski, and V. R. Misko, Phys. Rev. B **69**, 184504 (2004).
[21]D. Bothner, T. Gaber, M. Kemmler, D. Koelle, and R. Kleiner, Appl. Phys. Lett. **98**, 102504 (2011).
[22]W. Vinckx, J. Vanacken, and V. V. Moshchalkov, J. Appl. Phys. **100**, 044307 (2006).
[23]U. Welp, Z. L. Xiao, J. S. Jiang, V. K. Vlasko-Vlasov, S. D. Bader, G. W. Crabtree, J. Liang, H. Chik, and J. M. Xu, Phys. Rev. B **66**, 212507 (2002).
[24]J. Eisenmenger, M. Oettinger, C. Pfahler, A. Plettl, P. Walther, and P. Ziemann, Phys. Rev. B **75**, 144514 (2007).
[25]O. Jessensky, F. Müller, and U. Gösele, Appl. Phys. Lett. **72**, 1173 (1998).
[26]W. Wu, D. Dey, O. G. Memis, A. Katsnelson, and H. Mohseni, Nanoscale Res. Lett. **3**, 351 (2008).
[27]E. H. Brandt and M. Indenbom, Phys. Rev. B **48**, 12893 (1993).
[28]P. Lahl and R. Wördenweber, IEEE Trans. Appl. Supercond. **13**, 2917 (2003).
[29]G. Ghigo, F. Laviano, L. Gozzelino, R. Gerbaldo, E. Mezzetti, E. Monticone, and C. Portesi, J. Appl. Phys. **102**, 113901 (2007).

Publication IV

nature COMMUNICATIONS

ARTICLE

Received 25 Mar 2013 | Accepted 31 Jul 2013 | Published 29 Aug 2013

DOI: 10.1038/ncomms3380

Manipulation and coherence of ultra-cold atoms on a superconducting atom chip

Simon Bernon[1,*,†], Helge Hattermann[1,*], Daniel Bothner[1], Martin Knufinke[1], Patrizia Weiss[1], Florian Jessen[1], Daniel Cano[1], Matthias Kemmler[1], Reinhold Kleiner[1], Dieter Koelle[1] & József Fortágh[1]

The coherence of quantum systems is crucial to quantum information processing. Although superconducting qubits can process quantum information at microelectronics rates, it remains a challenge to preserve the coherence and therefore the quantum character of the information in these systems. An alternative is to share the tasks between different quantum platforms, for example, cold atoms storing the quantum information processed by superconducting circuits. Here we characterize the coherence of superposition states of ^{87}Rb atoms magnetically trapped on a superconducting atom chip. We load atoms into a persistent-current trap engineered next to a coplanar microwave resonator structure, and observe that the coherence of hyperfine ground states is preserved for several seconds. We show that large ensembles of a million of thermal atoms below 350 nK temperature and pure Bose–Einstein condensates with 3.5×10^5 atoms can be prepared and manipulated at the superconducting interface. This opens the path towards the rich dynamics of strong collective coupling regimes.

[1] CQ Center for Collective Quantum Phenomena and their Applications in LISA$^+$, Physikalisches Institut, Eberhard-Karls-Universität Tübingen, Auf der Morgenstelle 14, D-72076, Tübingen, Germany. * These authors contributed equally to this work. † Present address: Quantronics Group, SPEC (CNRS URA 2464), IRAMIS, DSM, CEA-Saclay, 91191 Gif-sur-Yvette, France. Correspondence and requests for materials should be addressed to J.F. (email: fortagh@uni-tuebingen.de).

The quantum physics of interfaces is attracting great interest because quantum state transfer between subsystems is required for quantum measurements, quantum information processing and quantum communication[1]. To overcome the fast decoherence of superconducting qubits, the engineering of various hybrid quantum systems recently became a subject of intensive research[2–8]. The success of strong coupling between superconducting two-level systems and microwave cavities[9], the implementation of quantum algorithms with superconducting circuits[10–12] and the successful realization of superconducting surface traps for ultra-cold atoms[13–15] encourage the development of superconductor/cold atom hybrids. So far, some fundamental interactions between the two systems have been observed[15–17]. However, coherent coupling between the systems remains a scientific and technological challenge. Although theoretical proposals suggest using atomic ensembles as quantum memories in a hybrid quantum computer[18–20], the trapping of atoms in the vicinity of a superconducting coplanar microwave resonator (CPR) is still required.

Long coherence times and state transfer are central issues for quantum information processing. In cold atomic ensembles, the fine control of inhomogeneous dephasing sources[21,22] allows long storage times of a single collective excitation[23]. A similar control in chip-based trapped atomic clocks[24] allowed to preserve coherent states of rubidium hyperfine levels over tens of seconds[25]. In addition, the energy spectrum of rubidium atoms can be used to convert the quantum information to the near infrared, in the telecom band[22], where long-distance quantum communication can be realized[26]. Hybrid systems of cold atoms and superconductors are therefore very appealing for a solid state, atomic and photonic quantum interface. Nevertheless, the question how to preserve such coherence and optical properties in the complex environment of a hybrid system needs to be solved.

Here, we report on the preparation of coherent atomic samples at a superconducting interface. We load ultra-cold ^{87}Rb atoms into a magnetic trap generated by a superconducting niobium thin film structure. We measure exceptionally long lifetimes of fully spin-polarized states (>4 min). In either of the hyperfine ground states of rubidium, we reach the critical temperature of Bose – Einstein condensation with more than one million atoms. The coherence of the superpositions of these ground states is measured for various positions on the superconducting interface. In a self-centred persistent-current trap engineered in the vicinity of a CPR we observe a coherence time $T_2 \sim 8$ s. This demonstrates that cold atom trap inhomogeneities can be controlled in this complex environment to a metrological level, paving the way towards long-living single excitations.

Results

Experimental apparatus. The experimental apparatus combines a cryostat (Janis ST-400, 2 W cooling power) holding a superconducting atom chip and a cold atom setup integrated in a single ultrahigh vacuum chamber (Fig. 1a). The pressure of the chamber, as measured by an ion gauge, is $\sim 10^{-11}$ mbar. Owing to the strong cryopumping, the pressure close to the chip surface is probably even lower. Such vacuum constitutes an excellent heat isolation between the superconducting chip surface at a temperature of $T = 4.2$ and the room temperature electromagnets that are used for the preparation of cold atomic samples[27]. A copper radiation shield at ~ 20 K protects the chip from the room temperature thermal radiation. A slit of 2 mm height on the shield gives optical access to an optical tweezers that transports atom clouds from the room temperature environment to the superconducting atom chip.

The superconducting chip with Z-shaped wires (red line) and a quarter-wave CPR structure is shown in Fig. 1b,c. The niobium film structures (500 nm thickness) were fabricated on monocrystalline sapphire by magnetron sputtering, optical lithography and reactive ion etching (SF_6). Niobium is, in our experimental conditions, a type II superconductor with a transition temperature of 9.2 K. At 4.2 K, the wires carry mean current densities of up to 4×10^6 A cm^{-2}, corresponding to a current of 1 A for a wire of 50 μm width. Supply wires (normal conducting copper) are connected by ultrasonic soldering to the niobium. The sapphire substrate is similarly soldered to the copper mount of the cryostat. Two superconducting wires of 100 μm diameter pass below the chip and help to maintain the longitudinal confinement of the trap (Fig. 1b).

The preparation of atomic clouds follows the standard techniques of magneto-optical (MOT) and magnetic trapping (see Methods for details) and leads, in the room temperature environment, to a cold cloud of 5×10^6 atoms at $T < 1.5$ μK. After transfer to an optical dipole trap, the cloud is transported into the cryogenic environment to the loading position at ~ 400 μm from the superconducting chip surface. The atoms are then transferred into a harmonic magnetic trap[28] formed by superposing the field generated by the current $I_{\mathrm{Trap}} = 0.8$ A driven through the largest Z-shaped trapping wire with a homogeneous magnetic bias field $B_{\mathrm{bias}} = 4$ G applied along y and a magnetic offset field $B_{\mathrm{off}} = 0.6$ G applied along x. The atoms loaded are then adiabatically compressed in a trap with oscillation frequencies $\{\omega_x, \omega_y, \omega_z\}/2\pi = \{19{,}145{,}128\}$ Hz and subsequently cooled by radio-frequency (RF) forced evaporation to temperatures of ~ 200 nK. By changing the length of the initial MOT phase (1–10 s), the atom number in the superconducting trap (10^4–10^6) and the final state (thermal cloud or Bose – Einstein condensate (BEC)) can be conveniently controlled without affecting the temperature. Owing to the strong cryopumping and the suppression of thermally driven magnetic field fluctuations[17], the lifetimes of the atoms in such a surface trap are predicted to be exceptionally long[29–31]. For a cloud of $N_{\mathrm{at}} = 10^5$ atoms polarized in state $|F = 1, m_F = -1\rangle$ (Fig. 1f) at a density of 10^{13} at cm^{-3} held in the compressed trap with an offset field $B_{\mathrm{off}} = 0.6$ G, we measure a lifetime of more than 4 min. From this result and the lifetime of 10 min obtained in Emmert *et al.*[32], we expect excellent vacuum conditions for sub-kelvin cryostats where both cold atoms and superconducting circuits will behave quantum mechanically.

We form pure BECs with up to 3.5×10^5 atoms in either of the spin states, $|F = 1, m_F = -1\rangle$ or $|F = 2, m_F = 2\rangle$. The lifetime of such a condensate in the $|F = 1, m_F = -1\rangle$ state in a trap with frequencies $\{15, 72, 43\}$ Hz is 30(3) s and is density limited by three-body collisional losses[33]. Such high atom number BECs are of special interest for superradiance experiments, for the realization of an on-chip maser[34] and for quantum information protocols in which an effective strong coupling regime is reached by a collective enhancement[20]. For the latter a BEC is not mandatory. It could be better positioned than a thermal cloud but would suffer from a lower atom number and related weaker collective enhancement.

In the following, we explore the properties of the cold cloud in the vicinity of the superconducting CPR. We first consider the positioning of atoms in the close vicinity of the CPR, where we additionally engineer a persistent-current trap. As a further step, we study the coherence of atomic superposition states in different positions of the CPR mode volume. The resonator used in this report is designed to be 250 MHz off resonance from any hyperfine transitions and should therefore not affect the internal state dynamics of the atoms.

Positioning of atomic clouds into a CPR. In a CPR, the electromagnetic fields are concentrated in the gaps between the ground

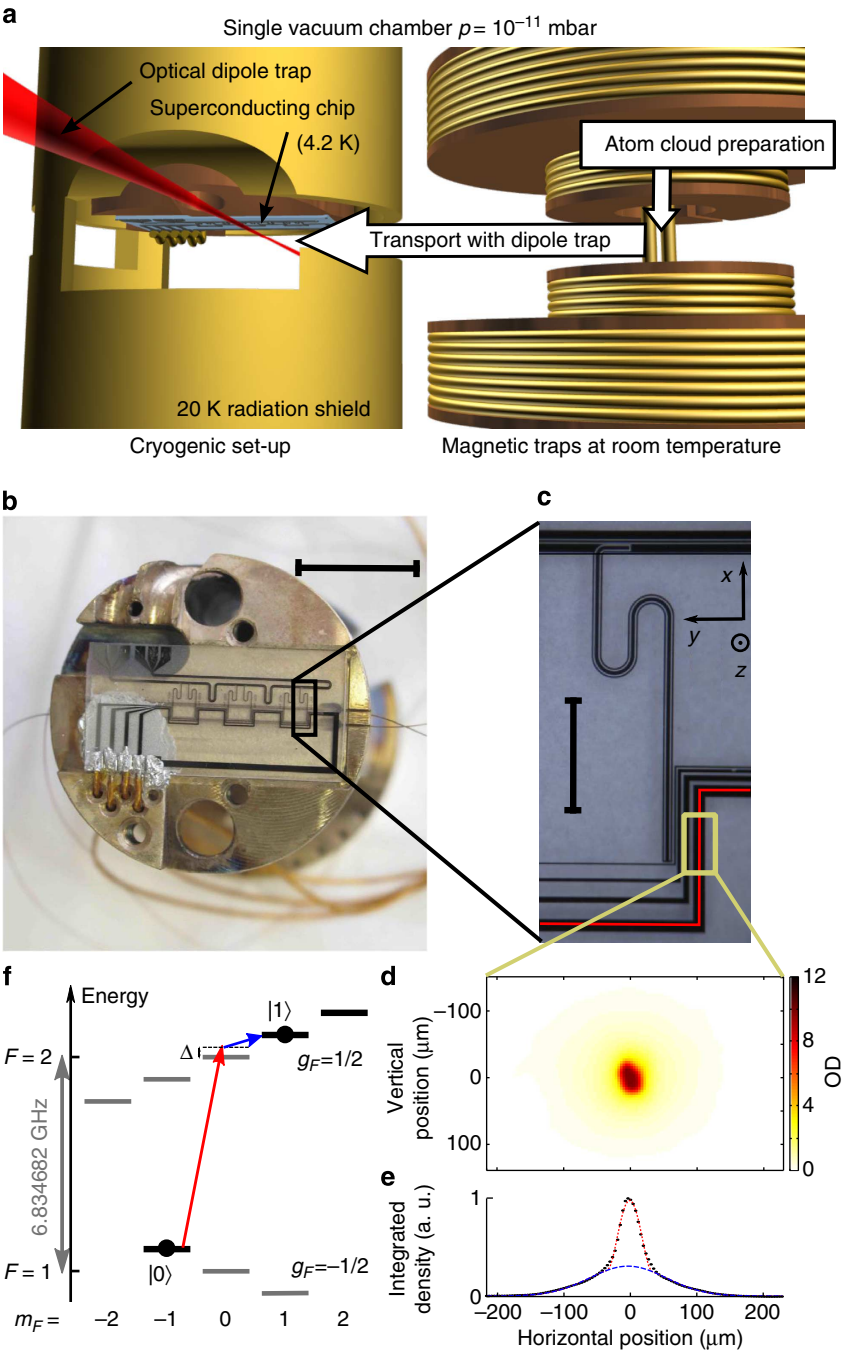

Figure 1 | Hybrid system of ultra-cold atoms and superconductors. (**a**) *In-vacuo* setup (to scale): on the right side, the atoms are trapped and cooled in a room temperature environment. The left part shows the superconducting chip attached to the cryostat at 4.2 K and surrounded by a gold-plated radiation shield at ~20 K. The atoms are transported from one environment to the other (40 mm distance) by optical tweezers. (**b**) Photograph of the superconducting atom chip mounted onto an oxygen-free copper holder. Scale bar, 1 cm. (**c**) Microscope image of the superconducting trapping structure. Visible are four *Z*-wires for trapping, one being highlighted by the red line and a quarter-wave CPR capacitively coupled to the feedline. Scale bar, 1 mm. (**d**) Absorption image of a BEC in state $|0\rangle$ with $N_{BEC} = 3 \times 10^5$ atoms after 15 ms TOF. Colour scale corresponds to optical density (OD). (**e**) Normalized integrated density showing the bi-modal structure of a BEC (black points). In dashed blue is shown a fit to the thermal background and in dotted red a fit to the central Thomas Fermi profile. (**f**) Energy diagram of ^{87}Rb in a magnetic field. In dark are shown the three magnetically trappable states. The coupling of $|F=1, m_F=-1\rangle$ ($|0\rangle$) and $|F=2, m_F=1\rangle$ ($|1\rangle$) is realized by a two-photon transition.

planes and the central conductor. To maximize the atom–cavity coupling, atoms need to be positioned in the close vicinity of these gaps. Nevertheless, for trap-wire distances smaller than the wire width, the trapping parameters are significantly affected by the Meissner–Ochsenfeld effect (MOE)[16,35]. To limit such deformations in the vicinity of the CPR, the design shown in Fig. 1c includes four *Z*-shaped wires with widths ranging from 100 to 15 μm. Starting from the largest *Z*-wire trap, the atoms are first horizontally transferred to the third *Z*-wire trap. The fourth and last wire (15 μm width) revealed to be unnecessary. At 100 μm below the third trapping wire, the trap needs to be rotated towards the CPR gap. Two parameters are classically used to

manipulate the atoms on a chip; the value of the trapping wire current modifies the trap-wire distance and the direction of the bias field rotates the trap around the trapping wire. Because of the MOE, positioning that is straightforward for a normal conducting chip is more subtle for a superconducting atom chip. In the present case, we take advantage of the conservation of magnetic flux in superconducting loops to directly guide the atoms below the gap of the CPR.

The design of the quarter-wave CPR includes a superconducting loop formed by the ground planes of the resonator (blue in Fig. 2). When a field perpendicular to the substrate is applied, such as the bias field, a screening current is induced in the ground planes and ensures the conservation of the magnetic flux in this superconducting loop. Such a current, that circulates just next to the gap, generates a magnetic field profile that guides the atoms into the gap. At distances comparable to the width of the ground planes, such guiding is further enhanced by the MOE that focuses magnetic field lines and generates magnetic gradients that centre the cloud in the gap. The guiding of atoms into the gap is observed by *in situ* measurements of the position of the atomic cloud for different bias field orientations (angle α in Fig. 3a) and different currents in the wire (Fig. 3a). For each experimental point, the cloud is first brought to a trap-wire distance of $\sim$100 µm, rotated to the angle α and then moved to the desired trapping current. The measured position (y, z) agrees well with a 2D simulation of the London equations[36] that includes gravity and the conservation of flux in the resonator loop (see Methods). The simulations are performed without free parameters. As experimentally observed and consistent with our model, we note that the two gaps of the CPR are not equivalent. Owing to the opposite direction of the current in the ground planes and the orientation of the bias field, only the closest gap to the trapping wire can be accessed. We call this trap, resulting from applied and induced currents, a hybrid trap.

A further advantage in using superconductors to manipulate cold atoms is the possibility to engineer traps induced by persistent currents. These persistent-current traps[14] render the direct injection of currents on the chip unnecessary and therefore suppress the related source of noise. In our geometry, such a trap can be generated directly below the CPR. Here we demonstrate a self-centred trap generated by a single homogeneous bias field and its induced screening currents. By trapping flux in the resonator loop with a freezing field applied during the cooling of the cryostat, the magnitude of the screening currents can be controlled independently from the applied bias field. This experimentally realized trap is simulated in Fig. 3b, where both the resulting potential and the current densities are depicted. The simulation presented includes the distortion due to the MOE, the conservation of magnetic flux in the loop and the effect of vortices trapped inside the film during the cooling of the cryostat[37,38]. The agreement of position and trap frequencies between the experiment and our simple model requires an adjustment of the input parameters by $<20\%$. In the trap of Fig. 3b with oscillation frequencies $\{35, 173, 107\}$ Hz, a cloud at $T\sim90$ nK starting with $>30\%$ condensed fraction and a central density $<8\times10^{13}$ at cm^{-3} has a lifetime of 10(4) s, probably limited by the shallow trap depth ($\sim$320 nK). We stress that, in this loop geometry, the conservation of magnetic flux should reduce the amplitude of external magnetic noise at the trap position.

Coherence in a superconducting CPR. To study the coherence lifetime of atomic ensembles in the close vicinity of a CPR, we perform Ramsey measurements at different positions below the superconducting chip. These measurements compare the coherence of a trapped atomic ensemble in a superposition of the states $|0\rangle = |F=1,\ m_F=-1\rangle$ and $|1\rangle = |F=2,\ m_F=1\rangle$ (Fig. 1f) with a high-stability 10 MHz reference oscillator that has a short-

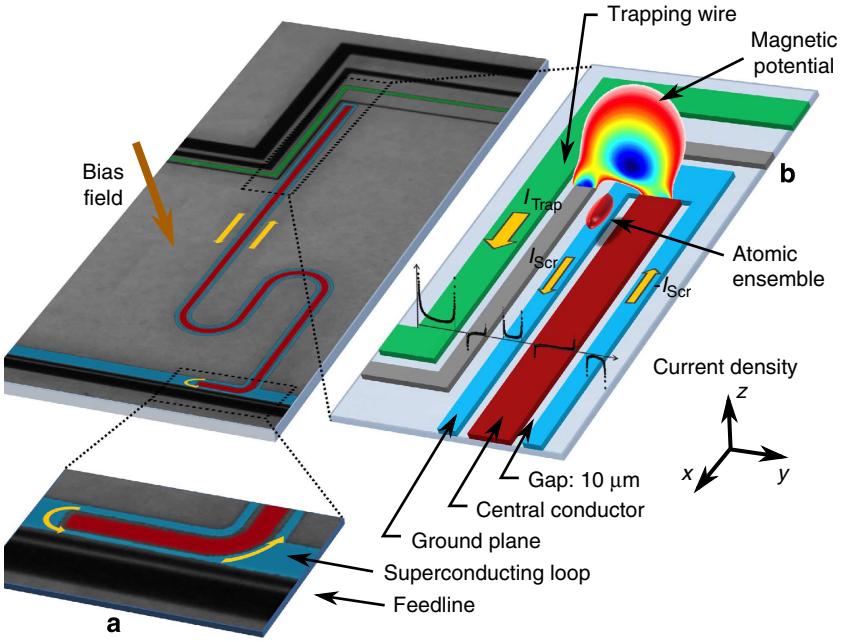

Figure 2 | Atom-trapping scheme. Scheme of the atoms trapped in the gap of a superconducting quarter wavelength coplanar microwave resonator (CPR). (**a**) Zoom of the superconducting link between the two ground planes of the CPR. (**b**) Zoom of the structure around the trapping region. The trap inside the gap is a result of the magnetic fields generated by the current of the trapping wire I_{Trap} and by the screening current I_{Scr} in the ground plane. These fields cancel with an externally applied bias field. The embedded plot (black dots) is the simulated distribution of the screening currents in the superconductor. These currents keep the flux in the superconducting loop constant and the interior of the films field free. The transverse profile of the magnetic potential is shown in colour. The dark blue corresponds to the potential minimum.

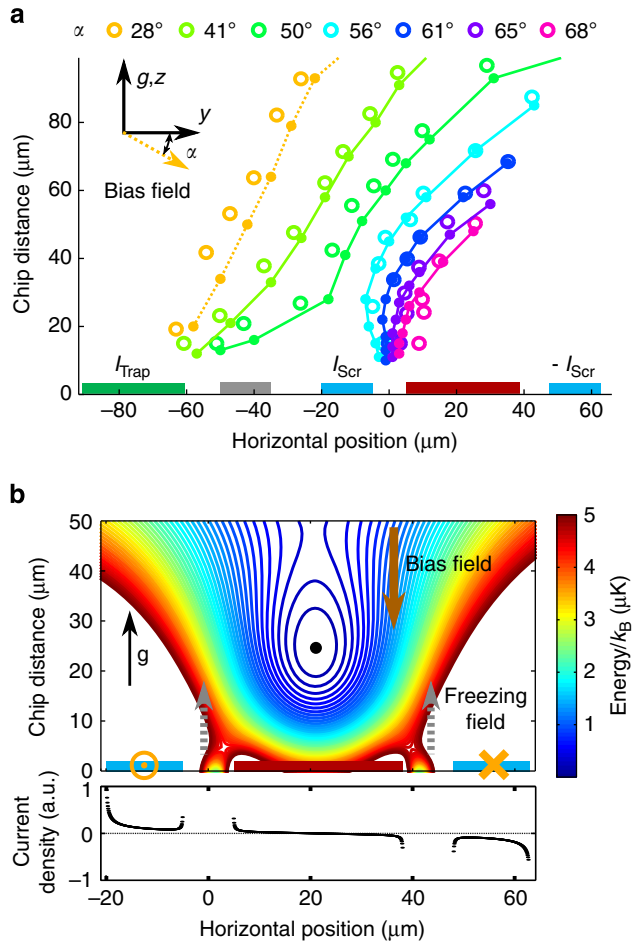

Figure 3 | Positioning atoms close to a superconducting coplanar microwave resonator. (**a**) Position of the trap for different currents in the trapping wire and different angles α between the bias field and the surface of the chip. $\alpha = \arctan(B_z^{bias}/B_y^{bias})$ is varied by changing B_z^{bias} with $B_y^{bias} = 2.3$ G constant. The position of the atoms has been measured by *in situ* absorption imaging (Methods). For small angles, the trap behaves as for a normal conducting chip, that is, when the current is reduced in the trapping wire (I_{Trap}), the trap moves towards it. For large angles, this behaviour is modified and the trap is focused into the gap between the centre conductor and the ground plane of the CPR. The agreement between measurement (circles) and simulations (dotted and solid lines with dots) proves that positioning of the atoms in the gap of the CPR can be facilitated by screening currents I_{Scr} in the ground planes. The simulations[36] are performed with no adjustable parameter and assume a Meissner state for the superconductor. Gravity, g, is oriented upwards. (**b**) Top: potential energy landscape of a persistent-current trap above the central conductor (red) of the CPR. This trap is generated by the superposition of a vertical homogeneous bias field $B_z^{bias} \approx 1.2$ G and the field induced by the screening currents. To enhance the screening currents at a given bias field, a non-zero flux is trapped in the gap of the CPR during the cool-down of the cryostat (freezing field, $B_z^{freezing} \approx 0.5$ G). Isolines are separated by 100 nK. Bottom: screening current density distribution induced by the combination of bias field and freezing field.

and long-term frequency stability $\Delta f/f < 5 \times 10^{-12}$. These two states are chosen for the low sensitivity of their transition frequency to magnetic inhomogeneities at a magnetic offset field of 3.228 G (see Methods)[39]. The atomic cloud is first prepared in a thermal and pure state of $|0\rangle$. The initialization of the coherent superposition is realized by a $\pi/2$ two-photon excitation that starts the interferometric sequence. After a variable waiting time T_R, the interferometer is closed by a second $\pi/2$ pulse. The populations $N_0(T_R)$ and $N_1(T_R)$ in, respectively, $|F=1\rangle$ and $|F=2\rangle$ are consecutively read out by state-selective absorption imaging (see Methods), and the resulting probability of $|F=2\rangle$: $N_1(T_R)/(N_0(T_R)+N_1(T_R))$ is displayed in Fig. 4a–c.

To study the capabilities of our setup, we first describe a reference measurement that is performed far from the CPR: 60 μm below the third trapping wire (green star: Fig. 4a). This measurement is conducted with $1.9(4) \times 10^4$ atoms at a temperature of 245(30) nK in a magnetic trap with oscillation frequencies {10, 215, 181} Hz, corresponding to a mean density (in units of 10^{12} at/cm^3) $\bar{n} \approx 0.4(1)$. In this configuration, the coherence time, as measured by the decay of the envelope, is $T_{coh} = 20.5(6.0)$ s ($1/e$ exponential decay time). Owing to magnetic noise in this non-shielded apparatus and drifts over the length of the scan (several hours), the phase starts to be lost for $T_R > 5$ s, corresponding to a technically induced reduction of the T_2 time of the ensemble. The observed decay time T_{coh} exceeds the time of 6 s predicted by the residual trap inhomogeneities $\Delta_0/2\pi \approx 0.04$ Hz (see Methods[40]). This indicates that we entered the spin self-rephasing (SSR) regime[25], where the identical spin rotation rate $\omega_{ex}/2\pi = 3$ Hz dominates both Δ_0 and the rate of lateral elastic collisions $\gamma_c = 1\,s^{-1}$. This regime can be understood as a continuous spin-echo process triggered by forward atomic collisions.

The second trap under study is the hybrid trap, situated 14 μm below the gap of the CPR. As mentioned before, this position is particularly privileged for the perspective of strong atom–cavity coupling. The Ramsey fringes shown by blue squares (Fig. 4b) were obtained for $1.25(40) \times 10^4$ atoms at a temperature of 320(20) nK held in a confined trap {16.9, 451, 390} Hz, corresponding to $\bar{n} \approx 1.24(40)$. The coherence time is $T_2 \approx T_{coh} = 3.9(5)$ s. The reduction with respect to the reference position is mainly explained based on the atom loss decay time of 3.4(2) s of the hybrid trap. This loss rate is asymmetric and mainly affects the state $|1\rangle$. It is partially explained by spin-exchanging collisions that transfer two collisioning atoms in $|1\rangle$ towards the states $|F=2, m_F=0\rangle$ (untrapped) and $|F=2, m_F=2\rangle$ (trapped). In Fig. 4b, this collision process is responsible for the asymmetry of the probability for large T_R. It comes as a drawback of the guiding mechanism that strongly compresses the trap and increases the atomic density (see Table 1). The spin-exchanging collision rate $\gamma_{22} = 1.6 \times 10^{-13}\,cm^3\,s^{-1}$ reported in Egorov *et al.*[41] is insufficient to fully explain our observed loss rate and other possible mechanisms are under study. The fringes presented in Fig. 4b result from an optimization of the temperature that is high enough to minimize collisional losses and low enough to enter the SSR regime ($\omega_{ex}/2\pi = 9.5$ Hz, $\gamma_c = 3.6\,s^{-1}$, $\Delta_0/2\pi = 0.12$ Hz).

The last position studied corresponds to the persistent-current trap previously mentioned (red disk: Fig. 4c). In this trap the measurement was performed with $1.25(40) \times 10^4$ atoms at 158(23) nK, corresponding to $\bar{n} \approx 0.78(30)$ and to the related SSR parameters $\omega_{ex}/2\pi = 6$ Hz, $\gamma_c = 1.6\,s^{-1}$ and $\Delta_0/2\pi = 0.1$ Hz. The coherence lifetime obtained is $T_2 \approx T_{coh} = 7.8(14)$ s and is mainly limited, in this shallow trap ($\sim$320 nK), by the atom loss decay time 4.8(3) s.

Discussion

The three measurements are compared in Table 1. It shows that the trap deformation induced by the superconducting CPR results in an increase in the trap frequencies, which impact the coherence of the atomic cloud. We do not expect that such coherence would change for a cavity on-resonance with the transition from $|0\rangle$ to

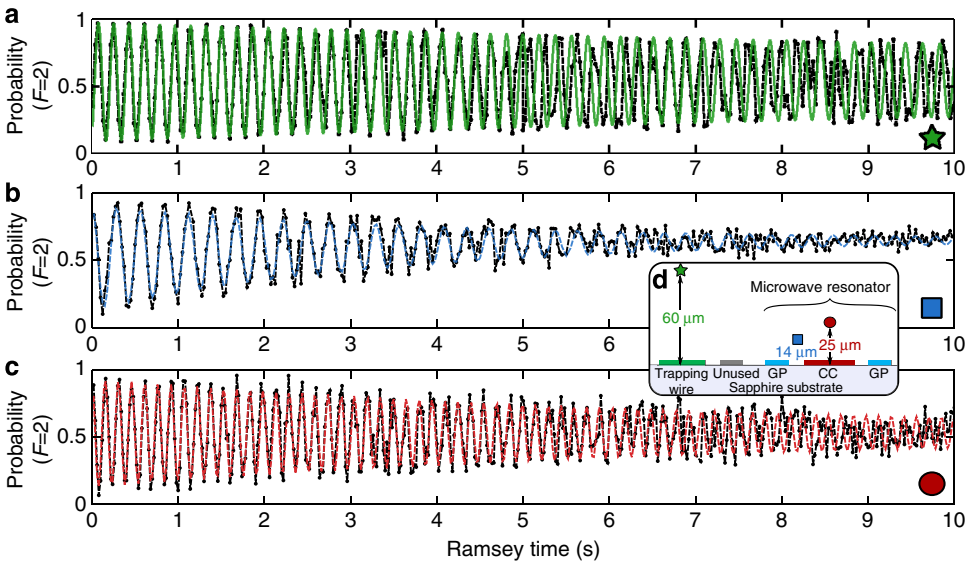

Figure 4 | Atomic coherence in a superconducting coplanar microwave resonator. Ramsey fringes measured in the time domain for different trapping positions on the superconducting atom chip. From top to bottom, the trapping positions correspond to: (**a**) the reference trap (green star in (**d**)), (**b**) the hybrid trap (blue square in (**d**)) and (**c**) the persistent-current trap (red disk in (**d**)). The coherence time obtained for the three sets are 20.5, 3.9 and 7.8 s, respectively, that indicate collision-induced SSR effects[25] (see main text and Methods). The coherence time of each set is estimated by measuring the fringe contrast decay on time intervals in which the phase is preserved. Black dots are experimental data and coloured lines are fits, with a fixed decay, to the first few seconds of the oscillation: 5, 3 and 4 s, respectively. Inset (**d**): positions of the different traps. The reference trap is situated 60 µm straight below the trapping wire. The hybrid trap, which is generated by applied and induced currents, stands 14 µm below the 10-µm-wide gap of the CPR. The persistent-current trap is 25 µm below the central conductor (CC) of the CPR that has a width of 33 µm. GP stands for ground planes. Horizontal and vertical axes are to scale. The experimental parameters for each measurement are summarized in Tables 1 and 2.

Table 1 | Results of atomic coherence.

	Reference	Hybrid	Persistent
Symbols	Green star	Blue square	Red disk
Trap frequencies (Hz)	10.3 (2)	16.9 (2)	35 (2)
	215 (5)	451 (5)	173.4 (6)
	181 (2)	390 (8)	107 (3)
Mean frequency (Hz)	73.7 (6)	144 (3)	87 (3)
Atomic density ($\times 10^{12}$ at. cm^{-3})	0.4 (1)	1.24 (40)	0.78 (30)
Coherence time (s)	20.5 (6.0)	3.9 (5)	7.8 (1.4)
Expected τ_{inh} without SSR (s)	6.5	1.8	2.1

Experimental parameters for the three measurements shown in Fig. 4. The density quoted is the mean atomic density. The mean frequency is the geometrical average. $\tau_{inh} = \sqrt{2}/\Delta_0$ is the coherence time expected without SSR for the corresponding residual frequency inhomogeneity Δ_0 (see Methods).

$|1\rangle$ that necessarily involves two photons. Nevertheless, thermal photons in a cavity that would be on resonance with one of the transitions from $|0\rangle$ or $|1\rangle$ to untrapped states could open an asymmetric loss channel and a corresponding loss of coherence. In the effective strong coupling limit that we target, this process could be used to cool the mode of the resonator[20].

In conclusion, we have demonstrated that, in the vicinity of a superconducting CPR, magnetic traps can be engineered to produce robust and controllable conditions for the coherent manipulation of atoms. The preparation of large BECs and thermal clouds of a million atoms opens the path to the strong collective coupling to a CPR, and to the transfer of quantum information between atomic and superconducting systems. The long coherence of atomic superposition states on the time scale of seconds encourages the development of cold atom/superconductor hybrid quantum systems in which cold atoms would serve as quantum memory. Although the motion of particles is usually considered as a source of decoherence, which, for example, prevents the use of spin-echo techniques, it has an important role in this experiment to maintain the coherence of the superposition state. If such a mechanism can be extended to preserve the coherence of single excitations, it will surely lead to very rich dynamics of collective states.

Methods

Atom cloud preparation. The magneto-optical trap (MOT) is loaded from a 2D-MOT. For a loading time of 6 s, the MOT contains $\sim 10^9$ ^{87}Rb atoms at a temperature of ~ 200 µK. With this method, we do not observe perturbation of the background pressure. After an optical molasses, the atomic cloud is optically pumped into one of the two hyperfine ground states $|0\rangle$ or $|F=2, m_F=2\rangle$ (total angular momentum states) and is transferred through a magnetic quadrupole into a harmonic Ioffe – Pritchard-type trap. It is further cooled by forced RF evaporation to a temperature of ~ 1.5 µK, slightly above the BEC transition. The remaining 5×10^6 atoms are loaded into optical tweezers ($\lambda = 1064$ nm laser, $P = 500$ mW, focused to $w_0 = 25$ µm beam waist) and transported without significant loss or heating over a distance of 40 mm to the superconducting chip. During the optical transfer, a quantization field of 350 mG along x is applied to maintain the polarization of the sample.

Magnetic field calibration. At the position of the atomic cloud, below the superconducting chip, the magnetic field is controlled by three orthogonal pairs of coils that allow to independently control the three directions of space. The calibration of the residual field and the field generated by the coils is realized *in situ* by microwave spectroscopy. To that purpose, the atoms are prepared in $|0\rangle$ and the magnetic field is set to the desired field of study. After all Eddy currents have damped out, the atoms are released from the optical dipole trap. The microwave transition considered is $|0\rangle$ to $|F=2, m_F=0\rangle$. In the absence of a magnetic field it has a frequency of 6.834682610 GHz and a first-order Zeeman sensitivity of 700 kHz G^{-1}. In a first coarse step, the absolute field is reduced to below 5 mG. In a second fine step, each pair of coils is switched on in a row to generate a frequency shift of approximately 200 kHz. This shift is then measured with an accuracy of $\pm$ 500 Hz. This way, each pair of coils is *in situ* and independently calibrated (residual contribution from other pairs below 1%) and the residual field is measured to below 1 mG, while the coils are calibrated with an accuracy better than 0.3%.

Table 2 | Experimental parameters for atomic coherence measurements.

Properties	Reference	Hybrid	Persistent
P_{MW} (dBm)	19	−10	−14
P_{RF} (dBm)	−2	11.5	11.5
$\Delta_R/2\pi$ (Hz)	5.7	3.5	6.5
$\Omega_R/2\pi$ (Hz)	432	416	179
B_1 (G)	3.193 (4)	3.203 (20)	3.20 (3)
B_1^{opt} (G)	3.197	3.17	3.17
$\Delta_O/2\pi$ (Hz)	0.04	0.12	0.1
τ_{inh} (s)	6.5	1.8	2.1

The parameters presented relate to the measurement shown in Fig. 4.

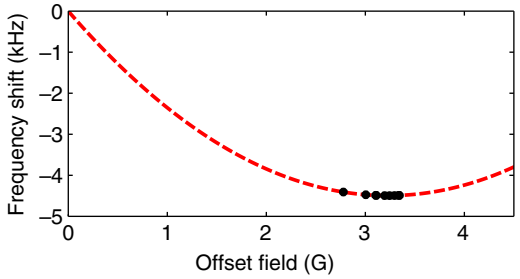

Figure 5 | Differential frequency shift of the $|0\rangle$ to $|1\rangle$ transition. The black points are experimental data. The red dashed line is the prediction given by the Breit-Rabi formula[45].

To avoid perturbation by the MOE of the nearby superconductor, this calibration is done with the cryostat at $T \approx 10$ K.

Imaging and measurement of position. The atoms are observed by absorption imaging with a variable time of flight (TOF). The large BEC in Fig. 1d was measured by off-resonance imaging, which was calibrated on a low-density cloud. Owing to eddy currents in the mechanical system, the measured atom number is not absolute and depends on the TOF. For TOF < 10 ms, the calibration of the detection of the state $|0\rangle$ with respect to the state $|1\rangle$ is obtained by minimizing the variance of the total atom number detected over the length of the scan. For TOF > 10 ms, atom numbers stay constant, showing that eddy currents are no more an issue at the corresponding distances. The absolute calibration of the atom number is obtained from the critical temperature of Bose − Einstein condensation. This calibration is the main source of uncertainty of the atom numbers (20%). Therefore, the atom number uncertainty quoted in the text does not represent shot-to-shot fluctuations.

The state-selective measurement realized for the coherence measurement is done by first measuring and blasting the atoms in $F = 2$, and second by repumping and measuring the atoms in $F = 1$. The two measurements are realized on orthogonal axes.

In situ, the position of the atomic cloud is measured along the three directions of space by two reflection imaging systems that are aligned along x and y. The calibration of distances is realized by TOF of the magnetically insensitive state $|F = 2, m_F = 0\rangle$. To avoid spurious effects, the chip is uncoated.

Magnetic field calculations. To calculate the current densities in the superconductor and the subsequent atomic trap deformation, we solved the London equations using the 2D algorithm described in Cano *et al.*[36] This treatment is particularly valid in the trapping region where thin films are parallel to each other. The assumption of a pure Meissner state can be justified by an estimate of the maximum fields at the lead edges[42]. In our field and current range, these edge fields remain considerably below the lower critical field of a dirty niobium film[43], assuming a penetration depth $\lambda_L \approx 100$ nm and a Ginzburg − Landau parameter $\kappa \approx 10$. The conservation of flux in the superconducting loop of the resonator is further taken into account by imposing net currents in the grounds of the resonator. The influence of an homogeneous density of vortices pointing along z is modelled by the superposition of an homogeneous field along z (undeformed) and the opposite field deformed by the superconducting structure in a pure Meissner state. In all simulations, the quantization of flux is neglected ($\Phi_0/\Phi \approx 5 \times 10^{-5}$). The simulations presented in Figs 2 and 3 have been confirmed using a 3D simulator (3D-MLSI[44]). The effect of gravity is included in all simulations.

Details on the measurement of coherence lifetime. The measurement of the T_{coh} time of the atomic qubit formed by the state $|0\rangle$ and $|1\rangle$ is realized by a Ramsey-type experiment. As shown in Fig. 1f, the two states are coupled via a two-photon transition involving a microwave photon at $f_{MW} = 6.83337816$ GHz and an RF photon at $f_{RF} = 1.3$ MHz. Both frequencies are generated by commercial synthesizer phase locked to a high-stability 10 MHz quartz oscillator (Oscillo-quartz, 8607-BHM15), and their sum is frequency detuned from the atomic transition by $\Delta_R/2\pi$. For all the measurement presented, the microwave with power P_{MW} is radiated by an helicoidal antenna situated outside the vacuum chamber at a distance of 20 cm from the atoms. The RF with power P_{RF} is coupled on the chip to the largest Z-wire. The Rabi frequency Ω_R obtained in each situation is summarized in Table 2. Figure 5 shows the differential frequency shift of the qubit transition that is well approximated by $\Delta\nu(\mathbf{r}) = \nu_{|1\rangle} - \nu_{|0\rangle} = \Delta\nu_0 + \beta(B(\mathbf{r}) - B_0)^2$, with $\Delta\nu_0 = 4.4973$ kHz, $B_0 = 3.228917(3)$ G (ref. 25) and $\beta = 431.36$ Hz/G^2 (ref. 39). At the magic offset field B_0, this shift is first-order insensitive to the magnetic field. The sensitivity of the coherence time to the magnetic inhomogeneities of the trap is therefore highly reduced. The measurements presented in Fig. 4 are performed with an offset field B_{off} slightly lower than B_0. This configuration is known as the mutual compensation scheme[39,40], which allows to compensate the negative collisional shift $\Delta_c(\mathbf{r})/2\pi = -0.4n(\mathbf{r})/10^{12}$ Hz by the positive magnetic shift $\Delta_B(\mathbf{r}) = 2\pi\Delta\nu(\mathbf{r})$. In such conditions, an optimum residual radial frequency homogeneity $\Delta_0 = \sqrt{\langle(\Delta_c(\mathbf{r}) + \Delta_B(\mathbf{r}))^2\rangle - \langle\Delta_c(\mathbf{r}) + \Delta_B(\mathbf{r})\rangle^2}$ is obtained for an optimal offset field B_1^{opt} that depends on the number of particles, the temperature and the geometry of the trap. In Table 2, we give the optimum value of Δ_0 for each experimental configuration. In the abscence of spin-rephasing, such inhomogeneities should result in a decay of the Ramsey contrast with a time constant $\tau_{inh} = \sqrt{2}/\Delta_0$ (ref. 40).

References

1. Wallquist, M., Hammerer, K., Rabl, P., Lukin, M. & Zoller, P. Hybrid quantum devices and quantum engineering. *Phys. Scr.* **2009,** 014001 (2009).
2. Kubo, Y. *et al.* Hybrid quantum circuit with a superconducting qubit coupled to a spin ensemble. *Phys. Rev. Lett.* **107,** 220501 (2011).
3. Zhu, X. *et al.* Coherent coupling of a superconducting flux qubit to an electron spin ensemble in diamond. *Nature* **478,** 221–224 (2011).
4. Amsüss, R. *et al.* Cavity QED with magnetically coupled collective spin states. *Phys. Rev. Lett.* **107,** 060502 (2011).
5. Camerer, S. *et al.* Realization of an optomechanical interface between ultracold atoms and a membrane. *Phys. Rev. Lett.* **107,** 223001 (2011).
6. O'Connell, A. D. *et al.* Quantum ground state and single-phonon control of a mechanical resonator. *Nature* **464,** 697–703 (2010).
7. Kálmán, O., Kiss, T., Fortágh, J. & Domokos, P. Quantum galvanometer by interfacing a vibrating nanowire and cold atoms. *Nano Lett.* **12,** 435–439 (2012).
8. Xiang, Z.-L., Ashhab, S., You, J. Q. & Nori, F. Hybrid quantum circuits: superconducting circuits interacting with other quantum systems. *Rev. Mod. Phys.* **85,** 623–653 (2013).
9. Wallraff, A. *et al.* Strong coupling of a single photon to a superconducting qubit using circuit quantum electrodynamics. *Nature* **431,** 162–167 (2004).
10. DiCarlo, L. *et al.* Demonstration of two-qubit algorithms with a superconducting quantum processor. *Nature* **460,** 240–244 (2009).
11. Fedorov, A., Steffen, L., Baur, M., Da Silva, M. P. & Wallraff, A. Implementation of a Toffoli gate with superconducting circuits. *Nature* **481,** 170–172 (2012).
12. Reed, M. D. *et al.* Realization of three-qubit quantum error correction with superconducting circuits. *Nature* **482,** 382–385 (2012).
13. Nirrengarten, T. *et al.* Realization of a superconducting atom chip. *Phys. Rev. Lett.* **97,** 200405 (2006).
14. Mukai, T. *et al.* Persistent supercurrent atom chip. *Phys. Rev. Lett.* **98,** 260407 (2007).
15. Müller, T. *et al.* Trapping of ultra-cold atoms with the magnetic field of vortices in a thin-film superconducting micro-structure. *New J. Phys.* **12,** 043016 (2010).
16. Cano, D. *et al.* Meissner effect in superconducting microtraps. *Phys. Rev. Lett.* **101,** 183006 (2008).
17. Kasch, B. *et al.* Cold atoms near superconductors: atomic spin coherence beyond the Johnson noise limit. *New J. Phys.* **12,** 065024 (2010).
18. Petrosyan, D. & Fleischhauer, M. Quantum information processing with single photons and atomic ensembles in microwave coplanar waveguide resonators. *Phys. Rev. Lett.* **100,** 170501 (2008).
19. Petrosyan, D. *et al.* Reversible state transfer between superconducting qubits and atomic ensembles. *Phys. Rev. A* **79,** 040304 (2009).
20. Verdú, J. *et al.* Strong magnetic coupling of an ultracold gas to a superconducting waveguide cavity. *Phys. Rev. Lett.* **103,** 043603 (2009).
21. Dudin, Y. O., Zhao, R., Kennedy, T. A. B. & Kuzmich, A. Light storage in a magnetically dressed optical lattice. *Phys. Rev. A* **81,** 041805 (2010).
22. Radnaev, A. G. *et al.* A quantum memory with telecom-wavelength conversion. *Nature Phys.* **6,** 894–899 (2010).

23. Bao, X. H., Reingruber, A., Dietrich, P. & Rui, J. Efficient and long-lived quantum memory with cold atoms inside a ring cavity. *Nature Phys.* **8,** 517–521 (2012).
24. Treutlein, P., Hommelhoff, P., Steinmetz, T., Hänsch, T. W. & Reichel, J. Coherence in microchip traps. *Phys. Rev. Lett.* **92,** 203005 (2004).
25. Deutsch, C. *et al.* Spin self-rephasing and very long coherence times in a trapped atomic ensemble. *Phys. Rev. Lett.* **105,** 020401 (2010).
26. Ritter, S. *et al.* An elementary quantum network of single atoms in optical cavities. *Nature* **484,** 195–200 (2012).
27. Cano, D. *et al.* Experimental system for research on ultracold atomic gases near superconducting microstructures. *Eur. Phys. J. D* **63,** 17–23 (2011).
28. Fortágh, J. & Zimmermann, C. Magnetic microtraps for ultracold atoms. *Rev. Mod. Phys.* **79,** 235–289 (2007).
29. Skagerstam, B. K., Hohenester, U., Eiguren, A. & Rekdal, P. K. Spin decoherence in superconducting atom chips. *Phys. Rev. Lett.* **97,** 070401 (2006).
30. Hohenester, U., Eiguren, A., Scheel, S. & Hinds, E. A. Spin-flip lifetimes in superconducting atom chips: Bardeen-Cooper-Schrieffer versus Eliashberg theory. *Phys. Rev. A* **76,** 033618 (2007).
31. Nogues, G. *et al.* Effect of vortices on the spin-flip lifetime of atoms in superconducting atom-chips. *Eur. Phys. Lett.* **87,** 13002 (2009).
32. Emmert, A. *et al.* Measurement of the trapping lifetime close to a cold metallic surface on a cryogenic atom-chip. *Eur. Phys. J. D* **51,** 173–177 (2009).
33. Söding, J. *et al.* Three-body decay of a rubidium Bose – Einstein condensate. *Appl. Phys. B* **69,** 257–261 (1999).
34. Henschel, K., Majer, J., Schmiedmayer, J. & Ritsch, H. Cavity QED with an ultracold ensemble on a chip: prospects for strong magnetic coupling at finite temperatures. *Phys. Rev. A* **82,** 033810 (2010).
35. Markowsky, A., Zare, A., Graber, V. & Dahm, T. Optimal thickness of rectangular superconducting microtraps for cold atomic gases. *Phys. Rev. A* **86,** 023412 (2012).
36. Cano, D. *et al.* Impact of the Meissner effect on magnetic microtraps for neutral atoms near superconducting thin films. *Phys. Rev. A* **77,** 063408 (2008).
37. Stan, G., Field, S. B. & Martinis, J. M. Critical field for complete vortex expulsion from narrow superconducting strips. *Phys. Rev. Lett.* **92,** 097003 (2004).
38. Emmert, A. *et al.* Microtraps for neutral atoms using superconducting structures in the critical state. *Phys. Rev. A* **80,** 061604(R) (2009).
39. Harber, D. M., Lewandowski, H. J., McGuirk, J. M. & Cornell, E. A. Effect of cold collisions on spin coherence and resonance shifts in a magnetically trapped ultracold gas. *Phys. Rev. A* **66,** 053616 (2002).
40. Rosenbusch, P. Magnetically trapped atoms for compact atomic clocks. *Appl. Phys. B* **95,** 227–235 (2009).
41. Egorov, M. *et al.* Precision measurements of s-wave scattering lengths in a two-component Bose – Einstein condensate. *Phys. Rev. A* **87,** 053614 (2013).
42. Zeldov, E., Clem, John R., McElfresh, M. & Darwin, M. Magnetization and transport currents in thin superconducting films. *Phys. Rev. B* **49,** 9802–9822 (1994).
43. Brandt., E. H. The flux-line lattice in superconductors. *Rep. Prog. Phys.* **58,** 1465–1594 (1995).
44. Khapaev, M. M., Kupriyanov, M. Y., Goldobin, E. & Siegel, M. Current distribution simulation for superconducting multi-layered structures. *Supercond. Sci. Technol.* **16,** 24–27 (2003).
45. Breit, G. & Rabi, I. I. Measurement of nuclear spin. *Phys. Rev.* **38,** 2082–2083 (1931).

Acknowledgements

We would like to thank Thomas Udem from the MPQ Munich as well as Max Kahmann and Ekkehard Peik from the PTB Braunschweig for the loan of the reference oscillators. This work was supported by the Deutsche Forschungsgemeinschaft (SFB TRR 21) and ERC (Socathes). H.H. and D.B. acknowledge support from the Evangelisches Studienwerk e.V.Villigst. M.Kn. and M.Ke. acknowledge support from the Carl Zeiss Stiftung.

Author contributions

D.K., R.K., J.F., S.B., H.H., F.J., M.Kn. and M.Ke. designed and mounted the experiment. D.B., M.Kn., M.Ke. and H.H. designed and fabricated the superconducting chip. S.B., H.H. and P.W. carried out the experiments and analysed the data. S.B., H.H., D.C., M.Kn. and D.B. made the numerical simulations. D.K., R.K. and J.F. supervised the project. S.B., H.H. and J.F. edited the manuscript. All authors discussed the results and commented on the manuscript.

Additional information

Competing financial interests: The authors declare no competing financial interests.

Reprints and permission information is available online at http://npg.nature.com/reprintsandpermissions/

How to cite this article: Bernon, S. *et al.* Manipulation and coherence of ultra-cold atoms on a superconducting atom chip. *Nat. Commun.* 4:2380 doi: 10.1038/ncomms3380 (2013).

Publication V

New Journal of Physics
The open access journal for physics

Inductively coupled superconducting half wavelength resonators as persistent current traps for ultracold atoms

D Bothner[1], M Knufinke, H Hattermann, R Wölbing, B Ferdinand, P Weiss, S Bernon, J Fortágh, D Koelle and R Kleiner

Physikalisches Institut and Center for Collective Quantum Phenomena in LISA$^+$, Universität Tübingen, Auf der Morgenstelle 14, D-72076 Tübingen, Germany
E-mail: daniel.bothner@uni-tuebingen.de

New Journal of Physics **15** (2013) 093024 (14pp)
Received 17 May 2013
Published 13 September 2013
Online at http://www.njp.org/
doi:10.1088/1367-2630/15/9/093024

Abstract. A crucial point in the experimental implementation of hybrid quantum systems consisting of superconducting circuits and atomic ensembles is bringing the two partners close enough to each other that a strong quantum coherent coupling can be established. Here, we propose to use the metallization structures of a half wavelength superconducting coplanar waveguide resonator as a persistent current trap for ultracold paramagnetic atoms. Trapping atoms with the resonator structure itself is provided by using short-ended and inductively coupled resonators instead of capacitively coupled ones as customary in circuit quantum electrodynamics. We analyze the external quality factor of short-ended coplanar waveguide resonators and show that it can be easily designed for the desired regime of quantum circuits. The magnetic field configuration at the resonator is calculated by means of numerical three-dimensional simulations of the London equations. We present a way to transport an atomic ensemble into the coplanar resonator gap where the magnetic field of the cavity mode is maximum. The configuration allows stable trapping by persistent currents and paves the route toward strong coupling between atomic clouds and the cavity mode which is required for cooperative effects and gives the interface between atoms and circuit quantum electrodynamics.

[1] Author to whom any correspondence should be addressed.

Contents

1. Introduction

The rise of quantum electrodynamics with superconducting circuits during the last decade has enabled a rich variety of experimental breakthroughs. For example, it is now possible to investigate the quantum nature of macroscopic linear and nonlinear electrical circuits [1–5] and even macroscopic mechanical objects at cryogenic temperatures [6, 7]. These quantum circuit systems are promising candidates as essential building blocks in quantum information technologies, as they are well controllable, scalable and addressable with both high velocity and fidelity. This has led to first implementations of quantum computer architectures and the demonstration of their feasibility for solving simple algorithms [8–12].

In spite of the advances in quantum state preparation and manipulation, superconducting circuits suffer from a fast decay in coherence due to their coupling to the environment. So far the coherence time is limited to below 100 μs [13, 14], which is not long enough to store quantum information during complex and time-demanding processing algorithms. Moreover, it is desirable to encode the quantum information in flying qubits by which the information can be transferred between distant locations. However, the typical frequencies for optical photons, which are today's standard for quantum communication, are several orders of magnitude higher than the frequencies of superconducting quantum circuits and the superconducting energy gap of typically used materials.

A proposed solution to these problems is the creation of hybrid systems, in which superconducting circuits are coupled to atomic dipolar or spin ensembles [15–19]. Atomic ensembles seem highly suitable as quantum memories due to their long coherence times [20, 21]. At the same time, atoms have a rich energy level structure and have been proposed as quantum transducers between the microwave and the optical regime [22]. The first steps toward the experimental realization of such hybrid systems have been carried out with solid state spin ensembles in diamond [23–26] and erbium [27] and with highly excited Rydberg atoms [28]. A different approach is to use large ensembles of ultracold atoms which could be prepared either as a thermal cloud or in a Bose–Einstein condensed quantum state. Recently, experiments have demonstrated that such atom clouds can be brought into the mode volume of a superconducting microwave resonator where long coherence times on the order of several seconds have been observed [29].

In the hybrid approach with ultracold atoms, the atoms are to be coupled to superconducting qubits by a quantum bus in the form of a superconducting coplanar waveguide resonator. In order to maximize the coupling strength between the two systems, it is important to trap the atoms in close proximity to the superconducting circuit. For paramagnetic atoms, this can be accomplished with on-chip transport current leads [30, 31], by persistent current

loops [29, 32] or by creating magnetic trap structures with the field of pinned Abrikosov vortices [33–35]. The solution which introduces the smallest amount of heat and minimizes the noise and hence the decoherence is a trap based on persistent on-chip supercurrents. Persistent traps can be created by freezing the desired amount of magnetic flux into a closed superconducting loop during the transition through the critical temperature and then switching off the external freezing fields.

In this work we propose to use a half wavelength superconducting microwave resonator that realizes a quantum bus and a persistent current trap for ultracold paramagnetic atoms in a single device. Besides minimizing the structural complexity of the integrated atom chip including a superconducting resonator, such a configuration is suitable for stable trapping and controlled guiding of ultracold atoms to the point of maximized coupling between the atoms and the cavity.

The paper is organized as follows. Since a persistent current requires closed metallization loops, we first discuss in section 2 the short-ended and inductively coupled half wavelength coplanar resonator which intrinsically contains this feature. We introduce the lumped element equivalent and the characteristic parameters of the resonators and exemplarily calculate the transmission characteristics for three different coupling inductances. By means of three-dimensional (3D) simulations of the London equations we demonstrate in section 3 how freezing magnetic flux into the closed loops of these resonators creates a trap for paramagnetic atoms when the corresponding magnetic field is combined with additional externally applied fields. Finally, we discuss how such a trap can be loaded with atoms and how the atoms can then be brought into the gap between center conductor and ground plane of the resonator, where the coupling between the cavity mode and the atoms is expected to be maximized. Section 4 concludes the paper.

2. Short-ended half wavelength resonators

In circuit quantum electrodynamics and quantum information processing with superconducting circuits, resonators in a planar structure are very favorable, as they are easy to fabricate and to integrate with other superconducting circuits. A widely adopted geometry is the coplanar waveguide which consists of a center signal line flanked by two ground conductors. As long as the lateral dimension is small compared to the wavelength of the propagating electromagnetic wave, the coplanar waveguide can be treated with the powerful tool of transmission line (TL) theory.

The most common way to build a coplanar waveguide resonator is to introduce two gaps into the center line of the TL, cf figure 1(a). An electromagnetic wave propagating along the waveguide is reflected at the gap due to the related impedance discontinuity, which to first order can be considered as an open end. The resonance frequencies of a resonator with length l are given by $f_{0n} = nc/(2l\sqrt{\epsilon_{\mathrm{eff}}})$, where n is the mode number, c is the vacuum speed of light and ϵ_{eff} is the effective dielectric constant of the waveguide. The gap can be described as a lumped element series capacitance C_{c} in the center line and hence the resonator is capacitively coupled to the feed lines on both sides.

Another simple method to create a local impedance discontinuity is to short the three conductors at one position which basically constitutes a shunt inductance L_{c} between center conductor and ground [36]. Again, for two shorts with distance l a half wavelength resonator is created, cf figure 1(b). However, the electric and magnetic fields change position in comparison with the gap coupled resonator. Short-ended and inductively coupled resonators are used for

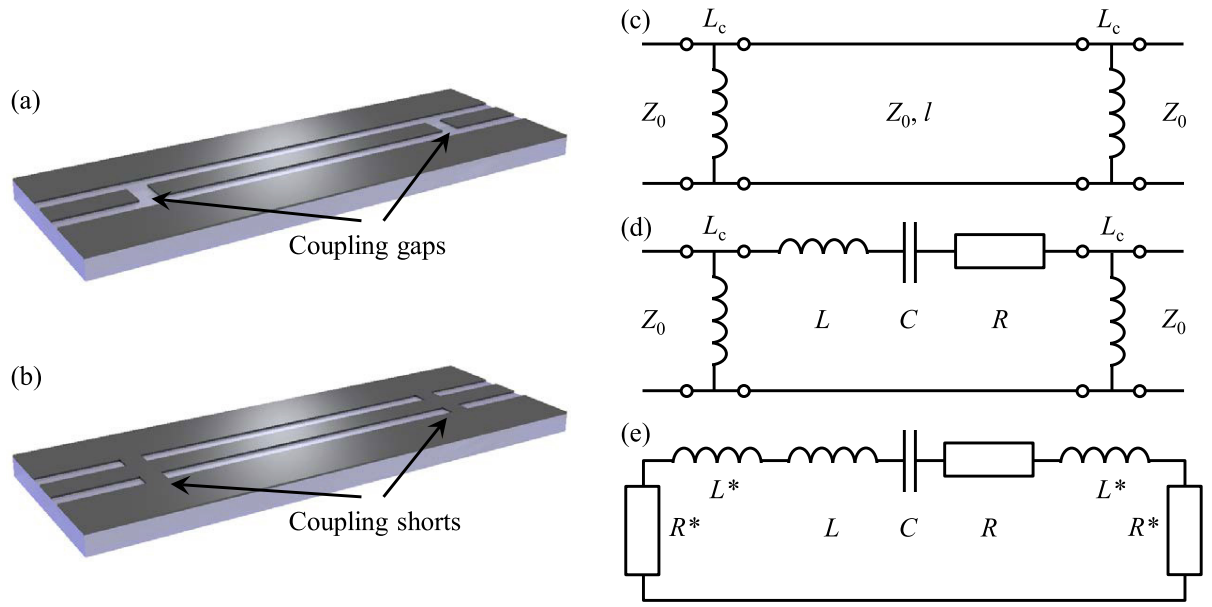

Figure 1. (a), (b) Sketches of half wavelength resonators based on the coplanar waveguide. The patterned thin layer on top is the metallization, whereas the thick bright layer below is a substrate. Panel (a) shows an open-ended and capacitively coupled resonator and (b) shows its short-ended and inductively coupled counterpart. (c) TL representation of a short-ended and inductively coupled resonator, where the line is assumed to have a characteristic impedance Z_0, the resonator has a length l and the coupling shorts have the total inductance $1/L_c$. (d) Lumped element equivalent of (c) around the resonance frequency $f_0 = \omega_0/2\pi$. With the line damping constant α, the equivalent lumped elements are $R = Z_0\alpha l$, $C = 2/Z_0\pi\omega_0$ and $L = Z_0\pi/2\omega_0$. (e) Full series lumped element representation of a TL resonator coupled via shorts at both ends to transmission feed lines. The parallel combination of coupling inductance and loading impedance on each side is transformed into its series equivalent.

microwave filter technologies [37, 38], but to our knowledge have not yet been investigated in circuit quantum electrodynamics.

The capacitively coupled resonator and its properties related to the parameters of the coupling gap have been extensively discussed in [39]. In the following, we give an analogous analysis of the inductively coupled TL resonator. The TL representation of the waveguide geometry depicted in figure 1(b) is shown in figure 1(c). The coupling inductances L_c can be calculated as a parallel combination of the two connection inductances to the left and to the right ground plane. When the transmission through a single lumped element shunt inductance is calculated by means of the $ABCD$ matrix method (cf e. g. [40]), one obtains the scattering parameter S_{21} as

$$S_{21}^{L} = \frac{2}{2 + Z_0/\mathrm{i}\omega L_c}, \tag{1}$$

which is identical to the transmission across a single series capacitance

$$S_{21}^{C} = \frac{2}{2 + 1/\mathrm{i}\omega C_{\mathrm{c}} Z_0} \tag{2}$$

for $L_{\mathrm{c}} = C_{\mathrm{c}} Z_0^2$. We will discuss in more detail below that the numbers for L_{c} obtained from typical numbers of Z_0 and C_{c} are feasible for practical geometries.

The input impedance of a shorted segment of TL is given by [40]

$$Z_{\mathrm{in}} = Z_0 \frac{\tanh(\alpha l) + \mathrm{i}\tan(\beta l)}{1 + \mathrm{i}\tan(\beta l)\tanh(\alpha l)}, \tag{3}$$

where α is the attenuation constant of the TL and $\beta = \omega\sqrt{\epsilon_{\mathrm{eff}}}/c$ is the phase constant with the angular frequency $\omega = 2\pi f$. The resonance condition for shorted ends on both sides is satisfied for $\beta l = n\pi$. If the attenuation is small ($\alpha l \ll 1$), the input impedance of equation (3) can be approximated around the lowest mode resonance frequency $\omega_0 = 2\pi f_0$ (mode number index $n = 1$ is omitted) by [40]

$$Z_{\mathrm{in}} \approx Z_0 \alpha l + \mathrm{i}\pi Z_0 \frac{\Delta\omega}{\omega_0}. \tag{4}$$

The impedance of a lumped element series resonant circuit is given by

$$Z_{LCR} = R + \mathrm{i}\omega L + \frac{1}{\mathrm{i}\omega C}, \tag{5}$$

which after Taylor expansion around $\omega_0 = 1/\sqrt{LC}$ can be approximated by

$$Z_{LCR} \approx R + \mathrm{i}2L\Delta\omega, \tag{6}$$

where $\Delta\omega = \omega - \omega_0$. Due to the formal equivalence between (4) and (6), the inductively coupled half wavelength resonator can be treated as a series LCR resonant circuit around its resonance frequency with the correspondences $R = Z_0\alpha l$, $L = Z_0\pi/2\omega_0$ and $C = 1/\omega_0^2 L = 2/Z_0\pi\omega_0$. Figure 1(d) is a schematic of the circuit. Although we only treat the lowest mode here, all our conclusions hold equally well for higher modes of the TL resonator for which the equivalent lumped elements can be calculated accordingly.

The internal quality factor of a series resonant circuit is given by $Q_{\mathrm{int}} = \omega_0 L/R$. For the case of a resonator coupled to external circuitry via shunt inductors, the quality factor is lowered as the coupling to TLs represents a loss channel. The resonance frequency is also shifted by a reactive coupling, because part of the energy is stored in the magnetic field of the coupling inductors. To see the influence of the coupling on both the loaded quality factor and the resonance frequency, the TLs can—for the case of a real impedance—be treated as simple additional resistors with magnitude Z_0. The parallel combination of coupling inductance L_{c} and resistive loading with Z_0 can then be transformed into an equivalent series impedance of a new inductance L^* and R^*, as seen from the resonator (cf figure 1(e)). The values of the new inductances and resistances are given by

$$L^* = \frac{L_{\mathrm{c}} Z_0^2}{Z_0^2 + \omega^2 L_{\mathrm{c}}^2} \tag{7}$$

and

$$R^* = \frac{\omega^2 L_{\mathrm{c}}^2 Z_0}{Z_0^2 + \omega^2 L_{\mathrm{c}}^2}. \tag{8}$$

As the discussion is only valid close to the resonance frequency, L^* and R^* can be made frequency independent, to a good approximation, by setting $\omega = \omega_0$. After this transformation, the loaded quality factor of the circuit can be simply expressed by $Q_L = \omega_0' L_{\rm tot}/R_{\rm tot}$, where the total inductance $L_{\rm tot} = L + 2L^*$, the total resistance $R_{\rm tot} = R + 2R^*$ and the shifted resonance frequency $\omega_0' = 1/\sqrt{L_{\rm tot}C}$. In general, the loaded quality factor here cannot be separated into an internal and external part by the standard formula $1/Q_L = 1/Q_{\rm int} + 1/Q_{\rm ext}$, where $Q_{\rm int} = \omega_0 L/R$ and $Q_{\rm ext} = \omega_0 L/2R^*$. This is because both resonance frequency and total inductance are modified by the additional reactive component L^* which depends on the load impedance Z_0. However, for low coupling inductances ($\omega_0 L_{\rm c} \ll Z_0$ and $L_{\rm c} \ll L$) the resonance frequency and total inductance are given by $\omega_0' \approx \omega_0$ and $L_{\rm tot} \approx L$, respectively. The loaded quality factor is then given by

$$\frac{1}{Q_{\rm L}} = \frac{R_{\rm tot}}{\omega_0 L} = \frac{R}{\omega_0 L} + \frac{2R^*}{\omega_0 L} = \frac{1}{Q_{\rm int}} + \frac{1}{Q_{\rm ext}}. \tag{9}$$

From this expression it follows that the external quality factor is well approximated by

$$Q_{\rm ext} \approx \frac{Z_0 L}{2\omega_0 L_{\rm c}^2}. \tag{10}$$

Comparing the above result with the expression for the external quality factor of the corresponding capacitively coupled resonator [39]

$$Q_{\rm ext}^C \approx \frac{C}{2\omega_0 Z_0 C_{\rm c}^2} \tag{11}$$

once more shows the equivalence of inductive and capacitive coupling, because the latter is identical to equation (10) for $L_{\rm c} = Z_0^2 C_{\rm c}$ (note that in (11) the equivalent capacitance is that of the parallel LCR circuit $C = \pi/2Z_0\omega_0$). Hence, $Q_{\rm ext} \propto 1/L_{\rm c}^2$.

As a final part of the analysis of the inductively coupled half wavelength resonator, we have calculated the inductance of different types of shorts between the center conductor and ground plane, and calculated the resulting transmission spectra by means of the $ABCD$ matrix method. Figure 2(a) is a schematic of the three different connections in dashed boxes. The first (left) one has a width of 25 µm and a length of 20 µm, the second (center) has a width of 5 µm and a length of 20 µm, while the third (right) has a width of 2 µm and a length of 80 µm. These geometries are easily fabricated using standard lithography techniques. Assuming a metallization thickness $d = 500$ nm and a London penetration depth $\lambda_{\rm L} = 120$ nm, we have calculated the corresponding inductances of the connection parts in dashed boxes individually with 3D-MLSI, a software package for the extraction of 3D inductances and for the simulation of the current distribution in layered superconducting circuits [41]. We obtained $L_1 \approx 5.1$ pH, $L_2 \approx 10.3$ pH and $L_3 \approx 26.6$ pH, which lead to the coupling inductances $L_{\rm c1} \approx 2.6$ pH, $L_{\rm c2} \approx 5.2$ pH and $L_{\rm c3} \approx 13.3$ pH with $1/L_{ci} = 2/L_i$. These values perfectly correspond to the range of typical coupling capacitances of 1–10 fF for gap coupled resonators, when considering the relation $L_{\rm c} = Z_0^2 C_{\rm c}$ and a typical characteristic impedance $Z_0 = 50\,\Omega$.

With the $ABCD$ matrix for a shunt inductance

$$\begin{pmatrix} A & B \\ C & D \end{pmatrix}_{L_{\rm c}} = \begin{pmatrix} 1 & 0 \\ \frac{1}{{\rm i}\omega L_{\rm c}} & 1 \end{pmatrix} \tag{12}$$

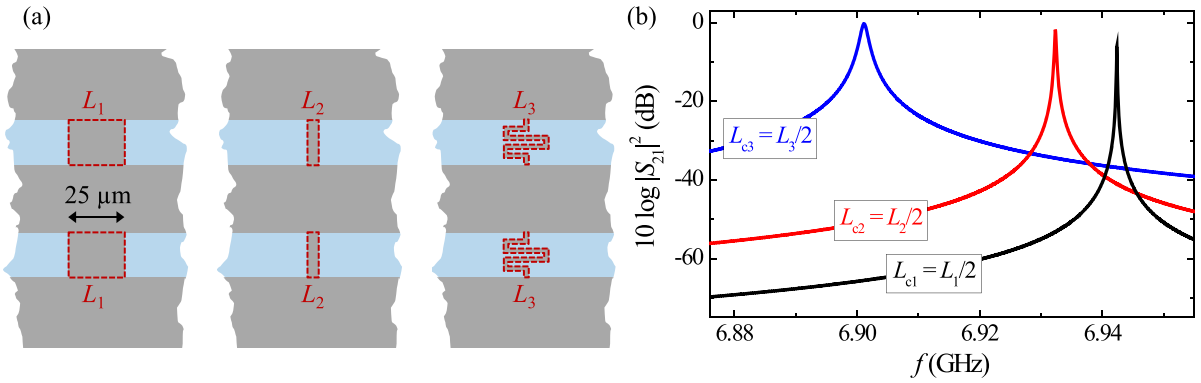

Figure 2. (a) Coplanar waveguide geometry with shorts (marked by dashed boxes) between center conductor and ground planes. Each connection has an inductance L_i which is calculated numerically to be $L_1 \approx 5.1\,\mathrm{pH}$, $L_2 \approx 10.3\,\mathrm{pH}$ and $L_3 \approx 26.6\,\mathrm{pH}$ for a film thickness $d = 500\,\mathrm{nm}$ and $\lambda_\mathrm{L} = 120\,\mathrm{nm}$. (b) Logarithmic transmitted power ratio versus frequency of a TL with $Z_0 = 50\,\Omega$, $\alpha = 0.001\,\mathrm{m}^{-1}$ and $\epsilon_\mathrm{eff} = 5.5$ interrupted by two shunt inductances $L_{ci} = L_i/2$ separated $l = 9.2\,\mathrm{mm}$ from each other, calculated by means of the $ABCD$ matrix method.

and the matrix for a section of TL with length l, characteristic impedance Z_0 and propagation constant $\gamma = \alpha + \mathrm{i}\beta$,

$$\begin{pmatrix} A & B \\ C & D \end{pmatrix}_\mathrm{TL} = \begin{pmatrix} \cosh(\gamma l) & Z_0 \sinh(\gamma l) \\ \frac{1}{Z_0}\sinh(\gamma l) & \cosh(\gamma l) \end{pmatrix}, \tag{13}$$

we get the total $ABCD$ matrix as product and from this the transmission parameter [40]

$$S_{21} = \frac{2}{A + B/Z_0 + CZ_0 + D}. \tag{14}$$

The transmitted power ratio $|S_{21}|^2$ calculated for $l = 9.2\,\mathrm{mm}$, $\alpha = 0.001\,\mathrm{m}^{-1}$ and $\epsilon_\mathrm{eff} = 5.5$ around the first resonance for the three different shorts shown in figure 2(a) is depicted in 2(b).

The external quality factors for the three inductances can be calculated according to equation (10) as $Q_\mathrm{ext1} \approx 158\,300$, $Q_\mathrm{ext2} \approx 38\,800$ and $Q_\mathrm{ext3} \approx 5800$. As the geometry of the shorts can be easily varied, any interesting coupling strength should thus be available. The external quality factor could also be made tunable by using superconducting quantum interference devices (SQUIDs) as shorts instead of simple connections. With a related approach, it has been demonstrated that the resonance frequency of coplanar resonators can be made tunable by integrating SQUIDs as tunable lumped element series inductances into the waveguide center conductor [24, 42, 43].

3. Persistent current trap for paramagnetic atoms

In this section, we show how the inductively coupled resonator can be used as a persistent current trap for ultracold atoms. Our calculations have been done for ^{87}Rb atoms, whose ground state hyperfine transition from $|0\rangle := \left|5S_{1/2}, F = 1, m_F = -1\right\rangle$ to $|1\rangle := \left|5S_{1/2}, F = 2, m_F = 1\right\rangle$

with a zero magnetic field transition frequency of $\omega_r/2\pi \approx 6.834\,\mathrm{GHz}$ [44] is to be coupled to the cavity. The magnetic trapping potential for these low field seeking states is given by $U(\vec{r}) = m_F g_F \mu_B |\vec{B}(\vec{r})|$ with the strength of the magnetic induction $|\vec{B}(\vec{r})|$ and the Bohr magneton μ_B. The Landé-factors for $|0\rangle$ and $|1\rangle$ are $g_{F=1} = -1/2$ and $g_{F=2} = +1/2$, respectively. In short, a local minimum of $|\vec{B}(\vec{r})|$ constitutes a trap for atoms in both states $|0\rangle$ and $|1\rangle$.

We show how such a trap can be created with the resonator structure described in section 2. The description follows the recently demonstrated method of [29]. The trap is created by freezing a magnetic flux into the closed loops of the resonator and superimposing an external field. For our simulations, we have simplified the resonator geometry, specifically we have reduced the length to $l_r = 1\,\mathrm{mm}$ and omitted the feed lines, cf figure 3(a). However, at a position half a millimeter away from the ends of the structure, where we characterize the trap, these changes have only a negligibly small influence on the magnetic field configuration, in particular for small distances to the resonator. We do not discuss the trap properties along the y-direction here, but there are well controllable methods at hand, for example perpendicular confinement wires below the chip which can be chosen to manipulate the position and the depth of the trap in the y-direction, almost independently of the trap geometry in the x–z-plane [29, 45]. Such additional trap wires can be mounted several hundreds of microns below the superconducting film structures [29] and create only small magnetic fields on the order of $\sim 100\,\mu\mathrm{T}$ at the chip surface. Hence, we do not expect the confinement wires to have a significant impact onto the resonator properties.

For the geometry shown in figure 3(a), we numerically solve the London equations for film thickness $d = 500\,\mathrm{nm}$ and magnetic penetration depth $\lambda_L = 120\,\mathrm{nm}$ with 3D-MLSI [41] for different magnetic field configurations. The first important input parameter is the freezing field B_{freeze}, which defines how much flux is trapped in the closed loops. In an experiment, this freezing field would correspond to a homogeneous field in z-direction $\vec{B}^z_{\mathrm{freeze}} = -B_{\mathrm{freeze}}\vec{e}_z$ which is applied as the resonator is cooled through the transition temperature. The field in the z-direction is then swept into the opposite direction to $B^z\vec{e}_z = (-B_{\mathrm{freeze}} + B_{\mathrm{bias}})\,\vec{e}_z$ with $B_{\mathrm{bias}} > B_{\mathrm{freeze}}$, where B_{bias} denotes the difference between the freezing field and the final B^z. This field change by B_{bias} does not change the amount of flux in the loops defined by B_{freeze}. To generate a harmonic potential at the trap minimum and to reduce Majorana atom losses by lifting the degeneracy of the Zeeman sublevels [46], an additional homogeneous offset field is applied in the y-direction $\vec{B}^y = B_{\mathrm{off}}\vec{e}_y$. Finally, we include gravity as $U_{\mathrm{grav}} = -m_{\mathrm{Rb}} g z$ with $g = 9.81\,\mathrm{m\,s^{-2}}$.

The resulting potential energy above the resonator structure is shown in figure 3(b) for $B_{\mathrm{freeze}} = 10^{-4}\,\mathrm{T}$, $B_{\mathrm{bias}} = 4 \times 10^{-4}\,\mathrm{T}$ and $B_{\mathrm{off}} = 3.228 \times 10^{-4}\,\mathrm{T}$. The chosen offset field corresponds to the *magic* offset field at which the differential Zeeman shift between $|0\rangle$ and $|1\rangle$ is in first order insensitive to magnetic field inhomogeneities [47]. The distance of the energy minimum from the surface of the chip z can be varied by changing B_{bias}, where an increase of B_{bias} is related to a decrease of z.

At the same time, a change of B_{bias} leads to a change of the trap properties, in particular of the trap frequencies $\omega_x/2\pi$ and $\omega_z/2\pi$. These frequencies correspond to the motional oscillation frequencies of trapped atoms in x- and z-direction, respectively. The trap frequencies can be extracted from our simulations by a harmonic approximation around the energy minimum. Figure 3(c) shows the extracted frequencies versus trap distance from the chip surface, calculated for different freezing and bias fields. Results of the simulations indicate that a field parameter set can be found for any distance between $z = 5$ and $40\,\mu\mathrm{m}$ that creates trapping

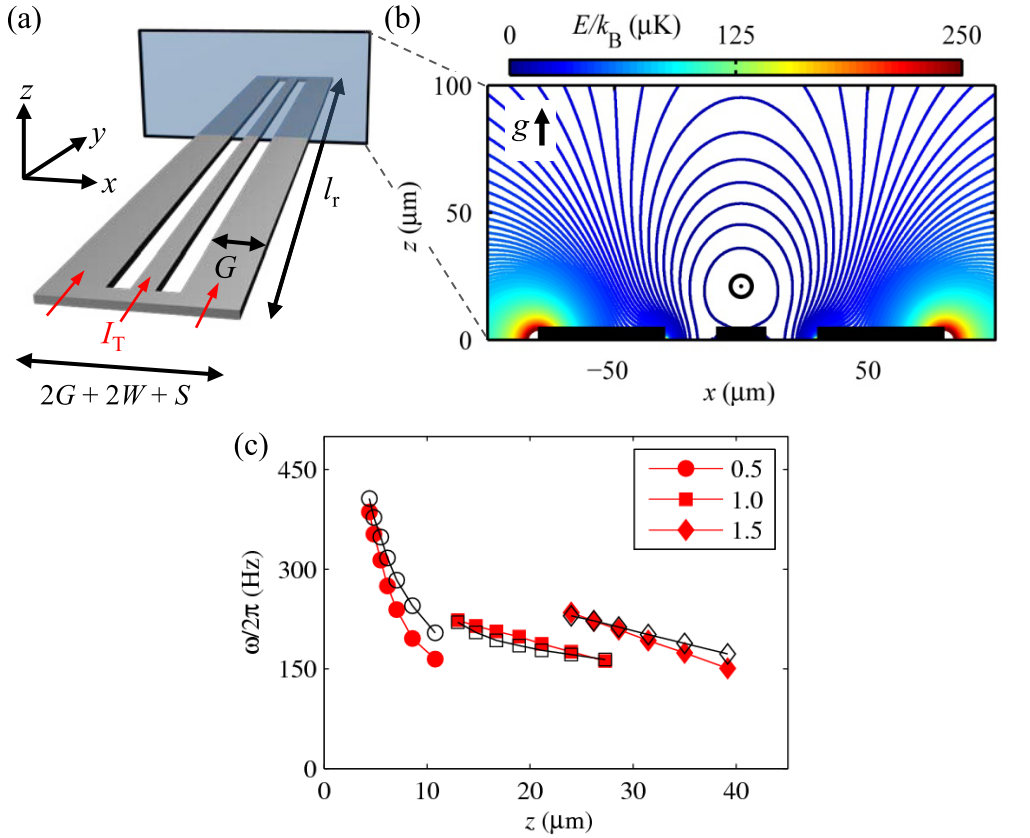

Figure 3. (a) Superconducting geometry used for the 3D simulation of magnetic fields. The x–z-plane, where we extract the magnetic fields for the trap calculations is marked by a transparent rectangle in the center of the structure. Here, the width of the center conductor is $S = 20\,\mu\text{m}$, the width of the gap is $W = 20\,\mu\text{m}$ and the ground plane width is $G = 50\,\mu\text{m}$. (b) Calculated potential energy for a ^{87}Rb atom in the vicinity of a structure as depicted in (a). The minimum is marked by the black encircled dot. The total magnetic field results from $B_{\text{freeze}} = 10^{-4}\,\text{T}$, $B_{\text{bias}} = 4 \times 10^{-4}\,\text{T}$ and $B_{\text{off}} = 3.228 \times 10^{-4}\,\text{T}$. Gravity g is included. Isolines are separated by $\Delta E/k_B = 2\,\mu\text{K}$. Black bars at the bottom represent the superconductor (thickness not to scale). (c) Trap frequencies $\omega_x/2\pi$ (open symbols) and $\omega_z/2\pi$ (full symbols) versus trap distance to the chip surface z. Different symbols correspond to different freezing fields, numbers in legend are given in $10^{-4}\,\text{T}$. Bias field step size is $\Delta B_{\text{bias}} = 0.25 \times 10^{-4}\,\text{T}$ with a maximum value of $B_{\text{bias}} = 5 \times 10^{-4}\,\text{T}$ for each freezing field (data point closest to the chip). Gravity and $B_{\text{off}} = 3.228 \times 10^{-4}\,\text{T}$ are included.

frequencies between 150 and 500 Hz. Traps characterized by this frequency range have been shown to be suitable for efficient evaporative cooling and are favorable for achieving long atomic coherence times [20]. We have also performed simulations for ground plane widths $G = 20$ and 100 μm and the results are qualitatively—and with minor adjustments in the trapping parameters also quantitatively—identical to the ones presented here.

A critical step in the experiments is the loading of cold atoms into such a persistent current trap. One way to bring the atoms to the superconducting chip is to prepare a cold cloud in a magneto-optical trap and transfer it to the surface of a cryostat by optical tweezers parallel to the chip surface [48]. For this transfer, the optical dipole trap has to be vertically offset from the chip surface by several 100 µm, because the laser beam must not be optically disturbed. When the atoms have reached the desired position above the chip surface, a magnetic trap generated by currents running on the chip has to be turned on and the tweezer is turned off to load the atoms from the optical dipole trap to the on-chip magnetic trap. This transfer has to be performed at a fixed vertical distance from the chip (the aforementioned several 100 µm), which is much larger than the surface distances of the persistent current trap discussed above.

In our approach, it is possible to use the resonator structure itself as transport current lead which is fed with a transport current on the order of $I_T = 0.5$ A in y-direction, cf figure 3(a). Together with a homogeneous field in the x-direction B^x, on the order of some 10^{-4} T, the magnetic trap needed for the atom transfer can be formed at a distance several 100 µm from the surface. By trapping flux in the holes of the resonator before the transport current is applied, and by a proper sweep of B^x, B^z, B_{off} and I_T the trap can be continuously transformed from the loading configuration to the persistent configuration shown in figure 3(b). Figure 4(a) schematically depicts the sweep of the control parameters which are used during such a freezing and transport procedure I–V, and in figure 4(b) the position and the trap frequencies during III–V are plotted.

Once the atoms are in the persistent trap, it is possible to shuttle the atoms directly into the resonator gap with another field sweep, where the electromagnetic field strength of the resonator mode reaches a maximum. For this, we start from the final configuration of the loading sequence (figure 3(b)) and ramp up B^x until the trap minimum is approximately above the right gap of the waveguide structure (V–VI in figure 4(a)). B^z is then increased until the trap center is a few micrometers above the chip surface (VI–VII). The corresponding position of the energy minimum together with the trap frequencies is plotted in figure 4(c). We note that the trap frequencies increase when the minimum is shifted very close to the surface due to the strong field gradients at that position. However, by altering the geometrical parameters of the resonator, such as the gap width, and by varying the applied fields, the trap parameters can be modified and optimized. But as the coupling strength between the atoms and the cavity is also sensitive to the resonator geometry, an ideal resonator trap must be the result of a careful balance between favorable trap frequencies and a maximized coupling.

We now address the possibility of Abrikosov vortices entering the resonator structures in a real experiment. For this discussion we must discriminate between vortices associated with the freezing field, the bias field and the transport current.

If the freezing procedure of flux into the loops is performed as discussed above, i.e. a homogeneous field on the order of 10^{-4} T is applied during cooldown, vortices will be trapped in the leads [49]. These vortices would probably modify the trap position and frequency, however according to our earlier experiments and simulations on a similar superconducting structure this change is relatively small (∼20%). These vortices can be controlled to a certain degree by artificially patterning preferential locations as antidots or slots for them into the structure, which at the same time would be feasible to reduce the vortex associated performance drop of the resonator [50–52]. Also, the magnetic noise generated by moving vortices, leading to atom spin flips in the cloud and hence to atom losses [53], can be reduced with artificial pinning sites [54]. Another possibility to load the loops with flux while simultaneously avoiding vortices

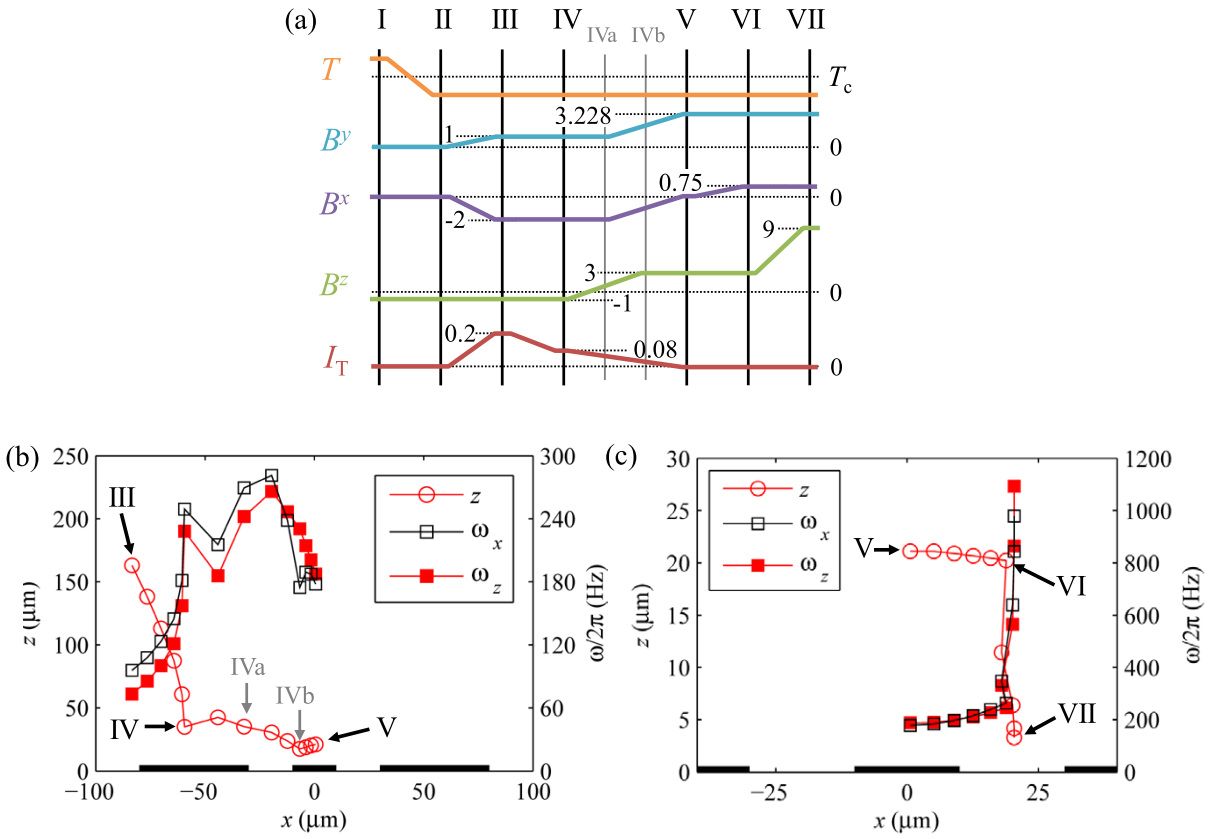

Figure 4. (a) Temperature, magnetic field and transport current sweep sequence to prepare the trap for the arrival of atoms (I–III), to continuously transfer atoms from the loading position into the persistent current trap (III–V) and to shuttle the atoms into the waveguide gap (V–VII). Numbers indicate fields in units of 10^{-4} T and currents in A. Numerically obtained position z of the energy minimum (open circles) and trap frequencies $\omega_x/2\pi$ (open squares) and $\omega_z/2\pi$ (full squares) versus position x are shown for III–V in (b) and for V–VII in (c). Gravity is included in all simulations.

would be to locally break the superconductivity in the ground conductors by lasers or on-chip resistive heaters. When a magnetic freezing field $B_{\text{freeze}} \sim 10^{-4}$ T is then applied and the heating is turned off, the flux related to the freezing field will be frozen into the loops.

Evaluating the possibility of vortices entering the structure due to magnetic fields applied in the superconducting state requires an estimation of the magnetic field at the edge of the resonator geometry. Assuming the thickness of the superconductor is $d = 500$ nm and a continuous $G_{\text{tot}} = 160\,\mu$m wide structure, we find according to [55] an edge field $B_{\text{edge}} = B^z\sqrt{G_{\text{tot}}/d} = 18 \times 10^{-3}$ T when $B^z = 10^{-3}$ T is applied perpendicular to the trap resonator. For comparison we calculate the lower critical field of typical (dirty) niobium films with $\lambda_L = 120$ nm and Ginzburg–Landau parameter $\kappa = 10$ according to [56] as $B_{c1} = 32 \times 10^{-3}$ T. This result indicates that vortices are unlikely to enter the structures in fields $B \leqslant 10^{-3}$ T which are applied in the superconducting state. Note, that here we have neglected edge barrier effects, which typically increase the penetration field.

Finally, we consider the fields generated by the loading transport current. The magnetic field at the edge of our structures of thickness $d = 500\,\mathrm{nm}$ can be estimated as $B^I_{\mathrm{edge}} = \mu_0 I_\mathrm{T}/(2\pi\sqrt{dG_\mathrm{tot}}) \approx 13 \times 10^{-3}\,\mathrm{T}$ under the assumption that it is just a single strip of total width G_tot [55]. For the calculation we have used $I_\mathrm{T} = 0.5\,\mathrm{A}$ the vacuum permeability $\mu_0 = 4\pi \times 10^{-7}\,\mathrm{V\,s\,A^{-1}\,m^{-1}}$ and $G_\mathrm{tot} = 120\,\mu\mathrm{m}$ which is the most conservative estimation for the total width of the structure. Again, the result is well below B_{c1}.

4. Conclusions

We have shown that superconducting short-ended half wavelength resonators can be designed with the desired properties for quantum information processing purposes, in particular regarding external quality factors. By using such inductively coupled instead of capacitively coupled resonators, it is possible to use the resonators to create a persistent current based magnetic trapping potential for ultracold atoms. Furthermore we have shown by means of numerical simulations that by varying external magnetic fields and a transport current in the resonator, the trapped atoms can be continuously transported from far away from the chip into the persistent trap and from there directly into the resonator gap. The simulations also revealed that in the persistent current resonator trap and during the transport, the trap frequencies can be kept in a regime very favorable for long atomic coherence times. In conclusion, the presented approach provides an elegant solution to the question how the coupling between superconducting circuits and atom clouds can be practically implemented.

Acknowledgments

This work was supported by the DFG via the SFB/TRR 21 and the Open Access Publishing Fund of Tübingen University. It was also supported by the European Research Council via SOCATHES. DB and HH gratefully acknowledge support from the Evangelisches Studienwerk e V Villigst. MK gratefully acknowledges support by the Carl–Zeiss Stiftung. The authors thank Stefan Wünsch from the Karlsruhe Insitute of Technology for fruitful discussions and Simon Bell from the University of Tübingen for valuable comments.

References

[1] Wallraff A, Schuster D I, Blais A, Frunzio L, Huang R-S, Majer J, Kumar S, Girvin S and Schoelkopf R J 2004 *Nature* **431** 162
[2] Fink J M, Göppl M, Baur M, Bianchetti R, Leek P J, Blais A and Wallraff A 2008 *Nature* **454** 315
[3] Hofheinz M *et al* 2009 *Nature* **459** 546
[4] Niemczyk T *et al* 2010 *Nature Phys.* **6** 772
[5] Wilson C M, Johansson G, Pourkabirian A, Simoen M, Johansson J R, Duty T, Nori F and Delsing P 2011 *Nature* **479** 376
[6] O'Connell A D *et al* 2010 *Nature* **464** 697
[7] Zhou X, Hocke F, Schliesser A, Marx A, Huebl H, Gross R and Kippenberg T J 2013 *Nature Phys.* **9** 179
[8] DiCarlo L *et al* 2009 *Nature* **460** 240
[9] Mariantoni M *et al* 2011 *Science* **334** 61
[10] Reed M D, DiCarlo L, Nigg S E, Sun L, Frunzio L, Girvin S M and Schoelkopf R J 2012 *Nature* **482** 382

[11] Lucero E *et al* 2012 *Nature Phys.* **8** 719
[12] Fedorov A, Steffen L, Filipp S, da Silva M P and Wallraff A 2012 *Nature* **481** 170
[13] Paik H *et al* 2011 *Phys. Rev. Lett.* **107** 240501
[14] Rigetti C *et al* 2012 *Phys. Rev.* B **86** 100506
[15] André A, DeMille D, Doyle J M, Lukin M D, Maxwell S E, Rabl P, Schoelkopf R J and Zoller P 2006 *Nature Phys.* **2** 636
[16] Rabl P, DeMille D, Doyle J M, Lukin M D, Schoelkopf R J and Zoller P 2006 *Phys. Rev. Lett.* **97** 033003
[17] Petrosyan D and Fleischhauer M 2008 *Phys. Rev. Lett.* **100** 170501
[18] Verdú J, Zoubi H, Koller C, Majer J, Ritsch H and Schmiedmayer J 2009 *Phys. Rev. Lett.* **103** 043603
[19] Henschel K, Majer J, Schmiedmayer J and Ritsch H 2010 *Phys. Rev.* A **82** 033810
[20] Deutsch C, Ramirez-Martinez F, Lacroûte C, Reinhard F, Schneider T, Fuchs J N, Piéchon F, Laloë F, Reichel J and Rosenbusch P 2010 *Phys. Rev. Lett.* **105** 020401
[21] Dudin Y O, Li L and Kuzmich A 2013 *Phys. Rev.* A **87** 031801
[22] Hafezi M, Kim Z, Rolston S L, Orozco L A, Lev B L and Taylor J M 2012 *Phys. Rev.* A **85** 020302
[23] Schuster D I *et al* 2010 *Phys. Rev. Lett.* **105** 140501
[24] Kubo Y *et al* 2010 *Phys. Rev. Lett.* **105** 140502
[25] Wu H, George R E, Wesenberg J H, Mølmer K, Schuster D I, Schoelkopf R J, Itoh K M, Ardavan A, Morton J J L and Briggs G A D 2010 *Phys. Rev. Lett.* **105** 140503
[26] Amsüss R *et al* 2011 *Phys. Rev. Lett.* **107** 060502
[27] Probst S, Rotzinger H, Wünsch S, Jung P, Jerger M, Siegel M, Ustinov A V and Bushev P 2013 *Phys. Rev. Lett.* **110** 157001
[28] Hogan S D, Agner J A, Merkt F, Thiele T, Filipp S and Wallraff A 2012 *Phys. Rev. Lett.* **108** 063004
[29] Bernon S *et al* 2013 *Nature Commun.* **4** 2380
[30] Nirrengarten T, Qarry A, Roux C, Emmert A, Nogues G, Brune M, Raimond J-M and Haroche S 2006 *Phys. Rev. Lett.* **97** 200405
[31] Cano D, Kasch B, Hattermann H, Kleiner R, Zimmermann C, Koelle D and Fortágh J 2008 *Phys. Rev. Lett.* **101** 183006
[32] Mukai T, Hufnagel C, Kasper A, Meno T, Tsukada A, Semba K and Shimizu F 2007 *Phys. Rev. Lett.* **98** 260407
[33] Shimizu F, Hufnagel C and Mukai T 2009 *Phys. Rev. Lett.* **103** 253002
[34] Müller T, Zhang B, Fermani R, Chan K S, Lim M J and Dumke R 2010 *Phys. Rev.* A **81** 053624
[35] Siercke M, Chan K S, Zhang B, Beian M, Lim M J and Dumke R 2012 *Phys. Rev.* A **85** 041403
[36] Matthaei G L, Young L and Jones E M T 1964 *Microwave Filters, Impedance-Matching Networks and Coupling Structures* (New York: McGraw-Hill)
[37] Everard J K A and Cheng K K M 1993 *IEEE Trans. Microw. Theory Technol.* **41** 1568
[38] Vogt A and Jutzi W 1997 *IEEE Trans. Microw. Theory Technol.* **45** 492
[39] Göppl M, Fragner A, Baur M, Bianchetti R, Filipp S, Fink J M, Leek P J, Puebla G, Steffen L and Wallraff A 2008 *J. Appl. Phys.* **104** 113904
[40] Pozar D M 1998 *Microwave Engineering* 2nd edn (New York: Wiley)
[41] Khapaev M M, Kupriyanov M Y, Goldobin E and Siegel M 2003 *Supercond. Sci. Technol.* **16** 24
[42] Sandberg M, Wilson C M, Persson F, Bauch T, Johansson G, Shumeiko V, Duty T and Delsing P 2008 *Appl. Phys. Lett.* **92** 203501
[43] Palacios-Laloy A, Nguyen F, Mallet F, Bertet P, Vion D and Esteve D 2008 *J. Low Temp. Phys.* **151** 1034
[44] Bize S, Sortais Y, Santos M S, Mandache C, Clairon A and Salomon C 1999 *Europhys. Lett.* **45** 558
[45] Fortágh J and Zimmermann C 2007 *Rev. Mod. Phys.* **79** 235
[46] Sukumar C V and Brink D M 1997 *Phys. Rev.* A **56** 2451
[47] Harber D M, Lewandowski H J, McGuirk J M and Cornell E A 2002 *Phys. Rev.* A **66** 053616
[48] Cano D, Hattermann H, Kasch B, Zimmermann C, Kleiner R, Koelle D and Fortágh J 2011 *Eur. Phys. J.* D **63** 17

[49] Stan G, Field S B and Martinis J M 2004 *Phys. Rev. Lett.* **92** 097003
[50] Song C, DeFeo M P, Yu K and Plourde B L T 2009 *Appl. Phys. Lett.* **95** 232501
[51] Bothner D, Gaber T, Kemmler M, Koelle D and Kleiner R 2011 *Appl. Phys. Lett.* **98** 102504
[52] Bothner D *et al* 2012 *Appl. Phys. Lett.* **100** 012601
[53] Nogues G, Roux C, Nirrengarten T, Lupaşcu A, Emmert A, Brune M, Raimond J-M, Haroche S, Plaçais B and Greffet J-J 2009 *Eur. Phys. Lett.* **87** 13002
[54] Selders P and Wördenweber R 2000 *Appl. Phys. Lett.* **76** 3277
[55] Zeldov E, Clem J R, McElfresh M and Darwin M 1994 *Phys. Rev.* B **49** 9802
[56] Brandt E H 1995 *Rep. Prog. Phys.* **58** 1465

Publication VI

Suppression of dissipation in Nb thin films with triangular antidot arrays by random removal of pinning sites

M. Kemmler,[1,*] D. Bothner,[1] K. Ilin,[2] M. Siegel,[2] R. Kleiner,[1] and D. Koelle[1]
[1]*Physikalisches Institut—Experimentalphysik II and Center for Collective Quantum Phenomena and their Applications, Universität Tübingen, Auf der Morgenstelle 14, D-72076 Tübingen, Germany*
[2]*Institut für Mikro- und Nanoelektronische Systeme, Universität Karlsruhe, Hertzstr. 16, D-76187 Karlsruhe, Germany*
(Received 10 September 2008; revised manuscript received 9 April 2009; published 8 May 2009)

The depinning current I_c versus applied magnetic field B close to the transition temperature T_c of Nb thin films with randomly diluted triangular arrays of antidots is investigated. Our experiments confirm essential features in $I_c(B)$ as predicted by Reichhardt and Olson Reichhardt [Phys. Rev. B **76**, 094512 (2007)]. We show that, by introducing disorder into periodic pinning arrays, I_c can be enhanced. In particular, for arrays with fixed density n_p of antidots, an increase in dilution P_d induces an increase in I_c and decrease of the flux-flow voltage for $B > B_p = n_p \Phi_0$.

DOI: 10.1103/PhysRevB.79.184509 PACS number(s): 74.25.Qt, 74.25.Sv, 74.78.Na

I. INTRODUCTION

The investigation of vortices in type-II superconductors in the presence of tailored pinning potential landscapes has attracted a lot of theoretical and experimental interest. On the one hand, vortices in superconductors may act as a model system in order to investigate general properties such as the dynamics and phase transitions in systems of interacting particles (e.g., colloidal suspensions,[1,2] Wigner crystals,[3] charge-density waves,[4] or various types of ratchets and Brownian motors[5–7]). On the other hand, the ability to manipulate and control the static and dynamic properties of vortices is fundamental for superconducting device applications.[8]

Modern lithography techniques allow the placement of artificial pinning sites into superconducting thin films with well-defined size, geometry, and spatial arrangement. In case of periodic arrangements, enhanced vortex pinning was found for magnetic fields, at which the vortex lattice is commensurate with the pinning array.[9–14] The enhanced pinning leads, e.g., to peaks in the critical depinning current I_c at multiples of a so-called first matching field $B_p = n_p \Phi_0$; here the density of vortices carrying one flux quantum $\Phi_0 = h/2e$ equals the density of pinning sites n_p. However, at nonmatching fields the vortex lattice is less pinned due to elastic deformations and formation of interstitial vortices. Hence, the question arises whether other arrangements—between the two extremes of periodic and random pinning arrangements—may lead to an enhanced vortex pinning over a broader range of applied magnetic field B.

Recently, it has been shown by numerical simulations[15,16] and experimentally[17–19] that a quasiperiodic arrangement of pinning sites produces additional commensurability effects and hence an enhanced pinning below the first matching field. A different proposal was made very recently by Reichhardt and Olson Reichhardt.[20] By molecular-dynamics simulations they investigated periodic pinning arrays that have been diluted by randomly removing the fraction P_d of pins, while keeping the pin density n_p fixed. Such arrays are very interesting, since with increasing dilution the pinning potential undergoes a gradual transition from periodic to purely random. Therefore, this model is suitable to explore the intermediate region between order and disorder, as it is usually found in real world. Interestingly, the simulations showed that the introduction of disorder leads to an enhanced critical current above the first matching field. In periodic pinning arrays the vortices sitting at the pinning sites form easy flow channels for interstitial vortices,[21] while for randomly diluted pinning arrays channeling should be suppressed.[20] This approach is also interesting from a general point of view, as the presence of disorder in competition with periodic potentials is also investigated in many other physical systems, e.g., two-dimensional conductors,[22] Ising ferromagnets,[23] and Josephson junction arrays.[24,25] For related recent work on vortex phases, see Ref. 26.

In this work, we present results on the experimental investigation of vortex pinning and flow in superconducting Nb thin films containing randomly diluted triangular arrays of submicron holes (antidots) as pinning sites. We studied $I_c(B)$ at variable temperature T close to the superconducting transition temperature T_c and we compare pinning arrays having different dilution, considering two different scenarios: (i) *Scaled lattices*. For different values of P_d, we fix the density n_p of pinning sites. Accordingly, the lattice parameter (smallest separation between pinning sites) scales as $a(P_d) = a(0)\sqrt{1-P_d}$. In this scenario a controlled transition from periodic to random arrangement of antidots is investigated. (ii) *Fixed lattices*. Here, we fix the lattice parameter a for different values of P_d. Accordingly, the density of pinning sites scales as $n_p(P_d) = (1-P_d) n_p(0)$. Here, with increasing P_d a transition to plain films (no antidots) is treated.

Our experimental results confirm essential features as predicted in Ref. 20. The fixed and scaled lattices show two different kinds of matching effects, which differently depend on temperature. Furthermore, the scaled lattices show an enhancement of I_c at magnetic fields above B_p with increasing dilution P_d. This effect is caused by suppression of vortex channeling and can be also observed in the dynamic regime, i.e., by measuring current-voltage (IV) characteristics.

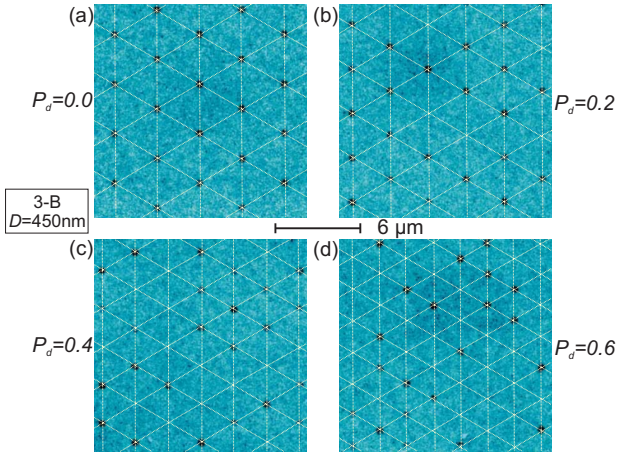

FIG. 1. (Color online) Scanning electron microscopy images of Nb thin films with randomly diluted antidot arrays; lines illustrate the triangular lattices. Lattice parameters $a(P_d)=3.4-2.1$ μm, for dilutions $P_d=0-0.6$, are scaled to maintain constant antidot density $n_p=0.1$ μm^{-2}.

II. SAMPLES

The experiments were carried out on $d=60$ nm thick Nb films which were deposited by dc magnetron sputtering in the same run on four separate Si substrates with 1 μm thick SiO_2 on top. Patterning was performed by *e*-beam lithography and lift off to produce Nb bridges of width $W=200$ μm and length $L=640$ μm. The bridges contain circular antidots (diameter $D=260-550$ nm) arranged in a triangular lattice that has been randomly diluted, with dilutions $P_d=0$ ("undiluted array"), 0.2, 0.4, 0.6, 0.8, and 1 ("plain" film, without antidots). Each chip (nos. 1–4) contains two or three sets (A, B, C) of bridges. Each set has six bridges with different values for $P_d=0-1$. The antidot diameter D is kept constant within each set and varies from set to set. Chips 1 and 2 contain sets of bridges with fixed lattice parameter $a=1.5$ μm, i.e., the density of vertices of the corresponding triangular lattice is $n_l=\frac{2}{\sqrt{3}}\frac{1}{a^2}=0.5$ μm^{-2}, which corresponds to the "lattice matching field" $B_l\equiv n_l\Phi_0=1.1$ mT (denoted as B_ϕ^* in Ref. 20). For those two chips, the antidot density n_p decreases from 0.5 to 0.1 μm^{-2} with increasing P_d from 0 to 0.8. Chips 3 and 4 contain sets of bridges with scaled lattice parameters $a(P_d)=3.4-1.5$ μm for $P_d=0$ to $P_d=0.8$, respectively, in order to have a fixed antidot density $n_p=0.1$ μm^{-2} and "pin density" matching field $B_p=0.21$ mT (denoted as B_ϕ in Ref. 20), with $N_p\approx 12\,500$ antidots in each bridge. Below we present results obtained on bridges from sets 1-B ($D=300$ nm), 3-B ($D=450$ nm), [c.f. Fig. 1], 4-B ($D=360$ nm), and 4-A ($D=260$ nm). A summary of the relevant sample parameters is given in Table I.

III. EXPERIMENTAL SETUP

For electric transport measurements, the samples are mounted in an evacuated chamber which is inserted into a glass fiber cryostat filled with liquid helium. The cryostat is surrounded by a three-layer magnetic shield and is placed in an rf-shielded room. A superconducting magnet allows to apply a well-controlled magnetic field. The sample is mounted together with a Si-diode temperature sensor on a sapphire substrate. Heating the backside of the sapphire substrate (covered by an absorbing layer) via a temperature-stabilized diode laser, the sample temperature can be adjusted from 4.2 up to 100 K. Using a temperature controller with a feedback loop to control the laser heating power, we achieve a temperature stability, measured at the Si diode, of about 1 mK. The setup allows to perform electric transport measurements on four bridges on a chip simultaneously.

TABLE I. Antidot diameter D, antidot density n_p, and vertex density $n_l\propto 1/a^2$ of the sets of bridges with randomly diluted antidot arrays used in this paper. Each set contains five bridges with different dilutions $P_d=0$ (undiluted array), 0.2, 0.4, 0.6, 0.8, and 1 (plain film, without antidots).

	D (nm)	n_p (μm^{-2})	n_l (μm^{-2})
1-B	300	$(1-P_d)0.5$	0.5 (fixed a)
3-B	450	0.1 (scaled a)	$0.5/(1-P_d)$
4-A	260	0.1 (scaled a)	$0.5/(1-P_d)$
4-B	360	0.1 (scaled a)	$0.5/(1-P_d)$

IV. RESULTS

To characterize our devices, we first measured resistance R vs T at $B=0$ and determined T_c and normal resistance $R_n\equiv R(T=10$ K) (with bias current $I=2$ μA) of the different bridges on each chip. Due to the strong influence of the reduced temperature $t\equiv T/T_c$ (for T close to T_c) on the characteristic length scales, i.e., the London penetration depth $\lambda(t)$ and coherence length $\xi(t)$, and on $I_c(t)$, the determination of T_c plays an important role for the comparison and interpretation of the performance of pinning arrays with different P_d. We defined T_c by linear extrapolation of the $R(T)$ curves in the transition region to $R=0$, i.e., T_c marks the onset of resistance. For all samples we find $T_c\approx 8.5$ K with a variation of a few mK within each set of bridges and $R_n=5.0-5.8$ Ω, depending on n_p and D. Within the sets ($D=const$) with $n_p=const$ (scaled lattices), R_n varies by less than $\pm 2\%$ from bridge to bridge. The plain film (from set 4-A) has $R_n=5.0$ Ω, which yields a normal resistivity $\rho_n=R_n dW/L=9.4$ $\mu\Omega$ cm. With the relation $\rho\ell=3.72\times 10^{-6}$ $\mu\Omega$ cm^2,[27] we estimate for the mean-free path $\ell=4.0$ nm. All I_c values were determined with a voltage criterion $V_c=1$ μV.

A. Commensurability effects in randomly diluted triangular arrays

Figure 2 shows $I_c(B/B_p)$ patterns of four randomly diluted bridges with similar antidot size at various temperatures $t=T/T_c=0.9995-0.9965$. I_c was normalized to its maximum value at $B=0$. Two bridges (from set 4-A) have the same antidot density $n_p=0.1$ μm^{-2} and dilution $P_d=0.2$ (a) and $P_d=0.4$ (c). The two other bridges (from set 1-B) have larger

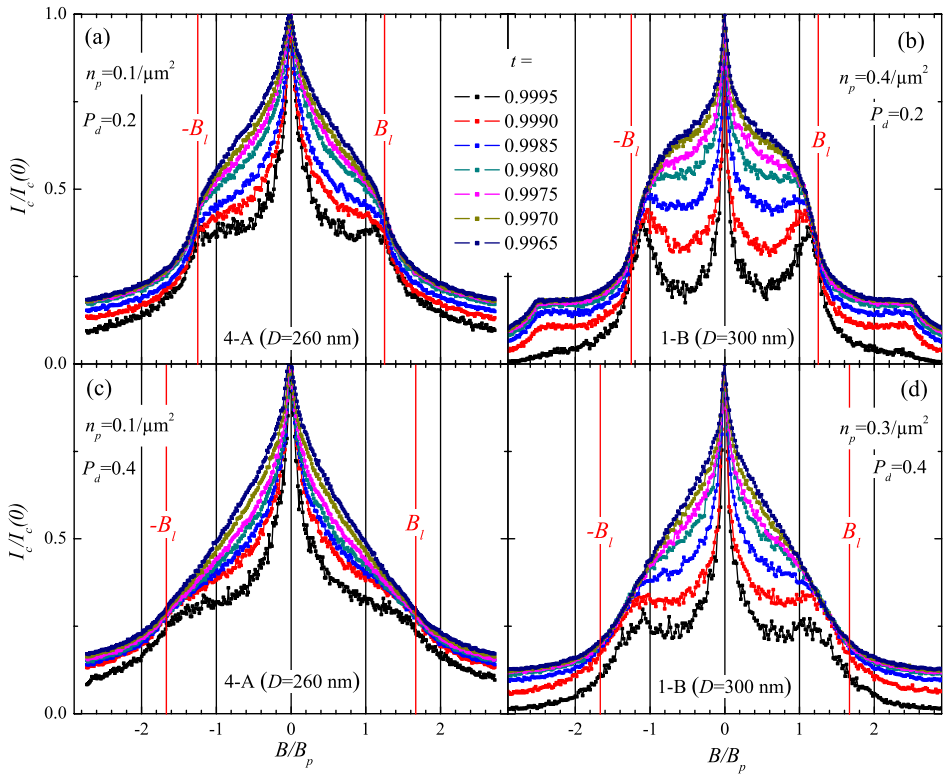

FIG. 2. (Color online) (Double column) $I_c/I_c(0)$ vs B/B_p for randomly diluted arrays at different reduced temperatures (I_c increases with decreasing t). Comparison of the dependence on the antidot density n_p for samples with [(a) and (b)] P_d=0.2 and [(c) and (d)] P_d=0.4.

antidot densities n_p=0.4 μm^{-2} with P_d=0.2 (b) and n_p =0.3 μm^{-2} with P_d=0.4 (d). The applied field is always normalized to $B_p \propto n_p$.

For the highest t=0.9995, a clear peak in $I_c(B)$ indicates matching of the vortex lattice with the pinning array, as shown in Fig. 2(b). The position of the peak is located between B_p and B_l. This indicates that indeed "pin density matching" is observed; however, as pointed out in Ref. 20, for a diluted periodic pinning array at $B=B_p$, the vortex configuration contains numerous topological defects. Hence, commensurability effects at B_p can only be observed when pinning is so strong that the lattice distortion energy, associated with the deviation from an ideal triangular vortex lattice, can be overcome. This is most likely to be observed for the samples with higher density of pinning sites. Accordingly, for a given P_d, the matching peak is more pronounced in the samples with 3 and 4 times larger n_p, as shown in Fig. 2 by comparison of graphs (a) and (b) for P_d=0.2 and by comparison of graphs (c) and (d) for P_d=0.4.

With decreasing n_p and t and with increasing P_d, the peak in $I_c(B)$ gradually transforms into a shoulderlike structure, located close to B_p. Following the evolution of $I_c(B)$ with decreasing temperature shows that $I_c(B<B_p)/I_c(0)$ increases most whereas $I_c(B_l)/I_c(0)$ is almost independent of t. For the larger P_d=0.4, this leads gradually to a transformation of the shoulderlike structure into a triangular-shaped $I_c(B)$ pattern without any indication of matching effects, either at B_p or B_l. Nevertheless, I_c for P_d=0.4 is still significantly enhanced over I_c for samples without antidots, as will be shown below.

B. Different dilution

In the following, we directly compare pinning arrays having different dilutions P_d at the same reduced temperature.

1. Fixed lattice parameter—transition to plain

Figure 3 shows $I_c(B)$ patterns of samples with fixed lattice parameter a=1.5 μm (n_l=0.5 μm^{-2}) at t=0.9990 (a) and t =0.9965 (b). The B axis is normalized to the lattice matching field B_l, which is the same for all perforated bridges within this set. The sample with P_d=0 shows pronounced peaks in $I_c(B)$ which are located at $\pm B_l$ and $\pm 2B_l$, indicating a saturation number $n_s \geq 2$ (Refs. 28 and 29) for both temperatures.

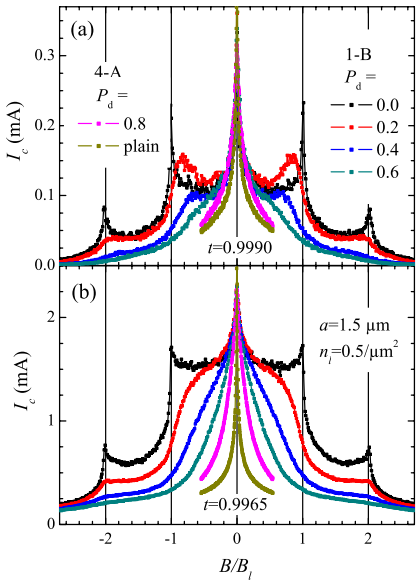

FIG. 3. (Color online) I_c vs B/B_l at (a) t=0.9990 and (b) 0.9965 for arrays with fixed lattice parameter a and variable dilution P_d. $I_c(B>B_l)$ decreases with increasing P_d.

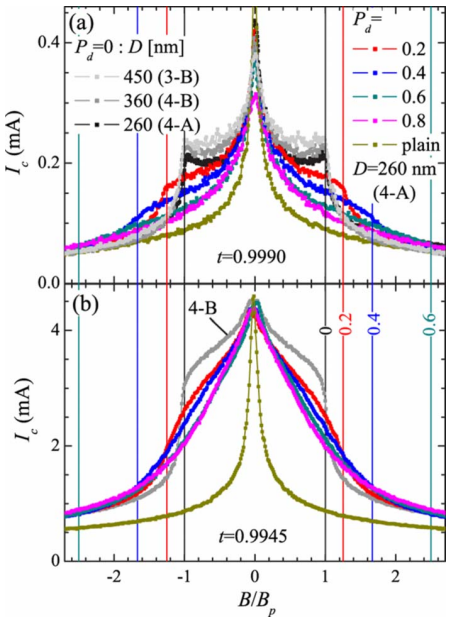

FIG. 4. (Color online) I_c vs B/B_p at (a) $t=0.9990$ and (b) 0.9945 for arrays with scaled lattice parameters $a(P_d)$ (fixed antidot density $n_p=0.1\ \mu\text{m}^{-2}$ and matching field B_p). Comparison of samples having different dilutions P_d and different antidot diameters D for $P_d=0$. $I_c(B \lesssim B_p)$ decreases with decreasing D (for $P_d=0$) and with increasing P_d. Vertical solid lines indicate $\pm B_l(P_d)/B_p$, labeled with corresponding values for P_d.

In the samples with small dilution ($P_d=0.2$ and 0.4) we also find peaks in $I_c(B)$ for the higher temperature shown in Fig. 3(a). The matching peaks are significantly broader than the matching peaks of the undiluted bridge and they are located at magnetic fields between B_l and $B_p(P_d)$. This is also visible in Figs. 2(b) and 2(d). With increasing P_d we find a gradual transition of the $I_c(B)$ patterns at $B<B_l$ from the undiluted array ($P_d=0$) to the plain film ($P_d=1$). As predicted in Ref. 20, for fixed lattices an increase in P_d generally results in a decrease of I_c (for all values of applied field $B \neq 0$), as expected for the gradual transition from a periodic pinning array to a plain film without antidots. However, we would like to mention one exception, which we observed for the highest temperature. For $t=0.9990$ [c.f., Fig. 3(a)] the diluted sample with $P_d=0.2$ shows a higher I_c than the undiluted sample ($P_d=0$) for $B<B_l$ and very similar I_c values for all other fields, except for the matching fields B_l and $2B_l$. This effect is quite counterintuitive, as it means that simply by removing 20% of the antidots (without rescaling the antidot distance and density), I_c can be increased for fields below B_l. This effect has not been predicted in Ref. 20 and is probably due to a subtle interplay between pinning energy and elastic energy of the vortex lattice, which may lead to a transition from plastic to elastic depinning for this special case.

2. Scaled lattice parameter—transition to random

Figure 4 shows $I_c(B/B_p)$ patterns of bridges with scaled lattice parameters $a(P_d)$, i.e., $n_p=const$, with different $P_d=0-1$ at $t=0.9990$ (a) and $t=0.9945$ (b). In Fig. 4(a) data from set 4-A ($D=260$ nm) are complemented by results from two undiluted bridges with $D=360$ nm (4-B) and $D=450$ nm (3-B) in order to demonstrate the effect of antidot size. All bridges with $P_d=0$ and different D show qualitatively the same $I_c(B)$ patterns. The major difference is a slight increase in I_c at $B<B_p$ with increasing D. This dependence can be explained with the increase of the pinning strength of the antidots with increasing D. For $B<B_p$, each vortex can be captured by an antidot and hence the increasing pinning strength with D leads to an increase of I_c. In contrast, for $B>B_p$, vortices occupy interstitial pinning sites where they are weakly pinned. Hence, I_c is drastically reduced and determined by the motion of interstitial vortices, which should not depend on the antidot size. This is exactly what we find experimentally, i.e., $I_c(B>B_p)$ is independent of D for the samples with $P_d=0$.

With increasing P_d (decreasing a in order to keep the antidot density n_p constant) the shape of the $I_c(B/B_p)$ patterns is strongly affected. The diluted arrays show "lattice matching" effects around B_l. It is interesting to note that with decreasing t the matching effects become less pronounced and the $I_c(B)$ pattern approaches more and more a triangular shape. This shape is reminiscent of the $I_c(B)$ pattern of randomly arranged antidots.[18] This can be understood as with increasing P_d and fixed n_p, the antidot arrangement approaches that of a random arrangement.

3. Suppression of channeling

For $P_d=0$ from set 4-A we have no data for the full range of t, as the bridge was damaged after taking first data. Hence, to facilitate the comparison of different P_d at $t=0.9945$ [Fig. 4(b)], we also show data from another bridge with $P_d=0$ (from set 4-B). For both temperatures ($t=0.9990$ and $t=0.9945$) we find a decrease in I_c with increasing P_d for $B<B_p$. However, for $B>B_p$ the diluted arrays show an enhanced I_c as compared to the undiluted sample(s). Both observations are in qualitative agreement with the simulations in Ref. 20. We do find that the enhancement of I_c above B_p persists up to the highest dilution $P_d=0.8$. This enhancement was explained in Ref. 20 with the suppression of channeling of interstitial vortices for fields in the range $B_l<B<B_p$. For undiluted arrays, this channeling effect causes the rapid decrease of I_c with increasing B slightly above B_p [c.f. Fig. 4]. Our experimental data clearly confirm that this rapid drop in I_c at B_p is absent for the diluted arrays.

The suppression of channeling should also be visible in the current-voltage characteristics. Figure 5(a) shows the $V(I)$ curves of differently diluted samples at $B=2B_p$ and $t=0.9945$, and Fig. 5(b) shows the corresponding differential resistance dV/dI vs current curves. The $V(I)$ curves directly correspond to the $I_c(B)$ pattern shown in Fig. 4(b). For Fig. 5 we have chosen values of t and B for which I_c is essentially the same for all values of P_d (except for $P_d=1$) in order to facilitate the comparison for different values of P_d regarding the evolution of the flux-flow voltage with increasing current. For the undiluted bridge at $B=2B_p$ one expects the same number of vortices sitting in the antidots and at interstitial positions. In this case we find two critical depinning currents $I_{c,1}$, $I_{c,2}$ in the $V(I)$ curves [c.f. inset of Fig. 5(b)]. $I_{c,1} \approx 1$ mA corresponds to the current above which a finite

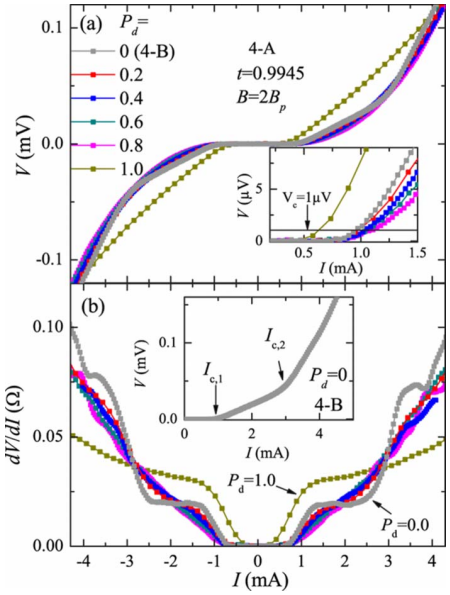

FIG. 5. (Color online) (a) $V(I)$ curves and (b) $dV/dI(I)$ curves at $B=2B_p$ and $t=0.9945$ for arrays with scaled lattice parameters $a(P_d)$ (fixed antidot density $n_p=0.1$ μm^{-2} and matching field B_p). Inset in (a) shows magnification of V vs I at small voltages; $V(I>1$ mA) decreases with increasing P_d, except for the plain film ($P_d=1$) with lowest I_c. Inset in (b) shows V vs I for $P_d=0$ only with the critical depinning current $I_{c,1}(I_{c,2})$ of interstitial (pinned) vortices.

voltage appears. This voltage is caused by the motion of weakly pinned interstitials. At a higher current $I_{c,2}\approx 3$ mA the slope of the IV curve changes. This is due to the depinning of vortices sitting in the antidots. The value of $I_{c,2}$ can also be found in the $I_c(B)$ pattern shown in Fig. 4(b). $I_{c,2}$ fits quite well to the critical current at the first matching field $I_c(B_p)$. The $dV/dI(I)$ curves in Fig. 5(b) reveal some further features, which are not easily visible in the $V(I)$ curves shown in Fig. 5(a). The undiluted sample ($P_d=0$) shows a sharp increase in dV/dI at $I_{c,1}$, followed by an almost constant $dV/dI\approx 18$ mΩ. For the diluted arrays, this steplike change in dV/dI gets smeared out, and with increasing P_d the $dV/dI(I)$ curves become increasingly smooth. The undiluted sample shows another steplike increase in $dV/dI(I)$ at $I_{c,2}$, followed by another plateau at ≈72 mΩ, i.e., a factor of 4 above the first plateau. Finally, a third steep increase in dV/dI sets in at $I\approx 3.9$ mA. This value of bias current seems to coincide with the value of $I_c(B\approx 0.2B_p)$ at which the initial steep decrease in $I_c(B)$ (with increasing B) for the undiluted sample transforms into the broad domelike structure, as shown in Fig. 4(b). Currently, we cannot explain this feature. Finally we note that all diluted samples ($P_d=0.2-0.8$) have a similar $I_{c,1}$ but do not show a pronounced dV/dI change at $I_{c,2}$. The inset in Fig. 5(a) clearly shows that with increasing P_d the voltage due to flux motion decreases, i.e., in the diluted pinning arrays dissipation is reduced, due to the more effective suppression of vortex channeling.

V. CONCLUSIONS

In conclusion, we experimentally investigated Nb thin films with triangular arrays of antidots, which have been randomly diluted, by measurements of the critical current I_c vs applied magnetic field B and current-voltage (IV) characteristics close to the transition temperature T_c. The antidot lattices could be tuned to find two different matching effects, related to the antidot density and to the lattice parameter of the antidot lattice, as predicted in Ref. 20. For samples with fixed lattice parameter, with increasing dilution P_d a gradual transition from a periodic pinning array to a plain film without pinning sites has been observed. Obviously, with increasing P_d the critical current decreases. However, very close to T_c, for small dilutions ($P_d=0.2$) we do find a broad peak in $I_c(B)$ located between B_p and B_l, corresponding to an increase in I_c by removing 20% of the pinning sites. We speculate that this counterintuitive effect is due to the introduction of disorder; an understanding of this effect is still lacking and deserves further investigations. On the other hand, for samples with fixed antidot density, an increasing dilution corresponds to a gradual transition from a periodic to purely random distribution of pinning sites. Our experiments clearly show an enhancement of I_c for magnetic fields above B_p with increasing P_d. This was the main prediction in Ref. 20 and can be explained with the suppression of channeling of interstitial vortices. This effect is also observed in IV measurements, i.e., the suppression of channeling causes an increasing reduction in the flux-flow voltage with increasing P_d. As a consequence, the concept of introducing disorder by randomly removing pinning sites in tailored periodic pinning arrays seems to provide a feasible way for enhancing the critical current in superconductors for magnetic fields above the matching field B_p.

ACKNOWLEDGMENTS

This work was supported by the DFG via the SFB/TRR21 and in part by the DFG Research Center of Functional Nanostructures. M.K. gratefully acknowledges support from the Carl-Zeiss-Stiftung.

*kemmler@pit.physik.uni-tuebingen.de

[1] P. T. Korda, M. B. Taylor, and D. G. Grier, Phys. Rev. Lett. **89**, 128301 (2002).
[2] D. J. Pine, J. P. Gollub, J. F. Brady, and A. M. Leshansky, Nature (London) **438**, 997 (2005).
[3] E. Y. Andrei, G. Deville, D. C. Glattli, F. I. B. Williams, E. Paris, and B. Etienne, Phys. Rev. Lett. **60**, 2765 (1988).
[4] G. Grüner, Rev. Mod. Phys. **60**, 1129 (1988).
[5] M. O. Magnasco, Phys. Rev. Lett. **71**, 1477 (1993).
[6] P. Reimann, Phys. Rep. **361**, 57 (2002).
[7] P. Hänggi, F. Marchesoni, and F. Nori, Ann. Phys. **14**, 51 (2005).
[8] V. V. Moshchalkov, V. Bruyndoncx, L. Van Look, M. J. Van

Bael, Y. Bruynseraede, and A. Tonomura, in *Handbook of Nanostructured Materials and Nanotechnology: Electrical Properties*, edited by H. S. Nalwa (Academic, New York, 2000), Vol. 3, p. 451.
[9] O. Daldini, P. Martinoli, J. L. Olsen, and G. Berner, Phys. Rev. Lett. **32**, 218 (1974).
[10] A. T. Fiory, A. F. Hebard, and S. Somekh, Appl. Phys. Lett. **32**, 73 (1978).
[11] M. Baert, V. V. Metlushko, R. Jonckheere, V. V. Moshchalkov, and Y. Bruynseraede, Phys. Rev. Lett. **74**, 3269 (1995).
[12] J. I. Martin, M. Velez, J. Nogues, and I. K. Schuller, Phys. Rev. Lett. **79**, 1929 (1997).
[13] M. J. Van Bael, K. Temst, V. V. Moshchalkov, and Y. Bruynseraede, Phys. Rev. B **59**, 14674 (1999).
[14] J. E. Villegas, E. M. Gonzalez, M. I. Montero, I. K. Schuller, and J. L. Vicent, Phys. Rev. B **68**, 224504 (2003).
[15] V. Misko, S. Savel'ev, and F. Nori, Phys. Rev. Lett. **95**, 177007 (2005).
[16] V. R. Misko, S. Savel'ev, and F. Nori, Phys. Rev. B **74**, 024522 (2006).
[17] J. E. Villegas, M. I. Montero, C.-P. Li, and I. K. Schuller, Phys. Rev. Lett. **97**, 027002 (2006).
[18] M. Kemmler, C. Gürlich, A. Sterck, H. Pöhler, M. Neuhaus, M. Siegel, R. Kleiner, and D. Koelle, Phys. Rev. Lett. **97**, 147003 (2006).
[19] A. V. Silhanek, W. Gillijns, V. V. Moshchalkov, B. Y. Zhu, J. Moonens, and L. H. A. Leunissen, Appl. Phys. Lett. **89**, 152507 (2006).
[20] C. Reichhardt and C. J. Olson Reichhardt, Phys. Rev. B **76**, 094512 (2007).
[21] M. Velez, D. Jaque, J. I. Martin, M. I. Montero, I. K. Schuller, and J. L. Vicent, Phys. Rev. B **65**, 104511 (2002).
[22] A. Dorn, E. Bieri, T. Ihn, K. Ensslin, D. D. Driscoll, and A. C. Gossard, Phys. Rev. B **71**, 035343 (2005).
[23] R. B. Griffiths, Phys. Rev. Lett. **23**, 17 (1969).
[24] Y.-H. Li and S. Teitel, Phys. Rev. Lett. **67**, 2894 (1991).
[25] E. Granato and D. Domínguez, Phys. Rev. B **63**, 094507 (2001).
[26] W. V. Pogosov, V. R. Misko, H. J. Zhao, and F. M. Peeters, Phys. Rev. B **79**, 014504 (2009).
[27] A. F. Mayadas, R. B. Laibowitz, and J. J. Cuomo, J. Appl. Phys. **43**, 1287 (1972).
[28] G. S. Mkrtchyan and V. V. Schmidt, Sov. Phys. JETP **34**, 195 (1972).
[29] G. R. Berdiyorov, M. V. Milosevic, and F. M. Peeters, Phys. Rev. B **74**, 174512 (2006).

Publication VII

Supercond. Sci. Technol. **25** (2012) 065020 (6pp) doi:10.1088/0953-2048/25/6/065020

The phase boundary of superconducting niobium thin films with antidot arrays fabricated with microsphere photolithography

D Bothner[1], C Clauss[2], E Koroknay[3], M Kemmler[1], T Gaber[1], M Jetter[3], M Scheffler[2], P Michler[3], M Dressel[2], D Koelle[1] and R Kleiner[1]

[1] Physikalisches Institut and Center for Collective Quantum Phenomena in LISA$^+$, Universität Tübingen, Auf der Morgenstelle 14, D-72076 Tübingen, Germany
[2] 1. Physikalisches Institut, Universität Stuttgart, Pfaffenwaldring 57, D-70550 Stuttgart, Germany
[3] Institut für Halbleiteroptik und Funktionelle Grenzflächen and Research Center SCoPE, Universität Stuttgart, Allmandring 3, D-70569 Stuttgart, Germany

E-mail: daniel.bothner@uni-tuebingen.de

Received 12 March 2012, in final form 6 April 2012
Published 4 May 2012
Online at stacks.iop.org/SUST/25/065020

Abstract
The experimental investigation of the $I_c(B)$–$T_c(B)$ phase boundary of superconducting niobium films with large area quasihexagonal hole arrays is reported. The hole arrays were patterned with microsphere photolithography. We investigate the perforated niobium films by means of electrical directed current transport measurements close to the transition temperature T_c in perpendicularly applied magnetic fields. We find pronounced modulations of the critical current with applied magnetic field, which we interpret as a consequence of commensurable states between the Abrikosov vortex lattice and the quasihexagonal pinning array. Furthermore, we observe Little–Parks oscillations in the critical temperature versus magnetic field.

(Some figures may appear in colour only in the online journal)

1. Introduction

Nowadays superconducting thin films are used for a huge variety of superconducting microelectronic devices such as Josephson junctions, superconducting quantum interference devices (SQUIDs) and coplanar waveguide resonators. Typically, these thin films are made of type-II superconductors and are penetrated by quantized magnetic flux when operated in magnetic fields or when biased with sufficiently high currents. The investigation of these magnetic flux lines (Abrikosov vortices) and their individual and collective interactions with natural and artificial defects in the superconductor is of high interest and has been subjected to many experimental and theoretical studies for several decades now.

One reason for this sustained scientific attention is that unpinned Abrikosov vortices respond with a dissipative motion to any current flowing in their vicinity. In many cases this motion is directly related to a reduction of the performance of the microelectronic devices (increased noise, lowered quality factor, shortened coherence time). Defects, however, act as local energy minima (pinning sites) and are able to reduce or even completely suppress vortex motion and the related dissipation [1–5]. For instance, it has been demonstrated that the flux noise in SQUIDs and the dissipation in coplanar microwave resonators can be reduced by strategically positioned microholes (antidots) [6, 7].

A second and more fundamental point is associated with the fact that an ensemble of Abrikosov vortices interacting with an ensemble of defects constitutes a highly designable

model system for repulsively interacting particles in a two-dimensional potential landscape. In such systems it is possible to investigate static effects such as the formation of quasicrystals [8–12] or the controlled introduction of potential landscape disorder [13–15] as well as dynamic effects such as mode locking phenomena [16–18] and ratchet dynamics [19, 20].

Of particular interest in both research branches is the case, when the typical length scales of the defect topology, i.e. size and mutual distance, are comparable to the intrinsic length scales of the superconductor, namely the coherence length ξ and the magnetic penetration depth λ, which are both temperature dependent and diverge at the critical temperature T_c. Well below the critical temperature, λ and ξ can usually be found in the micro- to nanometer range. The patterning of large areas of superconducting films with submicron-scaled high density arrays of defects constitutes a non-trivial challenge to standard optical lithography (limited by resolution) or electron beam lithography (limited by time).

It has been demonstrated with different approaches that taking advantage of self-assembling structures can provide a way out of the difficulties in covering large areas with tiny structures on reasonable timescales. The techniques used vary from using anodized aluminum as substrate material [21], to over depositing the superconducting film on a layer of microspheres [22], to generating structures by inverse diblock copolymer micelle formation [23]. These fabrication methods, however, are limited to certain substrate materials or they induce changes in the substrate properties and/or the properties of the superconductor.

Here we adopt another method to fabricate large area quasihexagonal arrays of submicron sized antidots which is independent of the substrate material and does not influence the superconducting material more than any standard lithography process [24, 25]. In a previous study we have demonstrated that with this fabrication technique it is possible to reduce the vortex associated losses in superconducting microwave resonators by more than one order of magnitude [26]. In this paper we analyze the properties of our microsphere patterned Nb thin films by means of transport measurements close to the transition temperature with a particular focus on signatures of commensurabilities between the antidot and vortex lattices. We also investigate the transition between the wire network and the thin film regime in our samples. The critical parameter for this transition is the coherence length $\xi(T)$, which in the network regime is larger than the width W of the superconductor between the antidots and which is smaller than W in the thin film regime.

2. Experimental details

We fabricated our samples by first depositing a $t = 150$ nm thick niobium film on an r-cut sapphire wafer by dc magnetron sputtering. Afterwards we cut the wafer into individual chips and carried out the lithography steps. For the fabrication of perforated samples the chips were covered with photoresist and on top of that with a monolayer of

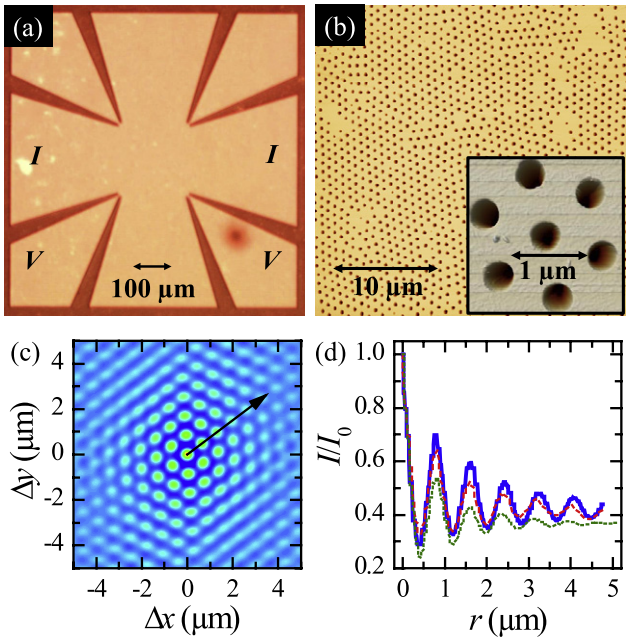

Figure 1. (a) Optical image of the 800 × 800 μm^2 large cross-shaped bridge structure with a square center area of 200 × 200 μm^2 for the four-probe current voltage characterization of superconducting thin films with pinning landscapes. (b) Atomic force microscope (AFM) image of a 30 × 30 μm^2 large section of the niobium film with the microsphere patterned quasihexagonal array of antidots; the inset shows a zoom-in. (c) Autocorrelation function I/I_0 of the large AFM image in (b); the arrow indicates the position and direction of the linescan shown in (d) (blue solid line) together with corresponding linescans of two different 30 × 30 μm^2 array sections (red dashed and green dotted lines); for the definition of I see text.

water suspended polystyrene colloids in a Langmuir–Blodgett deposition process [27]. The microspheres have a diameter of $D_s = 770$ (±25) nm and act as a self-assembled array of UV-light focusing microlenses, leading to a quasihexagonal hole array after the exposure, their removal and the resist development. For a perfect, hexagonal close-packed array with $D_s = 770$ nm one would obtain a corresponding hole density of $n_h \approx 1.95$ μm^{-2}. In reality, however, one could expect deviations from the ideal packaging due to disorder during the self-assembling.

After transferring the hole array into the Nb film via reactive ion etching (SF_6) we patterned cross-shaped bridge structures for electric transport characterizations into the films. For this we used standard optical shadow-mask lithography and another SF_6 reactive ion etching step. Figure 1(a) shows one of the bridge structures with a square center area of 200 × 200 μm^2. The antidots have an approximate diameter of $D_a = 370$ nm, which in principle can be easily varied by adjusting the lithography exposure time. In figure 1(b) an atomic force microscopy image of the niobium film with antidots is depicted, which shows a domain-like pattern of holes with dislocations and imperfections.

To quantify the amount of missing antidots, we chose twelve different sections such as the one shown in figure 1(b) and counted the antidots. By doing so we found a mean antidot density of $n_a \approx 1.55$ μm^{-2} with a rather large

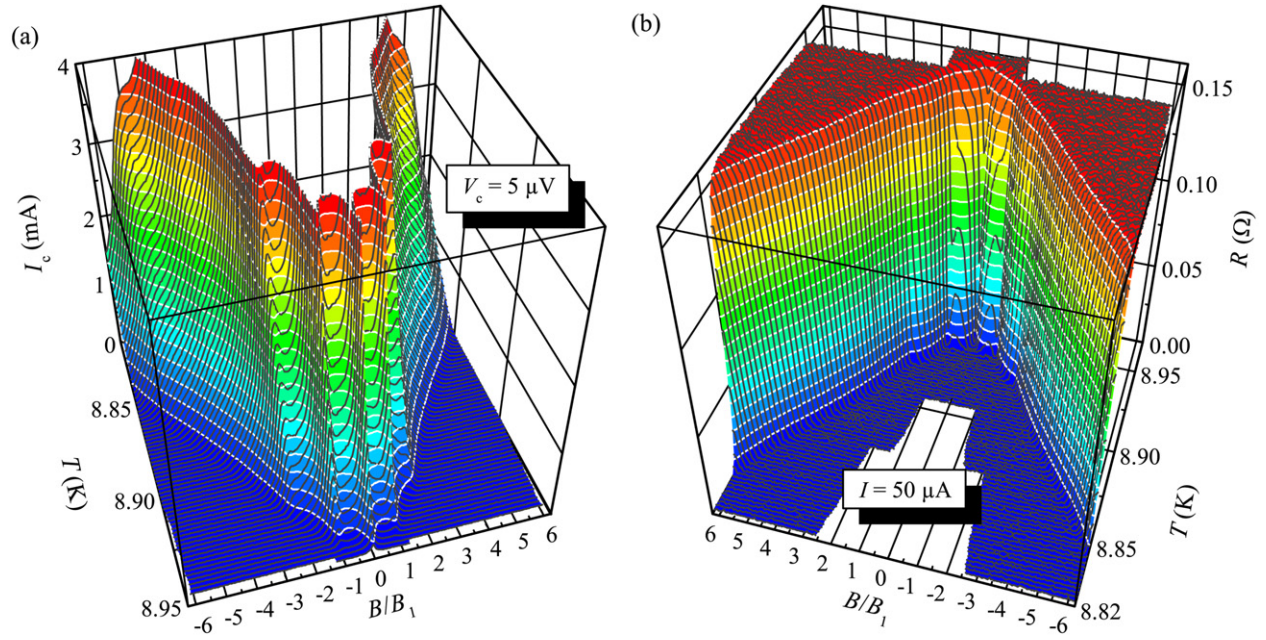

Figure 2. (a) Critical current I_c versus temperature T and magnetic flux density B of a superconducting thin film with a quasihexagonal lattice of antidots for a voltage criterion of $V_c = 5$ μV. (b) Resistance R of the niobium film versus T and B measured with a current $I = 50$ μA. The flux density axes are normalized to the first matching flux density $B_1 \approx 3.4$ mT.

variance between $n_a \approx 1.28$ and 1.78 μm^{-2}. That means that approximately 20% of the antidots are missing as compared to the perfect lattice with $n_h \approx 1.95$ μm^{-2}.

Another interesting analysis of the lattice is related to the typical correlation length of the antidot array. For this purpose we assigned each single pixel of figure 1(b) the value -1, if it belongs to an antidot, and $+1$, if it does not. The result was a 512×512 matrix $M_{i,j}$, for which we calculated the autocorrelation function $I(k, l) = \sum_{i,j} M_{i,j} M_{i+k,j+l}$ with $k, l = 1, \ldots, 512$. We used a cyclic continuation of the matrix, i.e. $(i + k) \equiv (i + k - 512)$ if $(i + k) > 512$ and $(j + l) \equiv (j+l-512)$ if $(j+l) > 512$. The result for I/I_0 with $I_0 = I(0, 0)$ is plotted in figure 1(c) for the array section shown in the large image of figure 1(b), where the shift between the matrices (k, l) is expressed by the corresponding spatial distances $(\Delta x, \Delta y)$. There is a sixfold symmetry visible, indicating that the domains have a clearly preferential orientation in this array section. The larger the section under consideration is, however, the more the sixfold symmetry is expected to wash out to ring-like structures.

For a more detailed view of the correlation amplitude, we plot in figure 1(d) a linescan of I/I_0 along the arrow in (c) (blue line) together with two corresponding linescans from different array sections. All three linescans show exponentially decaying oscillations with a periodicity of approximately 800 nm up to at least 4 μm, i.e. up to about five lattice constants and a 'strong' correlation (exponential decay length) of about two lattice constants.

Due to the cross shape of our bridges, the transport current in the center area is not homogeneous but somewhat spread. For ratchet devices, it has been discussed that such a sample geometry may strongly affect experimental results [28–30]. Also in our case, this geometry might have an effect on the absolute values of the measured quantities, such as the critical current I_c, which, e.g., impedes a precise determination of critical current densities. However, the results presented in this paper sensitively depend on neither the absolute values of the measured quantities nor the local direction of the transport current.

We also patterned and characterized bridges with 100×100 μm^2 and 50×50 μm^2 large center squares, but the experimental results showed no dependence on the bridge size. Note that the niobium chips were taken from the same wafer as the chips for our previous study on resonators [26].

To characterize our samples we mount them into a low-temperature setup, that provides a temperature stability of $\Delta T < 1$ mK, and contact them electrically with wire bonds. We apply a magnetic field perpendicular to the film plane using a superconducting coil, and monitor current voltage characteristics (*IV*Cs) for many values of magnetic field and temperature. After collecting all *IV*Cs we extract the desired information as the critical current I_c, the critical temperature T_c or the resistance R versus magnetic flux density B and temperature T. We choose the threshold voltage V_c defining I_c and the measurement current I for the resistance R during the evaluation. To reduce the voltage noise, we take several *IV*Cs at each value for B and T and post-process the raw data (averaging and smoothing), such that we are more sensitive to modulations of the I_c–T_c phase boundary with respect to the applied magnetic flux.

3. Results and discussion

As an overview of the whole phase boundary figure 2 depicts (a) the critical current I_c and (b) the resistance R versus magnetic flux density and temperature of one of our samples

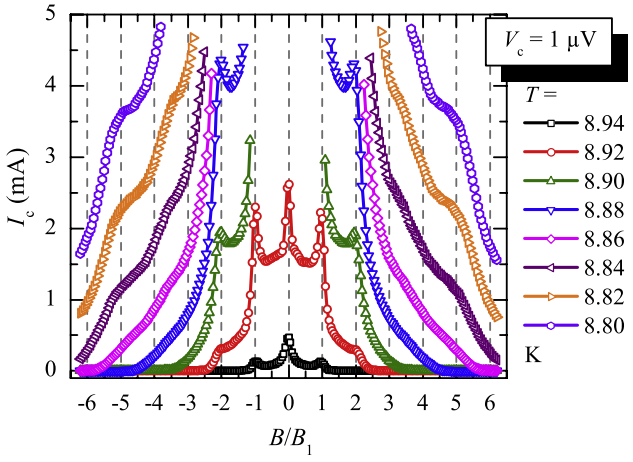

Figure 3. Critical current I_c versus magnetic flux density B of a superconducting thin film with a quasihexagonal lattice of antidots; different curves correspond to different temperatures T. The flux density axis is normalized to the first matching flux density $B_1 \approx 3.4$ mT.

close to T_c. Obviously, the phase boundary is non-monotonic. The critical current $I_c(B)$, the critical temperature $T_c(B)$ and the resistance $R(B)$ strongly modulate with the applied flux density. There are several 'canyons' and 'ridges' indicating commensurate states between the flux line lattice and the hole array.

For a more detailed view of the positions of the maxima and minima in the 3D phase boundary, it is convenient to extract single parameter slices. Figure 3 shows several individual curves for $I_c(B)$, which correspond to vertical cuts through figure 2(a) for constant temperatures. The flux density axes in figures 2 and 3 are normalized to the first pronounced maximum in the critical current $B_1 \approx 3.4$ mT. This corresponds to a vortex density of $n_v = B_1/\Phi_0 = 1.65\ \mu\text{m}^{-2}$, which is well below the 'ideal' hole density of $n_h \approx 1.95\ \mu\text{m}^{-2}$ and slightly above the real antidot density of $n_a \approx 1.55\ \mu\text{m}^{-2}$ determined by counting. Despite the difference between n_v and n_a, we think that a plausible explanation for the reduced matching field as compared to the ideal one is that at $B = B_1$ the matching is rather local and predominantly determined by the hole density.

The difference between n_v and n_a might be explained by some vortices at interstitial positions in larger antidot-free areas and/or by antidots, which are already doubly occupied at $B = B_1$. In a previous study the effect of randomly diluting a periodic pinning array has been investigated systematically [14]. In these experiments a similar effect was observed. The first matching maximum in some samples with diluted pinning arrays was found at field values between the one corresponding to the hole density and the one corresponding to the ideal hexagonal lattice.

For higher magnetic field values we find three more matching features, cf figure 3. The first of these is found for $B \approx 2B_1 = B_2$ and most likely corresponds to two vortices per pinning site. Then there are two shoulder-like bumps for $B \approx 3.5B_1$ and $5B_1$ but none at $B = 3B_1$ and $4B_1$, which is rather unconventional and on first sight surprising.

For a perfect triangular pinning lattice, one would expect always matching features at integer multiples of the first matching field. They can correspond to a multiple occupation of the pinning sites or to composite triangular vortex lattices in antidots and at interstitial positions. In the case of interstitial, 'caged' vortices it might happen that one of the regular peaks is suppressed or missing [31–34], but to our knowledge it has never been reported that two consecutive ones are missing as in our case ($3B_1$ and $4B_1$) and that an additional one appears in between instead ($3.5B_1$).

We think that the peak structure of the phase boundary of our samples can be explained by a related but somewhat different mechanism. With increasing field values, the mean artificial pinning strength decreases and the vortex–vortex interaction becomes more important due to the increasing vortex density. In this situation, the vortices tend more and more to form a perfect hexagonal lattice with a homogeneous density and thus fill up the positions of missing antidots. As the vortex lattice as a whole, however, is still interacting with the pinning sites in this case, the length scale of the pinning array determines the energetically most favorable length scale of the vortex lattice. Then the matching effects might appear at integer multiples of the 'ideal' pinning lattice with $n_h = 1.95\ \mu\text{m}^{-2}$. Strikingly, the values of $3.5B_1$ and $5B_1$ with $B_1 \approx 3.4$ mT correspond quite well to $3B_1^*$ and $4B_1^*$ with $B_1^* = n_h\Phi_0 \approx 4$ mT. Again, a similar effect has been observed in randomly diluted pinning arrays before, where for a dilution of 20% the first matching peak corresponded more to the real antidot density and the second matching peak to the lattice constant [14].

Finally, it has been observed that the artificial introduction of disorder into a periodic pinning lattice leads to broadened matching peaks [15]. This observation also supports our interpretation of local matching for low vortex densities, as the peaks at $B = B_1$ and B_2 are rather sharp and the pinning lattice is locally highly ordered. When the matching becomes non-local at higher vortex densities, however, the global disorder of the pinning lattice becomes important and broadens the peaks at $B = 3.5B_1$ and $5B_1$.

Besides analyzing the phase boundary by taking horizontal slices, we can also take vertical slices for chosen currents or voltages of the 3D boundary and end up with the critical temperature versus magnetic field plots (or second critical magnetic field versus temperature, respectively) for different T_c (B_{c2}) criteria. Figure 4 shows a plot of $T_c(B)/T_c(0) = T_c/T_{c0}$ of a perforated sample (symbols) for a resistance criterion of $R_c/R_n = 0.5$ and measured with an applied current of $I = 50\ \mu$A. R_n denotes the normal state resistance at $T = 10$ K. Oscillations of the critical temperature with the applied flux are clearly visible, which we associate with Little–Parks oscillations [35], as already observed in many studies on superconducting wire networks and thin films with pinning arrays [36–39].

We also plot the critical temperature versus magnetic field of a plain reference sample in figure 4(a) and calculate from these data the coherence length $\xi(0) = 16$ nm of the niobium by fitting it to the bulk expression $B_{c2} = \phi_0/[2\pi\xi(T)^2]$ with $\xi(T) = \xi(0)(1 - T/T_c)^{-1/2}$ [40]. As the coherence length

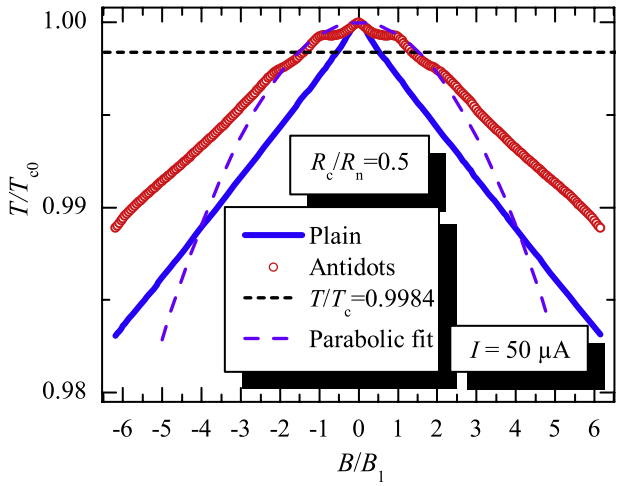

Figure 4. Reduced critical temperature T_c/T_{c0} versus normalized magnetic flux density B/B_1 of a plain superconducting thin film (blue line) and a sample with a quasihexagonal lattice of antidots (red circles). The horizontal dashed line represents the temperature at which $\xi(T_W/T_{c0}) = W$, the dashed parabola is a fit to the three data points of the antidot sample at $B = 0$, B_1 and $-B_1$.

is significantly smaller than the BCS coherence length for niobium, $\xi_0 = 39$ nm, our films are in the 'dirty limit' with a free mean path of $l = 1.37\xi(0)^2/\xi_0 = 9$ nm. Assuming that the coherence length is not changed by the antidot patterning process and remembering that the minimal width of superconducting material between two holes is $W = D_s - D_a = 400$ nm, we calculate the reduced temperature, at which $\xi(T_W) = W$, to be $T_W/T_{c0} = 0.9984$.

Above T_W, which is marked with a dashed horizontal line in figure 4, the superconductivity in our system can be viewed as one-dimensional and the thin film expression $B_{c2} = \sqrt{12}\phi_0/[2\pi W\xi(T)]$ should apply [21, 40]. This gives a parabolic dependence of $T_c/T_{c0} \propto B^2$ for $T/T_{c0} > 0.9984$, which seems to be in reasonable agreement with our data. T_c/T_{c0} of the perforated sample indeed appears like a Little–Parks modulated nonlinear background close to T_{c0} with a development to a nearly linear behavior for smaller temperatures $T/T_{c0} < 0.9984$.

By fitting the three single points at $B = 0$, B_1 and $-B_1$ to the above parabolic expression and using $W = 400$ nm, we calculate a coherence length of $\xi(0) \approx 18.2$ nm, in good agreement with the number extracted from the plain sample, although it is probably somewhat overestimated. The effective remaining superconductor width between the holes, W, is certainly larger than the used minimal value of 400 nm for two reasons. First, the holes have a circular shape and, second, some of them are missing. So it might even be that the coherence length in the perforated sample is somewhat smaller than in the plain one, which would be supported by the impression of a slightly smaller slope in the more linear regime. A fit of the data for the perforated sample in this region, however, is difficult, as there are still modulations due to the antidots superimposed.

4. Conclusion

In summary we have investigated the $I_c(B) - T_c(B)$ phase boundary of superconducting Nb films, which were patterned with quasihexagonal arrays of submicron sized antidots. This fabrication method is especially interesting for microwave devices as it does not change the substrate or superconductor properties significantly. Our experiments revealed signatures for both local and non-local commensurabilities between the vortex and the antidot lattice, which was patterned by using a monolayer of self-assembling polystyrene colloids as microlenses for optical lithography. Pronounced sharp maxima of the critical current in the first and second matching field indicate a high local ordering of the pinning sites, whereas the shoulder-like structures at non-integer higher field values might be related to pinning lattice disorder on a non-local scale. We also observe Little–Parks oscillations of the critical temperature and approximately identify the wire network to thin film transition in our samples. The coherence length of the perforated film, extracted from the critical temperature versus magnetic field dependence, is in good agreement with that of a plain film, confirming that our patterning method has hardly influenced the properties of the niobium.

We have performed experiments close to T_c, but when using superconductors with a higher magnetic penetration depth, the results are also relevant at temperatures of $T = 4.2$ K or even in the mK regime. This situation occurs in very thin or dirty superconducting films and in different superconducting materials, although in some of these cases (e.g. $YBa_2Cu_3O_7$) the artificial pinning will compete with strong intrinsic pinning. In principle our patterning technique could be used with even smaller spheres [24], which would lead to commensurability effects at much lower temperatures and higher magnetic fields. In these cases, the critical current and the pinning efficiency would modulate with the applied field in a similar manner to that presented, which has to be considered for the design of possible devices.

Acknowledgments

This work has been supported by the Deutsche Forschungsgemeinschaft via the SFB/TRR 21 and by the European Research Council via SOCATHES. DB gratefully acknowledges support by the Evangelisches Studienwerk eV Villigst. MK gratefully acknowledges support by the Carl-Zeiss Stiftung.

References

[1] Fiory A T, Hebard A F and Minnich R P 1978 *J. Phys. Colloq.* **39** 633
[2] Martín J I, Veléz M, Nogués J and Schuller I K 1997 *Phys. Rev. Lett.* **79** 1929
[3] Moshchalkov V V, Baert M, Metlushko V V, Rosseel E, Bael M J V, Temst K, Bruynseraede Y and Jonckheere R 1998 *Phys. Rev.* B **57** 3615
[4] Häffner M, Kemmler M, Löffler R, Vega Gómez B, Fleischer M, Kleiner R, Koelle D and Kern D P 2009 *Microelectron. Eng.* **86** 147003

[5] Song C, DeFeo M P, Yu K and Plourde B L T 2009 *Appl. Phys. Lett.* **95** 232501
[6] Selders P and Wördenweber R 2000 *Appl. Phys. Lett.* **76** 3277
[7] Bothner D, Gaber T, Kemmler M, Koelle D and Kleiner R 2011 *Appl. Phys. Lett.* **98** 102504
[8] Misko V, Savel'ev S and Nori F 2005 *Phys. Rev. Lett.* **95** 177007
[9] Kemmler M, Gürlich C, Sterck A, Pöhler H, Neuhaus M, Siegel M, Kleiner R and Koelle D 2006 *Phys. Rev. Lett.* **97** 147003
[10] Villegas J E, Montero M I, Li C-P and Schuller I K 2006 *Phys. Rev. Lett.* **97** 027002
[11] Kramer R B G, Silhanek A V, Van de Vondel J, Raes B and Moshchalkov V V 2009 *Phys. Rev. Lett.* **103** 067007
[12] Misko V R, Bothner D, Kemmler M, Kleiner R, Koelle D, Peeters F M and Nori F 2010 *Phys. Rev.* B **82** 184512
[13] Reichhardt C and Olson-Reichhardt C J 2007 *Phys. Rev.* B **76** 094512
[14] Kemmler M, Bothner D, Ilin K, Siegel M, Kleiner R and Koelle D 2009 *Phys. Rev.* B **79** 184509
[15] Rosen Y J, Sharoni A and Schuller I K 2010 *Phys. Rev.* B **82** 014509
[16] Martinoli P, Daldini O, Leemann C and Stocker E 1975 *Solid State Commun.* **17** 205
[17] Van Look L, Rosseel E, Van Bael M J, Temst K, Moshchalkov V V and Bruynseraede Y 1999 *Phys. Rev.* B **60** R6998
[18] Kokubo N, Besseling R, Vinokur V M and Kes P H 2002 *Phys. Rev. Lett.* **88** 247004
[19] Villegas J E, Savel'ev S, Nori F, Gonzalez E M, Anguita J V, García R and Vicent J L 2003 *Science* **302** 1188
[20] de Souza Silva C C, Van de Vondel J, Morelle M and Moshchalkov V V 2006 *Nature* **440** 651
[21] Welp U, Xiao Z L, Jiang J S, Vlasko-Vlasov V K, Bader S D, Crabtree G W, Liang J, Chik H and Xu J M 2002 *Phys. Rev.* B **66** 212507
[22] Vinckx W, Vanacken J and Moshchalkov V V 2006 *J. Appl. Phys.* **100** 044307
[23] Eisenmenger J, Oettinger M, Pfahler C, Plettl A, Walther P and Ziemann P 2007 *Phys. Rev.* B **75** 144514
[24] Wu W, Katsnelson A, Memis O G and Mohseni H 2007 *Nanotechnology* **18** 485302
[25] Wu W, Dey D, Memis O G, Katsnelson A and Mohseni H 2008 *Nanoscale Res. Lett.* **3** 351
[26] Bothner D *et al* 2012 *Appl. Phys. Lett.* **100** 012601
[27] Blodgett K B and Langmuir I 1937 *Phys. Rev.* **51** 964
[28] Gonzalez E M, Nunez N O, Anguita J V and Vicent J L 2007 *Appl. Phys. Lett.* **91** 062505
[29] Silhanek A V, Van de Vondel J, Moshchalkov V V, Leo A, Metlushko V, Ilic B, Misko V R and Peeters F M 2008 *Appl. Phys. Lett.* **92** 176101
[30] Gonzalez E M, Nunez N O, Anguita J V and Vicent J L 2008 *Appl. Phys. Lett.* **92** 176102
[31] Silhanek A V, Van Look L, Jonckheere R, Zhu B Y, Raedts S and Moshchalkov V V 2005 *Phys. Rev.* B **72** 014507
[32] Berdiyorov G R, Milošević M V and Peeters F M 2006 *Phys. Rev.* B **74** 174512
[33] Cao R, Horng L, Wu T C, Lin J C, Wu J C, Yang T J and Koláček J 2011 *J. Appl. Phys.* **109** 083920
[34] Latimer M L, Berdiyorov G R, Xiao Z L, Kwok W K and Peeters F M 2012 *Phys. Rev.* B **85** 012505
[35] Little W A and Parks R D 1962 *Phys. Rev. Lett.* **9** 9
[36] Pannetier B, Chaussy J, Rammal R and Villegier J C 1984 *Phys. Rev. Lett.* **53** 1845
[37] Behrooz A, Burns M J, Deckman H, Levine D, Whitehead B and Chaikin P M 1986 *Phys. Rev. Lett.* **57** 368
[38] Nori F, Niu Q, Fradkin E and Chang S-J 1987 *Phys. Rev.* B **36** 8338
[39] Patel U, Xiao Z L, Hua J, Xu T, Rosenmann D, Novosad V, Pearson J, Welp U, Kwok W K and Crabtree G W 2007 *Phys. Rev.* B **76** 020508(R)
[40] Tinkham M 1996 *Introduction to Superconductivity* (NewYork: McGraw-Hill)

Publication VIII

Enhancing the critical current in quasiperiodic pinning arrays below and above the matching magnetic flux

V. R. Misko,[1,2] D. Bothner,[3] M. Kemmler,[3] R. Kleiner,[3] D. Koelle,[3] F. M. Peeters,[1] and Franco Nori[2,4]
[1]*Departement Fysica, Universiteit Antwerpen, B-2020 Antwerpen, Belgium*
[2]*Advanced Science Institute, RIKEN, Wako-shi, Saitama 351-0198, Japan*
[3]*Physikalisches Institut-Experimentalphysik II and Center for Collective Quantum Phenomena, Universität Tübingen, D-72076 Tübingen, Germany*
[4]*Physics Department, University of Michigan, Ann Arbor, Michigan 48109-1040, USA*
(Received 2 July 2010; published 8 November 2010)

Quasiperiodic pinning arrays, as recently demonstrated theoretically and experimentally using a fivefold Penrose tiling, can lead to a significant enhancement of the critical current I_c as compared to "traditional" regular pinning arrays. However, while regular arrays showed only a sharp peak in $I_c(\Phi)$ at the matching flux Φ_1 and quasiperiodic arrays provided a much broader maximum at $\Phi<\Phi_1$, both types of pinning arrays turned out to be inefficient for fluxes larger than Φ_1. We demonstrate theoretically and experimentally the enhancement of $I_c(\Phi)$ for $\Phi>\Phi_1$ by using non-Penrose quasiperiodic pinning arrays. This result is based on a qualitatively different mechanism of flux pinning by quasiperiodic pinning arrays and could be potentially useful for applications in superconducting microelectronic devices operating in a broad range of magnetic fields.

DOI: 10.1103/PhysRevB.82.184512 PACS number(s): 74.25.Sv, 74.25.Wx, 74.78.−w

I. INTRODUCTION

Pinning of Abrikosov vortices in superconductors is a topic that has attracted considerable interest, both with respect to the fundamental physical properties of so-called "vortex-matter" and with respect to device applications. In the latter case, for bulk or thick film superconductors, the inclusion of nanodefects, acting as pinning sites, typically randomly distributed within the superconductors, has been shown to significantly enhance the critical current density, which is important for increasing the current-carrying capacity of wires and tapes, e.g., for applications in superconducting magnets (see, e.g., Ref. 1 and references therein). On the other hand, recent progress in the fabrication of nanostructures has provided a wide variety of well-controlled lithographically defined artificial pinning sites, and experiments can control both the location and the strength of each pinning center in vortex-confining arrays of pinning sites (APS) (see, e.g., Refs. 2–5). In this context it has been shown that, e.g., microholes (antidots) or magnetic dots may improve the performance of microelectronic thin-film devices. Examples are the suppression of low-frequency flux noise in superconducting quantum interference devices by strategically positioned antidots[6,7] or the enhancement of the quality factor of superconducting microwave resonators operated in magnetic fields, which can be achieved by incorporating antidot arrays into the thin-film structures.[8] From a basic point of view, it is interesting to explore the optimum pinning landscape provided by APS. One convenient way to do this is to investigate the critical current I_c versus magnetic flux Φ for different arrangements of pinning sites.

Periodic artificial APS were proposed as devices able of trapping magnetic flux and thus enhancing I_c. However, the efficiency of periodic APS is strongly limited to so-called matching fields, i.e., when the number of vortices is commensurate with the number of pins, thus resulting in strong but very *narrow* peaks in the critical current versus magnetic flux, $I_c(\Phi)$. This shortcoming can be overcome by using more sophisticated pinning topologies, e.g., quasiperiodic (QP) APS.[9–14] In particular, using a fivefold Penrose tiling (see, e.g., Refs. 15–21) as an APS (i.e., placing pins on the vertices of a Penrose tiling) results in a considerable enhancement of $I_c(\Phi)$, i.e., significant broadening of the peak in $I_c(\Phi)$, as was recently demonstrated theoretically[9,10] and experimentally.[12,13] The underlying idea of using QP APS is that, contrary to regular APS, they include *many* periodicities and thus can trap vortices for magnetic fluxes other than matching values Φ_i. As shown for Penrose-tiling APS,[9,10,12,13] in addition to the matching-flux peak at $\Phi=\Phi_1$, $I_c(\Phi)$ acquires a remarkably *broad* maximum for $\Phi<\Phi_1$. This maximum turned out to be even more robust with respect to variations in parameters of APS than the sharp peak at $\Phi=\Phi_1$.[9,10] However, in theory and experiments, $I_c(\Phi)$ decreases rapidly for fluxes $\Phi>\Phi_1$ for QP Penrose-tiling APS as well as for regular APS. Here, we discuss the essential difference in the flux pinning for magnetic fluxes below and above the matching value $\Phi=\Phi_1$ and we demonstrate, theoretically and experimentally, how the critical current $I_c(\Phi)$ can be improved in the important regime where $\Phi>\Phi_1$, by using novel artificial APS.

The paper is organized as follows: the model and experiment are described in Secs. II and III, respectively. In Sec. IV, we analyze the enhancement of the critical current below the first matching field in different aperiodic pinning arrays and compare the results to those for a fivefold Penrose-tiling APS. The mechanisms of vortex "conductivity" leading to the enhancement of the critical current below and above the matching flux are discussed in Sec. V. In Sec. V, we also present our experimental and numerical results for QP APS demonstrating the enhancement of the critical current for $\Phi>\Phi_1$. Finally, the conclusions are given in Sec. VI.

II. SIMULATION

We model a three-dimensional slab, infinitely long in the z direction, by a two-dimensional (2D) (in the xy plane) simulation cell with periodic boundary conditions. Note that following Refs. 9 and 10 we apply periodic boundary conditions at the boundaries of the square simulation cell while the quasiperiodic array is taken smaller than the cell. This is done in order to prevent imposing *ad hoc* periodicity to the vortex motion in a QP APS: the free-of-pinning region between the QP APS and the boundary of the simulation cell serves as a reservoir of vortices that mimics the external applied magnetic field. This reservoir (of thickness on the order of few intervortex distances) erases the memory, i.e., the information on the coordinate of a vortex leaving the cell. Each additional vortex enters the QP sample at the current point of "least resistance to entry," similarly to the way vortices enter any other sample when placed in an external magnetic field. This approach has been successfully used in numerous simulations in the past (see, e.g., Refs. 9, 10, and 22–24).

To study the dynamics of vortex motion, we perform simulated annealing simulations by numerically integrating the overdamped equations of motion (see, e.g., Refs. 9 and 10 for a description of the method),

$$\eta \mathbf{v}_i = \mathbf{f}_i = \mathbf{f}_i^{vv} + \mathbf{f}_i^{vp} + \mathbf{f}_i^T + \mathbf{f}_i^d. \tag{1}$$

Here $\mathbf{f}_i$ is the total force per unit length acting on vortex i, $\mathbf{f}_i^{vv}$ and $\mathbf{f}_i^{vp}$ are the forces due to vortex-vortex and vortex-pin interactions, respectively, $\mathbf{f}_i^T$ is the thermal stochastic force, and $\mathbf{f}_i^d$ is the driving force; $\mathbf{v}_i$ is the velocity and η is the viscosity. All the forces are expressed in units of $f_0 = \Phi_0^2/8\pi^2\lambda^3$, where $\Phi_0 = hc/2e$, and lengths (fields) are in units of λ (Φ_0/λ^2).

Following Refs. 9 and 10, we model vortex pinning by short-range parabolic potential wells located at positions $\mathbf{r}_k^{(p)}$. The pinning force is

$$\mathbf{f}_i^{vp} = \sum_k^{N_p} \left(\frac{f_p}{r_p}\right) |\mathbf{r}_i - \mathbf{r}_k^{(p)}| \Theta\left(\frac{r_p - |\mathbf{r}_i - \mathbf{r}_k^{(p)}|}{\lambda}\right) \hat{\mathbf{r}}_{ik}^{(p)}, \tag{2}$$

where N_p is the number of pinning sites, f_p is the maximum pinning force of each potential well, r_p is the range of the pinning potential, Θ is the Heaviside step function, and $\hat{\mathbf{r}}_{ik}^{(p)} = (\mathbf{r}_i - \mathbf{r}_k^{(p)})/|\mathbf{r}_i - \mathbf{r}_k^{(p)}|$.

The ground state of a system of moving vortices is obtained by simulating the field-cooled experiments (e.g., Ref. 25). For deep short-range (δ-like) potential wells, the energy required to depin vortices trapped by pinning sites is proportional to the number of pinned vortices, $N_v^{(p)}$. Therefore, in this approximation, we can define the normalized critical current as follows:[9,10]

$$I_c(\Phi) = j_0 \frac{N_v^{(p)}(\Phi)}{N_v(\Phi)}, \tag{3}$$

and study the dimensionless value $J_c = I_c/j_0$, where N_v is the total number of vortices within the simulation cell of the area A, and j_0 is a constant (i.e., the current needed to depin N_v noninteracting vortices, $j_0 = N_v j_v^{dp}$). Since the area of the QP pattern A_{qp} is less than A, the critical current Eq. (3) acquires a prefactor $A_{qp}/A \approx 0.58$ (Refs. 9, 10, and 26) in the simulations below. We use narrow potential wells as pinning sites, with the maximum pinning force f_p and the radius $r_p = 0.04\lambda$ to 0.1λ.

III. EXPERIMENT

Experiments were performed on $d = 60$-nm-thick Nb films containing circular antidots (diameter $D = 400$ nm) at the vertices of various types of QP APS (see insets of Figs. 1 and 2) in an area of 200×200 μm^2. The average antidot density is $n_p \approx 0.5$ μm^{-2}, corresponding to a first matching field $B_1 = n_p \Phi_0 \approx 1$ mT. Electric transport measurements for the determination of the critical current $I_c(\Phi)$ of perforated Nb bridges were performed at well-controlled temperatures T and magnetic fields; for details of sample fabrication and experimental setup see Refs. 12 and 27. The bridges had transition temperatures $T_c \approx 8.4$ K and transition widths varying from 15 to 25 mK. The temperature dependence of the critical current at $B = 0$ differed from bridge to bridge leading to different absolute values of $I_c(B=0)$ at the same reduced temperatures T/T_c. The experimental data shown below, were recorded at $T/T_c = 0.9995$, where the absolute values of I_c for different samples were very similar. Note that according to our estimates based on a simple core pinning model (see Ref. 12), the maximum value of the critical depinning current in quasiperiodic pinning arrays of antidots reached the values of about 0.5 of the Ginzburg-Landau depairing current, for the used parameters.

IV. CRITICAL CURRENT IN QP TILING APS

For a fivefold Penrose-tiling APS,[9,10,12,13] pinning arrays with many periodicities[28] can enhance the critical current[29] for a broader range of magnetic fluxes as compared to periodic APS. In order to examine and possibly further optimize $J_c(\Phi)$ in APS, in this section we study the critical current as a function of applied magnetic flux, for different QP tilings.

First, we consider a tiling consisting of the simplest shapes, squares and triangles (both compatible with the lowest-energy vortex lattices). The result for a quasiperiodic square-triangle tiling[30] is shown in Fig. 1(a). For comparison, Fig. 1 also shows the $J_c(\Phi)$ dependence for a fivefold Penrose-tiling APS. $J_c(\Phi)$ for the QP square-triangle tiling has a broad maximum at $\Phi_m < \Phi_1$, which is formed due to the rearrangement of vortices between the square and triangular tiles when their density changes. Note the absence of a peak at Φ_1, indicating that the local matching conditions between the APS and the vortex lattice are not fulfilled at the given parameters of the APS (i.e., the average distance between the pinning sites, their maximum strength and radius). However, a peak in $J_c(\Phi)$ at Φ_1 is observed for the Penrose-tiling APS. Another tiling consisting of the same simple shapes (i.e., squares and triangles) is the nonpisot square-triangular tiling[30] shown in the inset of Fig. 1(b). Although these two types of tilings are characterized by different inflation rules (i.e., different arrangements of the tiles), they contain the same elements, i.e., hexagons formed by six tri-

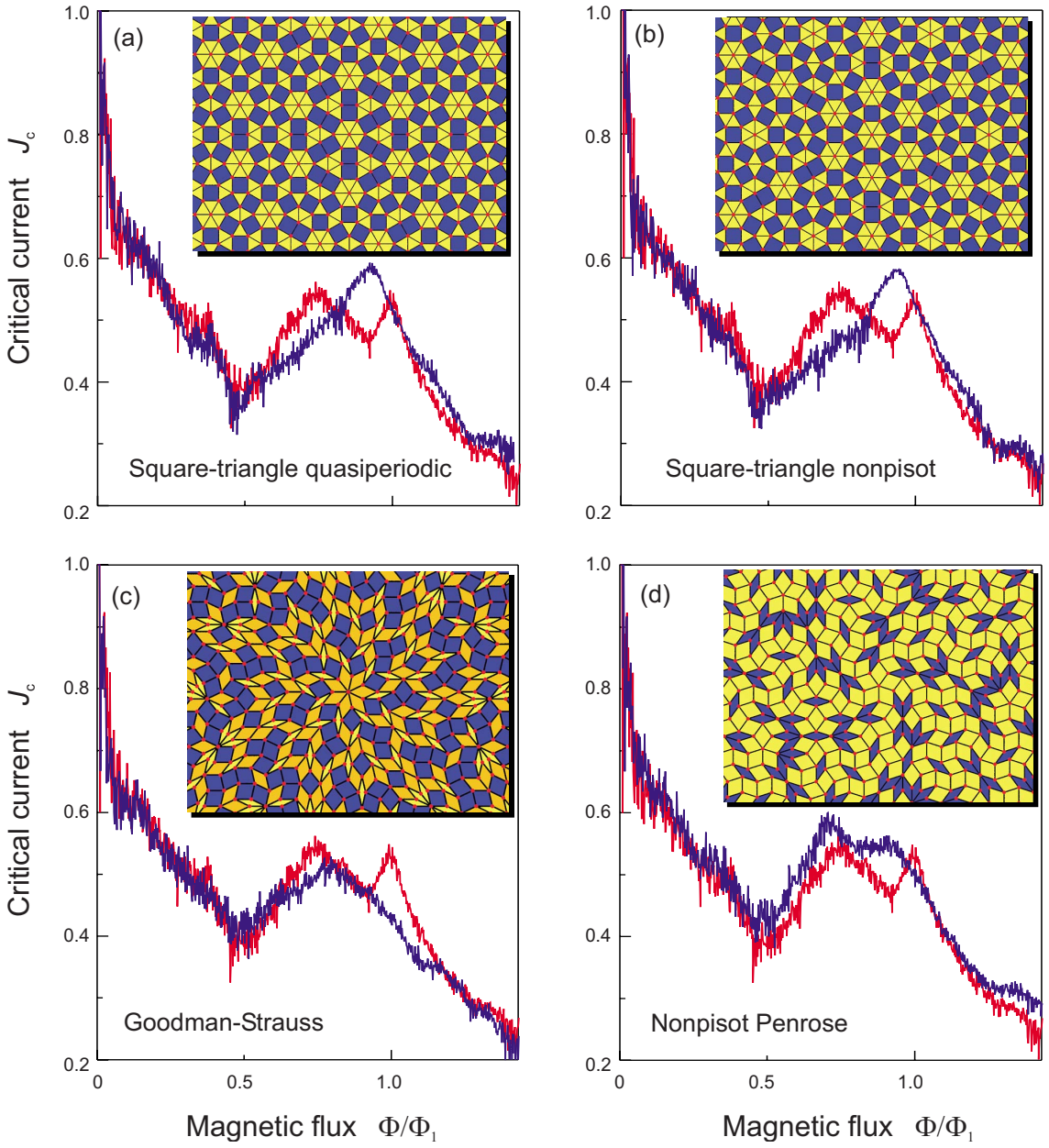

FIG. 1. (Color online) Normalized critical current, J_c versus normalized magnetic flux, Φ/Φ_1 ($\propto$ number of vortices N_v), for different QP APS [shown by solid blue (dark gray) lines]: (a) square-triangle quasiperiodic tiling, (b) square-triangle nonpisot tiling, (c) Goodman-Strauss tiling, and (d) nonpisot Penrose tiling. Insets show the corresponding tiling patterns. For comparison, the function $J_c(\Phi/\Phi_1)$ for a fivefold Penrose-tiling APS is shown by a red (gray) line. The $J_c(\Phi/\Phi_1)$ curves are shown for $f_p/f_0=2$ and $r_p/\lambda=0.1$. These values of f_p and r_p are also used in Figs. 2–4.

angles surrounded by six squares. This similarity in the structure determines similar local matching effects between vortices and the pinning centers for these two tilings. As a result, the $J_c(\Phi)$ curve for the nonpisot square-triangular tiling [Fig. 1(b)] turns out to be practically identical to that for the quasiperiodic square-triangular tiling [compare to Fig. 1(a)]. An example of a tiling consisting of three different tiles (three types of rhombuses) is a Goodman-Strauss tiling[21] shown in the inset of Fig. 1(c). Surprisingly, the behavior of $J_c(\Phi)$ for this APS is very similar to that of the Penrose-tiling APS, although it has an obvious shortcoming: it does not contain the maximum at the matching flux Φ_1 [Fig. 1(c)].

These examples indicate that the considered tilings provide, in general, a weaker enhancement of the critical current as compared to the fivefold Penrose-tiling APS which seems to be the best among these competitors. Let us then consider a different modification of a Penrose tiling, namely, a nonpisot Penrose tiling.[21] This tiling also consists of two types of rhombuses. It is shown in the inset of Fig. 1(d). As shown in the main panel of Fig. 1(d), this APS provides an even better enhancement of $J_c(\Phi)$ within nearly the same, as for the fivefold Penrose tiling, range of magnetic flux: it is charac-

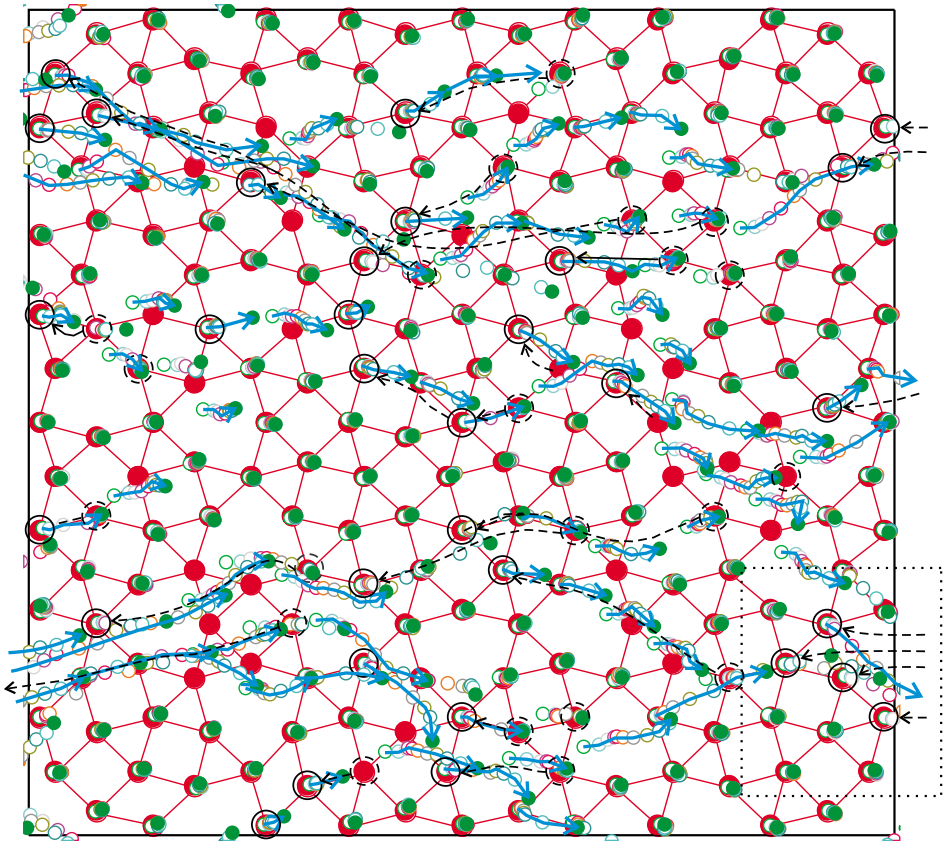

FIG. 2. (Color online) Flow pattern for vortices driven by an external current illustrating the holelike vortex conductivity in the Shield-tiling APS for $\Phi \lesssim \Phi_1$: $\Phi \approx 0.95\Phi_1$. The pinning sites are shown by filled large red (gray) circles. Vortex positions are shown for ten successive time intervals t_i, where $i=1-10$: by open small circles, for $i=1-9$, and by filled small green (gray) circles, for $i=10$. The Lorentz force drives vortices from the left to the right. Most of the vortices do not move: their positions just slightly change (polarized) with respect to the centers of the pinning sites. The trajectories of moving vortices (from the left to the right) are shown by thick blue (gray) arrows. The motion of vortices results in effective propagation of vacancies (holes) from the right to the left (shown by thin dashed black arrows), including holes entering the sample from outside, as in the region marked by the dotted rectangle. Newly created holes are shown by thin solid black circles while annihilated holes (i.e., filled by vortices) are shown by thin dashed black circles.

terized by an almost-flat plateau within the broad maximum in $J_c(\Phi)$. This improvement of the pinning properties is explained by the specific arrangement of the rhombuses in this kind of tiling, which turns out to be closer to the energetically favorable arrangement of vortices in the lattice, thus providing better vortex-pin matching conditions for various densities. For the fivefold Penrose-tiling APS,[9,10,12,13] the maximum of the critical current at $\Phi=\Phi_1$ is separated from the main broad maximum and is not as stable as the broad maximum with respect to changes in the parameters of the APS (i.e., the maximum pinning strength).[9,10] The advantage of the APS based on the nonpisot Penrose tiling is that it provides a smooth transition from the matching-field configuration (i.e., at $\Phi=\Phi_1$) to lower-density pinned states (i.e., when some of the vertices of the small tiles become unoccupied[9,10]). This provides a flattening of the $J_c(\Phi)$ curve [Fig. 1(d)] and thus increases the overall value of the maximum J_c within the range of the plateaulike maximum. This important improvement could be useful for applications of QP APS.

V. "HOLELIKE" AND "ELECTRONLIKE" VORTEX CONDUCTIVITY

As can be seen in Fig. 1, all the above results obtained using different APS, while providing different profiles of $J_c(\Phi)$, still have a common feature: J_c drops drastically for $\Phi>\Phi_1$ as it does in periodic APS (for both cases, $\Phi>\Phi_1$ and $\Phi<\Phi_1$).

Can we improve this? One might think that in practice we can increase the density of the pinning sites in the array and thus trap flux for any Φ. Indeed this might work to some extent but the efficiency of an APS, especially QP APS, is determined not only by the ratio of the average intervortex distance to the average period of the APS ($d_{\mathrm{av}}^{\mathrm{APS}}$) but also by the ratio of those distances to the magnetic field penetration depth λ, which is specific for a given superconductor. To understand this, let us now briefly recall the essential difference between vortex lattice pinning by periodic and quasiperiodic APS. In the former case, if the symmetry of the vortex lattice coincides with that of the pinning array (e.g., for a triangular pinning array; in case of a square APS, transitions

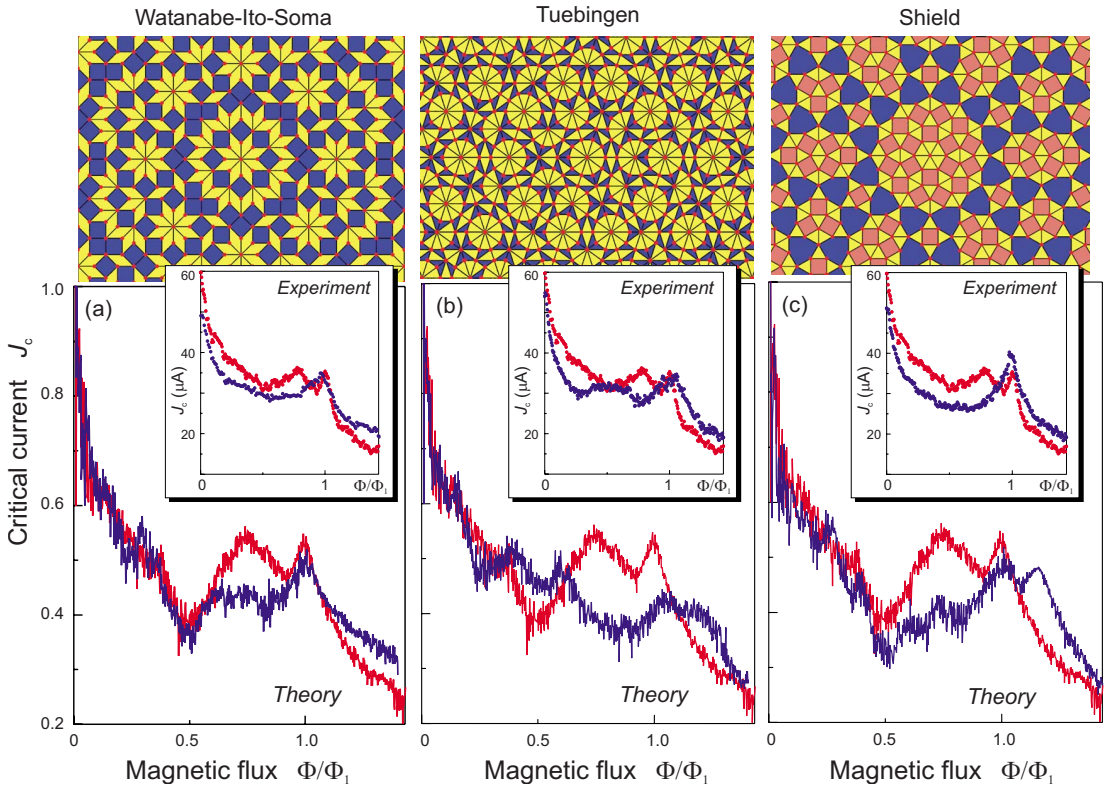

FIG. 3. (Color online) Normalized critical current (experiment and theory), J_c versus normalized magnetic flux, Φ/Φ_1 ($\propto$ number of vortices N_v), for different QP APS [solid blue (dark gray) line]: (a) Watanabe-Ito-Soma tiling, (b) Tuebingen tiling, and (c) Shield tiling. Insets show the corresponding tiling patterns. The function $J_c(\Phi/\Phi_1)$ for a fivefold Penrose-tiling APS is shown by red (gray) line, for comparison.

between the triangular, half-pinned, and square lattices occur—see, e.g., Ref. 31) the vortex lattice and the pinning array are commensurate for any $d_{\mathrm{av}}^{\mathrm{APS}}/\lambda$. In contrast to periodic APS, the pinning efficiency of a QP APS is sensitive to this ratio $d_{\mathrm{av}}^{\mathrm{APS}}/\lambda$ since the elastic deformations of the vortex lattice are involved in its collective pinning by QP APS.

This is explained by the fact that a vortex lattice is incommensurate with any QP tiling (see Refs. 9 and 10). Thus, the efficiency of a QP APS does *not* scale with the density of pinning sites. On the other hand, shifting the broad maximum in $J_c(\Phi)$ toward larger values of Φ, i.e., $\Phi > \Phi_1$, results in the loss of pinning efficiency for $\Phi < \Phi_1$. Moreover, the problem of the effective pinning for magnetic flux for $\Phi > \Phi_1$ is of fundamental interest and, as we show below, is related to a qualitatively different type of flux pinning in aperiodic APS.

The fast drop of $J_c(\Phi)$ for $\Phi > \Phi_1$ is explained by the enhanced mobility of interstitial vortices, which is rather high even in QP APS. Note that a very low concentration of interstitial vortices (as compared to pinned vortices) is sufficient to drastically reduce the critical current. Using the language of conductivity in metals and semiconductors, we can call the motion of interstitial vortices "electronlike vortex conductivity." Correspondingly, the situation $\Phi < \Phi_1$ when there are vacancies, i.e., unoccupied pinning sites, is similar to hole-type conductivity, since in this case the motion of vacancies is similar to the motion of holes in semiconductors. For fluxes $\Phi \lesssim \Phi_1$, the concentration of "holes" is low but the "vortex conductivity" is still provided by the motion of vortices (Fig. 2). However, in contrast to periodic arrays where this motion is possible due to the channeling of vortices [leading to the drop of $J_c(\Phi)$ for $\Phi < \Phi_1$], the process of channeling is strongly suppressed in QP systems (as in metallic quasicrystals where the usual periodic Bloch solution for electrons does not exist[32]). Thus this can explain the presence of the maxima and the fast drop of $J_c(\Phi)$ in QP APS, for $\Phi < \Phi_1$ and for $\Phi > \Phi_1$, correspondingly.

Therefore, the problem is how to immobilize the additional (i.e., electronlike) vortices for $\Phi > \Phi_1$. Although in a QP APS they appear to be less mobile than in periodic APS (no Bloch-type solutions), they can jump to adjacent tiles (hopping conductivity) or "push" pinned vortices and thus unpin them producing secondary interstitial vortices. To prevent this scenario, we propose to immobilize extra vortices in a special way, namely, to create well-separated "reservoirs" for them which themselves are arranged in a *quasiperiodic order*. This will prevent the extra vortices from (i) hopping-type motion (due to the isolation of the reservoirs) and (ii) channeling (due to the QP order).

Among 2D tilings, the Watanabe-Ito-Soma tiling[21,33] (consisting of squares and rhombuses) and Tuebingen tiling[34] (consisting of two types of triangles) shown in the insets of Figs. 3(a) and 3(b), respectively, are possible candidates. These tilings contain isolated "islands" formed by triangles and rhombuses and the density of pinning sites on these islands is rather high. The plots of $J_c(\Phi)$ in Figs. 3(a) and 3(b)

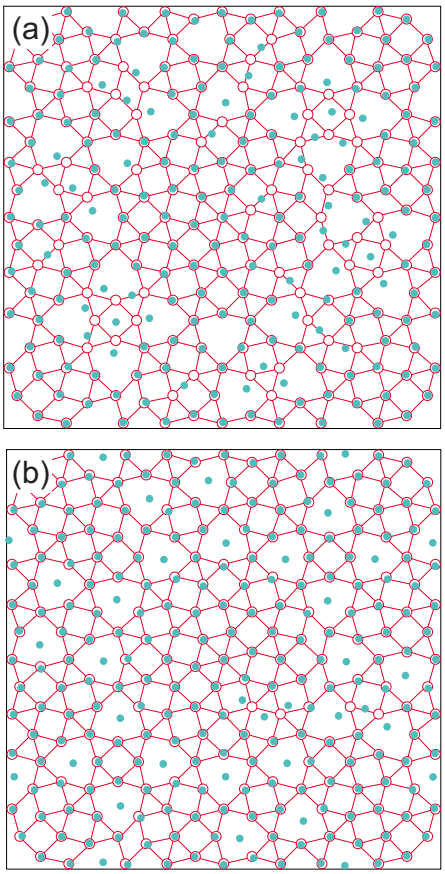

FIG. 4. (Color online) Distribution of vortices in a Shield-tiling APS calculated for: $\Phi=\Phi_1$ (a) and $\Phi=1.18\Phi_1$ (b). The vortices are shown by green (light gray) solid dots while the pinning sites by red (gray) open circles.

show that indeed there is an appreciable increase in the critical current for $\Phi>\Phi_1$, although the overall value of J_c for $\Phi>\Phi_1$ for both tilings is rather low. These features of $J_c(\Phi)$ can be seen in both experimental and theoretical $J_c(\Phi)$ curves. Note that the experimental curves in Figs. 3(a)–3(c) qualitatively [and to a certain extent quantitatively—see Figs. 3(a) and 3(b)] reproduce the features under discussion of the calculated $J_c(\Phi)$ curves, i.e., the enhancement of $J_c(\Phi)$ for $\Phi>\Phi_1$. A more detailed quantitative comparison will require additional analysis of $J_c(\Phi)$ for different parameters of pinning arrays (e.g., radii of the antidots) and various temperatures. Such analysis is beyond the scope of the present work and will be reported elsewhere.[35]

A significant enhancement of $J_c(\Phi)$ for $\Phi>\Phi_1$ is obtained with the Shield tiling[21,36] (with squares, triangles, and threefold hexagons) [Fig. 3(c)]. The large tiles are excellent traps for interstitial vortices (see Fig. 4). These tiles are well separated (i.e., do not have common sides) and are arranged in a QP order [see inset of Fig. 3(c)]. Thus, $J_c(\Phi)$ obtains a pronounced maximum of the same magnitude as the maximum at the first matching flux Φ_1. (However the broad maximum for $\Phi<\Phi_1$ is suppressed, compared to the fivefold Penrose-tiling APS.)

VI. CONCLUSIONS

The critical depinning current $J_c(\Phi)$ was analyzed theoretically and experimentally for different quasiperiodic-tiling arrays of pinning sites. We showed that a fivefold Penrose-tiling APS provides stronger enhancement of $J_c(\Phi)$ than other 2D QP tilings for a broad range of the applied magnetic flux. It was demonstrated that the pinning properties of the Penrose-tiling APS can be improved by using a different modification of the tiling, i.e., nonpisot Penrose tiling. This leads to an overall higher value of J_c for a broader range of magnetic fields. We proposed a mechanism for the flux pinning in QP APS which implies an effective trap and space separation of interstitial vortices. This prevents hopping-type motion and channeling of vortices in the APS and thus results in an increase in the critical current for flux values larger than the matching flux Φ_1. These results might be useful for future applications in microelectronic devices requiring a high J_c over a broad range of the applied flux. Our proposal can be easily extended, mutatis mutandi, to other related systems, including colloidal suspensions interacting with pinning traps provided by arrays of optical tweezers[37] or vortices in rotating Bose-Einstein condensates pinned by potential landscapes created by corotating lasers.[38]

ACKNOWLEDGMENTS

This work was supported by the "Odysseus" Program of the Flemish Government and the Flemish Science Foundation (FWO-Vl), the Interuniversity Attraction Poles (IAP) Programme—Belgian State—Belgian Science Policy, the FWO-Vl, and by the DFG via SFB/TRR21. V.R.M. is grateful to the FWO-Vl for the support of the research stay at the DML (ASI, RIKEN), and to F.N. for hospitality. M.K. gratefully acknowledges support from the Carl-Zeiss-Stiftung, and D.B. from the Evangelisches Studienwerk e.V. Villigst. F.N. acknowledges partial support from the Laboratory of Physical Sciences, National Security Agency, Army Research Office, DARPA, AFOSR, National Science Foundation under Grant No. 0726909, JSPS-RFBR under Contract No. 09-02-92114, Grant-in-Aid for Scientific Research (S), MEXT Kakenhi on Quantum Cybernetics, and Funding Program for Innovative R&D on S&T (FIRST).

[1] J. Gutiérrez, A. Llordés, J. Gázquez, M. Gibert, N. Romà, S. Ricart, A. Pomar, F. Sandiumenge, N. Mestres, T. Puig, and X. Obradors, Nature Mater. **6**, 367 (2007).

[2] V. V. Moshchalkov, M. Baert, V. V. Metlushko, E. Rosseel, M. J. Van Bael, K. Temst, R. Jonckheere, and Y. Bruynseraede, Phys. Rev. B **54**, 7385 (1996).

[3] J. E. Villegas, S. Savel'ev, F. Nori, E. M. Gonzalez, J. V. Anguita, R. García, and J. L. Vicent, Science **302**, 1188 (2003).

[4] R. Wördenweber, P. Dymashevski, and V. R. Misko, Phys. Rev. B **69**, 184504 (2004).
[5] V. R. Misko, S. Savel'ev, A. L. Rakhmanov, and F. Nori, Phys. Rev. Lett. **96**, 127004 (2006); Phys. Rev. B **75**, 024509 (2007).
[6] P. Selders and R. Wördenweber, Appl. Phys. Lett. **76**, 3277 (2000).
[7] P. Lahl and R. Wördenweber, Appl. Phys. Lett. **81**, 505 (2002).
[8] P. Bushev, D. Bothner, J. Nagel, M. Kemmler, K. Konovalenko, A. Loerincz, K. Ilin, M. Siegel, D. Koelle, R. Kleiner, and F. Schmidt-Kaler, arXiv:1009.3425 (unpublished).
[9] V. Misko, S. Savel'ev, and F. Nori, Phys. Rev. Lett. **95**, 177007 (2005).
[10] V. R. Misko, S. Savel'ev, and F. Nori, Phys. Rev. B **74**, 024522 (2006).
[11] J. E. Villegas, M. I. Montero, C.-P. Li, and I. K. Schuller, Phys. Rev. Lett. **97**, 027002 (2006).
[12] M. Kemmler, C. Gürlich, A. Sterck, H. Pöhler, M. Neuhaus, M. Siegel, R. Kleiner, and D. Koelle, Phys. Rev. Lett. **97**, 147003 (2006).
[13] A. V. Silhanek, W. Gillijns, V. V. Moshchalkov, B. Y. Zhu, J. Moonens, and L. H. A. Leunissen, Appl. Phys. Lett. **89**, 152507 (2006).
[14] R. B. G. Kramer, A. V. Silhanek, J. Van de Vondel, B. Raes, and V. V. Moshchalkov, Phys. Rev. Lett. **103**, 067007 (2009).
[15] R. Penrose, Math. Intell. **2**, 32 (1979).
[16] D. Levine and P. J. Steinhardt, Phys. Rev. Lett. **53**, 2477 (1984).
[17] H. C. Jeong and P. J. Steinhardt, Phys. Rev. B **55**, 3520 (1997).
[18] P. J. Steinhardt, H.-C. Jeong, K. Saitoh, M. Tanaka, E. Abe, and A. P. Tsai, Nature (London) **396**, 55 (1998).
[19] *Quasicrystals: The State of the Art*, 2nd ed., edited by P. J. Steinhardt and D. P. Divincenzo (World Scientific, Singapore, 1999).
[20] *Quasicrystals*, edited by J.-B. Suck, M. Schreiber, and P. Häussler (Springer, Berlin, 2002).
[21] B. Grünbaum and G. C. Shephard, *Tilings and Patterns* (W.H. Freeman, New York, 1987).
[22] R. A. Richardson, O. Pla, and F. Nori, Phys. Rev. Lett. **72**, 1268 (1994).
[23] F. Nori, Science **271**, 1373 (1996).
[24] C. J. Olson, C. Reichhardt, and F. Nori, Phys. Rev. B **56**, 6175 (1997).
[25] K. Harada, O. Kamimura, H. Kasai, T. Matsuda, A. Tonomura, and V. V. Moshchalkov, Science **274**, 1167 (1996).
[26] Small variation in this factor is related to slightly different numbers of pinning sites which fit within area A_{qp} for different QP tilings.
[27] M. Kemmler, D. Bothner, K. Ilin, M. Siegel, R. Kleiner, and D. Koelle, Phys. Rev. B **79**, 184509 (2009).
[28] Note that while QP APS contain an infinite number of periodicities, the corresponding diffraction patterns in the reciprocal k space form a QP hierarchical self-similar set of δ peaks of decreasing intensity. As a result, only few periodicities turn out to be significant in QP APS.
[29] We would like to emphasize that using various quasiperiodic pinning arrays we increase the critical current $J_c(\Phi)$ in regions below ($\Phi<\Phi_1$) and above the matching flux ($\Phi>\Phi_1$) where $J_c(\Phi)$ decreases very rapidly in periodic APS. Thus by broadening the maximum in $J_c(\Phi)$ we significantly *enhance* the critical current as compared to the case of periodic APS. However, we do *not* increase the magnitude of the $J_c(\Phi)$ peak at $\Phi=\Phi_1$.
[30] R. Paredes, J. L. Aragón, and R. A. Barrio, Phys. Rev. B **58**, 11990 (1998).
[31] W. V. Pogosov, V. R. Misko, H. J. Zhao, and F. M. Peeters, Phys. Rev. B **79**, 014504 (2009).
[32] B. Freedman, G. Bartal, M. Segev, R. Lifshitz, D. N. Christodoulides, and J. W. Fleischer, Nature (London) **440**, 1166 (2006); Shahar Even-Dar Mandel and R. Lifshitz, arXiv:0808.3659 (unpublished).
[33] Y. Watanabe, M. Ito, and T. Soma, Acta Crystallogr., Sect. A: Found. Crystallogr. **43**, 133 (1987).
[34] M. Baake, P. Kramer, M. Schlottmann, and D. Zeidler, Int. J. Mod. Phys. B **4**, 2217 (1990).
[35] D. Bothner, M. Kemmler, V. R. Misko, F. M. Peeters, F. Nori, R. Kleiner, and D. Koelle, (unpublished).
[36] F. Gähler, in *Quasicrystalline Materials*, edited by Ch. Janot and J. M. Dubois (World Scientific, Singapore, 1988).
[37] J. C. Crocker and D. G. Grier, J. Colloid Interface Sci. **179**, 298 (1996).
[38] S. Tung, V. Schweikhard, and E. A. Cornell, Phys. Rev. Lett. **97**, 240402 (2006).

Publication IX

,

Unusual commensurability effects in quasiperiodic pinning arrays induced by local inhomogeneities of the pinning site density

D. Bothner,[1,*] R. Seidl,[1] V. R. Misko,[2] R. Kleiner,[1] D. Koelle,[1] and M. Kemmler[1]

[1] *Physikalisches Institut – Experimentalphysik II and Center for Collective Quantum Phenomena in LISA*$^+$, *Universität Tübingen, D-72076 Tübingen, Germany*

[2] *Departement Fysica, Universiteit Antwerpen, B-2020 Antwerpen, Belgium*

(Dated: January 31, 2014)

We experimentally investigate the magnetic field dependence of the critical current $I_c(B)$ of superconducting niobium thin films patterned with periodic and quasiperiodic antidot arrays on the submicron scale. For this purpose we monitor current-voltage characteristics at different values of B and temperature T. We investigate samples with antidots positioned at the vertices of two different tilings with quasiperiodic symmetry, namely the Shield Tiling and the Tuebingen Triangle Tiling. For reference we investigate a sample with a triangular antidot lattice. We find modulations of the critical current for both quasiperiodic tilings, which have partly been predicted by numerical simulations but not observed in experiments yet. The particularity of these commensurability effects is that they correspond to magnetic field values slightly above an integer multiple of the matching field. The observed matching effects can be explained by the caging of interstitial vortices in quasiperiodically distributed cages and the formation of symmetry induced giant vortices.

PACS numbers: 74.25.Uv, 74.25.Sv 74.25.Dw, 75.50.Kj

I. INTRODUCTION

Thin film structures constitute the basis for many superconducting microelectronic devices as microwave resonators, superconducting quantum interference devices (SQUIDs), superconducting quantum bits and atom chips. For an operation of the devices in external magnetic fields, which during the last years became of increasing importance for hybrid quantum systems consisting of superconducting circuits and spin ensembles [1–8] or electron spin resonance spectroscopy [9, 10], the film structures must be optimized with regard to dissipation, decoherence and noise induced by the presence of Abrikosov vortices. These undesired consequences of the Shubnikov phase are mainly related to thermal or driven vortex motion, and a well-known approach for their minimization is to pin the vortices at defects in the superconductor [11–15]. It has for example been demonstrated that trapping and pinning the vortices in microfabricated defects as microholes or slots is suitable to reduce the dissipation in coplanar microwave resonators [16–18] and the low-frequency noise in SQUIDs [19].

An important parameter for the pinning efficiency of the defects and its dependence on the magnetic field strength is the spatial defect arrangement [20]. As an ensemble of repulsively interacting Abrikosov vortices tends to order in a hexagonal lattice, the pinning strength of the arrangement on the vortex lattice is given by an interplay of vortex lattice deformation energy and collective pinning energy [21]. Hence, many efforts are taken to investigate the magnetic field dependent pinning properties of different unconventional defect arrangements such as quasiperiodic arrays [22–28], randomly diluted [29, 30], hyperbolic [31] or graded pinning landscapes [32–35]. This is typically done by determining the critical current, the resistance or the ac susceptibility of a film structure patterned with the corresponding defect arrangement and exposed to a magnetic field. While periodic pinning arrays show enhanced pinning properties for few discrete field values, at which vortex density and defect density are integer multiples of each other [36, 37], quasiperiodic arrays have turned out as a valuable alternative, as they have many built-in periodicities to which the vortex lattice can be approximately commensurate [22, 24]. This leads to broadened maxima of the pinning efficiency and to a reduced sensitivity of the sample properties to magnetic field variations.

Very recently, another exciting proposal regarding a pinned vortex lattice has been made [38]. The idea is to use a vortex lattice occupying a nanoengineered pinning array as magnetic potential for ultracold atoms. Besides the possibility to reach potential modulation lengthscales below those achieved by optical potentials, this would allow for an easy generation of unconventional trapping potentials with arbitrary, e.g. quasiperiodic, symmetry. Moreover, it is presumably of importance that the vortex lattice is pinned as strongly as possible in such a hybrid system, as magnetic noise can lead to atom losses and quantum decoherence [39].

In this work, we experimentally investigate the critical current of superconducting niobium thin films with three different arrangements of submicrometer sized holes (antidots), two kinds of quasiperiodic arrays and for reference a triangular lattice. In the two quasiperiodic arrays,

*Electronic address: daniel.bothner@uni-tuebingen.de

in which the antidots are positioned at the vertices of the Shield Tiling (ST) [40] and the Tuebingen Triangle Tiling (TTT) [41], we find unconventionally enhanced critical currents at field values slightly higher than the integer matching fields. These extra matching effects lead to a significant broadening of the critical current maxima at the usual integer matching fields, which is desirable for both microelectronics optimization and the creation of stable unconventional magnetic potentials for atoms. The reported matching effects have been predicted by numerical simulations, but have not been found in earlier experiments on antidot arrays according to the Shield Tiling and the Tuebingen Triangle Tiling [27]. For both tilings, the field values of the unusual additional matching effects can be related to particular structures in the tilings, which induce significant local inhomogeneities of the antidot density. The detailed mechanism behind the effect, however, is presumably different for the two tilings despite their general relation via the local inhomogeneities.

The paper is organized as follows. After the introductory Sec. I, we discuss the sample fabrication and the method for their characterization in Sec. II. In Sec. III we present and discuss the experimental results on the critical current of niobium thin films with antidot arrays arranged in a Shield Tiling and a Tuebingen Triangle Tiling, respectively. We also discuss experimental results on a sample with a hexagonal antidot array for reference. Section IV contains the conclusion of this work.

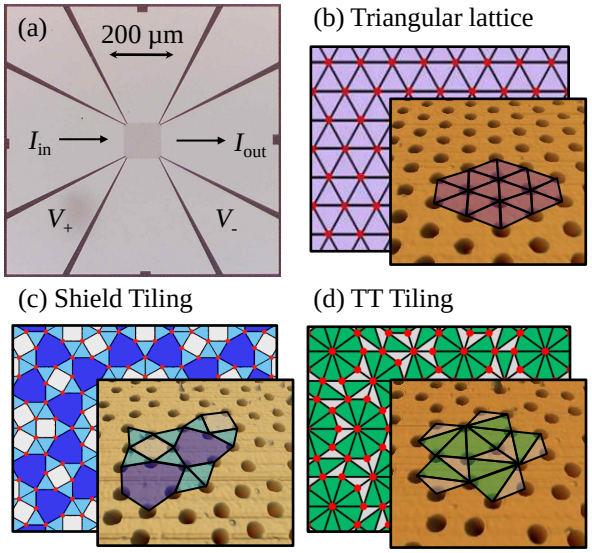

FIG. 1: (Color online) (a) Optical image of a $800 \times 800\,\mu\mathrm{m}^2$ cross-shaped Nb structure (bright parts are Nb) for a four-probe current(I)-voltage(V) characterization of a $100 \times 100\,\mu\mathrm{m}^2$ large area patterned with antidots (center square, slightly darkened by the presence of antidots). (b)-(d) Sketches of the tilings and atomic force microscopy (AFM) images of the antidot arrays showing (b) the triangular lattice, (c) the Shield Tiling and (d) the Tuebingen Triangle Tiling; the antidot density of all arrays is $n_p \approx 2\,\mu\mathrm{m}^{-2}$ and the diameter of the circular antidots is $D \approx 300\,\mathrm{nm}$.

II. SAMPLE FABRICATION AND CHARACTERIZATION

The experiments were carried out on cross-shaped structures patterned in $d = 60\,\mathrm{nm}$ thick dc magnetron sputtered Nb films. Figure 1 (a) shows an optical image of a $800 \times 800\,\mu\mathrm{m}^2$ sample (bright areas are Nb) with a $100 \times 100\,\mu\mathrm{m}^2$ large center area, which is patterned with different arrangements of circular antidots. Independent of the specific arrangement and array symmetry, the antidot density in the center area is $n_p \approx 2\,\mu\mathrm{m}^{-2}$ corresponding to a total number of antidots $N_p \approx 2 \cdot 10^4$ and a matching field $B_1 = n_p \Phi_0 \approx 4\,\mathrm{mT}$. The patterning of the structures including the antidots was performed by electron beam lithography and subsequent SF_6 reactive ion etching.

Each sample contains either a triangular array of antidots or quasiperiodically arranged antidots at the vertices of the Shield Tiling or the Tuebingen Triangle Tiling. The three different patterns and samples are shown in Fig. 1 (b)-(d). A more detailed discussion of the quasiperiodic tilings is given together with the results in Sec. III. The antidots have a diameter $D \approx 300\,\mathrm{nm}$.

The samples were mounted in a low-temperature setup with high temperature variability $4.2\,\mathrm{K} < T < 100\,\mathrm{K}$ and stability $\delta T < 1\,\mathrm{mK}$ [42]. The transition temperature in zero magnetic field was determined with a transport current $I = 50\,\mu\mathrm{A}$ and a 50% resistance criterion as $T_c \approx 8.450\,\mathrm{K}$ for the TTT sample and $T_c \approx 8.465\,\mathrm{K}$ for both the triangular lattice and the ST sample. The normal state resistance slightly above T_c of all samples is $R_n \approx 0.6\,\Omega$, which is related to an approximate resistivity of $\rho \approx 6\,\mu\Omega\mathrm{cm}$. We have considered the cross-shape of the samples in the calculations of ρ by assuming a cross sectional area twice as large as the cross section of the center square as suggested by numerical simulations. Using $\rho l = 3.72 \times 10^{-6}\,\mu\Omega\,\mathrm{cm}^2$ [43] we find an electron mean free path $l \approx 6\,\mathrm{nm}$, indicating that the niobium films are in the "dirty limit" $l \ll \xi_0 = 39\,\mathrm{nm}$.

For the sample characterization in the superconducting state, we record current-voltage characteristics (IVCs) for perpendicular magnetic fields between the critical fields $\pm B_{c2}$ and temperatures close to the transition temperature T_c. We keep the stepwidth between different temperatures ΔT and different values of magnetic field ΔB constant; so for each value of T we have IVCs for all values of B and vice versa. By means of data post-processing, this procedure enables us to extract all information as $I_c(B)$, $T_c(B)$ or $R(B)$-curves for arbitrary voltage criteria V_c, resistance criteria R_c and bias currents I.

Figure 2 shows (a) the critical current $I_c(T, B)$ and (b) the resistance $R(T, B)$ of a sample with a triangular antidot array. From Fig. 2 (a), single vertical and horizontal slices can be extracted, which correspond to $I_c(B)$-curves (dark lines) for constant T and to $T_c(B)$-curves (bright

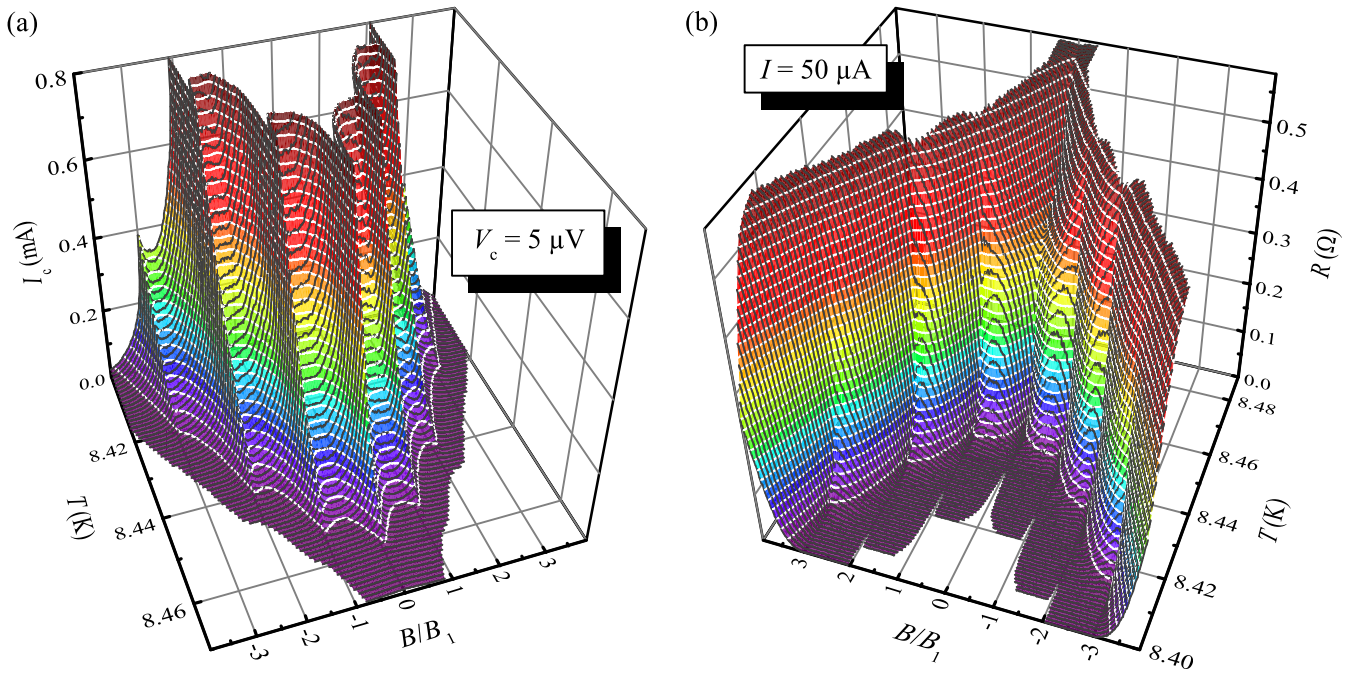

FIG. 2: (Color online) Data for Nb sample with a triangular antidot lattice vs temperature T and magnetic flux density B (normalized to the matching field $B_1 \approx 4\,\mathrm{mT}$). (a) Critical current I_c for a voltage criterion $V_c = 5\,\mu\mathrm{V}$; (b) Resistance $R = V/I$ measured with a bias current $I = 50\,\mu\mathrm{A}$.

lines) for constant I, respectively. Similarly, from Fig. 2 (b) we get $R(B)$-curves for constant T (dark lines) and $T_c(B)$-curves for constant V (bright lines) by taking vertical and horizontal slices, respectively.

The cross shape of the Nb structures used is expected to induce an inhomogeneous current density distribution across the center area. This point has been particularly discussed for a ratchet experiment [44–46], where the direction of the local driving force relative to the intrinsic symmetry axes of the pinning lattice is of great importance. Also in periodic and quasiperiodic potential landscapes with circular antidots, the vortex dynamics might depend on the direction of the local transport current density [47–50]. However, we do not find our experimental results to differ significantly for the two possible perpendicular directions of the bias current. It is most likely anyway that the depinning current density is first reached directly between the voltage pad contact points, where the mean current density reaches its maximum due to the smallest cross sectional area. Hence, we think that the essential results of this work are not influenced by the bridge geometry.

Due to the used voltage amplifier, we had to face a voltage noise of several 10^{-7} V. To improve the signal to noise ratio and the visibility of small matching features, the results presented in this paper are not single-shot raw data but have been averaged and smoothed. We measured five IVCs at each $B-T$ phase space point, each consisting of 1000 data points, and averaged them for the further processing. The averaged IVCs were slightly smoothed by a non weighted five-point adjacent-averaging before we extracted voltages for pre-defined currents or vice versa. To suppress the small remaining noise on the resulting $I_c(B)$, $T_c(B)$ and $R(B)$ slices, which we attribute to slow temperature fluctuations on the order of few hundred μK and with timescales comparable to the data point acquisition rate, we performed another non weighted three-point adjacent-averaging on the individual slices at the very end.

III. EXPERIMENTAL RESULTS

A. The Triangular Lattice

Before we discuss our results on quasiperiodic antidot arrays, we present the results on a sample with the triangular antidot lattice. The data in Fig. 2 reveal clear and strong features, which indicate commensurabilities between the flux line and antidot densities. Pronounced ridges in (a) and canyons in (b) are visible for $B = B_1$ (corresponding to one vortex per antidot). Similar but somewhat weaker structures can be found for flux densities corresponding to two and three vortices per antidot ($B/B_1 = 2$ and $B/B_1 = 3$). The data reveal not only strong commensurability features at integer matching fields, but also weaker ones at fractional matching flux densities $B/B_1 = n/m$ for certain $n,\ m \in \mathbb{N}$.

Figure 3 (a) shows several $I_c(B)$-slices for different temperatures and a voltage criterion $V_c = 1\,\mu\mathrm{V}$. Marked

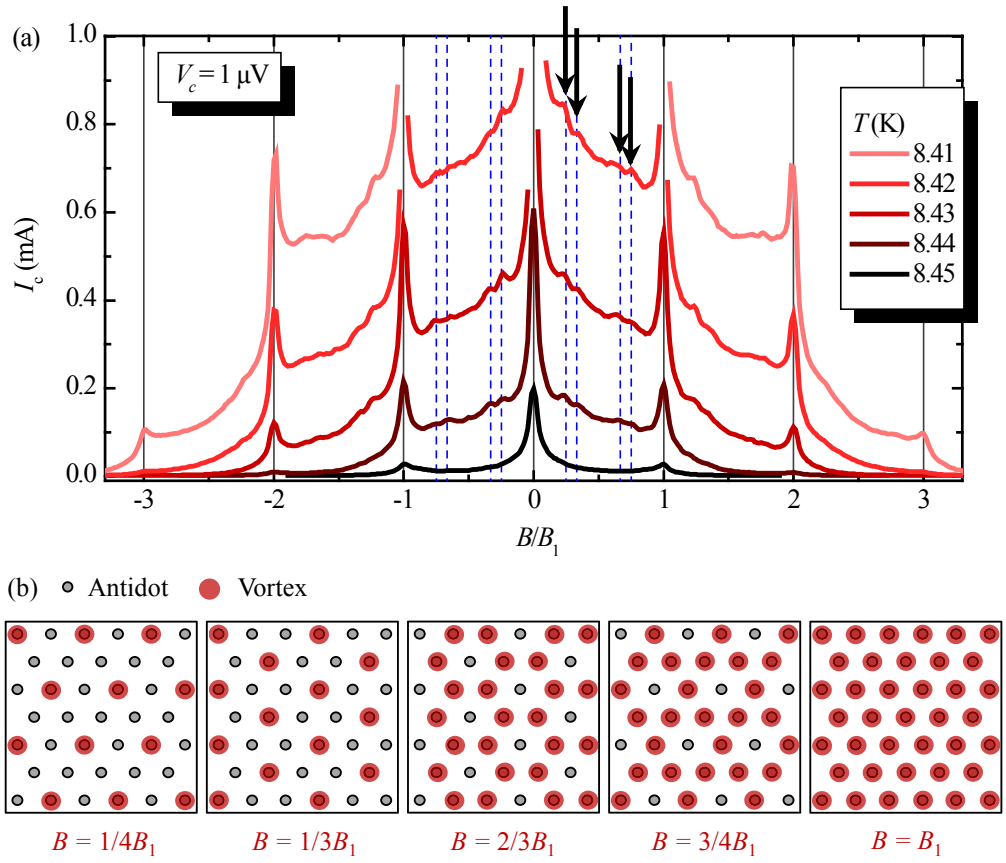

FIG. 3: (Color online) (a) Critical current I_c vs normalized magnetic flux density B/B_1 of a Nb structure with a triangular antidot lattice at five different temperatures T; dashed vertical lines indicate the fractional flux densities $B/B_1 = 1/4, 1/3, 2/3$ and $3/4$ and arrows point to the corresponding local maxima. (b) Sketches of (possible) vortex configurations corresponding to local maxima of I_c at $B/B_1 = 1/4, 1/3, 2/3, 3/4$ and 1.

with arrows between $B = 0$ and B_1, there are four small sub-peaks visible, which we attribute to the fractional filling factors 1/4, 1/3, 2/3 and 3/4 (dashed lines). Corresponding vortex configurations and in addition the one for $B = B_1$ are depicted schematically in Fig. 3 (b). The observed fractional matching peaks for $0 < B < B_1$ and the corresponding vortex configurations have been found in theoretical as well as some experimental studies on triangular pinning lattices before, cf. e.g. [36, 37]. We find very similar peaks for flux densities between $B = B_1$ and $B = 2B_1$,i.e. , for $B/B_1 = 5/4$, $4/3$, $5/3$ and $7/4$, indicating that the same configurations are stable for two-vortex occupations, that is when all antidots are already occupied by one vortex.

B. The Shield Tiling

The Shield Tiling [cf. Fig. 1 (c)] consists of three different tiles: a square, an equilateral triangle and a deformed hexagon with alternating interior angles of $\pi/2$ and $5\pi/6$. Two of these tiles locally resemble the energetically most favorable configurations of a periodic Abrikosov vortex lattice: the triangular and square array. Each hexagon as the third basic shape leaves a rather large antidot-free area, what leads to quasiperiodically distributed cages or reservoirs for interstitial vortices, cf. Ref. [27]. The pattern was created by starting with six hexagonally arranged triangles followed by an iterative application of inflation rules [40].

In a theoretical study on different quasiperiodic pinning arrays, it has been found that the critical current density of a superconductor with antidots arranged in the Shield Tiling shows two pronounced $I_c(B)$ maxima [27]. One of them corresponds to the first matching field $B = B_1$. The second maximum was found for a flux density of $B \approx 1.18B_1$. According to the simulations, this second maximum corresponds to the situation, where all antidots are occupied by one vortex and within each hexagon there is an additional interstitial vortex [27]. These interstitial vortices are caged, i.e., pinned by the repulsive interaction with the six surrounding vortices, which are pinned in the antidots at the hexagon vertices.

In the sample investigated here, we expect the additional maximum at $B \approx 1.16B_1$, which is at a slightly lower value than in Ref. [27]. This difference is due

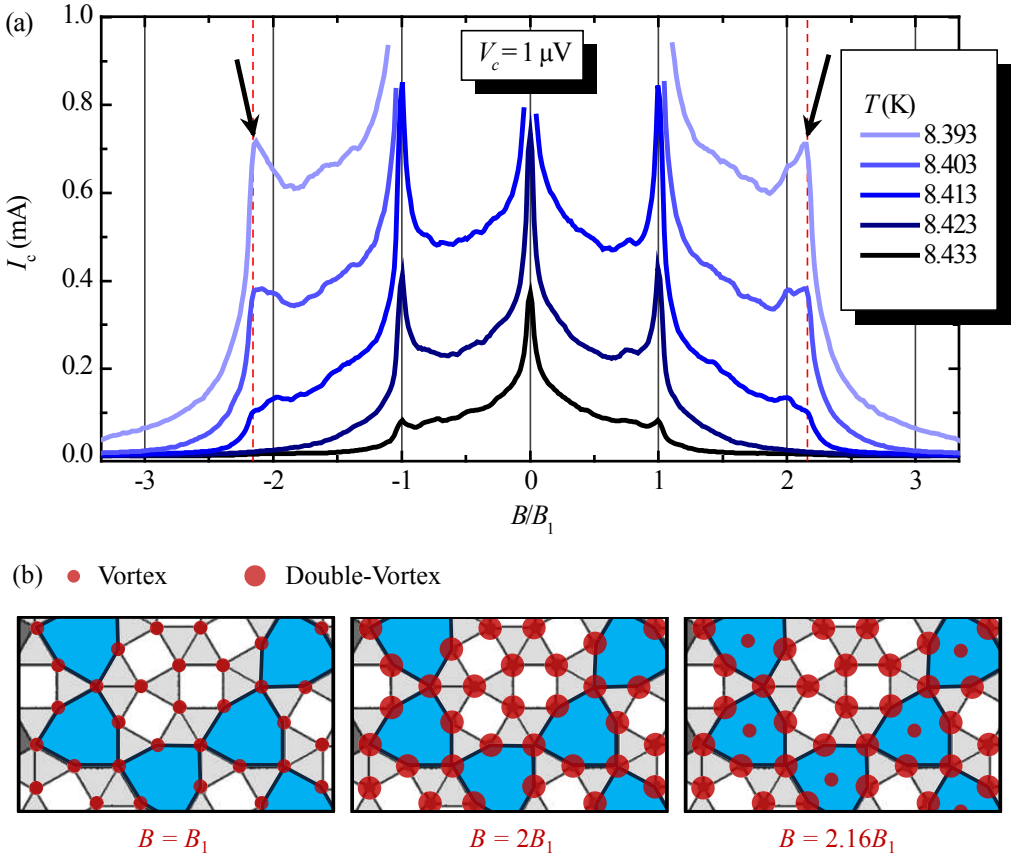

FIG. 4: (Color online) (a) Critical current I_c vs normalized magnetic flux density B/B_1 of a Nb structure with antidots arranged according to the Shield Tiling at five different temperatures T; dashed vertical lines indicate the fractional flux density $B/B_1 = 2.16$ and arrows point to the corresponding local maxima. (b) Sketches of (possible) vortex configurations corresponding to maxima of the critical current at $B/B_1 = 1, 2$ and 2.16.

to the fact that the maximum is expected at $B = (1 + N_h/N_p)B_1$, where N_h and N_p is the total number of hexagons and antidots, respectively. In the numerical approach in Ref. [27] $N_p \approx 500$ pinning sites with $N_h/N_p \approx 0.18$ have been used. In our experimentally used array with $N_p \approx 20000$ antidots we have $N_h/N_p \approx 0.16$.

Fig. 4 (a) shows $I_c(B)$-curves of the Shield Tiling sample at several different temperatures. At $B = 1.16B_1$ no peak is visible but only a strong and single maximum of the critical current at $B = B_1$. At lower temperatures, however, a double-peak structure appears around the second matching field with one peak at $B = 2B_1$ and one at a slightly higher field value $B \approx 2.16B_1$. This additional peak – or more precisely speaking its height relative to the one at $B = 2B_1$ – has a strong dependence on temperature. It is almost absent at $T = 8.413\,\mathrm{K}$ but then grows and becomes the dominating peak at $T = 8.393\,\mathrm{K}$. A very similar relation and development between two peaks with temperature has been reported for caged vortices in periodic pinning arrays before [51, 52] and might be attributed to an increasing interaction strength between the vortices due to a decreasing penetration depth.

In contrast to the results of earlier simulations [27], the additional matching peak does not appear above the first matching field but above the second. It is likely that in the samples used for the experiments singly occupied antidots are still too attractive for vortices entering the sample above $B = B_1$. Hence, they first occupy the antidots doubly before the centers of the hexagons become energetically more favorable. In Fig. 4 (b) the corresponding vortex configurations are sketched. Of course, the situation depicted here is somewhat idealized. In simulations we find similar configurations, but we also find a certain degree of disorder in the vortex lattice in any case. According to that, it might well be that at $B = 2B_1$ not all six antidots of the hexagons are doubly occupied. It is rather likely that one or two of them only host one vortex, while there are also interstitials present. The simulations we refer to here are not shown, as they were not performed exactly with the experimental parameters. However, they served as an inspiration for the proposed vortex configurations.

The discussed observations of commensurabilities in the Shield tiling are closely related to widely discussed caging effects in different kinds of periodic pinning arrays,

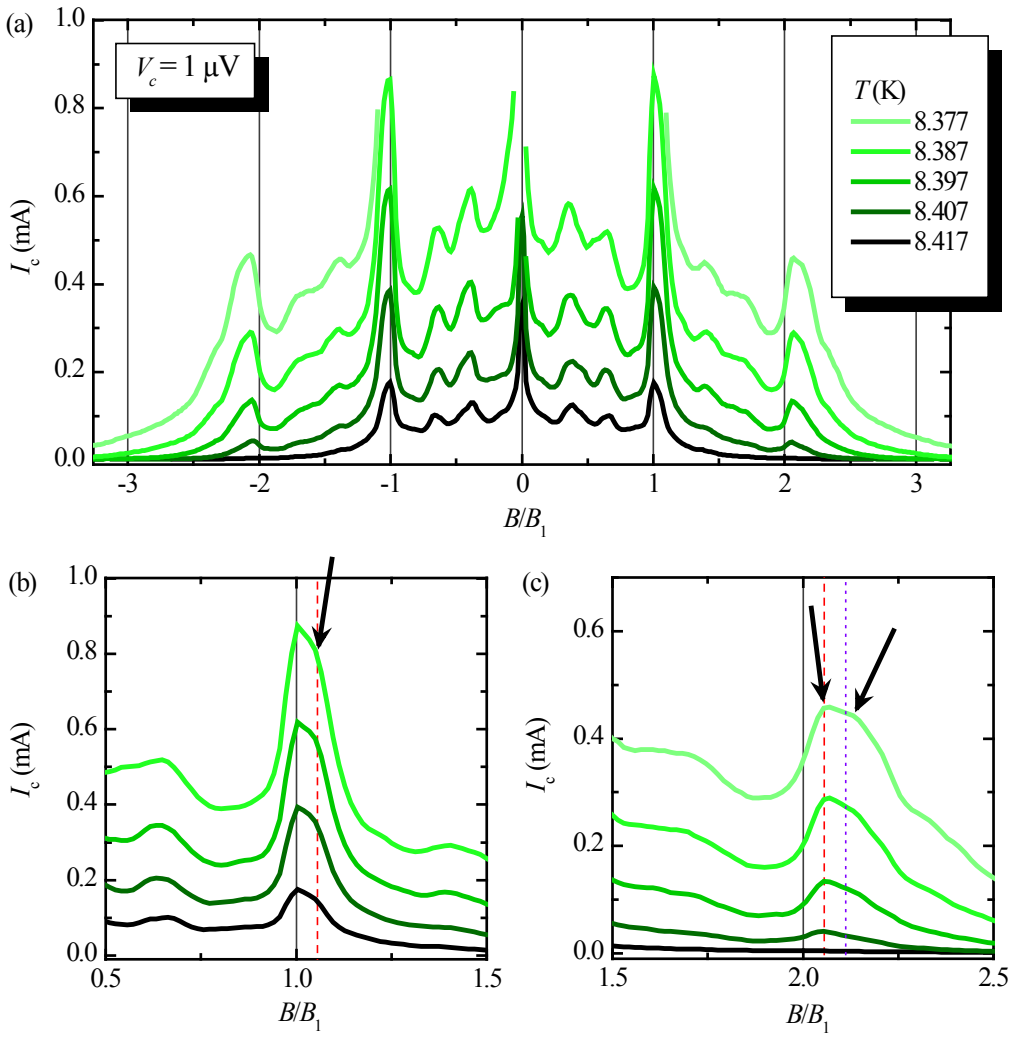

FIG. 5: (Color online) (a) Critical current I_c vs normalized magnetic flux density B/B_1 of a Nb structure with antidots arranged according to the Tuebingen Triangle Tiling at five different temperatures T; (b) and (c) show $I_c(B)$ in more detail at $B \approx B_1$ and $2B_1$, respectively. Arrows point to the maxima slightly above $B = B_1$ and $B = 2B_1$; dashed and dotted vertical lines mark the flux densities $B/B_1 = 1 + 1/\tau^6$ ((b), dashed), $B/B_1 = 2 + 1/\tau^6$ ((c), dashed) and $B/B_1 = 2 + 2/\tau^6$ ((c), dotted).

including randomly or periodically diluted triangular lattices [29, 30, 51, 53]. These studies have revealed that matching peaks can be shifted to higher field values than those for which vortex and antidot densities are equal. Whenever there are areas with locally reduced antidot density, these areas are filled up with interstitials, when the antidots are saturated, and these configurations with interstitials can be more stable than the configurations without interstitials.

C. The Tuebingen Triangle Tiling

The second quasiperiodic arrangement, the Tuebingen Triangle Tiling, is depicted in Fig. 1 (d). It consists of two different isosceles triangles, one acute-angled and one obtuse angled. This tiling can be constructed by an iterative application of inflation rules [41] after a starting configuration of ten acute-angled triangles. In contrast to the triangular lattice and the Shield tiling, the edge lengths are not equal for all basic shapes here, but we find two different lengths, whose ratio is the golden mean $\tau = (1 + \sqrt{5})/2 \approx 1.618$. This leads to a locally reduced pinning site density, when ten triangles are composed in a ring-like structure, as for example in the corners of Fig. 1 (d). Below, these full rings with ten antidots surrounding one as a circle are called 10/10-circles.

The 10/10-circles have a high antidot line density on the circle and a reduced density in the interior and may again be viewed as cages or reservoirs for interstitial vortices. In contrast to the cages in the Shield Tiling we here find the situation that there is one antidot in the center of each 10/10-circle. Analogously to the Shield Tiling discussion we have to calculate the ratio of the

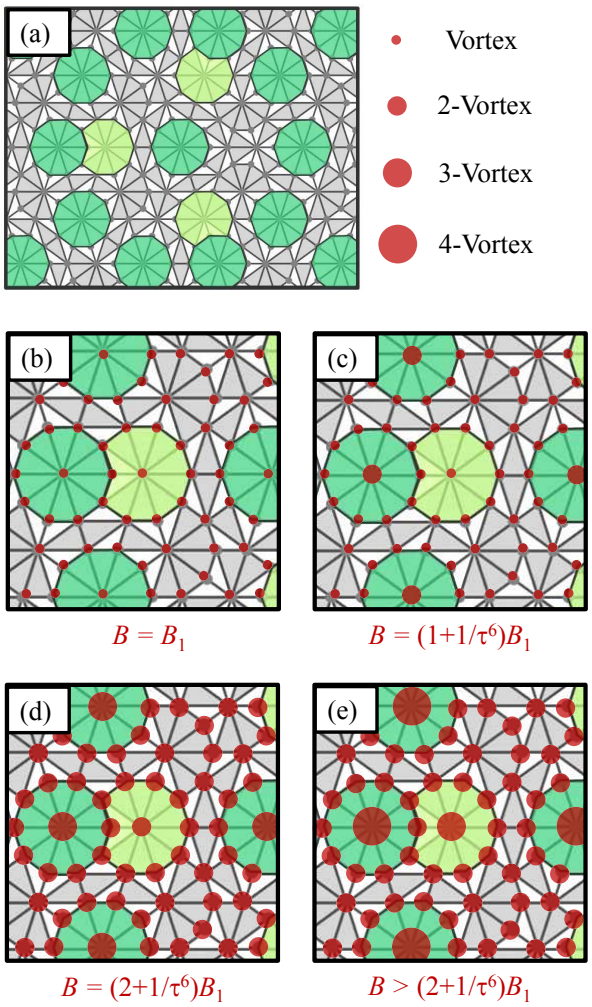

FIG. 6: (Color online) (a) Sketch of a part of the Tuebingen Triangle Tiling with colored 10/10-circles and 9/10-circles. (b)-(e) Possible vortex configurations related to the critical current maxima at (b) $B = B_1$, (c) $B = (1 + \tau^6)B_1$, (d) $B = (2 + \tau^6)B_1$ and (e) $B > (2 + \tau^6)B_1$ including higher order giant vortices.

number of 10/10-circles N_{10} over the total number of antidots N_p in order to assign the appearance of local maxima in $I_c(B)$ to vortex configurations related to the number of circles. This ratio is found to be $N_{10}/N_p = 1/\tau^6 \approx 0.056$ for $N_p \to \infty$, as after each iteration the total number of antidots increases by a factor of τ^2, i.e., $N_p^i = \tau^2 N_p^{i-1}$ for the ith iteration. After three iterations each antidot has transformed into a 10/10-circle, i.e., $N_{10}^i = N_p^{i-3} = (1/\tau^6)N_p^i$.

Figure 5 (a) shows $I_c(B)$-curves of the Tuebingen Triangle Tiling sample at five different temperatures. There are two strong sub-peaks for flux densities $B \approx 0.39B_1$ and $B \approx 0.65B_1$. Similarly to the triangular lattice this substructure for (probably irrational) fractionals of B_1 repeats itself with a somewhat smaller amplitude between $B = B_1$ and $2B_1$. This characteristic double-peak structure has been found in earlier investigations [27] at approximately the same values as in the present work. However, we have not found a simple connection between the field values at which these peaks appear and certain vortex configurations.

Figure 5 (b) reveals a peak structure around $B = B_1$, where two peaks seem to be merged into a broad one with two kinks at $B = B_1$ and at a slightly higher value (marked by arrow). The vertical dashed line indicates the position of $B = (1 + 1/\tau^6)B_1$ and matches very well the flux density value of the second kink. The second peak hence can be attributed to the flux value, where each antidot is occupied by one vortex and one additional vortex per 10/10-circle has entered the sample. One possibility is that each additional vortex occupies an interstitial position somewhere inside the circle or that the additional vortex pushes the vortex out of the center antidot, so that the two of them symmetrically occupy the circle interior as interstitials. We favour a third possibility.

The idea is connected to a recent imaging experiment of vortices in a quasiperiodic Penrose pinning array [54], which revealed the symmetry-induced formation of giant vortices. Relating our results to the reported observation, it is conclusive that in the Tuebingen Triangle Tiling each center antidot of the 10/10-circles is occupied by a double-vortex at $B = (1 + 1/\tau^6)B_1$, while all other pinning sites are occupied by one vortex. This double-vortex is supposed to compensate for the magnetic pressure from the surrounding vortices on the ten vortices pinned at the circle line. Exactly this vortex configuration with ten vortices forming a circle and one double-vortex in its center was found in Ref. [54] for pinning sites arranged in the Penrose tiling. In the Penrose pattern, however, the 10/10-circle is not complete, but has three pinning site free positions. The fact that the giant vortex configuration forms there anyway, strongly indicates its energetic favorability, which is probably even enhanced in the Tuebingen Triangle Tiling with complete 10/10-circles. Figure 6 depicts (a) the Tuebingen Triangle Tiling and possible vortex configurations corresponding to (b) $B = B_1$ and (c) $B = (1 + 1/\tau^6)B_1$.

Similarly to the results of the Shield Tiling sample, we find unusual features in $I_c(B)$ of the Tuebingen Triangle Tiling sample around $B = 2B_1$, cf. Fig. 5 (c). Surprisingly, there is no maximum visible at $B = 2B_1$. Nevertheless there is a double peak structure similar to the one around the first matching field. The first kink of the structure is approximately at a value $B = (2 + 1/\tau^6)B_1$ (dashed vertical line) and the second at a somewhat higher value, but not exactly at $B = (2+2/\tau^6)B_1$ (dotted line). The interpretation of the first peak in terms of vortex configurations is obvious. All antidots are occupied by two vortices, whereas those antidots in the center of a 10/10-circle are occupied by three, cf. Fig. 6 (d). The absence of the peak at $2B_1$ indicates that a third vortex in the center antidot is necessary to stabilize the configuration.

Analogously to the peak at $B = (1+1/\tau^6)B_1$ we would

expect a maximum when the antidots in the 10/10-circle center are occupied by twice the number of vortices as the surrounding pinning sites, i.e., by four vortices. The second kink of the double peak, however, is found at a higher value than $B = (2+2/\tau^6)B_1$ (dotted vertical line). We believe, that in this second peak another structure in the Tuebingen Triangle Tiling becomes relevant, which we call the 9/10-circle. The 9/10-circle is almost identical to the 10/10-circle but with one of the ten circle antidots sitting at a closer position to the center. In Fig. 6 (a) three 9/10-circles are visible in between the center 10/10-circle and the ten 10/10-circles surrounding the center. The 9/10-circles are always directly neighboring a 10/10-circle forming an eight-like structure. One possibility for a stable vortex configuration is sketched in Fig. 6 (e), where the center antidots of the 10/10-circles are occupied by four vortices, the center antidots of the 9/10-circles are occupied by three vortices and all other antidots by a double-vortex. Unfortunately, we cannot give an analytical expression for the corresponding flux density value, as we were not able to determine the ratio of the number of 9/10-circles to the total number of antidots.

Probably one has to consider more complicated configurations including interstitial vortices and also present 8/10-circles to find the true vortex configurations. Furthermore, there seem to be some more small shoulders and peaks above $2B_1$, which we cannot unambiguously attribute to simple vortex configurations.

IV. CONCLUSIONS

In conclusion, we have experimentally investigated the critical current of niobium thin films with periodic and quasiperiodic microtopology. We have done this by means of transport characterization measurements and discussed the results with the focus on unconventional commensurability effects. For both investigated quasiperiodic antidot arrangements, we have found matching effects for flux densities slightly larger than the matching flux which have not been observed before in similar experiments. The presented results, however, are consistent with and complementary to recent predictions obtained by numerical simulations. We attribute the reported matching effects to the caging of Abrikosov vortices in quasiperiodically distributed antidot-free hexagons and to the formation of giant vortices. Both mechanisms are related to a locally reduced antidot density with respect to the surrounding. The reported observations extend the accessible range of strong matching between vortices and pinning sites in quasiperiodic arrays from field values below and directly at the matching fields to field values above the matching field. Moreover, they lead to a broadened maximum of the critical current compared to a periodic pinning array. This might help to optimize superconducting microelectronic devices for an efficient operation in magnetic environments and could be used to generate stable magnetic potentials for ultracold atoms with unconventional quasiperiodic symmetry. To finally confirm our interpretations of the matching effects and to decide which vortex configurations are correct,however, it will be necessary to carry out imaging experiments such as magneto-optical imaging, Bitter decoration or Hall probe microscopy.

This work has been supported by the European Research Council via SOCATHES and by the Deutsche Forschungsgemeinschaft via the SFB/TRR 21. DB gratefully acknowledges support by the Evangelisches Studienwerk e.V. Villigst. MK gratefully acknowledges support by the Carl-Zeiss Stiftung. VRM gratefully acknowledges support by the “Odysseus” Program of the Flemish Government and the Flemish Science Foundation (FWO-VI). The authors thank Franco Nori for fruitful discussions on quasiperiodic pinning arrays.

[1] P. Rabl, D. DeMille, J. M. Doyle, M. D. Lukin, R. J. Schoelkopf, and P. Zoller, Phys. Rev. Lett. **97**, 033003 (2006)
[2] D. Petrosyan and M. Fleischhauer, Phys. Rev. Lett. **100**, 170501 (2008)
[3] J. Verdú, H. Zoubi, C. Koller, J. Majer, H. Ritsch, and J. Schmiedmayer, Phys. Rev. Lett. **103**, 043603 (2009)
[4] Y. Kubo, C. Grezes, A. Dewes, T. Umeda, J. Isoya, H. Sumiya, N. Morishita, H. Abe, S. Onoda, T. Ohshima, V. Jacques, A. Dréau, J.-F. Roch, I. Diniz, A. Auffeves, D. Vion, D. Esteve, and P. Bertet, Phys. Rev. Lett. **107**, 220501 (2011)
[5] X. Zhu, S. Saito A. Kemp K. Kakuyanagi S. Karimoto H. Nakano, W. J. Munro, Y. Tokura, M. S. Everitt K. Nemoto, M. Kasu, N. Mizuochi, and K. Semba, Nature **478**, 221 (2011)
[6] S. Probst, H. Rotzinger, S. Wünsch, P. Jung, M. Jerger, M. Siegel, A. V. Ustinov, and P. Bushev, Phys. Rev. Lett. **110**, 157001 (2013)
[7] S. Bernon, H. Hattermann, D. Bothner, M. Knufinke, P. Weiss, F. Jessen, D. Cano, M. Kemmler, R. Kleiner, D. Koelle, and J. Fortágh, Nat. Commun. **4**, 2380 (2013)
[8] D. Bothner, M. Knufinke, H. Hattermann, R. Wölbing, B. Ferdinand, P. Weiss, S. Bernon, J. Fortágh, D. Koelle, and R. Kleiner, New J. Phys.**15**, 093024 (2013)
[9] P. Bushev, A. K. Feofanov, H. Rotzinger, I. Protopopov, J. H. Cole, C. M. Wilson, G. Fischer, A. Lukashenko, and A. V. Ustinov, Phys. Rev. B **84**, 060501(R) (2011)
[10] C. Clauss, D. Bothner, D. Koelle, R. Kleiner, L. Bogani, M. Scheffler, and M. Dressel, Appl. Phys. Lett. **102**, 092601 (2013)
[11] H. Raffy, J. C. Renard, and E. Guyon, Solid State Commun. **11**, 1679 (1972)
[12] O. Daldini, P. Martinoli, J. L. Olsen, and G. Berner, Phys. Rev. Lett. **32**, 218 (1974)
[13] A. T. Fiory, A. F. Hebard, and S. Somekh, Appl. Phys.

Lett. **32**, 73 (1978)
[14] M. Baert, V. V. Metlushko, R. Jonckheere, V. V. Moshchalkov, and Y. Bruynseraede, Phys. Rev. Lett. **74**, 3269 (1995)
[15] J. I. Martín, M. Veléz, J. Nogués, and I. K. Schuller, Phys. Rev. Lett. **79**, 1929 (1997)
[16] C. Song, M. P. DeFeo, K. Yu, and B. L. T. Plourde, Appl. Phys. Lett. **95**, 232501 (2009)
[17] D. Bothner, T. Gaber, M. Kemmler, D. Koelle, and R. Kleiner, Appl. Phys. Lett. **98**, 102504 (2011)
[18] D. Bothner, C. Clauss, E. Koroknay, M. Kemmler, T. Gaber, M. Jetter, M. Scheffler, P. Michler, M. Dressel, D. Koelle, and R. Kleiner Appl. Phys. Lett. **100**, 012601 (2012)
[19] P. Selders and R. Wördenweber, Appl. Phys. Lett. **76**, 3277 (2000)
[20] M. Vélez, J. I. Martín, J. E. Villegas, A. Hoffmann, E. M. González, J. L. Vicent,and I. K. Schuller, J. Magn. Magn. Mater. **320**, 2547 (2008)
[21] G. R. Berdiyorov, M. V. Milošević, and F. M. Peeters, Phys. Rev. B **76**, 134508 (2007)
[22] V. Misko, S. Savel'ev, and F. Nori, Phys. Rev. Lett. **95**, 177007 (2005)
[23] V. R. Misko, S. Savel'ev, and F. Nori, Phys. Rev. B **74**, 024522 (2006)
[24] M. Kemmler, C. Gürlich, A. Sterck, H. Pöhler, M. Neuhaus, M. Siegel, R. Kleiner, and D. Koelle, Phys. Rev. Lett. **97**, 147003 (2006)
[25] J. E. Villegas, M. I. Montero, C.-P. Li, and I. K. Schuller, Phys. Rev. Lett. **97**, 027002 (2006)
[26] A. V. Silhanek, W. Gillijns, V.-V. Moshchalkov, B. Y. Zhu, J. Moonens, and L. H. A. Leunissen, Appl. Phys. Lett. **89**, 152507 (2006)
[27] V. R. Misko, D. Bothner, M. Kemmler, R. Kleiner, D. Koelle, F. M. Peeters, and F. Nori, Phys. Rev. B **82**, 184512 (2010)
[28] S. Rablen, M. Kemmler, T. Quaglio, R. Kleiner, D. Koelle, and I. V. Grigorieva, Phys. Rev. B **84**, 184520 (2011)
[29] C. Reichhardt and C. J. Olson Reichhardt, Phys. Rev. B **76**, 094512 (2007)
[30] M. Kemmler, D. Bothner, K. Ilin, M. Siegel, R. Kleiner, and D. Koelle, Phys. Rev. B **79**, 184509 (2009)
[31] V. R. Misko and F. Nori, Phys. Rev. B **85**, 184506 (2012)
[32] D. Ray, C. J. Olson Reichhardt, B. Jankó, and C. Reichhardt, Phys. Rev. Lett. **110**, 267001 (2013)
[33] Y. L. Wang, M. L. Latimer, Z. L. Xiao, R. Divan, L. E. Ocola, G. W. Crabtree, and W. K. Kwok, Phys. Rev. B **87**, 220501(R) (2013)
[34] M. Motta, F. Colauto, W. A. Ortiz, J. Fritzsche, J. Cuppens, W. Gillijns, V. V. Moshchalkov, T. H. Johansen, A. Sanchez, and A. V. Silhanek, Appl. Phys. Lett. **102**, 212601 (2013)
[35] S. Guénon, Y. J. Rosen, A. C. Basaran, and I. K. Schuller, Appl. Phys. Lett. **102**, 252602 (2013)
[36] C. Reichhardt, and N. Grønbech-Jensen, Phys. Rev. B **63**, 054510 (2001)
[37] S. Ooi, T. Mochiku, and K. Hirata, Physica C **469**, 1113 (2009)
[38] O. Romero-Isart, C. Navau, A. Sanchez, P. Zoller, and J. I. Cirac, Phys. Rev. Lett. **111**, 145304 (2013)
[39] G. Nogues, C. Roux, T. Nirrengarten, A. Lupaşcu, A. Emmert, M. Brune, J.-M. Raimond, S. Haroche, B. Plaçais, and J.-J. Greffet, Eur. Phys. Lett. **87**, 13002 (2009)
[40] F. Gähler, Quasicrystalline Materials , edited by Ch. Janot and M. J. Dubois (World Scientific, Singapore, 1988)
[41] M. Baake, P. Kramer, M. Schlottmann, and D. Zeidler, Int. J. Mod. Phys. B **4**, 2217 (1990)
[42] The absolute values of T have an uncertainty of $\pm 0.5\,\mathrm{K}$ due to the uncertainty in the calibration of the temperature sensor.
[43] A. F. Mayadas, R. B. Laibowitz, and J. J. Cuomo, J. Appl. Phys. **43**, 1287 (1972)
[44] E. M. Gonzalez, N. O. Nunez, J. V. Anguita, and J. L. Vicent, Appl. Phys. Lett. **91**, 062505 (2007)
[45] A. V. Silhanek, J. Van de Vondel, V. V. Moshchalkov, A. Leo, V. Metlushko, B. Ilic, V. R. Misko, and F. M. Peeters, Appl. Phys. Lett. **92**, 176101 (2008)
[46] E. M. Gonzalez, N. O. Nunez, J. V. Anguita, and J. L. Vicent, Appl. Phys. Lett. **92**, 176102 (2008)
[47] C. Reichhardt and F. Nori, Phys. Rev. Lett. **82**, 414 (1999)
[48] A. V. Silhanek, L. Van Look, S. Raedts, R. Jonckheere, and V. V. Moshchalkov, Phys. Rev. B **68**, 214504 (2003)
[49] J. E. Villegas, E. M. Gonzalez, M. I. Montero, Ivan K. Schuller, and J. L. Vicent, Phys. Rev. B **68**, 224504 (2003)
[50] C. Reichhardt and C. J. Olson Reichhardt, Phys. Rev. Lett. **106**, 060603 (2011)
[51] G. R. Berdiyorov, M. V. Milošević, and F. M. Peeters, Phys. Rev. B **74**, 174512 (2006)
[52] G. R. Berdiyorov, M. V. Milošević, and F. M. Peeters, Europhys. Lett. **74**, 493 (2006)
[53] M. L. Latimer, G. R. Berdiyorov, Z. L. Xiao, W. K. Kwok, and F. M. Peeters, Phys. Rev. B **85**, 012505 (2012)
[54] R. B. G. Kramer, A. V. Silhanek, J. Van de Vondel, B. Raes, and V. V. Moshchalkov, Phys. Rev. Lett. **103**, 067007 (2009)